Deflections and Natural Frequencies as Parameters for Structural Health Monitoring

The Effect of Fatigue and Corrosion on the Deflections and the Natural Frequencies of Reinforced Concrete Beams

Veerman, Rene

DOI
10.4233/uuid:45f42dab-8427-4113-ba56-50c9e7171a36

Publication date
2017

Document Version
Final published version

Citation (APA)
Veerman, R. (2017). *Deflections and Natural Frequencies as Parameters for Structural Health Monitoring: The Effect of Fatigue and Corrosion on the Deflections and the Natural Frequencies of Reinforced Concrete Beams*. [Dissertation (TU Delft), Delft University of Technology]. https://doi.org/10.4233/uuid:45f42dab-8427-4113-ba56-50c9e7171a36

Deflections and Natural Frequencies as Parameters for Structural Health Monitoring

The Effect of Fatigue and Corrosion on the Deflections and the Natural Frequencies of Reinforced Concrete Beams

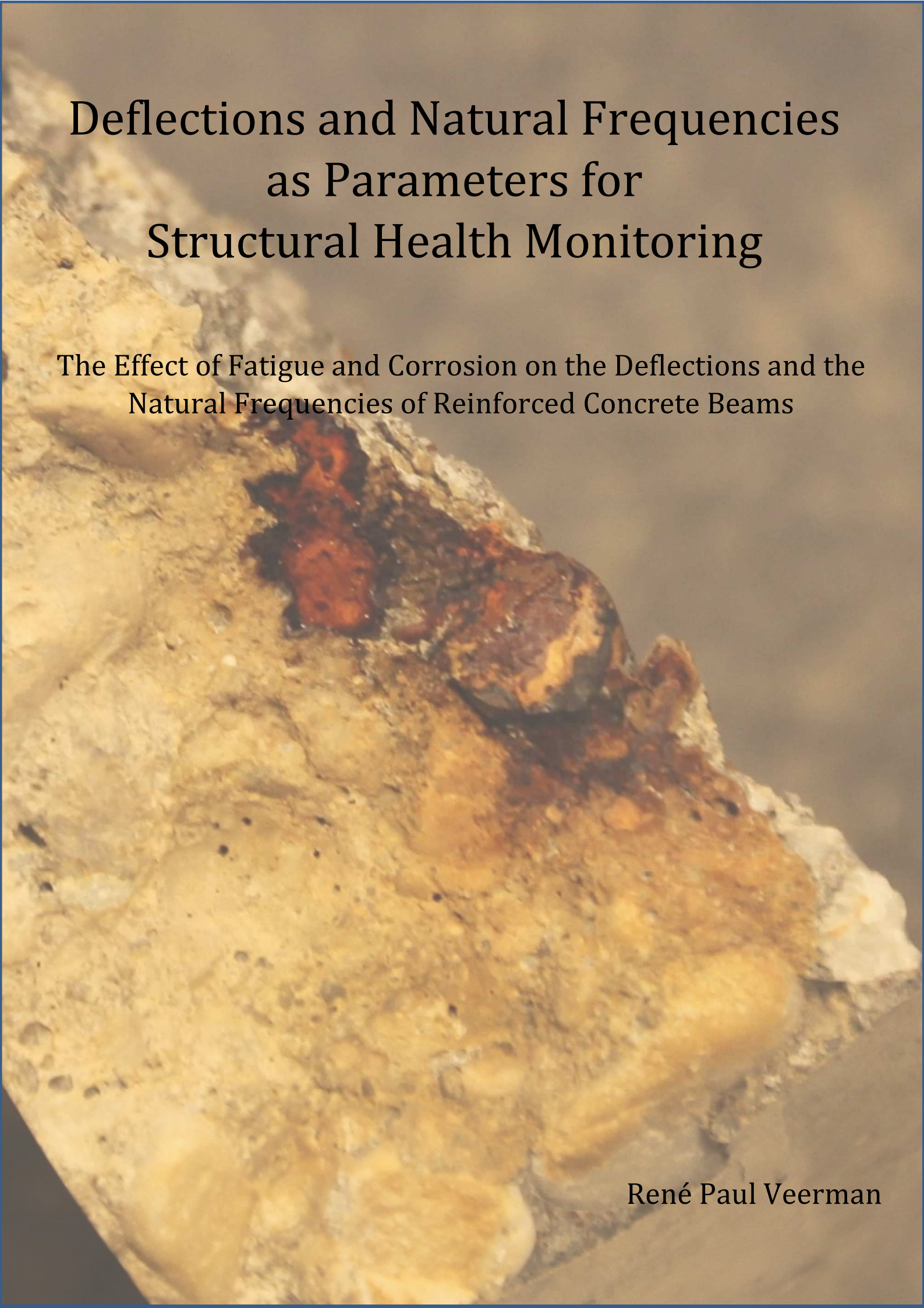

René Paul Veerman

Deflections and Natural Frequencies as Parameters of Structural Health Monitoring

The Effect of Fatigue and Corrosion on the Deflections and the Natural Frequencies of Reinforced Concrete Beams

Proefschrift

Ter verkrijging van de graad doctor
aan de Technische Universiteit Delft,
op gezag van Rector Magnificus prof.ir. K.C.A.M. Luyben,
voorzitter van het College voor promoties,
in het openbaar te verdedigen op
donderdag 7 december 2017 om 15:00 uur

door

René Paul VEERMAN

civiel ingenieur
geboren te Naarden, Nederland

This dissertation has been approved by the promoters:

Prof.dr.ir. K. van Breugel	Delft University of Technology
Prof.dr.ir. E.A.B. Koenders	Darmstadt University of Technology

Composition of the doctoral committee:

Rector Magnificus	chairman
Prof.dr.ir. K. van Breugel	Delft University of Technology
Prof.dr.ir. E.A.B. Koenders	Darmstadt University of Technology
Dr.ir. T.A. van Beek	SKG-IKOB

Independent members:

Prof.dr.-ing. R. Breitenbücher	Ruhr-University Bochum
Prof.dr. J.N. Kok	Leiden University
Prof.dr.ir. D.A. Hordijk	Delft University of Technology
Prof.dr. R.B. Polder	Delft University of Technology

This research is supported by the Dutch Technology foundation STW, which is part of the Netherlands Organization for Scientific Research (NWO) and partly funded by the Ministry of Economic Affairs (project number 19070). The project is part of the STW Perspective program “Integral Solution for Sustainable Construction (IS2C)”.

Printed by: Delft Academic Press

ISBN: 9789065624161

Table of Contents

Chapter 1

General Introduction

Asset owners would like to have an early warning system that detects malfunction of structures. Thanks to an early warning system, appropriate actions can be taken to prevent dangerous situations and to optimize maintenance plans. Measurements from sensors in a Structural Health Monitoring (SHM) system can be used as input for such early warning system. In this dissertation the possibilities for using measurements of sensors in a SHM system in a warning system are outlined. The study “Deflections and Natural Frequencies as Parameters for Structural Health Monitoring” in this dissertation is one of the three studies of the InfraWatch research project. This chapter gives insight in the outline of the InfraWatch project, the aim of the study “Deflections and Natural Frequencies as Parameters for Structural Health Monitoring” within the project, and the outline of this dissertation.

1.1 Research background

Concrete bridges make up a large part of the Dutch road infrastructural network [1]. The financial consequences and social impacts of malfunction of bridges can be enormous. It is, therefore, important to know how fast degradation of concrete bridges occurs and how fast the load bearing capacity of a concrete bridge reduces.

The Dutch road infrastructural network contains more than 40,000 bridges and viaducts [2]. 3500 of these bridges and viaducts are concrete bridges in the highway road network. 60% of these concrete bridges were built before 1975 [3]. It is possible that these bridges are approaching the end of their service-life.

Concrete bridges built before 1975 were designed with a limited concrete cover (15-30 mm) [4]. The probability that chlorides and other harmful substances reach the steel reinforcement is higher at a small concrete cover than at a large concrete cover. When chlorides and other harmful substances reach the steel reinforcement, the reinforcement starts to corrode. When this happens, degradation of these bridges can occur relatively fast. As result of degradation processes, the strength of concrete bridges decreases. On the other hand, progressing hydration of the cement increases the strength and the density of concrete in time. To discover whether a bridge becomes stronger due to the continuous hydration or weaker as result of degradation processes, each bridge should be investigated separately.

In the past fifty years, road traffic has increased significantly [5], i.e. heavier vehicles pass at higher frequencies and at higher velocities. Most of the older bridges in the Netherlands were not designed for such an increase of the road traffic. Potential decrease of the load-bearing capacity and increasing traffic loads result in an increased probability of failure of the bridge. When the probability of failure of a bridge becomes too high, the bridge is considered as unsafe. When this occurs, appropriate actions, like strengthening or replacing, should be taken. Both actions are expensive. High costs can be avoided by observing the health of a bridge frequently and to take actions when they are required.

Asset owners make maintenance and replacement plans to be in control of the performance of their assets in time. These plans have to be checked and updated on a regular basis. Normally information for such update comes from visual inspections. Visual inspections are time consuming and they do not always lead to reliable results [6]. To increase the reliability of the assessment, SHM technologies are emerging. SHM technologies are technologies whereby the deformations of a structure are monitored and the measurements are used to judge the health of a structure. However, there is no study that convincingly showed that SHM can assess damage of concrete bridges and viaducts better than visual inspections, or that SHM of concrete bridges has economic advantages. It is known that the vibrations of a damaged RC structure are different from the vibrations of the same structure under undamaged condition [7]. In order to investigate whether SHM data can be used for assessing the health of a concrete bridge and for predicting the remaining service-life of the bridge, the InfraWatch research project was initiated.

1.2 The InfraWatch research project

The InfraWatch research project is a joint research project of Leiden University and Delft University of Technology. The aim of this project was to scrutinize the interpretation and operationalization of SHM data. The InfraWatch project is one of the nine projects in the National STW Perspective program [8] called 'Integral Solutions for Sustainable Construction (IS2C)', which was initiated to generate elements necessary for the next generation for service-life assessment [9].

Three PhD researchers were involved in the InfraWatch project. Two of them worked at Leiden University and one at Delft University of Technology (this dissertation). They worked together in order to find the opportunities for using SHM data in predicting the health and the remaining service-life of a monitored concrete bridge. PhD 1 (U. Vespier) converted SHM data from raw data into manageable amounts of data, and visualized the data. PhD 2 (S. Miao) separated high quality data from low quality data, and analysed selections of the high quality data. PhD 3 (this dissertation) investigated the development of the deflections and the natural frequencies of concrete structures during their service-life and the effect of local damage on this development. All three studies together aims at a better assessment of concrete structures. Figure 1-1 shows a schematic overview of the PhD studies in the InfraWatch project.

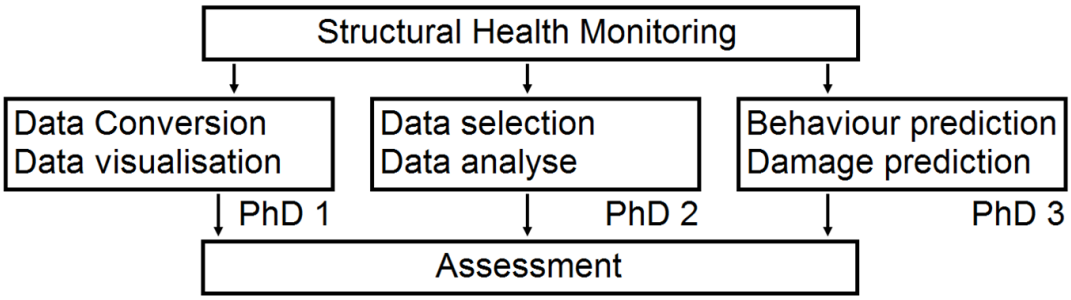

Figure 1-1: Schematic overview of the PhD studies in the InfraWatch project.

Three years of SHM data, provided by Rijkswaterstaat (part of the Dutch Ministry of Infrastructure and Environment), were available for the InfraWatch project. These data were obtained from a SHM system, which was installed in 2009 on a renovated concrete bridge (The Hollandse Brug) (Figure 1-2).

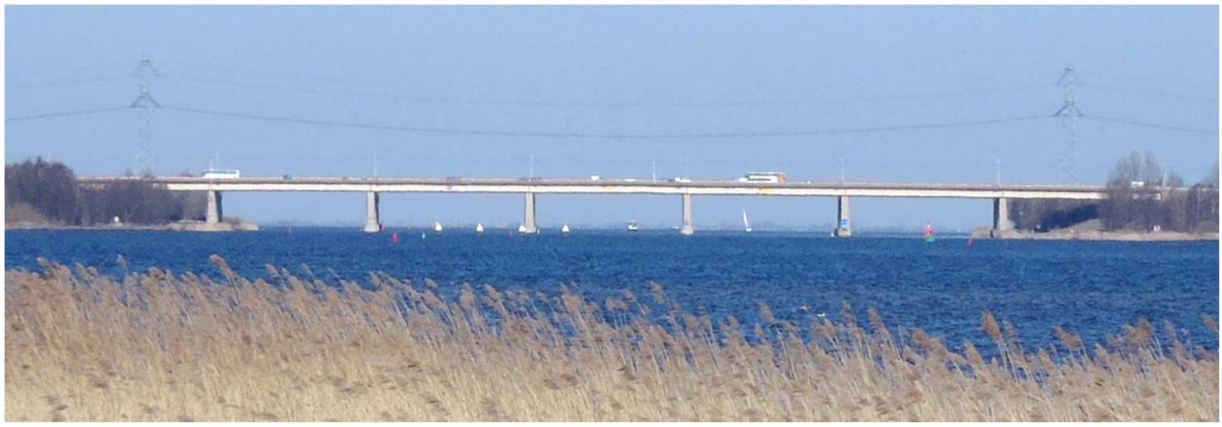

Figure 1-2: Picture of the Hollandse Brug, a monitored bridge in the Netherlands.

SHM data of the Hollandse Brug was the starting point of the InfraWatch project. The studies of PhD 1 and PhD 2 were mainly focused on analysing these data. As a joint subproject of the three studies, the modal properties (natural frequencies, damping ratios, and mode shapes) of the Hollandse Brug were obtained from SHM data and predicted using Finite Element (FE) calculations. The results of the different analyses have been compared. Limitations for a valid comparison have been further investigated in the different studies individually. This research was focussed on the relations between damage in reinforcing bars and deflections of Reinforced Concrete (RC) structures.

1.3 Aim and objectives

The main objective of the InfraWatch project was to develop a vision for efficient SHM systems necessary to assess the actual health of infrastructural assets. Sensors in a SHM system on a concrete bridge can measure the deflections and the vibrations of the bridge. Measurements of the vibrations can be used to calculate the modal properties of the bridge. It was assumed that the deflections and the natural frequencies can be used to obtain the health of a bridge. The health of the bridge can, however, only be obtained from SHM data when degradation of the bridge results in excessive changes in the deflections and/or in the natural frequencies of the bridge. To develop a monitoring system based on changes in the natural frequencies of a bridge, the relation between damage in the bridge and changes in the natural frequencies should be know. This research mainly focussed on obtaining information concerning this relation. The objectives of this research can be summarized in the following research questions:

- How can the comparison between the results of data-driven modal calculations and the results of FE modal calculations be used to identify structural damage and to predict the remaining service-life of a RC structure?
- How do deflections of a cyclic loaded RC structure change over its service-life?
- How does chloride-induced corrosion influence the deflections of a cyclic loaded RC structure?
- How can damage-induced changes in the deflections and/or in the natural frequencies of RC bridges be obtained from monitoring data?

1.4 Scope of the research

The main focus of this research was to provide information about the development of the deflections of RC structures during its service-life and the effect of local damage on this development. Many degradation mechanisms can result in changes in the natural frequencies. The investigated damage mechanism in this research was fatigue. The effect of chloride-induced corrosion on the fatigue life was investigated as well.

Traffic initiates vibrations in concrete bridges. Since SHM systems in bridges often contain sensors to monitor the vibrations of a the bridge, traffic-induced vibrations in concrete bridges have to be taken into account when the deformations of the bridge are analysed.

Traffic vibrations can initiate fatigue damage in the bridge. For bridges designed for 1975, the actual traffic on bridges is heavier and more intense than the traffic considered in design calculations. Therefore, the probability of fatigue damage in bridges designed before 1975 is increasing [2]. Today, concrete bridges are often designed with a higher slenderness. Due to a higher slenderness, the stress amplitudes in a bridge as result of traffic loads increase. Therefore, also in new concrete bridges, the probability of fatigue damage is relatively high. Since fatigue is a growing problem in concrete bridges [10], fatigue damage in concrete structures was investigated in this research.

In winter season, de-icing salts are commonly used to prevent water on the pavement from freezing. The de-icing salts can penetrate into the concrete and potentially generate corrosion of the steel reinforcement. In this research the combination between localized corrosion of reinforcing steel and fatigue failure of a RC beam was studied. Within this research, the maximum number of load cycles a RC beam can withstand until failure and the deflections of RC beams with and without localized corrosion were investigated.

1.5 Research contribution to Structural Health Monitoring

The number of SHM systems on concrete bridges is increasing. A huge amount of data will be obtained from SHM systems. A lot of money and energy is spent on storage of these data, on converting these data, and on analysing these data. These data only contribute to the predictions of the health of a structure when the data contain information about the damage level in the bridge. This is only the case when damage results in detectable changes in the deflections or in the natural frequencies of the bridge. In this research, tests, calculations, and simulations were performed to generate information about changes in the deflections of a RC beam during its total service-life and changes in the deflections of a RC beam as result of damage in a reinforcing bar.

Beside damage-induced changes in the deflections of RC structures, this research generated information about the relation between changes in the ambient condition and changes in the deflections of a RC beam. The effect of fluctuations in the ambient temperature around a RC beam on the deflections and on the natural frequencies of the beam was compared with the effect of local damage in a reinforcing bar of a RC beam on

the deflections and the natural frequencies of this beam. This comparison was performed in a sensitivity analysis. This sensitivity analysis showed whether analysing SHM data of a RC beam can be used to obtain the health of the beam. The results of this sensitivity analysis also provided information about the sensitivity of the deflections and the natural frequencies of a concrete bridge to local damage in the reinforcing bars.

1.6 Outline of the dissertation

This dissertation contains seven chapters. The first three chapters contain an introduction to the project and an overview of relevant information. A general introduction of the project is presented in Chapter 1. Chapter 2 contains the current state of the art of SHM. Chapter 3 contains an integral subproject prepared in cooperation with the other two PhDs of the InfraWatch project. In this integral subproject, modal properties of a concrete bridge were obtained from SHM data and predicted with FE calculations.

The fourth chapter of this dissertation contains information about the conducted tests. Two sets of tests were conducted in this research. In one set of tests, the dynamic behaviour of plain steel bars was tested. The other set of tests considered dynamically loaded RC beams in a four-point-bending configuration.

Chapter 5 and Chapter 6 are related to the predictions of failure, and the predictions of the deflections and the first natural frequency of a RC beam. For these predictions, FE models are developed (Chapter 5) and a sensitivity analysis is performed (Chapter 6). Chapter 7 contains the conclusions of this study.

Chapter 2

State of the Art Analysis

The current state of the art on knowledge about Structural Health Monitoring (SHM) is presented in this chapter. This chapter contains information about the structural health and changes in the probability of failure with time. Information about changes in the deformations and in the modal properties, including the possibilities of measuring deformations and modal properties of concrete bridges are presented in this chapter as well. This chapter also provides information about fatigue and corrosion damage in cracked and uncracked concrete structures.

2.1 Basic principles of Structural Health Monitoring systems

A SHM system is a system that obtains the health of a structure using measurements of changes in the response of the structure. A SHM system contains the following components:

- Predictions of changes in the response of a structure as result of natural changes of the material properties and damage in the structure;
- Sensors that measure changes in the response of a structure under its daily load;
- A datalogger that stores the data;
- Software that translates the measured data into information which can be used for a judgement of the health of the structure and a judgement of the risk of malfunction of the structure.

The dynamic response of a bridge can be expressed in its deformations and its vibrations. Studies have shown that the deflections and the natural frequencies of a bridge depends on the amount of damage in the bridge [11]. In this perspective, the natural frequencies of multiple bridges around the world have been monitored [12, 13]. The SHM system on these bridges were installed to increase the safety of the bridge by knowing the vibrations of the bridge. Some projects show that a well planned and executed monitoring project can provide actionable information to the owner and the bridge engineer [12]. Other studies have shown that monitoring the vibrations of a bridge can be used to demonstrate the recovery of a damaged Prestressed Concrete bridge after strengthening the bridge [14]. Although, the natural frequencies of the higher mode shapes of this bridge gave unstable results, it was concluded that natural frequencies and modal displacements are useful damage indicators [14].

2.2 Structural health

SHM systems which can be installed on a bridge were developed obtain the health of the bridge using deformations and vibrations of the bridge. These deformations and vibrations are mainly influenced by traffic on the bridge and the temperature/humidity in the bridge. Damage in the bridge can also change the deformations and vibrations of the bridge. The idea of SHM is that damage in a bridge introduces changes in the response of the bridge under traffic loads. When these changes can be observed by analysing SHM data, monitoring deflections or vibrations of a bridge can contribute to obtain the health of the bridge. However, it is undefined in the literature when a structure is healthy and when it is not. For humans, health is primarily a measure of a person's ability to do and become what he/she wants to become [15]. This definition of human's health was used to express the definition of structural health. In this dissertation, the definition of structural health is as follows: Structural health is primarily a measure of a structure's ability to fulfil its structural requirement. The structural requirement of a road bridge is that the bridge can resist traffic loads on the bridge with a high degree of reliability during the design service-life. The reliability of a bridge is one minus the probability of failure of the bridge. The probability of failure of a bridge can be derived from the mean value and the variability of the strength of the bridge (R, Resistance) and the loads on the bridge (S, stresses).

In design codes, a target probability of failure is mostly given as a target reliability index [16]. A higher target reliability index indicates a lower probability of failure and a higher safety level. When the reliability index of a bridge is higher than the target reliability index, the bridge is considered as 'safe'. As result of degradation in a bridge, the strength of the bridge decreases. The reliability index decreases as well. Therefore, the reliability index can be used as an indication of the structural health [17]. If the reliability index of a bridge hardly change, the bridge can be considered as 'healthy'. When the reliability index decreases and is lower than the target reliability index, the service-life has ended. Figure 2-1 shows an illustration of the reliability index (β), the indication of the health of a structure, and the end of service-life.

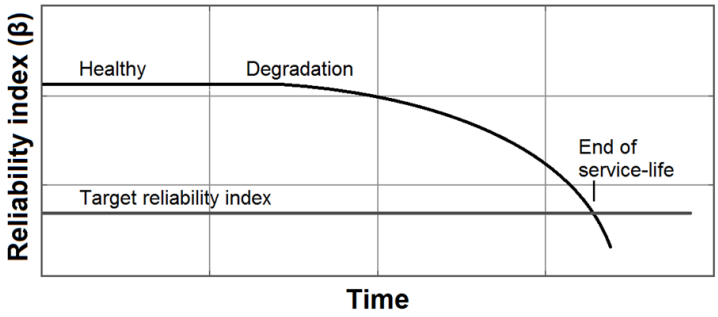

Figure 2-1: illustration of the reliability index (β), the health of a structure, and the end of service-life.

With the elapse of time, the strength of concrete bridges changes. Ongoing hydration of cement increases the strength of concrete. On the other hand, the strength of a bridge can be reduced by degradation mechanisms like fatigue and corrosion. A reduction of the strength of a bridge increases the probability of failure of the bridge.

In the past fifty years, traffic loads increased significantly [5], i.e. the mass of vehicles became higher, the number of vehicles has increased, and the average speed of vehicles is higher. Due to the increasing traffic loads the probability of failure of bridges has increased in time.

When, due to a reduction of the strength and/or an increase of loads, the probability of failure of a bridge becomes larger than the target probability of failure, the bridge does not fulfil the structural requirement. From a structural safety point, the service-life of the bridge has ended. Figure 2-2 shows a schematic illustration of an increase of the probability of failure in time. In this figure, the red upper bell-shaped curves correspond to the probability density of the resistance of a structure. The blue lower bell-shaped curves correspond to the probability density of the loads on the structure. The red curve below the probability densities curves indicates the cumulative density curve of failure of the structure. The cumulative density curve corresponds to the grey surface in between the bell-shaped curves [18]. When this curve exceeds the target reliability index, the service-life has ended.

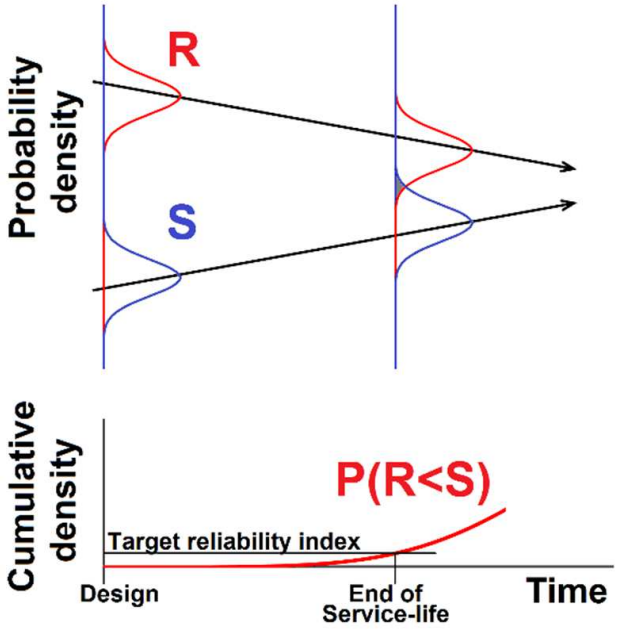

Figure 2-2: Schematic illustration of the probability of failure with time. The red upper bell-shaped curves correspond to the probability density of the resistance of the structure. The blue lower bell-shaped curves correspond to the probability density of the applied stress. The red curve below the probability densities indicates the cumulative density of failure of the structure.

The probability of failure can be derived from the mean value and the variability of the strength of a structure and the loads on the structure. When these properties change, the probability of failure changes. For the situations whereby the probability of failure is lower than 50%, the probability of failure decreases with decreasing uncertainties in the strength of a structure. Figure 2-3 shows the effect of decreasing the uncertainties of the strength of a structure on the predicted service-life of a structure in a schematic illustration. In this figure the bell-shaped curves of the resistance of a structure are narrower than the bell-shaped curves in Figure 2-2.

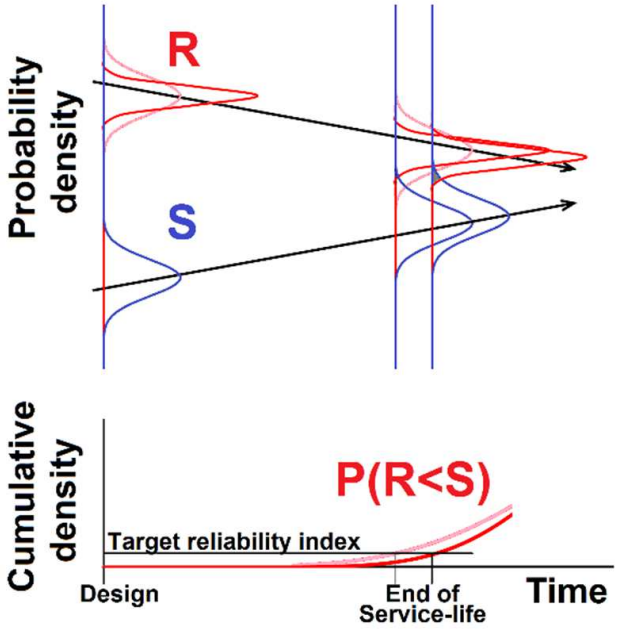

Figure 2-3: Schematic illustration of the probability of failure with time. The curves represent the same densities as in Figure 2-2. Due to a reduction of the uncertainty in the resistance, the probability of failure change. As result of this change, the service-life can be extended.

It was assumed that when the deformations and the natural frequencies of a bridge can be understood better, the strength of the bridge could be understood better as well [11]. A better understanding of the strength of a bridge can be used to predict the probability of failure of the bridge more precisely. A better estimation of the probability of failure can result in an extension of the design service-life (as shown in Figure 2-3).

2.3 Structural Health Monitoring systems

Information from visual inspections can be used to predict the probability of failure of a bridge more precisely. Therefore, such information can be used to obtain knowledge about the health of the bridge. The accuracy of such information is based on the experience of the inspector. For many years, visual inspection was the only method to provide information for the estimation of the health of a bridge. In literature about SHM, visual inspection is considered as monitoring system as well [19].

SHM systems contain sensors that measure a specific parameter of a structure such as deformations or vibrations. It was assumed that the deformations (Chapter 2.4) and modal properties (Chapter 2.5) of a bridge can be used to estimate the health of the bridge [20]. To obtain information about the deformations and the modal properties of a structure, sensors, SHM systems, and data analyses are required. This section contains information about such sensors, SHM systems, and data analyses.

2.3.1 Sensors and monitoring

A sensor is a device that detects events or changes in its environment. Events or changes in the environment of the sensor result in electrical or optical signals in the sensors. The

optical signals can be observed by humans. The electrical signals can be converted to digital signals which can be read by a computer. A sensor in a SHM system of a bridge is able to detect changes in the responses of the bridge. The measurements depend on the type of the sensor and on its position on the bridge.

A sensor network is a group of sensors which is connected to the same object. A SHM system is a sensor network which monitors the responses of a structure under in-service conditions. To monitor the actual deformations of a total bridge, a larger number of sensors is required. In most situations, a SHM system is a permanent installed sensor network, which can be used to monitor the response of a structure over a longer period of time. A mobile monitoring device can be used to measure the response of a structure during a short period of time. Within a short period of time, the development of the response of a structure could not be obtained. The development of the response of a structure can only be obtained by a mobile monitoring device when the measurements can be compared with the measurements from earlier periods of monitoring. Without a reference, mobile monitoring devices cannot be used as SHM systems.

Most sensors in a SHM system installed in concrete bridges provide electrical signals. A digital converter transforms these electrical signals into digital signals, which are stored in a computer. In large SHM systems, multiple computers can be used to store all data. Sensors in a SHM system installed on a concrete bridge can detect changes in the deformations of the bridge. These changes are partially initiated by traffic and partially by non-structural effects like wind and temperature. The measurements of changes in the deformations of a concrete bridge which were initiated by non-structural effects are considered as noise. Data analyses are required to eliminate the noise from the measurements. An ideal SHM system in a concrete bridge contains enough information for judging the health of the bridge. Figure 2-4 shows a schematic overview of an ideal SHM system.

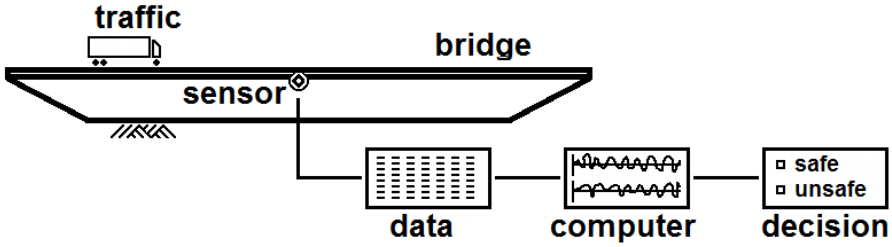

Figure 2-4: A schematic overview of an ideal SHM system on a concrete bridge. A sensor on a bridge monitors the deformations of the bridge. The data are transformed to a computer which convert the data. A computer algorithm concludes whether the bridge is safe or unsafe.

2.3.2 Different types of Structural Health Monitoring sensors

When a bridge is damaged, the load bearing capacity of the bridge has decreased. The main idea of SHM is that deformations and natural frequencies of a bridge change parallel to changes in the load bearing capacity [21]. For concrete bridges, it was suggested in literature that damage in bridges results in detectable changes in the deformations and in

detectable changes in the natural frequencies of bridges. Changes in the deformations and changes in the natural frequencies of a concrete bridge can, therefore, be used as damage indicators of bridges. Deformations of Reinforced Concrete (RC) structures are discussed in Section 2.4. Natural frequencies of concrete structures are discussed in Section 2.5.

Accelerometers (geo-phones) and strain gauges are by far the most commonly used sensors in SHM systems [22]. These devices have a low cost and are easy to install. When a strain gauge is glued on a structure, changes in the strain of the structure are similar to changes in the strain of the gauge. Changes in the strain of the gauge result in an electrical signal. This electrical signal can be converted and be used for further analyses. The signals of a stain gauge are influenced by the ambient condition around the strain gauge. Changes in the temperature result in changes in the strain of the gauge. This has influence on the measured strain. Smart strain gauges compensate such changes in the strain of the gauge [23]. Changes in the ambient condition around a strain gauge disturb the electrical signal of the gauge. This has as consequence that the signal which can be detect can be different than the signals transmitted by the strain gauge. Therefore, the measurements of the strain gauges can be different from the actual strains of the structure [24].

Deflections of a structure can also be measured by Linear Variable Differential Transformers (LVDTs). For measuring the vertical deformations, the LVDTs should be installed in such a way that the structure can move independently of the equipment. Due to the complex installation, LVDTs are hardly used for monitoring the deformations of larger structures. When LVDTs are installed, they can measure deflections directly and provide more valid results than strain gauges. Therefore, LVDTs are preferred for measuring the deflections of small structures. Data of accelerometers (geo-phones) can be used to calculate the modal properties of a monitored bridge. The modal properties of a bridge are: mode shapes, natural frequencies, and damping ratios. The modal properties are related to the free vibrations of the bridge. Table 2-1 shows the sensors which are used in this study and presented in this dissertation.

Table 2-1: Different sensors in SHM systems.

Type	Measurement	Damage indicators	Used in
Linear Variable Differential Transformer (LVDT)	Displacements	Deflections	Chapter 4
Accelerometer (geo-phone)	Vibrations	Modal properties	Chapter 3
Strain gauge	Strain	Deformations	Chapter 3
Temperature sensor	Temperature	-	Chapter 3, 4

The deflections and the natural frequencies of a bridge depend on the stiffness of the bridge. When, as result of damage, the stiffness of a bridge changes, the deflections and the natural frequencies of the bridge change as well. Therefore, deflections and natural frequencies are suggested to be damage indicators for bridges [12].

The vibration properties of a structure are influenced by the temperature of the structure [25]. Therefore, the deformations and the modal properties of a concrete bridge are

influenced by the temperature of the bridge. For existing structures, it is more difficult to measure the temperature of a bridge than to measure the ambient temperature around the bridge. When the ambient temperature around a concrete bridge is monitored, and it is known how the deflections of the bridge change as result of fluctuations in the ambient temperature, the effect of fluctuations in the ambient temperature on the deflections of the bridge can be eliminated from SHM data. Similarly, when the ambient temperature around a concrete bridge is monitored, and it is known how the natural frequencies of the bridge change as result of fluctuations in the ambient temperature, the effect of fluctuations in the ambient temperature on the natural frequencies of the bridge can be eliminated from SHM data. To monitor the ambient temperature near a concrete bridge, SHM systems often contain temperature sensors.

2.3.3 Monitoring corrosion

Damage in concrete bridges often finds its origin in corrosion of the reinforcing bars. Corrosion in the reinforcing bars of concrete bridges can change the properties of the material and the connection between different elements of the bridge. These changes might result in a reduction of the natural frequencies of the bridge. When corrosion results in detectable changes in the natural frequencies, the effect of corrosion on the natural frequencies of a bridge might be observed by monitoring the vibrations of the bridge.

Measuring the corrosion activity is a more direct method to observe corrosion damage in reinforcing bars than monitoring the effect of corrosion on the natural frequencies of a RC bridge. Several non-destructive methods to monitor the corrosion activity have been developed [26]. The most commonly used methods to monitor corrosion are the Half-cell Potential (HCP) and the Linear Polarization Resistance (LPR) [27]. Both methods are presented below and used in Section 4.7.

The aim of HCP is to measure the potential around a reinforcing bar in a concrete specimen. The potential indicates a probability of corrosion and is normally a negative value. A concrete specimen with a corroded reinforcing bar has a lower potential than a similar specimen with an uncorroded reinforcing bar [27]. When more negative potentials are measured, the probability of corrosion in the reinforcing bar is higher than when less negative potentials are measured. When the potentials are less negative than -200 mV, the probability of corrosion is less than 10%. When the potentials are more negative than -350 mV, the probability of corrosion is 90% [27, 28]. One of the disadvantages of HCP is that it does not provide information about the amount of corrosion or the corrosion rate.

LPR is a technique which estimates the corrosion density of steel [29]. The polarization resistance is the slope op the current density-potential curve [30]. The polarization resistance of corroded steel is lower than the polarization resistance of uncorroded steel. Monitoring the polarization resistance can indicate the corrosion rate of the reinforcing steel [31]. One of the disadvantages of LPR is that it does not provide information about

the actual amount of corrosion [28]. For both HCP and LPR, there can be a large scatter in the measurements.

For measuring the potential around a reinforcing bar in a concrete section, a 'three electrode electrochemical call' has to be created. This cell contains a working electrode, a reference electrode, and a counter electrode. Figure 2-5 shows a schematic representation of a three electrode electrochemical cell in a concrete section.

The working electrode is the reinforcing bar which is subjected to corrosion. The reference electrode is a device with a stable and well-known electrode potential. The reference electrode is positioned close to the working electrode (a few mm) and is required for the HCP method. The counter electrode is positioned at a larger distance (10-20 cm) from the working electrode. The counter electrode is required for the LPR method. A power source is positioned between the working electrode and the counter electrode. In this study, HCP and LPR are used to measure the corrosion activity in a RC beam with a single reinforcing bar (Section 4.7).

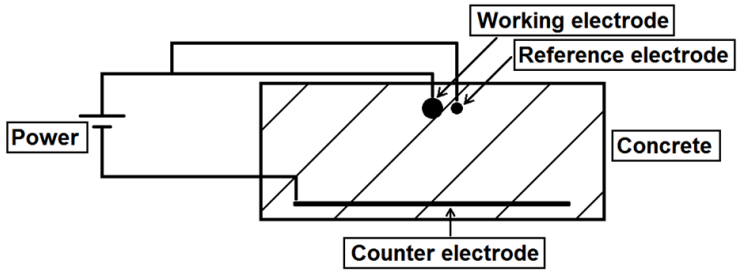

Figure 2-5: Schematic representation of a three electrode electrochemical cell in a concrete section. The working electrode is the reinforcing bar. The reference electrode is a device with a stable and well-known potential. The counter electrode is required for voltammetry analyses.

2.3.4 Processing Structural Health Monitoring data

In general, SHM systems provide large amounts of data. These data can be converted into manageable amounts of data. The computational process of analysing manageable amounts of data is called 'data mining'. By data mining, high quality sets of data can be obtained from the manageable amounts of data. Modal analyses can be performed on different sets of high quality data (data-driven modal calculations). The results of the data-driven modal calculations can be used in further analyses. Figure 2-6 shows an overview of the data analyses.

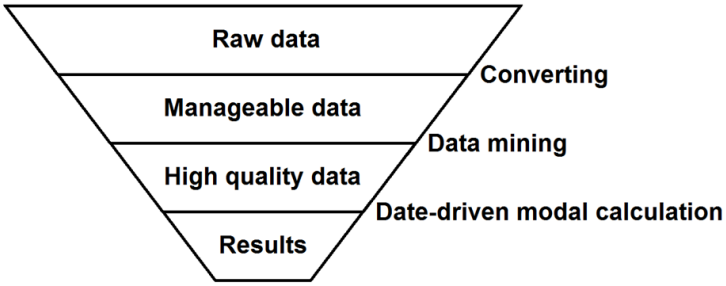

Figure 2-6: Overview of the data analyses.

When data of the dynamic input (loads) and data of the dynamic output (vibrations) are both available, Experimental Modal Analyses (EMA) can be used to calculate modal properties of a structure [21]. EMA include all methods which use both input and output data to calculate modal properties of an existing structure. Normally, SHM systems installed on concrete bridges only generate output data (vibrations). Therefore, EMA can hardly be used to obtain the modal properties from SHM data of concrete bridges. More recently, Operational Modal Analyses (OMA) were developed. OMA derive modal properties from output (vibrations) data only. OMA include all methods which use only output data for deriving modal properties. For analysing data from SHM systems installed on concrete bridges, OMA are most suitable. Two of the OMA methods (Peak-Picking and Stochastic Subspace Identification) are presented below and used for analysing SHM data (Section 3.3).

The Peak-Picking (PP) method within the OMA is widely used to estimate modal properties of a monitored structure [32]. The PP method converts vibration data from the time-domain into the frequency-domain. The peaks in the curves of the frequency-domain are used as estimations of the natural frequencies and the damping ratios. To limit errors in the calculated natural frequencies and damping ratios, a large number of modal calculations from multiple data spectra is required. Higher order natural frequencies have a limited amplitude. Since the PP method uses amplitudes to estimate the natural frequencies and the damping ratios, the estimated values of the higher order natural frequencies contain a larger scatter than the estimated values of the first order natural frequencies [33]. The PP method does not provide information about the mode shapes of a structure (Section 2.5.2). Therefore, the PP method is less suitable to identify natural frequencies [34].

The Stochastic Subspace Identification (SSI) method is a more advanced method to calculate the modal properties of a bridge than the PP method. A detailed explanation of this method can be found in the references [35, 36]. In the SSI method, a parametric model is aligned with high quality data. A large number of iterations are required to align the parametric model with the data. Therefore, the SSI method is time-consuming. To limit errors in the derived parameters, a large number of data sets needs to be analysed. The derived parameters can be used to calculate modal properties of the bridge. One advantage of the SSI method is that it provides information about the mode shapes, which can be used to identify different natural frequencies. Due to the identification of the

different natural frequencies, the obtained natural frequencies can be compared with results of FE modal calculations. One disadvantage of the SSI method is that when the estimated parameters are chosen incorrectly, the SSI method provides invalid results. Since the SSI method is sensitive for small miscalculations, it is recommended to validate results of SSI calculations with the results of other modal calculation methods. Both the PP method and the SSI method are used for analysing SHM data (Chapter 3).

2.3.5 Difficulties in judging SHM data

SHM data of the deflections and/or the vibrations of a bridge might contain enough information to judge the health of the bridge and to predict the remaining service-life of the bridge. It is, however, very complicated to obtain this information from SHM data. Four parameters, which makes judging of the health/condition of a bridge complicated, are given below.

First, the shape, velocity, and mass of traffic contain large fluctuations [20]. Due to these large fluctuations, the response of a bridge contains large fluctuations as well. Detecting patterns in a large scatter of measurements is very complex.

Changes in the temperature and in the humidity of a bridge result in changes in the modal properties of the bridge. As result of these temperature-induced changes in the modal properties of the bridge, small damage-induced changes in the deflections and in the natural frequencies of the bridge can hardly be observed from SHM data.

Third, in most of the situations, the deflections and the natural frequencies of a bridge were not measured from the construction of the bridge. Since it is possible that the bridge was already (slightly) damaged before the deflections and the natural frequencies of the bridge were measured for the first time, it cannot be sure that the deflections and the natural frequencies of a healthy bridge are known. Therefore, it is difficult to judge whether the deflections and the natural frequencies of a bridge have been changed compared to the deflections and the natural frequencies of the bridge under health conditions.

Fourth, the development of the deflections and the natural frequencies of a concrete bridge as result of natural changes in the material properties and/or structural damage is unknown. When changes in the deflections or in the natural frequencies are observed, and it is known that these were caused by changes in the modal properties of the bridge, the cause of these changes can be still uncertain. The effect of local damage (fatigue damage and corrosion damage) on the deflection and natural frequencies of RC structures are investigated in this research.

2.4 Deformations of Reinforced Concrete structures

2.4.1 Stress-strain relation of concrete material

Materials deform under applied loads. Generally, deformations of a specimen can be divided in a linear part and a nonlinear part. In the linear part, a specimen returns into their original shape after unloading (elasticity). In the non-linear part, a specimen does not return automatically into its original shape. Despite of that, a specimen remains deformed. Concrete in compression has a different non-linear behaviour than concrete in tension. When a strain controlled compression test on a concrete specimen is conducted, the stress-strain ratio (stiffness) decreases until the ultimate compression stress is reached, after which limit the compression strength reduces. When a strain controlled tensile test on a concrete specimen is conducted, the stress-strain relation remains rather constant until the ultimate tensile stress is reached, after which the tensile strength reduces rapidly [37].

As result of hydration of cement, the values of the mechanical properties of concrete increase with time whereby the increase is largest in the first days of hardening [38]. In daily design practice, the 28-day mechanical properties of the concrete are used for structural design calculations. However, water and non-hydrated cement are still left. Therefore, the strength and the elasticity of concrete can increase 20-50% in the remaining lifetime [39]. An increase of the elasticity (Young's modulus) of concrete results in an increase of the stiffness of a concrete bridge. Due to a higher stiffness, the deformations of a bridge decreases and the natural frequencies increase.

2.4.2 Cracks

The tensile strength of concrete is approximately 10% of the compressive strength. One of the most commonly used methods to increase the tensile strength of concrete structures is strengthening the structure with reinforcing steel. When the tensile stress in a concrete section exceeds the ultimate tensile strength of the concrete, cracks develop and the steel reinforcement takes over a main part of the tensile forces. Since the cross sectional area of concrete is much bigger than the cross sectional area of steel, a new equilibrium stage will go along with relatively large strains. As result of cracks in a RC beam, the deflections of a RC beam increase (Figure 2-7). Since concrete is a heterogeneous material, the tensile strength of concrete is not constant throughout the total volume of a RC structure. Therefore, it is difficult to predict the number and the locations of the cracks in a concrete bridge in detail [39].

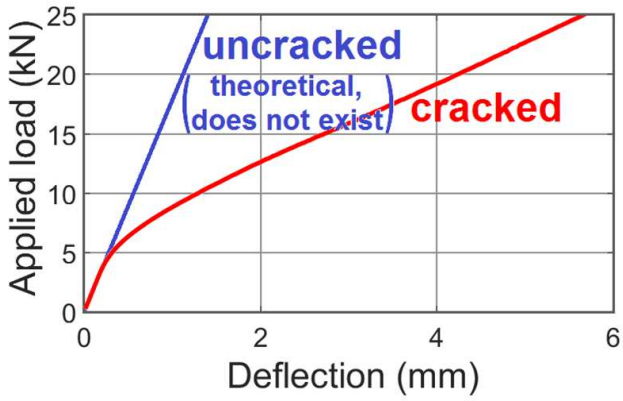

Figure 2-7: Load-deflection of a RC beam, loaded in a four-point-bending configuration. The red curve corresponds to the deflections of a cracked beam. The blue curve shows the theoretical deflections of a RC beam in an uncracked situation.

2.4.3 Temperature

The volume of concrete increases by increasing temperature of the concrete and decreases by decreasing temperature of the concrete. The thermal expansion and the thermal shrinkage of concrete depend on the mixture composition, humidity, temperature gradients, and exposure time [40].

A thermal load on a concrete structure can be theoretically divided in three components: an average temperature, a temperature differential, and an eigen temperature [41]. When a concrete element can freely deform, changes in the average temperature in the element can result in expansions or shrinkage of the element (Figure 2-8-A). Changes in the average temperature of concrete result in changes in the Young's modulus of concrete [42]. These changes in the Young's modulus result in changes in the deflection of a concrete structure loaded under mechanical loads. Changes in the Young's modulus of concrete change the natural frequencies of concrete structures as well.

A temperature differential is a linear distribution of the temperature over the height of an element. When an element can deform freely, a linear distribution of the temperature results in a curvature of the element (Figure 2-8-B). Although a linear distribution of the temperature can result in changes in the deflections of a concrete structure, the natural frequencies of a concrete structure are hardly influenced by a linear distribution of the temperature in the structure [43].

The eigen temperature is the remaining temperature of a structure. The summation of the eigen temperature over the cross-section of an element is zero. The eigen temperature of a structure does not cause deformations of the total structure. It is possible that the eigen temperature cause local deformations and the outer ends of the cross-section.

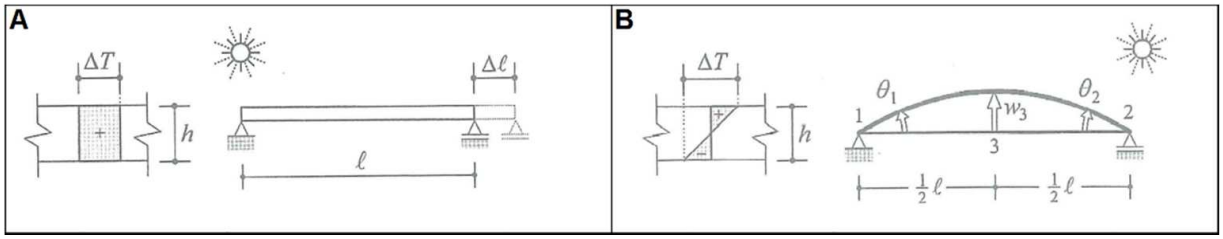

Figure 2-8: Effect of changes in the ambient temperature [44]. Figure 2-8-A is an increase of the average temperature. Figure 2-8-B shows a temperature differential. The eigen temperature do not result in changes in the deflections and/or in the natural frequencies and are not presented in this figure.

2.4.4 Humidity

Similar to changes in the temperature, drying and wetting of a concrete element can result in expansion or shrinkage of the concrete [45]. Changes in the humidity of concrete can result in changes in the deflections [46] and in the natural frequencies of a concrete structure [43].

When the deformations of RC structures are used to obtain damage in the structure, it is important to notice that temperature and humidity have a large influence on the deflections of the structure.

2.5 Modal properties

Modal properties are structure-related properties, concerning the free vibrations of a structure. Modal properties are: natural frequencies (Section 2.5.1), mode shapes (Section 2.5.2), and damping ratios (Section 2.5.3). The modal properties are functions of the physical properties of a structure (mass, damping, and stiffness). When a concrete bridge is damaged, the mass, damping ratios and/or the stiffness of the bridge can change. Since the modal properties depend on these properties, damage in a concrete bridge can change the modal properties of the bridge as well (Section 2.5.4). Therefore, modal properties could be used as indicators of damage in a bridge.

2.5.1 Natural frequencies

A natural frequency is a frequency in which a structure can vibrate freely after force/displacement equilibrium in the structure is disturbed. Natural frequencies exist in all six degrees of freedom (translation x,y,z & rotation xx,yy,zz). In theory, an unlimited number of natural frequencies exists in all six directions, whereby the amplitudes of the first order natural frequencies are larger than the amplitudes of the second and higher order natural frequencies.

To explain the natural frequencies of a system, often an undamped single-mass-spring-system has been used. A single-mass-spring-system is a 1D system with a single degree of freedom (vertical displacement), a single mass (m), and a single spring (K). An illustration of a single-mass-spring-system is given in Figure 2-9.

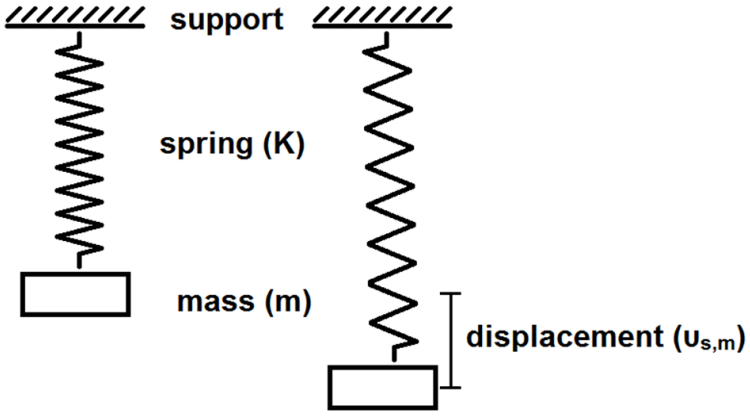

Figure 2-9: Illustration of a single-mass-spring-system.

For equilibrium in the system, the force in the spring (elongation of the spring times the stiffness of the spring) is equal to the gravitation acceleration times the mass (Equation (2-1)). In a static situation, this equilibrium is reached at a certain displacement ($\upsilon_{s,m}$) of the mass. When the mass was pulled down and released, the static equilibrium between the force in the spring and the gravity was disturbed and the equilibrium stage should be considered as a dynamic situation. In a dynamic situation, force equilibrium is a function of time and Equation (2-1) becomes a differential equation. The results of this differential equation is commonly used to calculate the natural frequencies of an undamped single-mass-spring-system (Equation (2-2)). It is also possible to express the natural frequencies as function of gravity acceleration and the stationary displacement (derived from the same differential equation). This function is given in Equation (2-3).

$$mg = \upsilon_{s,m} K \tag{2-1}$$

$$f_n = \frac{n^2}{2\pi}\sqrt{\frac{K}{m}} \tag{2-2}$$

$$f_n = \frac{n^2}{2\pi}\sqrt{\frac{g}{\upsilon_{s,m}}} \tag{2-3}$$

where:

m = mass;
g = gravitation acceleration (9.81 m/s^2);
$\upsilon_{s,m}$ = stationary displacement of the mass;
K = spring stiffness;
f_n = nth order natural frequency;
n = order natural frequency.

The mass of a concrete bridge is not concentrated in one point but distributed over the total bridge. Also the bending stiffness and the rotational stiffness of the bridge is a function of the total bridge. Therefore, Equation (2-2) and Equation (2-3) cannot be used to calculate the natural frequencies of a concrete bridge. A concrete bridge can be considered as a multi-mass-spring-system, whereby the total bridge is divided in 'i'

sections. Each of the sections contains a mass and a stiffness. By analysing the multi-mass-spring-system, Equation (2-4) can be derived [47]. Equation (2-4) is used in Section 4.8.

$$f_n = \frac{1}{2\pi}\sqrt{\frac{g\sum_i m_i \upsilon_{i,n}}{\sum_i m_i \left(\upsilon_{i,n}\right)^2}} \qquad (2\text{-}4)$$

where:

i = element;

m_i = mass per element;

$\upsilon_{i,n}$ = displacement of the mass per element and per natural frequency.

2.5.2 Mode shapes

A mode shape is a specific pattern of vibrations executed by a mechanical system at a specific frequency. This pattern depends on the degrees of freedom of the system. In the example of the single-mass-spring-system, there is only one degree of freedom: translation in vertical direction. The mode shape of the single-mass-spring-system is the up-and-down movement of the mass.

The deck of a bridge has six degrees of freedom (translation x,y,z & rotation xx,yy,zz). In each of these degrees of freedom, the bridge can vibrate. Normally, by modal analyses of the deck of a bridge, only the rotational degrees of freedom are taken into account. Figure 2-10 shows an illustration of four different rotational mode shapes of a deck.

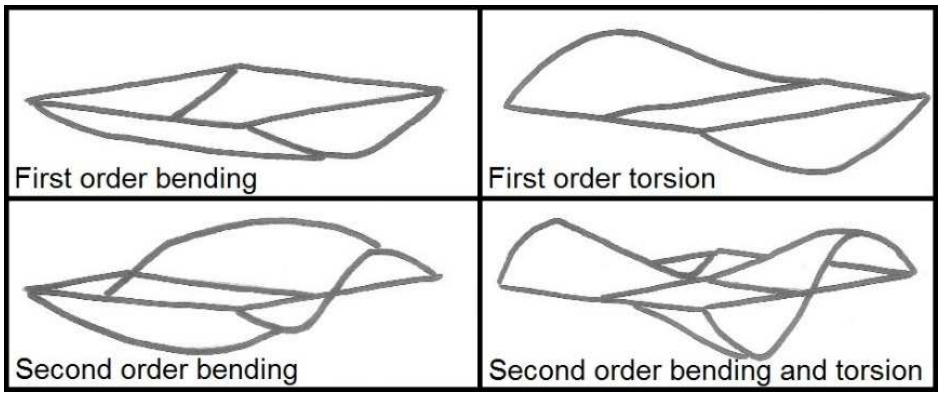

Figure 2-10: Illustration of four different rotational mode shapes of a deck.

Each natural frequency of a bridge is related to a specific mode shape. As result of damage in a bridge, the stiffness of the bridge can decrease. A reduction of the stiffness of a bridge results in lower natural frequencies but will hardly change the shape of the modes. If damage results in an excessive change in the natural frequencies, it is possible that different natural frequencies are being mixed up. The mode shapes can be used in order to avoid incorrect comparisons.

2.5.3 Damping ratios

Damping is the phenomenon of dissipation of mechanical energy in dynamically loaded systems. In a damped system, damping slows the motion of the system (Figure 2-11). Equation (2-5) describes the vibration behaviour of a damped single-mass-spring system for a single natural frequency [48]. Different natural frequencies in the same system can have different damping ratios.

$$u(t) = u_0 e^{-\varsigma\omega_0 t} \sin(\omega_0 t\sqrt{1-\varsigma^2} + \psi) \qquad (2\text{-}5)$$

where:

u = displacement;
u_o = initial displacement;
ζ = damping ratio;
ω_o = angular frequency $\left(\sqrt{\frac{k}{m}}\right)$;
t = time;
ψ = phase.

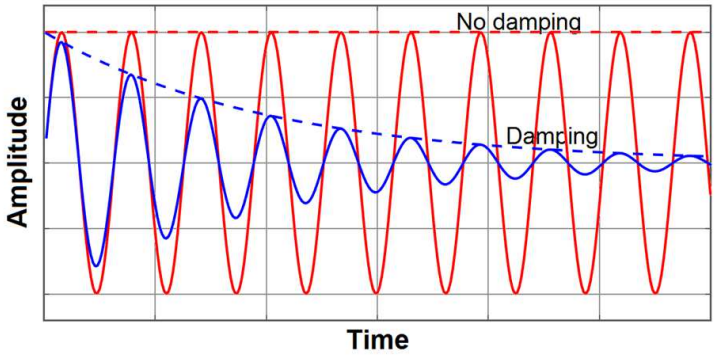

Figure 2-11: Illustration of the effect of damping on the amplitude of a mode.

Damping in concrete bridges can be divided in internal damping and external (structural) damping. Internal damping is the mechanical energy dissipation within the material. Structural damping is the mechanical energy dissipation caused by friction between components and is caused by impacting or intermitted connections in the bridge. Due to a large number of uncertainties in the material properties and in the structural behaviour, damping in concrete bridges can hardly be predicted in advance [49].

2.5.4 Damage indicators

Damage can reduce the strength and the stiffness of a concrete bridge. When the stiffness of a bridge decreases, the deflections of the bridge increase, the natural frequencies of the bridge decrease, and the damping ratios increase.

It has been concluded by Maeck at al. [14] and by Farrar & Cone [50] that a large amount of damage results in significant changes in the natural frequencies of a bridge. In line with this conclusion, it was suggested that natural frequencies can be used as indicators for structural damage. However, situations whereby daily traffic had initiated such amount of

damage in a concrete bridge that changes in the natural frequencies of the bridge could be detected were not found in literature.

Natural frequencies of a concrete bridge are no constant values. One of the most important parameters for changes in the natural frequencies of a concrete bridge is the annual fluctuation in the ambient temperature. The natural frequencies of most concrete bridges increase at a lower ambient temperature and decrease at a higher ambient temperatures [25]. Fluctuations of 4-6% in the natural frequencies of concrete bridges caused by annual temperature fluctuations are found in the literature [51-53].

The effect of changes in the ambient temperature on different natural frequencies of the same structure is different. In the literature, contradictory results were found about which of the natural frequencies is the most suitable frequency to be used as indicator for damage in a structure [11]. The higher order natural frequencies are more affected by local changes in the structure than the first natural frequency. Therefore, higher order natural frequencies are more sensitive for local damage in a structure. However, the higher order natural frequencies are also more sensitive to fluctuations in the ambient condition than the first natural frequency.

As result of cracks in a RC structure, the internal damping in the structure increases significantly. Changes in the sizes of cracks will also result in an increase of internal damping. Therefore, damping ratios are assumed to be damage indicators as well. According to Modena et al. [54] damping ratios are better indicators for structural damage than natural frequencies. However, the effect of damage on the different damping ratios is not constant either. Furthermore, damping ratios can hardly be predicted by FE calculations. Therefore, damping ratios are not further discussed in this study.

2.6 Fatigue

During the service-life of a road bridge, millions of heavy vehicles pass the bridge. These vehicles exert a cyclic loading on the bridge. Materials under cyclic loading can exhibit fatigue damage. Since the traffic intensity has significantly increased in the past fifty years [5], the cycling loads on bridges have significantly increased as well. By increasing the cyclic loads, the probability of fatigue damage is increasing. Therefore, it is important to take fatigue damage into account by analysing and observing existing bridges. Fatigue damage can occur in both steel (Section 2.6.2) and concrete (Section 2.6.3), as well as, in the bond between concrete and steel (Section 2.6.4).

2.6.1 General fatigue behaviour

Since failure of a railway axle in 1842, fatigue is considered to be a serious problem. Wöhler did a lot of experimental research on the failure criteria of steel axles under cyclic mechanical loading [55]. Wöhler's work was the scientific foundation for fatigue analyses [56]. Based on the results of Wöhler's tests, double-logarithm stress-cycle (S-N) curves were developed. These S-N curves (or Wöhler curves) show a double logarithmic relation

between a constant stress amplitude and the maximum number of load cycles. Today, S-N curves are still commonly used to predict the maximum number of load cycles for several structures and materials. Figure 2-12 shows a standard S-N curve. The curve in this figure shows three stages. In the first stage, the effect of fatigue damage is limited and the static yield stress is decisive for the load bearing capacity. The second stage contains a double logarithmic relation between the maximum number of load cycles and the stress amplitudes. This relation can be described with Equation (2-6).

$$\log(S) = A - \frac{a}{b}\log(N) \tag{2-6}$$

where:

S = stress amplitude;

N = number of cycles.

In the third stage, the stress amplitudes are limited and at these low stress levels, the number of load cycles before failure tends to infinity [57].

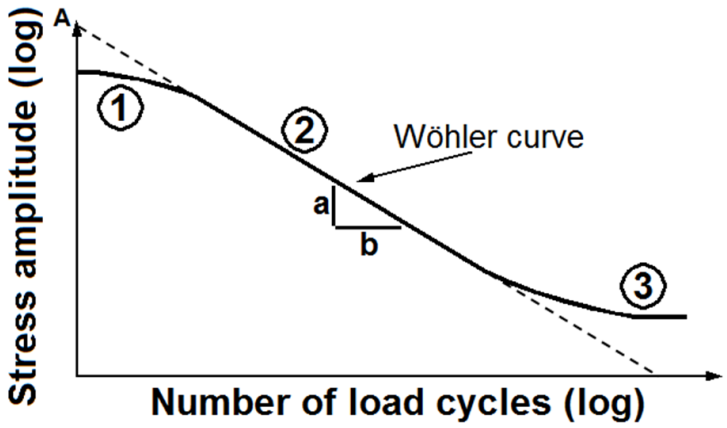

Figure 2-12: Standard S-N (Wöhler) curve. In the first stage, the yielding strength is decisive in the load bearing capacity. The second stage contains a logarithmic relation between stresses and cycles. This relation is expressed in Equation (2-6). In the third stage, the number of load cycles before failure tends to infinity.

When a structure is loaded under cyclic loads with variable stress amplitudes, the S-N curves cannot be used directly. In the past, many researchers investigated the effects of cyclic loading under variable stress amplitudes on the maximum number of load cycles. The Palmgren-Miner damage model is the most commonly used model to describe the effect of repeating load cycles with variable stress amplitudes [58]. The Palmgren-Miner damage model assumes that damage accumulates in a linear manner and does not depend on the order of loading. Therefore, the fatigue damage of the different stress amplitudes can be summed linearly. The maximum number of load cycles with different load amplitudes a structure can withstand until failure can be calculated using Equation (2-7).

$$\sum_{p=1}^{q} \frac{N_p}{N_{max,p}} = 1 \qquad (2\text{-}7)$$

where:
N_p = number of cycles per amplitude;
$N_{max,p}$ = maximum number of cycles until failure for amplitude 'p'.

Since the Palmgren-Miner damage model was introduced, more than 50 fatigue damage models have been proposed. These models are based on different theories and contained different boundary conditions [59]. All these models are specified to a specific situation and can predict the amount of fatigue damage for that specific situation rather well. However, on average, the Palmgren-Miner damage model provides better predictions than the other fatigue damage models. Therefore, the Palmgren-Minder rule is still the most commonly used model to predict the maximum number or load cycles for structures which are loaded by cyclic loads with different stress amplitudes [59].

The S-N curves are based on the stress level and the number of load cycles. The Palmgren-Miner damage model is based on a linear relation between the amount of damage and the number of load cycles. The theory behind the S-N curves and the theory behind the Palmgren-Miner damage model are independent of the mechanical properties of a material and can be used for steel as well for concrete [60, 61]. The parameters for the S-N curves for the different materials need to be validated with laboratory tests.

2.6.2 Fatigue in steel reinforcement

In a beam configuration, bending moments result in a zone with tensile stresses and in a zone with compressive stresses. In a RC beam, reinforcing bars are normally present in the zone with tensile stresses. In a cracked situation, the largest part of the tensile forces is carried by the reinforcing steel. The fatigue behaviour of the reinforcement is similar to the fatigue behaviour of a plain steel bar [62].

By increasing the number of load cycles, fatigue cracks in steel will appear and grow. After a small number of load cycles (in the early age of the structure), the number of fatigue cracks is limited and the fatigue cracks are relatively small. In this early stage of a structure's service-life, it is not clear which of the cracks will grow till failure [63].

2.6.3 Fatigue in concrete sections

Since the development of RC railway bridges in the beginning of the twentieth century, the interest of fatigue behaviour of concrete structures has increased a lot. Due to the heterogeneous properties of concrete, the fatigue behaviour of concrete is more complex than the fatigue behaviour of steel. In a RC beam, the compressive forces are mainly carried by the concrete and hardly by the reinforcement. For the fatigue analysis, the zones with compressive stresses in a RC beam are generally considered as plain concrete sections [61].

Mallett [61] showed that the Young's modulus of concrete can decrease with the number of load cycles. The reduction of the Young's modulus of concrete is strongly related to the load amplitude of the cyclic load [64]. A possible development of the Young's modulus of concrete as function of the number of load cycles is given in Figure 2-13 [60].

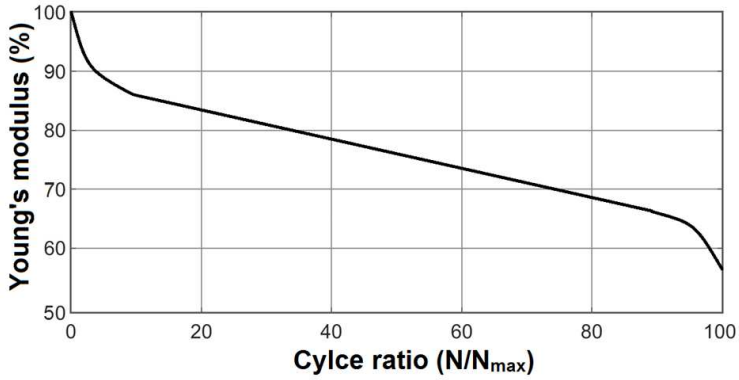

Figure 2-13: Potential development of the Young's modulus of concrete [60]. The horizontal axis shows the ratio between the number of load cycles (N) and the maximum number of load cycles until failure (N_{max})

The maximum number of load cycles of a concrete structure depends on many parameters [65]. The strength of the concrete, the ratio between the minimum stress and the maximum stress, the stress amplitude, and the load frequency are the most important parameters [64].

2.6.4 Fatigue in the bond between steel and concrete

The load bearing capacity of RC structures depends on the concrete, the steel, and the bond between reinforcing steel and concrete. The maximum number of load cycles until fatigue failure of the bond between steel and concrete occurs depends on the concrete strength, the ratio between the maximum bond stress and the minimum bond stress, the anchorage length of the reinforcing bar, and the number and width of the cracks in the concrete to the reinforcing bar [66]. Fatigue failure of the bond between steel and concrete will only occur when the anchorage length of the reinforcing bars is limited.

2.7 Corrosion

During winters, de-icing salts are frequently used in the Netherlands [67]. These de-icing salts are used to reduce freezing of the top layer of roads. Preventing the freezing of the top layer reduces the risks of slippery roads and thus the risks of accidents. Unfortunately, de-icing salts dissolved in water can penetrate into cracked concrete bridges, and could generate corrosion of the steel reinforcing bars [68].

Due to the high alkaline pore solution in the concrete, a thin sub-microscopic layer will be formed by a chemical reaction between steel and oxygen [69]. This passive layer protects the reinforcing steel against corrosion. When this layer is damaged (for example by carbon

dioxide or chloride-ions in the concrete near the steel reinforcing bars) corrosion of the steel reinforcing bars can be initiated [70].

2.7.1 Effects of corrosion

Due to the formation of corrosion products, the volume of the steel reinforcing bars increases. Since corrosion products can 'fill' the empty pores in the concrete around the reinforcing bars, a small amount of corrosion products can result in an increase of the bond strength between the reinforcing bars and the concrete [71]. By ongoing corrosion, the amount of corrosion products increases and initiates tensile stresses in the concrete [72]. When these stresses exceed the tensile strength of concrete, cracks will be initiated [73]. In this phase, the bond strength between the reinforcing bars and the concrete reduces significantly. A large amount of corrosion products can result in spalling of the concrete cover [74].

Corrosion of steel reinforcing bars has three main effects. The first effect is a reduction of the cross-section of the bar. This results in a reduction of the load bearing capacity of the bar. The second effect is a reduction of the bond strength between steel and concrete after cracks were initiated. The third effect is that a corroded steel bar has a more brittle behaviour than an uncorroded steel bar [69]. This lower ductility of the reinforcing bars reduces the deformation capacity of a RC structure. Therefore, a structure can fail more brittle than expected.

After cracking of the concrete, corrosion produces reduce the bond strength between steel and concrete [75]. It was shown in literature that the reduction of the stiffness of a RC structure is mainly caused by a reduction of the bond strength [76]. It was also shown in literature that the reduction of the bond strength due to corrosion of the reinforcing bar is far larger in dynamically loaded specimens than in statically loaded specimens [77, 78].

2.7.2 Initiation of corrosion

Corrosion category

Corrosion can be divided in three categories: general corrosion, localized corrosion, and fatigue corrosion. Fatigue corrosion mainly occurs in high-strength materials in a corrosive environment [79]. This category is not relevant to RC structures and not further discussed in this dissertation.

The ingress of carbon dioxide in concrete reduces the alkalinity in the pore solution in the concrete [80]. A reduced alkalinity in the pore solution of the concrete can damage the passive layer. Since the ingress of carbon dioxide is related to a larger surface, the ingress of carbon dioxide normally results in general corrosion [81].

Free chloride ions at the surface of the steel reinforcement can penetrate locally into the concrete and can damage the passive layer locally. Therefore, chloride ingress results in

localized corrosion [82]. Already a low concentration of free chloride ions can damage the passive layer locally. Therefore, already a small amount of free chlorides ions is enough to initiate a large reduction of the steel cross-section [83].

Corrosion periods

The development of corrosion in RC structures can be divided in two periods: the initiation period and the propagation period (Figure 2-14) [84]. During the initiating period, harmful substances penetrate into a concrete specimen and damage the passive layer around the steel reinforcement. In this period, corrosion has not started. In the propagation period, the steel reinforcement is corroding [85].

The initiation period for cracked concrete structures is different from the initiating period for uncracked concrete structures. In uncracked structures, harmful substances have to penetrate through the concrete cover before corrosion in the reinforcing bar starts. In cracked concrete structures harmful substances can penetrate easily via the cracks. Therefore, cracks shorten the initiation period and initiate corrosion far earlier than in uncracked situations [86].

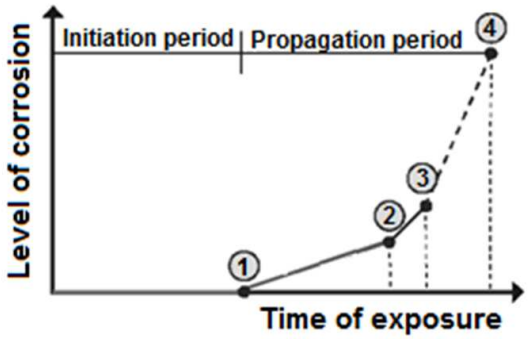

Figure 2-14: Different levels of corrosion [84] (1: damaging the passive layer around the reinforcement; 2: formation of cracks; 3: spalling of concrete; 4: structural failure).

Visual inspections can only detect corrosion during the propagation period. It was assumed that corrosion could be detected earlier by a SHM system than by visual inspections [13]. However, corrosion can only change the deflections and the natural frequencies of a bridge in the propagation period. Therefore, it is debatable whether SHM can detect corrosion in an earlier stage than visual inspection. In this study, the effect of corrosion on the dynamic behaviour of a RC beam is investigated.

2.7.3 Shear reinforcement

The shear capacity of RC structures can be increased by adding steel stirrups in the structure. Normally, these stirrups have a rectangular shape and are positioned around the main reinforcement (Figure 2-15). In these situations, the concrete cover on the stirrups is smaller than the concrete cover on the main reinforcement. Due to this smaller cover, chlorides and other harmful substances can reach the shear reinforcement earlier than the main reinforcement.

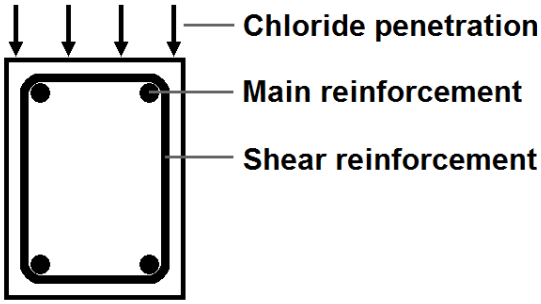

Figure 2-15: Illustration of the position of the main reinforcement and the shear reinforcement in a cross-section of a RC beam. When chlorides penetrate from the top surface, they reach the shear reinforcement earlier than the main reinforcement.

The shear forces are mainly carried by the vertical parts of the stirrups. The horizontal parts of the stirrups act as anchorage of the vertical parts of the stirrups. When the upper horizontal part of a stirrup is heavily corroded, the stirrup keeps a limited shear capacity. When a main reinforcing bar is heavily corroded, the load bearing capacity of the bar has reduced significantly. The effect of corrosion in the main reinforcement on the load bearing capacity of the RC structure can be more significant than the effect of corrosion in the shear reinforcement. Therefore, this study was focused on corrosion of a main reinforcing bar. Corrosion of stirrups is not further discussed in this dissertation.

2.8 Summary

In this chapter the current state of the art on SHM, as far as relevant for this thesis, was presented. Since the deflections of a bridge as well as the modal properties of a bridge depend on the material properties, it is suggested in the literature that the deflections and the modal properties of a bridge can be used as indicators for damage in concrete bridges. Real monitoring data of a concrete bridge are used to obtain data-driven modal properties. These modal properties are compared with the results of FE modal calculations (Chapter 3).

It was shown in this chapter that fluctuations in ambient temperature and fluctuations in the ambient humidity can result in changes in the deflections and in the modal properties of a concrete bridge. To obtain information about damage of a structure, SHM data should be filtered in such a manner that damage-induced changes in deflections or in the modal properties can be separated from changes in the deflections or in the modal properties initiated by fluctuations in the ambient conditions. Studies on obtaining these separations were not found in the literature. The effect of changes in the ambient temperature on the natural frequencies of a Presetressed Concrete bridge is discussed in Chapter 3. The effect of changes in the ambient temperature and in the ambient humidity of a RC beam is investigated in Chapter 4.

Chapter 3

Analysing Real Monitoring Data of a Concrete Bridge and Comparing Results with Predictive Models

Structural Health Monitoring (SHM) systems on bridges often contains sensors to measure the vibrations of the bridges. These data can be used to calculate the modal properties (natural frequencies, damping ratios, and mode shapes) of the bridge. Since the modal properties of a damaged bridge are different from the modal properties of the same bridge under undamaged condition, the modal properties could be used as indicators for structural damage. In this chapter, the relation between the results of data-driven modal calculations have been compared with the results of Finite Element (FE) modal calculations. This comparison was done on a practical case, The Hollandse Brug.

3.1 General approach

It has been suggested in literature (Section 2.5.4) that natural frequencies of a concrete bridge can be used as indicators for structural damage. Two methods for obtaining potential damage using natural frequencies of a concrete structure are presented in this study. In the first method, FE calculations are used to predict the natural frequencies of a concrete structure in damaged and undamaged situations. When the measured natural frequencies match with the results of the FE modal calculations, it could be possible that the actual amount of damage in the structure is similar to the simulated amount of damage in the FE calculations. For this first method, it is important that the natural frequencies of an existing bridge can be well predicted. The comparison between data-driven modal calculations and FE modal calculation is presented in this chapter. The second method is to obtain the development of the natural frequencies with time. When damage results in detectable changes in the natural frequencies, these changes can be observed in the development of the natural frequencies with time. For this method, it is important to know how the natural frequencies change. To investigate this development, laboratory tests on RC beams have been conducted (Chapter 4).

3.2 Description of the monitored bridge

The bridge, discussed and analysed in this chapter, is a prestressed concrete bridge; called the 'Hollandse Brug', and is located in the centre part of the Netherlands. This bridge is one of the main connections in the highway system between Amsterdam and the Northeast of the Netherlands. The bridge is daily used by more than 100,000 traffic units (single way) [87].

Figure 3-1: Picture of the Hollandse Brug, a monitored bridge in the middle of the Netherlands.

3.2.1 Technical properties

The bridge was designed according to the design codes that were used in the 1960s. The bridge was opened for traffic in 1969. The bridge has seven spans, each with a length of 50.75 meters (length of the girders: 50.55 meters, total length of the bridge: 355 meters). Every span contains nine prefabricated prestressed girders with a spacing of 4.11 meters (63 girders in total). A drawing of the Hollandse Brug is given in Figure 3-2. A dilatation joint was placed between each span. Due to this dilatation joint, bending moments cannot

be transferred from one span to another. Therefore, each span can be considered separately. The width of the bridge is 34 meters.

A concrete deck with a thickness of 200 mm was created between the girders. Extra concrete was added to create a cant in the road. A layer of approximately 50 mm asphalt was placed om top of this extra concrete. Each span contains four cross girders, which were cast in situ and post tensioned. The locations of the cross girders are given in Figure 3-2.

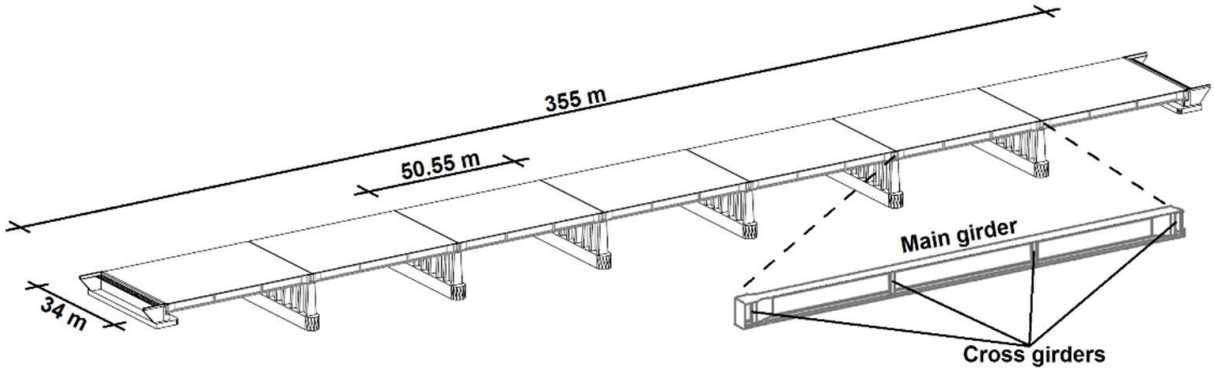

Figure 3-2: Drawing of the Hollandse Brug, including span dimensions.

TNO (the Dutch Organisation for Applied Scientific Research) inspected the Hollandse Brug in 2007 and concluded that the bridge was not safe enough to carry traffic loads over 12 tons [88]. To avoid these heavy loads on the bridge, it was forbidden for all trucks to pass the bridge until necessary renovations and strengthening were finished. Closure of the bridge had a large economic impact on the transport of products through the Netherlands [89].

In addition to the renovation in 2008, the bridge was enlarged with four meters in width, by adding one extra girder at both sides of the bridge. By widening the bridge, a third traffic lane could be realized in both traffic directions. Table 3-1 shows some parameters of a single span of the Hollandse Brug.

Table 3-1: Parameters of Hollandse Brug (single span only).

Parameters	Value	Unit
Weight of an original girder	2830	kg m^{-1}
Number of original girders	9	-
Weight of new girder	2220	kg m^{-1}
Number of new girders	2	-
Weight of bridge deck	500	kg m^{-2}
Original width of the deck	34	m
New width of the deck	38	m
Girder length	50.55	m

3.2.2 Structural Health Monitoring system

During the reconstruction activities, the bridge was used by cars. These cars generated traffic-induced vibrations in the bridge. It was assumed that these vibrations might influence the compacting of the fresh concrete of the new deck of the bridge. In order to understand the traffic-induced vibrations of the bridge during the construction works, a sensor network of 145 sensors (34 geo-phones, 91 strain gauges, and 20 temperature sensors) was installed underneath the first span of the bridge [90, 91]. A picture of some of the sensors on the first span is presented in Figure 3-3.

After the reconstruction activities, the sensors were still collecting data. In 2010, it was considered by Rijkswaterstaat that the measurements of these sensors could be used to obtain information about the health of the Hollandse Brug. With this, the sensor network became a Structural Health Monitoring (SHM) system. The data of this SHM system was handed over to the researchers of the InfraWatch project.

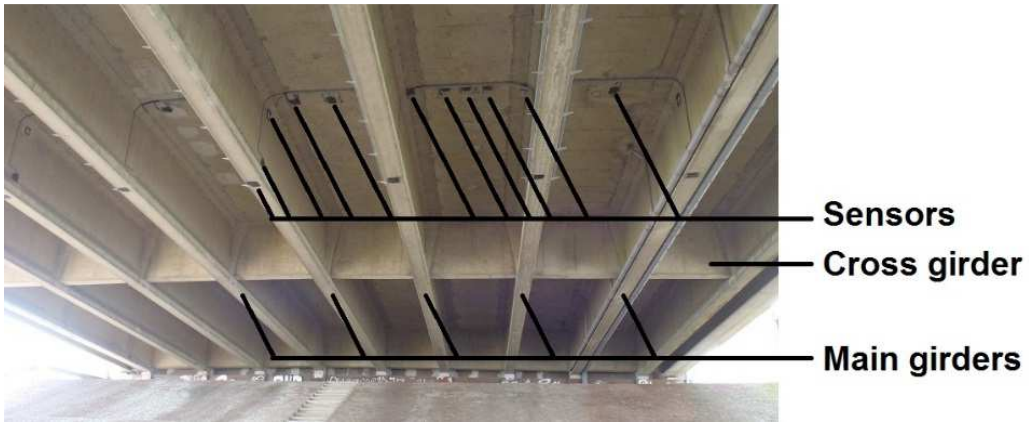

Figure 3-3: Part of the SHM network on the first span of the Hollandse Brug.

3.3 Data-driven modal calculations of the Hollandse Brug

Data-driven modal analyses use vibration data to calculate modal properties of a monitored structure. In this study, SHM data of the Hollandse Brug were used to calculate the modal properties of the Hollandse Brug. These modal properties are compared with modal properties obtained from FE calculations. For a better understanding of the comparison between the results of the data-driven modal calculations and the results of FE modal calculations, the principles of the data-driven modal calculations and the principles of the FE modal calculations are briefly discussed. Most of the data-driven modal calculations were performed by Miao [92-94]. A summary of his work is given in this section. The principles of the FE calculations are explained in Section 3.4.

3.3.1 Selection of vibration data

If, at several locations, the vertical vibrations are measured and these vertical vibrations can be related to the horizontal position of the sensor on the bridge, the mode shapes of an analysed frequency can be derived. A larger number of sensor locations results in a better approximation of the mode shapes. Deriving mode shapes is important for

identifying the natural frequencies (Section 2.5). The sensors of the SHM system on the Hollandse Brug are positioned on three cross-sections of a single span (Figure 3-4), whereby 114 sensors are located at midspan (first cross-section), 4 sensors are located on a second cross-section, and 27 sensors are located at a third cross-section. With this configuration of the sensors, only a grid of 12 geo-phones (4 girders x 3 cross-sections) can be used for modal calculations.

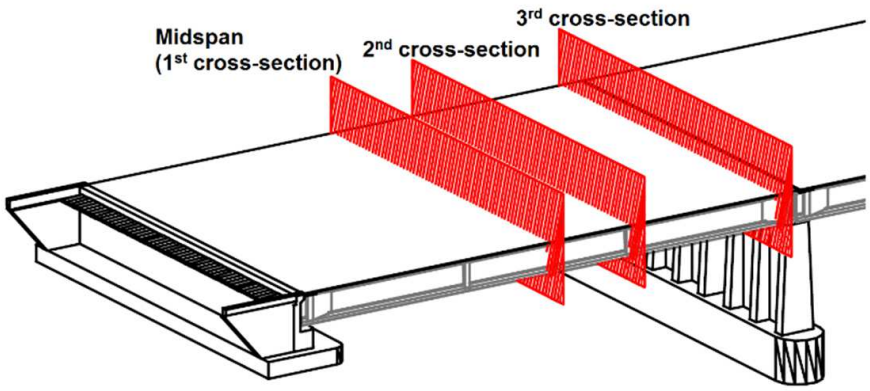

Figure 3-4: Different cross-sections of the locations of the sensors.

The vibrations of the bridge which are measured by the geo-phones are strongly influenced by vibrations of the traffic. To obtain vibration data without traffic vibrations, free vibration periods were selected from the data. A free vibration period is the period between one vehicle has passed the bridge and a second vehicle enters the bridge (Figure 3-5). The first seconds after a vehicle has passed the bridge are most important to obtain the fundamental natural frequency of the bridge. Free vibration periods can seldom be found in daytime data. Therefore, the selected data was derived from measurements between two and three at night.

At the first cross-section (midspan), strain gauges are closely located to the geo-phones. Data from these strain gauges were used to verify the presence and the absence of traffic on the bridge. To obtain stable calculation results, 149 spectra of 149 different truck events during multiple nights were analysed.

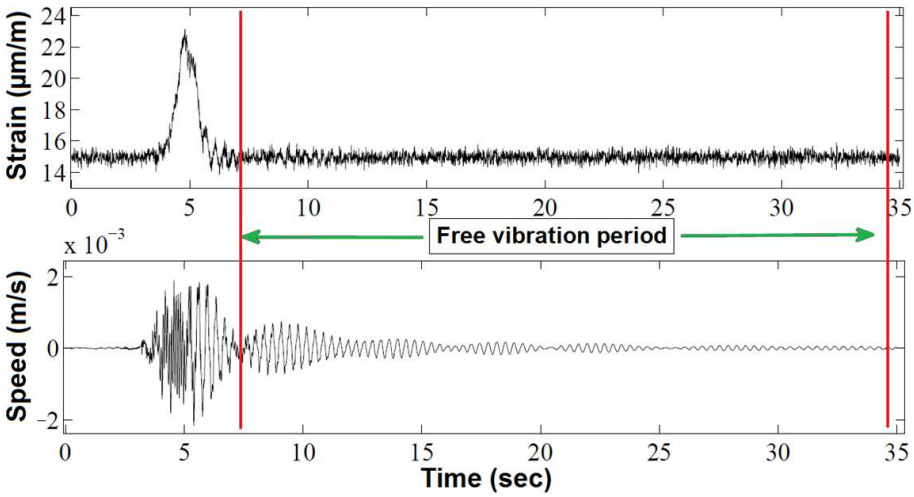

Figure 3-5: Free vibration period. The upper graph is obtained from a strain gauge. The lower graph is obtained from a geo-phone.

3.3.2 Calculation results

The data-driven modal calculations were performed using the Peak-Picking (PP) method and the Stochastic Subspace Identification (SSI) method (Section 2.3.4). Six natural frequencies were found by using the SSI method (three first order natural frequencies and three second order natural frequencies). Two of the second order natural frequencies could not be found by using the PP method. The results of the PP method and the SSI method are given in Table 3-2. The amplitudes of the second order natural frequencies are smaller than the amplitudes of the first order natural frequency and have the same magnitude as the amplitudes of noise in the data. This makes identification of the second order natural frequencies more difficult. Identification of the second order natural frequency is also difficult due to the limited number of measurements per load cycle, whereby the maximum amplitude of the second order natural frequencies might not be found.

Table 3-2: Natural frequencies of the Hollandse Brug by data-driven modal calculations [92].

Mode	Mode shape	Order	Frequency (PP)	Frequency (SSI)
1	Bending	First	2.61 Hz	2.51 Hz
2	Torsional	First	2.90 Hz	2.81 Hz
3	Bending & Torsional	First	5.75 Hz	5.74 Hz
4	Bending	Second	Not found	10.09 Hz
5	Torsional	Second	11.41 Hz	11.47 Hz
6	Bending & Torsional	Second	Not found	11.99 Hz

3.3.3 Influence of ambient conditions on the natural frequencies

Concrete bridges are exposed to variable ambient conditions such as temperature, humidity, wind, rain, and sunlight radiation. These conditions influence the deflections and the natural frequencies of a bridge. The effect of fluctuations of the ambient temperature on strains in the bridge is clearly visible in Figure 3-6, which shows a 24 hours

strain signal together with a temperature curve of the same period. Changes in the strain signal as result of traffic jams are also visible in Figure 3-6. The data for these signals are derived from sensors which are located below the deck in the middle of the first span of the bridge. The temperature measurements concern the ambient temperature below the deck.

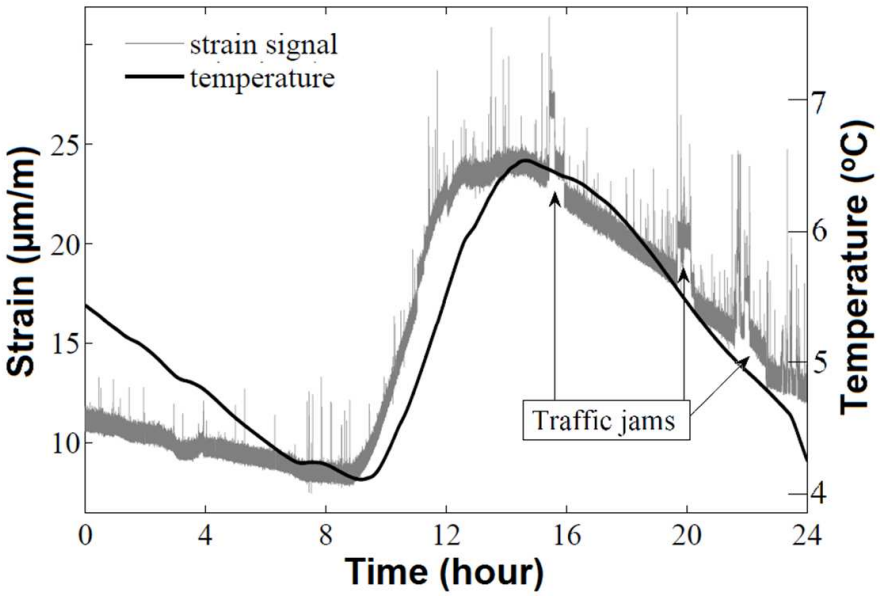

Figure 3-6: Influence of temperature and traffic jams on a strain signal. The data for these signals are derived from sensors which are located in the middle of the first span of the bridge.

The relation between changes in the ambient temperature and changes in the natural frequencies of the bridge is less straightforward than the relation between changes in the ambient temperature and changes in the strains in the bridge. To obtain the relation between changes in the ambient temperature and changes in the natural frequencies, three years of SHM data have been analysed. The measured first order natural frequencies in relation to the measured ambient temperature are given in Figure 3-7. The analyses resulted in a fluctuation of 0.12 Hz/K for the first order natural frequencies (2.1 - 6.2 Hz) and a fluctuation of 0.27 Hz/K for the second order natural frequencies (9.0 – 13 Hz). The scatter in the analyses are relatively high. Therefore, a relation between changes in the ambient temperature and changes in the natural frequencies of the Hollandse Brug could not be used for practical applications.

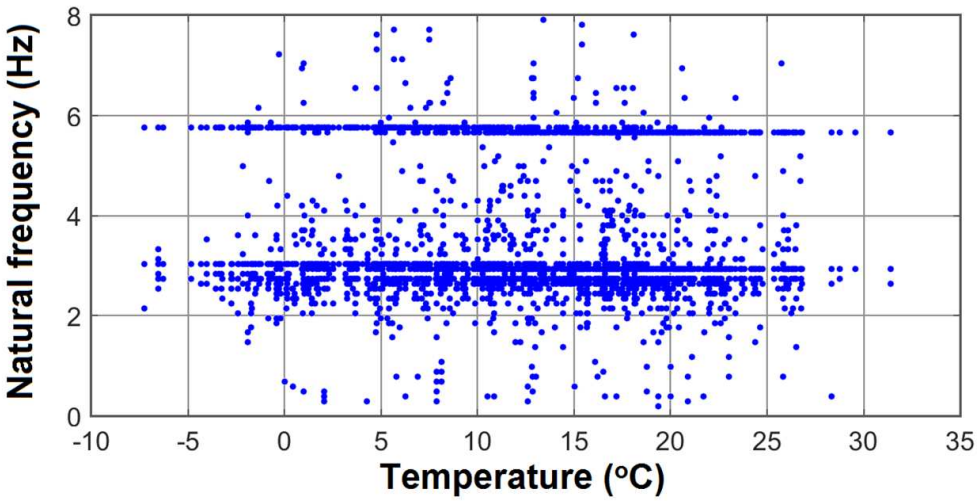

Figure 3-7: Measured first order natural frequencies of the Hollandse Brug in relation to the measured ambient temperature.

3.4 Finite Element calculations of the Hollandse Brug

The natural frequencies of the Hollandse Brug were calculated using two FE programs. The simulation of a bridge in a FE program is called a "FE model". The first FE model contains a 2D schematization of the bridge. For this FE model, the Scia Engineer software [95] was used. The second FE model contains a 3D schematization of the bridge, for which the DIANA FEA software [96] was used. The setup and the results of both FE models are presented in this section. The comparison between natural frequencies obtained by data-driven calculations and natural frequencies calculated using the FE models is presented in Section 3.5.

3.4.1 Configuration of the bridge

As discussed in Section 3.2, all spans of the Hollandse Brug can deform independently. Since all spans of the bridge are similar, the results of the FE calculations of a single span can be used to predict the behaviour of the total bridge. It was also discussed in Section 3.2 that every span contains nine girders from the 1960s and 2 girders, installed in 2008. Most information which was required for modelling the girders from the 1960s was found in preserved blueprints of the bridge [97-99]. These blueprints contain information about the dimensions of the bridge. The unit masses and the Young's moduli are important material properties for obtaining modal properties. Unfortunately, the exact values of the unit masses and the Young's moduli of the different sections of the bridge are unknown. The unit mass and the Young's modulus can be obtained by tests on cores from the bridge. It is, however, not practical to drill cores in all different sections of the bridge.

A guideline of Rijkswaterstaat (part of the Dutch Ministry of Infrastructure and Environment) [100] provides information about the quality of the concrete of existing bridges. According to this guideline, the quality of the concrete of the prestressed girders from the 1960s is C55/67, and the quality of the concrete of the cross-girders from the

1960s is C35/45. These qualities of concrete were used in the calculations. The Young's moduli of these qualities of concrete [101] are presented in Table 3-3.

In 2008, the quality of the concrete of the new girders was C60/75 and the quality of the new part of the deck was C35/45 [102]. It was assumed that these qualities did not significant change in the past years. The concrete qualities and the corresponding Young's moduli are given in Table 3-3. The effect of changes in the Young's moduli on the natural frequencies of the bridge has been investigated in a sensitivity analysis (Section 3.4.5).

Table 3-3: Estimated concrete quality and the corresponding Young's moduli of different elements of the Hollandse Brug.

Element	Concrete class	Young's modulus
Old girders	C55/67	38000 N/mm^2
Cross girders	C35/45	34000 N/mm^2
New girders	C60/75	39000 N/mm^2
Old deck	C35/45	34000 N/mm^2
New deck	C35/45	34000 N/mm^2
Additional concrete	C25/30	31000 N/mm^2

3.4.2 Unit mass

The unit mass of Reinforced Concrete (RC) and Prestressed Concrete (PC) depends on the composition of the concrete and on the amount of steel. The average value of the unit mass of plain normal weight concrete is 24.0 kN/m^3 [103]. For RC and PC with a normal amount of reinforcement, an unit mass of 25.0 kN/m^3 has to be used in design calculations [103].

According to the blueprints, two layers were located on top of the concrete deck: a layer of concrete and a layer of asphalt. The top layer is a layer of asphalt with a thickness of approximately 50 mm (unit mass is 23.0 kN/m^3). A small layer of concrete is present between the structural concrete of the deck and the asphalt layer. This layer of concrete has a thickness of 30-80 mm and results in a cant of the road.

Since the actual thickness of these layers was not investigated in this research, the thickness had to be estimated. For the asphalt layer, a thickness of 50 mm was schematized in the FE model. For the additional concrete, an average thickness of 50 mm (C25/30) was schematized. The effects of uncertainties in the mass on the natural frequencies of the bridge have been investigated in a sensitivity analysis (Section 3.4.5).

3.4.3 Stiffness of the bearings

The bridge is supported with rubber bearings which are reinforced with steel plates. The properties of the bearings were not investigated in this research. The dimensions of the bearings were estimated at the site. The estimated dimensions of the bearings are given in Table 3-4. Figure 3-8 shows an illustration of a bearing of the Hollandse Brug as it was estimated.

Table 3-4: Dimension of the bearings.

Parameters	Value
Length	500 mm
Width	500 mm
Height	41 mm

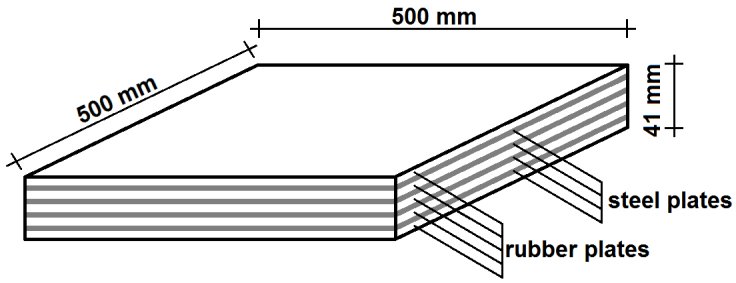

Figure 3-8: Illustration of the bearings of the Hollandse Brug.

The natural frequencies of the bridge depend on the stiffness of the girders and the deck, but also on the stiffness of the supports. As indication: the first natural frequency of a line element with an equally distributed mass and supported by two rotational fixed ends is 130% higher than the first natural frequency of a line element with an equally distributed load and supported by two rotational free ends [104]. The bearings of the Hollandse brug were designed as rotational free supports. However, it is possible that the bearings slightly limit the rotation of the bridge. The amount of limitation depends on the horizontal and vertical stiffness of the bearings.

The horizontal stiffness and the vertical stiffness of the bearings were estimated using equations of the European code for elastomeric bearings [105]. For this estimation, 4 reinforcing plates, a shear modulus of the bearing of 1.0 N/mm^2, and a bulk modulus of 2000 N/mm^2 were used. A sensitivity of the stiffness of the bearings on the natural frequencies of the bridge is investigated in a sensitivity analysis (Section 3.4.5).

In the FE model in Scia Engineer, the bearings were schematized as vertical and horizontal springs. In the FE model in DIANA FEA, the bearings were schematized as 3D solid elements. Due to the different schematizations, the input parameters for the bearings for the two FE models are different. The input parameters for the bearings of both FE models are given in Table 3-5.

Table 3-5: Input parameters for the bearings for two FE models.

Parameters	Value (Scia Engineer)	Value (DIANA FEA)
Vertical spring stiffness	$6.7*10^6$ N/mm^1	26.8 N/mm^3
Horizontal spring stiffness	$8.6*10^3$ N/mm^1	$34.5*10^{-3}$ N/mm^3

3.4.4 Finite Element models of the Hollandse Brug

Two FE models were made to calculate the modal properties of the Hollandse Brug. The first FE model is a plate model made with the Scia Engineer software [95, 106]. The second FE model is a volume model and made with the DIANA software [96, 107].

In the FE model in Scia Engineer, the deck was schematized as an orthotropic plate with 2D elements of approximately 1.0*1.0 m^2. The asphalt layer and the additional concrete could not be schematized separately from the deck. Therefore, the deck, the additional concrete, and the asphalt layer were schematized as a single layer. The Parallel-axis Theorem [108] was used to calculate one value of the unit mass and one value of the Young's modulus for the combination of the deck, the additional concrete, and the asphalt layer. The plate theory of Mindlin-Reissner [109, 110] was used in the calculation model. The girders were modelled as 1D elements. These 1D elements were connected to the 2D elements in such a way that the deformations of the girders are the same as the deformations of the deck. Figure 3-9 shows the FE model of the Hollandse Brug in Scia Engineer.

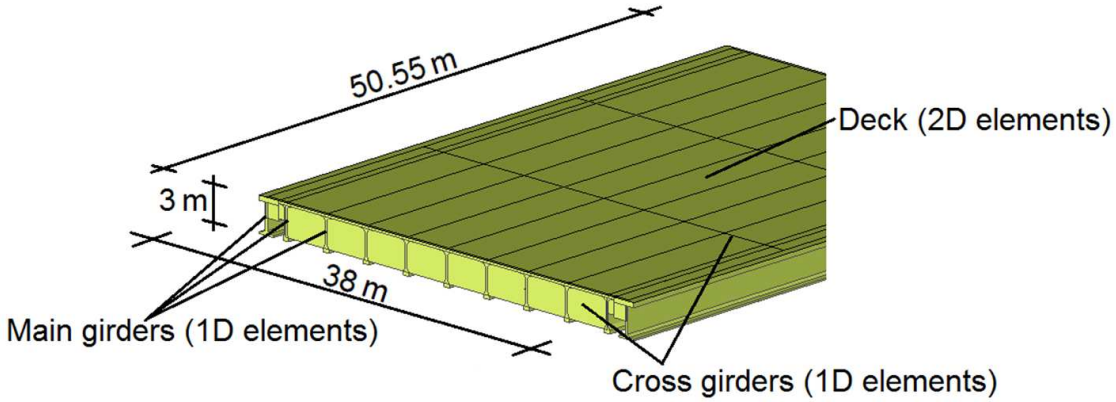

Figure 3-9: FE model of the Hollandse Brug in Scia Engineer.

In the FE model in DIANA FEA, the main girders, the cross girders, the deck, the cant in the bridge, and the asphalt layer were schematized with different solid components. These components were filled with a mesh of tetrahedrons [111] with rips of approximately 250 mm. Figure 3-10 shows the FE model of the Hollandse Brug in DIANA FEA.

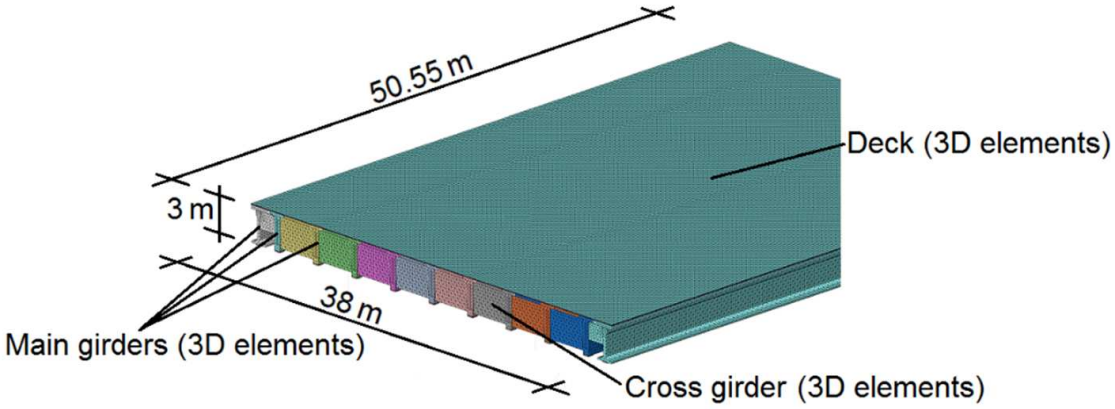

Figure 3-10: FE model of the Hollandse Brug in DIANA FEA.

Both calculation programs contain routines to calculate the natural frequencies of a modelled structure. The results of the modal calculations showed local vibrations of the girders and the deck, and global vibrations of the total bridge. The mode shapes were used to separate the global mode shapes from the local mode shapes. The results of the global mode shapes of both FE modal calculations are given in Table 3-6.

Table 3-6: Natural frequencies of the Hollandse Brug calculated by two FE models.

Mode	Mode shape	Order	Frequency (Scia Engineer)	Frequency (DIANA FEA)
1	Bending	First	2.30 Hz	2.36 Hz
2	Torsional	First	2.47 Hz	2.58 Hz
3	Bending & Torsional	First	4.86 Hz	5.15 Hz
4	Bending	Second	8.53 Hz	8.68 Hz
5	Torsional	Second	8.94 Hz	9.20 Hz
6	Bending & Torsional	Second	10.32 Hz	10.81 Hz

3.4.5 Sensitivity analysis

For modelling the Hollandse Brug, assumptions were made for the Young's moduli, the unit masses, and the stiffness of the bearings (Sections 3.4.1, 3.4.2, and 3.4.3). A sensitivity analysis was made to investigate the effect of changes in the estimated values on the natural frequencies of the bridge.

In the sensitivity analysis, it was assumed that difference between the actual Young's modulus and the Young's modulus given in Section 3.4.1 can be 7%. The difference in the unit mass was estimated to 4%, which corresponds to 100 kg/m^3. The volume of the girders and the deck are presented in the blue prints. It was assumed that the girders were schematized correctly and that the scatter in the cant of the bridge and the thickness of the asphalt layer is 50 mm. This 50 mm corresponds to 13% of total mass of the deck of the bridge. FE modal calculations showed that the scatters presented above can result in a variation in the natural frequencies of 18%.

It was discussed in Section 3.4.3 that the horizontal stiffness and the vertical stiffness of the bearings could have a large influence on the natural frequencies of the bridge. This

stiffness is calculated using estimated dimensions of the bearings, an estimated number of reinforcing plates, and estimated values of the shear modulus and bulk modulus.

Calculations showed that the horizontal stiffness and the vertical stiffness of the bearings can be 12 times higher than calculated values by increasing the length and the width of the bearings by 50 mm, increasing the thickness of the steel plate by 2 mm, and taking one steel plate less into account. When the length and the width of the bearings are 50 mm smaller, the steel plates are 1 mm thinner, and there is one steel plate more, the horizontal stiffness and the vertical stiffness of the bearings reduce to approximately 10% of the calculated values.

The natural frequencies were calculated using the increased stiffness and the reduced stiffness as presented above. The mode shapes were used to identify the natural frequencies. The results of these calculations are presented in Table 3-7. This table shows a scatter of 17% in the calculated natural frequencies.

Table 3-7: Sensitivity of the bearing stiffness on the natural frequencies of the Hollandse Brug.

Mode	Frequency original calculation*	Frequency low stiffness bearings		Frequency high stiffness bearings	
1	2.36 Hz	2.15 Hz	91% **	2.74 Hz	116% **
2	2.58 Hz	2.41 Hz	94% **	3.01 Hz	117% **
3	5.15 Hz	4.99 Hz	97% **	5.64 Hz	110% **
4	8.68 Hz	8.26 Hz	95% **	8.33 Hz	96% **
5	9.20 Hz	8.91 Hz	97% **	10.67 Hz	116% **
6	10.81 Hz	10.46 Hz	97% **	11.33 Hz	105% **

* Frequency of original DIANA calculation as presented in Table 3-6.

** Percentage of original DIANA calculation.

3.5 Comparison of the modal calculation results

The natural frequencies of the Hollandse Brug were calculated with four models. Two of these models were data-driven models and were based on SHM data of the bridge (PP method and SSI method). The natural frequencies calculated by the PP method and the SSI method were presented in Table 3-2. The other two models are FE models, which were mainly based on information from blueprints. The natural frequencies predicted by the FE models were presented in Table 3-6. Since damping was not simulated in the FE models, the damping ratios were not considered in the comparison. The natural frequencies and the corresponding mode shapes are compared.

3.5.1 First natural frequency: first order bending

The first natural frequency is the fundamental frequency of the structure and shows a first order bending shape. The fundamental frequency is decisive for the overall deflections of the bridge. The fundamental frequency depends mainly on the bending stiffness of the bridge and the mass of the total bridge. Table 3-8 shows the first natural frequency

calculated using different methods and computer programs. Figure 3-11 shows the mode shape of the first natural frequency of the bridge.

Table 3-8: First natural frequency of the bridge (first order bending), calculated by different methods and computer programs.

Monitored (SSI method)	Monitored (PP method)		Calculated (Scia Engineer)		Calculated (DIANA FEA)	
2.51 Hz	2.61 Hz	104% of SSI	2.30 Hz	92% of SSI	2.36 Hz	94% of SSI

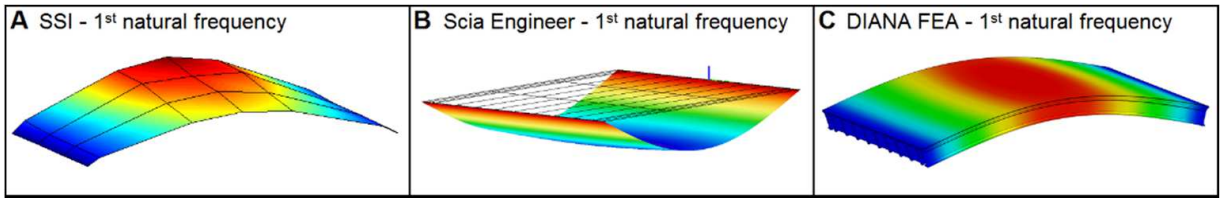

Figure 3-11: Mode shape of the first natural frequency of the bridge (first order bending). Different methods and computer programs were used (SSI, Scia Engineer, DIANA FEA).

3.5.2 Second natural frequency: first order torsion

The second natural frequency has a torsional shape, whereby the midspan of the bridge rotates in transversal direction (Figure 3-12). This frequency depends on the torsional stiffness of the bridge. The torsional stiffness of the bridge is related to the bending stiffness of the cross girders and the connection between the main girders and the cross girders. Table 3-9 shows the second natural frequency calculated using different methods and computer programs.

Table 3-9: Second natural frequency of the bridge (first order torsion), calculated by different methods and computer programs.

Monitored (SSI method)	Monitored (PP method)		Calculated (Scia Engineer)		Calculated (DIANA FEA)	
2.81 Hz	2.90 Hz	103% of SSI	2.47 Hz	88% of SSI	2.58 Hz	92% of SSI

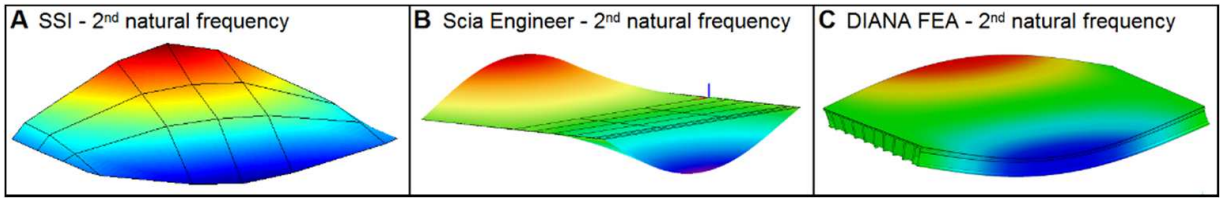

Figure 3-12: Mode shape of the second natural frequency of the bridge (first order torsion). Different methods and computer programs were used (SSI, Scia Engineer, DIANA FEA).

3.5.3 Third natural frequency: combination of first order bending and first order torsion

The third natural frequency is a combination of first order bending and first order torsion. The shape of this natural frequency is a curvature (half sine) in both longitudinal and transversal direction (Figure 3-13). This frequency depends on the bending stiffness and the torsional stiffness of the bridge. The third natural frequency is given in (Table 3-10).

Table 3-10: Third natural frequency (combination of bending and torsion), calculated by different methods and computer programs.

Monitored (SSI method)	Monitored (PP method)		Calculated (Scia Engineer)		Calculated (DIANA)	
5.74 Hz	4.75 Hz	100% of SSI	4.86 Hz	85% of SSI	5.12 Hz	90% of SSI

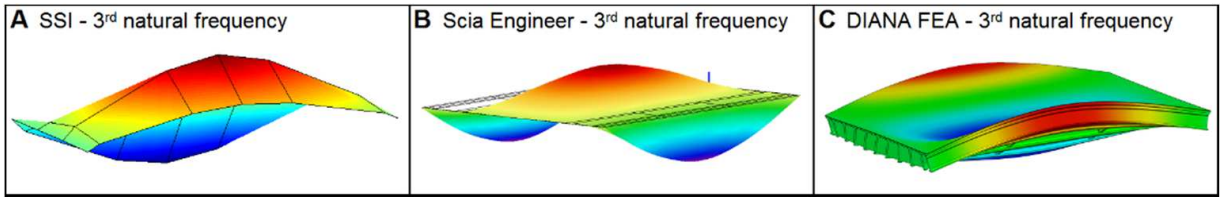

Figure 3-13: Mode shape of the third natural frequency of the bridge (combination of first order bending and first order torsion. Different methods and computer programs were used (SSI, Scia Engineer, DIANA FEA).

3.5.4 Second order natural frequencies

The amplitudes of the second order natural frequency are smaller than the amplitudes of the first order natural frequencies. Therefore, the second order natural frequencies are more difficult to obtain from SHM data. Data of 12 geo-phones are available for the modal analyses. As a result of this limited number of sensors (Section 3.3.1), the mode shapes can hardly be visualized. This makes it difficult to identify the second order natural frequencies. On the other hand, the second order natural frequencies are more sensitive to uncertainties in the bending stiffness of the bridge, in the torsional stiffness of the bridge, and in the stiffness of the bearings than the first order natural frequencies. Therefore, the predicted values of the second order natural frequencies (using FE calculations) could differ more from monitored values of the second order natural frequencies than difference between the calculated vales and the monitored values of the first order natural frequencies.

The mode shapes (Figure 3-14) where used for the comparison of the natural frequencies between the monitored natural frequencies and the natural frequencies predicted using FE models. Table 3-11 shows the second order natural frequencies calculated by different methods and computer programs.

Table 3-11: Second order natural frequencies of the bridge.

Monitored (SSI method)	Monitored (PP method)		Calculated (Scia Engineer)		Calculated (DIANA FEA)	
10.09 Hz	Not found		8.53 Hz	85% of SSI	8.68 Hz	86% of SSI
11.47 Hz	11.41 Hz	99% of SSI	8.94 Hz	78% of SSI	9.20 Hz	80% of SSI
11.99 Hz	Not found		10.32 Hz	86% of SSI	10.81 Hz	90% of SSI

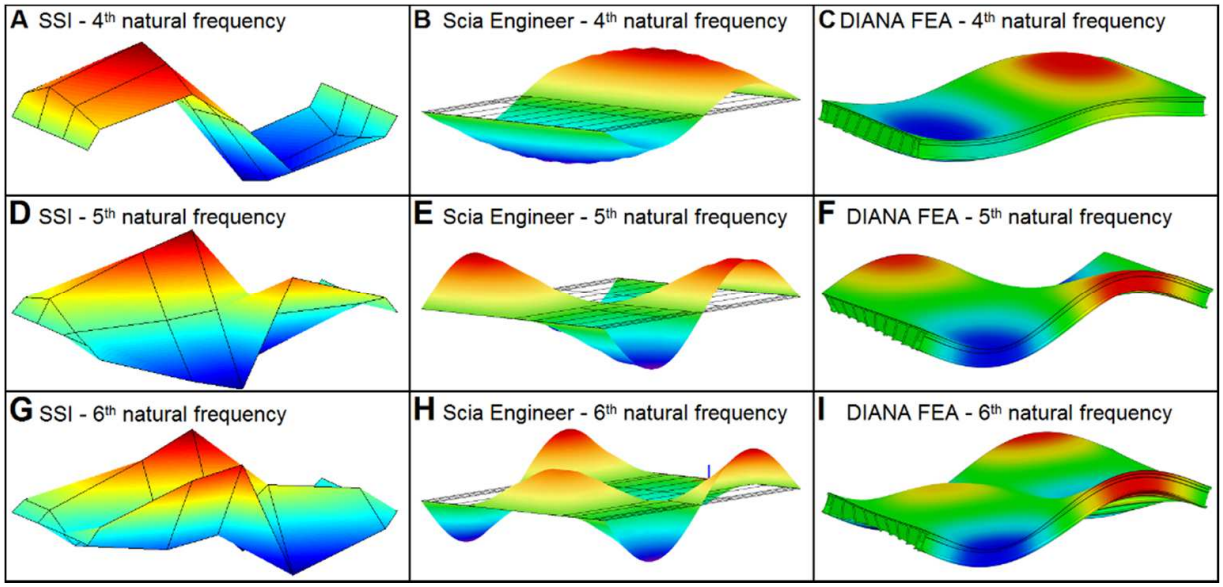

Figure 3-14: Mode shapes of the second order natural frequencies of the bridge (4th, 5th, and 6th natural frequency). Different methods and computer programs were used (SSI, Scia Engineer, DIANA FEA).

3.5.5 Higher order natural frequencies

For the higher order natural frequencies (>6th mode), the number of data points per period is limited compared to the number of data points per period of the first order natural frequencies. Furthermore, the amplitudes of the higher order frequencies are very small and can hardly be selected from the data. It is unlikely that the comparison between the higher order natural frequencies obtained by different methods will result in smaller differences than in the first and second order natural frequencies. Therefore, higher order natural frequencies will not be analysed further.

3.6 Measuring damage in a concrete bridge

The Hollandse Brug is prestressed in both longitudinal and transversal direction. Damage in the prestressing steel in a Prestressed Concrete (PC) bridge can result in a reduction of the prestressing forces. When the reduction of the prestressing forces is limited and the applied loads remain lower than the load at which the bridge starts to crack, the effective Young's modulus will hardly change. Therefore, the natural frequencies of the PC bridge will hardly change either. When the reduction of the prestresing forces is larger and the PC bridge starts to crack, the natural frequencies of the PC bridge are excessively changed (reduction of 70%). However, when this happens, the load bearing capacity of the PC bridge has reduced significantly (reduction of 90% of the load bearing capacity is possible) [112].

A Reinforced Concrete (RC) bridge is normally cracked. Damage in the reinforcing bars of a RC bridge can result in larger cracks in the concrete. When the cracks increase, the stiffness of the bridge decreases. This results in larger deflections and lower natural frequencies. Damage-induced changes in the natural frequencies of a RC bridge can

probably be detected earlier than damage-induced changes in the natural frequencies of a PC bridge.

To illustrate the effect of damage on the deflections of a concrete structure, two force-deflection diagrams are illustrated in Figure 3-15. Figure 3-15-A shows a force-deflection diagram of a statically loaded PC element. As a result of losses in the prestressing force, the load at which the structure starts to crack decreases. When the applied load is lower than this reduced value, the stiffness of the element hardly changes and the natural frequencies of the structure with hardly change either. Figure 3-15-B shows a force-deflection diagram of a statically loaded RC element. In this situation, the element is cracked. Larger cracks results in a reduction of the bending stiffness. Due to a reduced bending stiffness, the natural frequencies decrease. Changes in the natural frequencies can earlier be observed in RC bridges than in PC bridges.

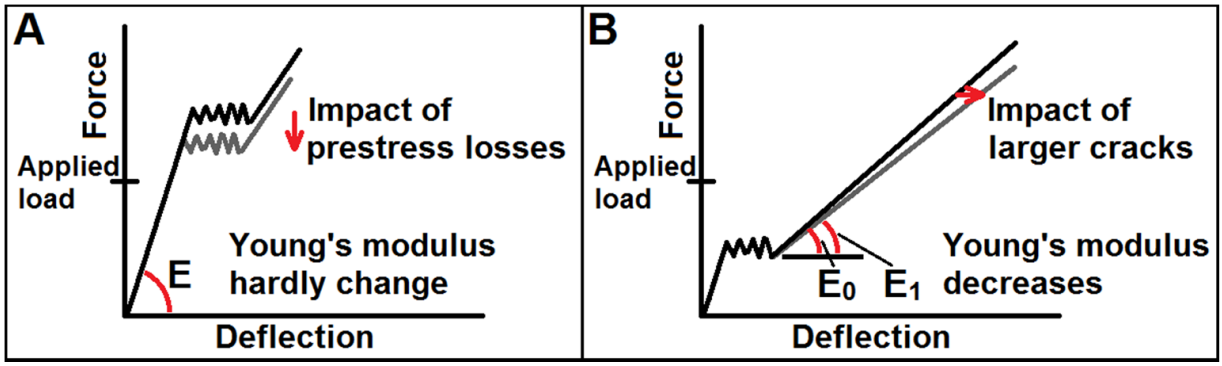

Figure 3-15: Illustration of the effect of damage on a concrete element. Figure 3-15-A shows a force-deflection diagram of a PC structure. Figure 3-15-B shows a force-deflection diagram of a RC structure.

An example of a RC bridge which is heavily damaged by corrosion is the Nijkerkerbrug in the Netherlands. This bridge (Figure 3-16) was built in the 1960s and is the main road connection between the province of Gelderland and the province of Flevoland. Corrosion of the reinforcing steel and spalling of the concrete were observed at the pylons and the deck of this bridge. Due to the heavy traffic loads on the bridge, it was suggested that the bridge was heavily damaged by fatigue as well [113, 114]. This is, however, never been investigated. Due to the large amount of damage, it is likely that the natural frequencies of this bridge have changed. Since no sensors were installed on this bridge, the changes in the natural frequencies of this bridge could not be obtained from SHM data.

Figure 3-16: Corrosion and spalling of a supporting beam from the Nijkerkerbrug, a RC bridge in the Netherlands.

3.7 Discussion and summary

SHM data of a prestressed concrete bridge (Hollandse Brug, located in the centre of the Netherlands) were used to calculate modal properties (mode shapes, natural frequencies, and damping ratios) of a bridge. Two data-driven modal calculations have been used (using the PP method and the SSI method). Calculation results of both methods were required to discover which of the obtained frequencies are stable (related to the bridge) and which of the obtained frequencies were unstable (related to traffic). The instable natural frequencies were eliminated from the calculation results.

Two FE models (one 2D FE model and one 3D FE model) were used to calculate the natural frequencies of the bridge. The results of the modal calculations of both FE models were compared with the results of the data-driven modal calculation. The mode shapes were used to find the corresponding natural frequencies in the different calculations. A difference (5-10%) in the first three modes (first order natural frequencies) was found between data-driven modal calculations and FE modal calculations. The second order natural frequencies (mode 4, 5, and 6) show higher differences (10-20%). The third and higher order natural frequencies were not compared in this study. It was assumed that the differences in the higher order natural frequency are larger than the differences in the first and second order natural frequencies.

The monitoring system on the Hollandse Brug contained 34 geo-phones, 91 strain gauges, and 20 temperature sensors. Because the sensors in the Hollandse Brug were not initially installed as SHM system, most of the sensors were not installed on the most favourable position to obtain the modal properties of the bridge. Data of 12 geo-phones (4 girders x 3 cross-sections) were used to calculate the modal properties of the Hollandse Brug. The mode shapes of the first order natural frequencies could be derived from this number of sensors. The limited number of sensors makes identification of the second order natural frequency more difficult. This increases the uncertainties in the second order natural frequencies compared to the uncertainties in the first order natural frequencies.

Monitored data of geo-phones contain vibrations of the bridge. These vibrations could be initiated by traffic, but also by wind or other random vibrations (noise). Furthermore, the vibrations are disturbed by vibrations of the traffic. In the higher order natural frequencies, the amplitude of the vibrations of the bridge are in the same magnitude as the amplitude of the noise. Therefore, it is difficult to separate the vibrations as results of the natural frequencies from the vibrations as result of noise. This results in large uncertainties in the calculated natural frequencies.

The dimensions of the bridge were obtained from blueprints or estimated by site-visiting. The stiffness and the strength of the concrete were estimated using a guideline for existing structures. Samples of the bridge can be taken to obtain the unit mass, stiffness, and the strength of the concrete at specific locations in the bridge. However, taking samples reduces the strength of the bridge locally. Furthermore, cores cannot be drilled at every location of the bridge. Therefore, material properties always contain uncertainties. The bearings of the bridge will contain uncertainties as well.

A sensitivity analysis was performed to investigate the sensitivity of the natural frequencies on changes in stiffness, mass, and mechanical properties of the bearings. It was shown that changes in the stiffness and the mass of the bridge can result in a scatter of the natural frequencies of 16%. Changes in the stiffness of the bearings can result in a scatter of 17% in the natural frequencies of the bridge. Due to the large scatter in the predicted natural frequencies, there is a high probability that the results of the FE modal calculations do not match well with the results of data-driven modal calculations. On the other hand, when the natural frequencies have been changed, these changes might be obtained as scatter in the natural frequencies.

In the presented situation, it was not possible to predict the health and the remaining service-life of the bridge. Therefore, it cannot be confirmed that comparing the results of FE calculations with the results of data-driven modal calculations can be used to predict the health and the remaining service-life of concrete bridges. For a better understanding of how natural frequencies of concrete structures change during its total service-life, fundamental research on concrete structures is required. To investigate potential patterns in monitoring data, tests were conducted. Since it was assumed that changes in the natural frequencies can earlier be detected in RC structures than in PC structures, the tests were conducted with RC beams. The setup and the results of the tests are presented in Chapter 4.

Chapter 4

Dynamic Tests on Plain Steel Bars and Reinforced Concrete Beams

Traffic load on existing bridges can be far heavier than the design traffic load of these bridges. Due to this heavier load, the probability of fatigue failure of existing structures increases [115]. As result of the use of de-icing salts, the probability of corrosion damage in existing Reinforced Concrete (RC) structures increases as well [116]. To which extent corrosion of steel reinforcing bars reduces the fatigue load capacity of RC structures is unknown. Tests on plain steel bars and on RC beams were conducted to provide information about the deflections of the RC structures during its total service-life and information about the influence of chloride-induced corrosion on the fatigue load capacity. The setup of the tests, the development of the elongations of the bars, and the development of the deflections of the RC beams are presented in this chapter. The development of the deflections of a RC beam might be used to gain information about damage in the RC beam.

4.1 Dynamic tensile tests of plain steel bars

Two series of tests are conducted. The first series of tests, called 'Bar Test', is on plain steel bars, which were dynamically loaded in axial direction. The setup and the results of the Bar Test are presented in this section. The results of the Bar Test are used to understand the fatigue failure mechanism of RC beams. In the second series of tests, called 'Beam Test', RC beams were loaded dynamically in a four-point-bending configuration. The setup and the results of the Beam Test are presented in Section 4.2.

4.1.1 Setup of the tests

The Bar Test was developed to investigate the elongations of a steel bar under dynamic loading. The main purpose of the Bar Test was to investigate the failure mechanism of a dynamic loaded plain steel bar with and without localized corrosion. This failure mechanism could be used to understand better the failure mechanism of a RC beam (Section 4.6).

Bars with a length of 420 mm were installed in a computer-controlled tensile testing machine [117]. Between both ends of the bar, a Linear Variable Differential Transformer (LVDT) was installed. This LVDT measured the elongations of the bar during the tests. The elongations of the bars are presented in Section 4.1.4.

Different local environments were created to investigate the effect of localized corrosion on the elongations of the bar and on the maximum number of load cycles until failure. To create a local environment, a plastic cup was glued on the bar. The cup was filled with water with different chloride concentrations (Section 4.1.2).

All tested bars were made of standard reinforcing steel (Steel quality: FEB 500 HKL, cold rolling) [118] and had a diameter of 12 mm. Bars with the same quality were used as reinforcing bars in the RC beams of the beam test (Section 4.2.2). A picture of the test setup is presented in Figure 4-1. A detail of a plain steel bar is presented in Figure 4-2.

Figure 4-1: Picture of the test setup. In most dynamic tests, the cup was filled with a chloride-solution to create a local chloride rich environment.

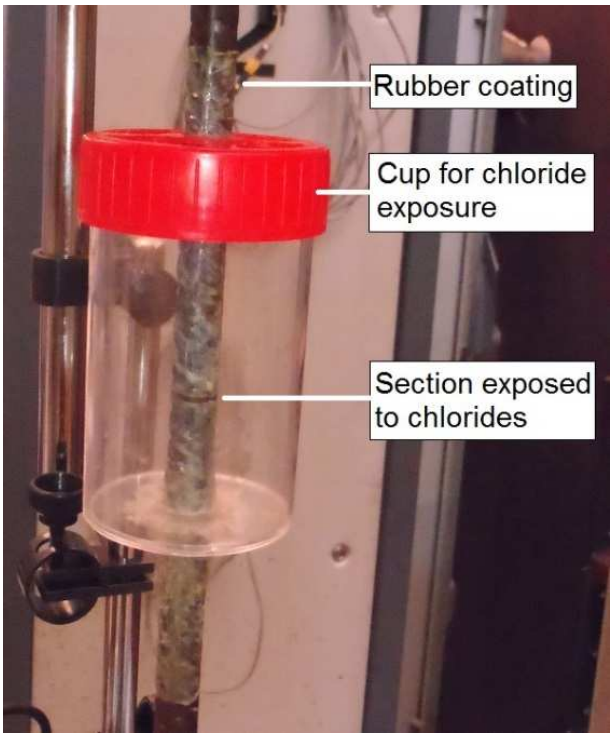

Figure 4-2: Detail of a plain steel bar. In this figure, the rubber coating on the bar and the section of the bar which was exposed to a chloride-solution are shown.

4.1.2 Loading and exposure conditions

All bars were dynamically loaded in axial direction. The bars were loaded in a load-controlled mode. Two different load amplitudes have been used. Seven bars were tested with a load amplitude of 28.25 kN. This corresponds to 250 N/mm^2 with regard to the initial cross-section of the bars, which is 42% of the yield stress. Six other bars were loaded with a stress amplitude of 33.90 kN. This corresponds to 300 N/mm^2 with regard to the initial cross-section of the bars, which is 50% of the yield stress. The load configurations are given in Table 4-1. Due to time limitations, tests with smaller load amplitudes were not conducted

All bars were loaded with a frequency of 2.5 Hz. This frequency was low enough to avoid preliminary failure and high enough to conduct several tests in a limited time period. An illustration of the applied dynamic loads is given in Figure 4-3.

Table 4-1: Overview of the loads applied on the reinforcing bar. The stresses concern the stresses in the initial cross-section of the bars.

Minimum load Minimum stress	Maximum load Maximum stress	Load average Stress average	Load amplitude Stress amplitude
2.83 kN 25 N/mm^2 *	31.08 kN 275 N/mm^2 *	16.95 kN 150 N/mm^2 *	28.25 kN 250 N/mm^2 *
2.83 kN 25 N/mm^2 *	36.73 kN 325 N/mm^2 *	19.78 kN 175 N/mm^2 *	33.90 kN 300 N/mm^2 *

* The stresses concern the stresses in the initial cross-section of the bars.

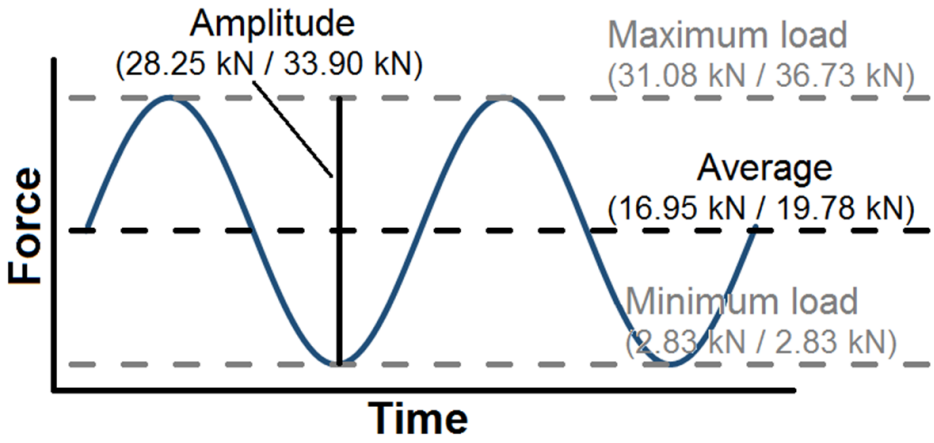

Figure 4-3: Illustration of the applied dynamic loads on the plain steel bars.

The plain steel bars were tested in a room with an ambient temperature of T=20 ±5°C and an ambient humidity of RH=70 ±25%. In RC structures, chloride ingress via cracks in the concrete results in a local environment with a high probability of corrosion. This situation was simulated by exposing a limited length of the bar (2 mm) by water with a Sodium Chloride (NaCl) concentration. The cup on the bar (presented in Section 4.1.1) was filled with water with a concentration of 5, 10, or 20% Sodium Chloride (NaCl) (by mass). The amount of chlorides in the solution was different for the different tested bars.

Except for the 2 mm exposure length, the bar was covered with a neoprene rubber coating. The only purpose of this coating was to avoid corrosion of the bar. Since the strength of the coating was far lower than the strength of the bar and the stiffness of the coating is far lower than the stiffness of the bar, the coating hardly influence the elongations and the fatigue life of the bar. The rubber coating on the bar and the section of the bar exposed to chlorides is shown in Figure 4-2. Table 4-2 shows an overview of the bars in the Bar Test.

Table 4-2: Overview of the bars in the Bar Test.

Test number	Load amplitude	Average amplitude	Chloride concentration	Number of tested bars
S250_E00	28.3 kN	17.0 kN	No chlorides *	1
S250_E05	28.3 kN	17.0 kN	5% NaCl (by mass)	2
S250_E10	28.3 kN	17.0 kN	10% NaCl (by mass)	2
S250_E20	28.3 kN	17.0 kN	20% NaCl (by mass)	2
S300_E00	33.9 kN	19.8 kN	No chloirdes *	3
S300_E05	33.9 kN	19.8 kN	5% NaCl (by mass)	1
S300_E10	33.9 kN	19.8 kN	10% NaCl (by mass)	2

* Ambient condition of T=20 ±5°C, RH=70 ±25%

4.1.3 Failure of the plain steel bars

A bar fails at the location where the stress/strength ratio is largest. To avoid early failure in a bar due to high stress concentrations at the supports [119], special attention was paid in the alignment the bars in the setup. The tested bars were not pre-damaged. Damage in the bar should be initiated by loading and exposure. Since all tested bars which were exposed to a chloride-solution failed at the chloride-exposed section, it was concluded that the chloride exposure reduced the maximum number of load cycles until fatigue failure. Figure 4-4 shows a picture of the cross-section of a bar after failure. In this figure, the corroded part of the cross-section can be separated from the uncorroded part of the cross-section. The bar is only damaged over a limited length of the bar. The cross-section of the bar as shown in Figure 4-4 is representative for all bars which were exposed to a chloride-solution.

Figure 4-4: A picture of the cross-section of the bar after failure.

The maximum number of load cycles per tested bar is given in Table 4-3. Test S250_E00 (stress amplitude of 250 N/mm^2 and no chloride exposure) was aborted before the bar had failed (after 1,693,576 load cycles). The other bars in the Bar Test were loaded until failure. When a lower stress amplitude was used (corresponding to stresses in a RC structure), the time per test was larger and less tests could be conducted.

From the bars loaded with a stress amplitude of 300 N/mm^2, it was concluded that the chloride-exposed bars can resist approximately 30% less load cycles than the bars without chloride exposure. The bars exposed to 5% chloride concentration can resist slightly more load cycles than the bars exposed to 10% chloride concentration. From the bars with a stress amplitude of 250 N/mm^2, it was observed that the bars exposed to 5% chloride concentration could resist less load cycles than the bars exposed to 10% chloride concentration or 20% chloride concentration. It was concluded that a larger chloride concentrations does not automatically result in a larger amount of corrosion and in a larger reduction of the number of load cycles until failure of the bar.

Table 4-3: Maximum number of load cycles for the different bars.

Test number	Cycles test 1	Cycles test 2	Cycles test 3	Average	Standard deviation
S250_E00	1,693,576 *	-	-	1,693,576 *	-
S250_E05	549,646	559,240	-	655,514	89,305
S250_E10	699,550	627,342	-		
S250_E20	688,261	809,042	-		
S300_E00	540,959	741,600	530,971	604,510	97,023
S300_E05	492,772	-	-	406,667	71,402
S300_E10	317,933	409,296	-		

* test was aborted before failure

4.1.4 Elongations of the bar

A Linear Variable Differential Transformer (LVDT) was used to measure changes in the distance between both ends of the bar (elongations). The measurements of the average elongation and the elongation amplitude were stored every minute, which corresponds to one measurement per 150 load cycles. Figure 4-5 shows a schematic illustration of the elongations of the plain steel bar.

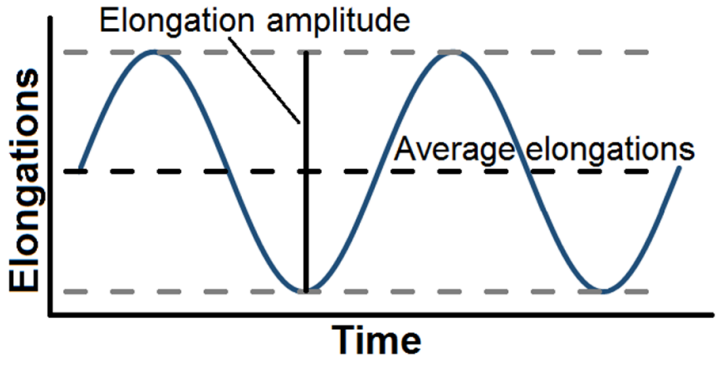

Figure 4-5: Schematic illustration of the elongations of the plain steel bars.

The elongations of the bar depends on the load on the bar, the length, diameter, and cross-section of the bar. Due to small differences in the anchorage length of the bar in the test-setup, the initial elongations of the bar is not the same for all tested bars. The difference between the initial elongations (at n=1 load cycle) of the bar and the elongations of the bar at n=n load cycles is called 'increase of the elongations'. The increase of the elongations mainly depends on the damaged section. The increase of the elongations of the bar are presented below.

Elongation amplitude of the bars loaded by an load amplitude of 33.9 kN

Figure 4-6 shows the increase of the elongation amplitude of the bars which were loaded with an amplitude of 33.9 kN (300 N/mm^2 with regard to the initial cross-section of the bars). The curves correspond to three different exposure conditions. Three bars (blue curves) were exposed to the ambient conditions in the laboratory (T=20 ±5°C, RH=70 ±25%) and were not exposed to a solution. The three other bars were exposed to respectively 5% (one red curve) and 10% chloride solution (two green curves). The main difference between the different curves is the number of load cycles until failure (Table 4-3). All curves in Figure 4-6 show a similar behaviour, whereby the elongation amplitude show small fluctuations during the first 99% of the load cycles and an increase of the elongation amplitude during the last few thousand load cycles.

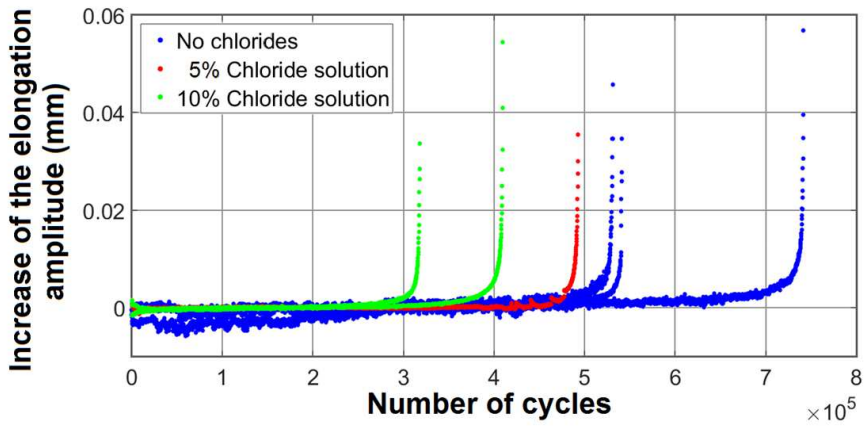

Figure 4-6: Increase of the elongation amplitude of six bars. All curves correspond the a bar loaded with an amplitude of 33.9 kN (300 N/mm^2 with regard to the initial cross-section of the bars).

Elongation amplitude of the bars loaded by an load amplitude of 28.3 kN

The increase of the elongation amplitude of the bars which were loaded with an amplitude of 28.25 kN (250 N/mm^2 with regard to the initial cross-section of the bars) are given in Figure 4-7. The bar which was not exposed to chlorides was not loaded until failure and the elongations of this bar are not plotted in this figure. Figure 4-7 shows that the bars exposed to 5% chloride concentration (red curves) had failed at a lower number of load cycles than the bars exposed to 10% chloride concentration (green curves) or 20% chloride concentration (cyan curves). Similar to Figure 4-6, the curves in Figure 4-7 shows small fluctuations during the first 99% of the load cycles and a larger increase of the elongation amplitude during the last few thousand load cycles.

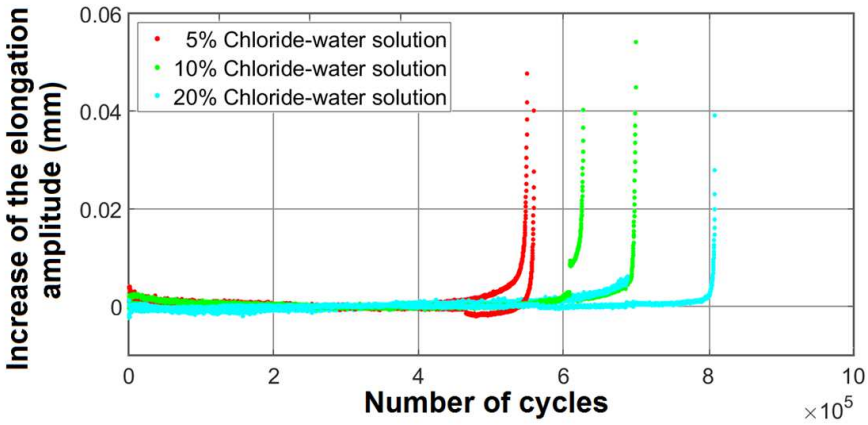

Figure 4-7: Increase of the elongation amplitude of six bars. All curves correspond the a bar loaded with an amplitude of 28.3 kN (250 N/mm^2 with regard to the initial cross-section of the bars). The bar which was not exposed to chlorides did not fail and is not presented in this figure.

Average elongation of the bar loaded by an average load of 17.8 kN

Similar to the elongation amplitude, the increase of the average elongation of the plain steel bar was analysed. Figure 4-8 shows the curves of the increase of the average elongation for the same bars as were used for the curves in Figure 4-6. From the similarity between the curves of Figure 4-6 and Figure 4-8, it is inferred that the increase of the elongations of the bar was caused by a decrease of the axial stiffness at the damaged section of the bar. The last two data points of the average elongation of all three bars are not plotted in Figure 4-8. These data points present an increase of the average elongation of 0.4-0.6 mm and do not fit in the scale of the vertical axis in Figure 4-8. Since this larger increase was not observed by the elongation amplitude, it was concluded that these larger increases of the average elongation were caused by local yielding of the bar.

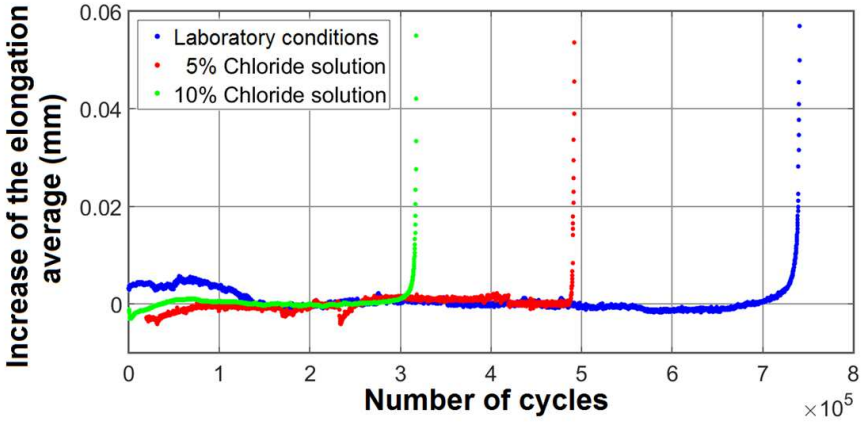

Figure 4-8: Increase of the average elongation caused by local damage. All curves correspond the a bar loaded with an average load of 19.8 kN (175 N/mm^2 with regard to the initial cross-section of the bars). The same data were used for the curves in Figure 4-6. The last two data points (average elongation of 0.4-0.6 mm) of all tested bars are not plotted in this figure.

4.2 Dynamic tests of Reinforced Concrete beams

The Beam Test was conducted to investigate the development of the deflections of a RC beam during its total service-life. Since fatigue was considered as decisive failure mechanism, the fatigue life of a tested RC beams was considered as service-life of the beam. The possibilities of using the development of the deflections of the RC beam for the prediction of the remaining service-life of the beam was analysed as well [120]. Twelve sets of two RC beams were tested in the Beam Test. Four different configurations in the loads on the beams and in the reinforcement in the beams (1 till 4) were investigated. Each configuration was repeated up to five times (A till E). The tests were numbered from 1A till 4C. An overview of the tested beam is given in Table 4-4.

Table 4-4: Overview of the tested RC beams.

Test	Load*	Shear reinforcement**
Test 1A, 1B	1.7 – 17.0 kN	No stirrups
Test 2A, 2B, 2C, 2D, 2E	2.0 – 12.0 kN	No stirrups
Test 3A, 3B	2.0 – 12.0 kN	Rectangular stirrups
Test 4A, 4B, 4C	2.0 – 12.0 kN	Triangular stirrups

* Loads are discussed in Section 4.2.3.

** Shear reinforcements are discussed in Section 4.2.2.

4.2.1 Configuration of the setup

Traffic on bridges produces a stress spectrum which may initiate fatigue damage [121]. To simulate this situation, a test setup was developed in which the RC beams were loaded dynamically. Figure 4-9 shows a picture of the test set-up of the dynamically loaded RC beams. The configuration of the RC beams is presented in Section 4.2.2.

De-icing salts can penetrate into the top layer of concrete bridges. When a RC bride is cracked, de-icing salts can penetrate into the concrete via the cracks and can reach the reinforcement at the top of a bridge relative fast. At the mid-supports of multi span bridges, the reinforcement at the top of a bridge is decisive for the flexural load bearing capacity of the bridge. Damage in this reinforcement can reduce the load bearing capacity of the bridge. In the tests, mid-supports of multi span bridges were simulated by positioning lab-scale beams in a loading frame in such a way that the cracks develop at the top side of the RC beams. A four-point-bending configuration was used to initiate cracks over a larger length of the bar. Every set of RC beams contains two similar RC beams. Corrosion of the reinforcing bar in one of these beams was initiated by exposing one RC beam to a chloride solution for two days per week. The other RC beam, which acts as a reference, was exposed to tap water during the same period of two days. The frequency of two days wet and five days dry were standardized within the IS2C program [122]. The RC beams were positioned on top of each other, both supported by the same frame setup and loaded by the same force actuator.

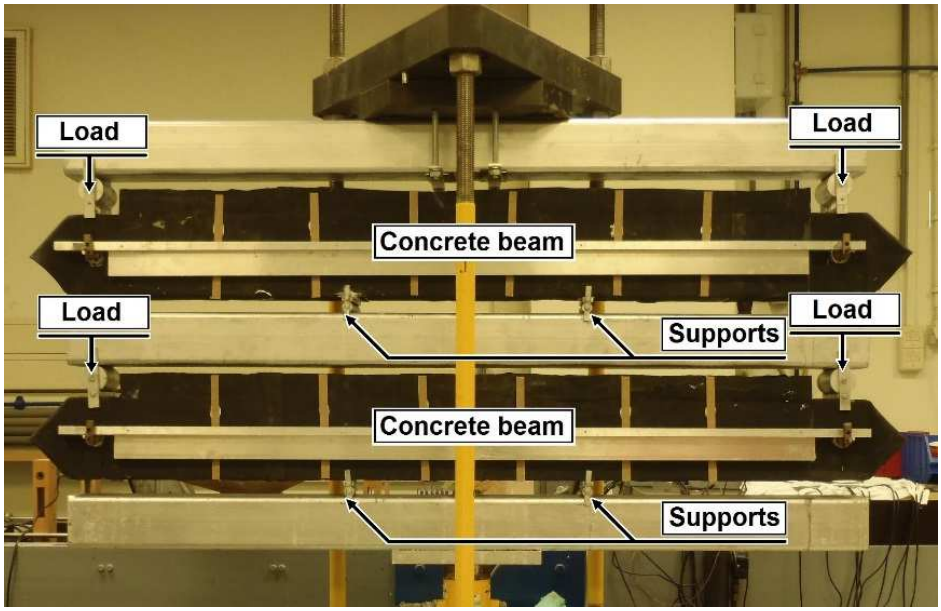

Figure 4-9: Picture of the test setup of the dynamically loaded RC beams.

Changes in the vertical distance between the ends and the middle of the beams were measured. These changes indicate the deflections of the RC beam. The initial vertical distance between the measurement point at the ends and the middle was 70 mm. Figure 4-10 shows the method of measuring the vertical deflections of the RC beam. The deflections were measured at the front and the rear side of the beams. The deflection of the RC beams, presented in this chapter, are the average values of the measurements at both sides of the RC beams.

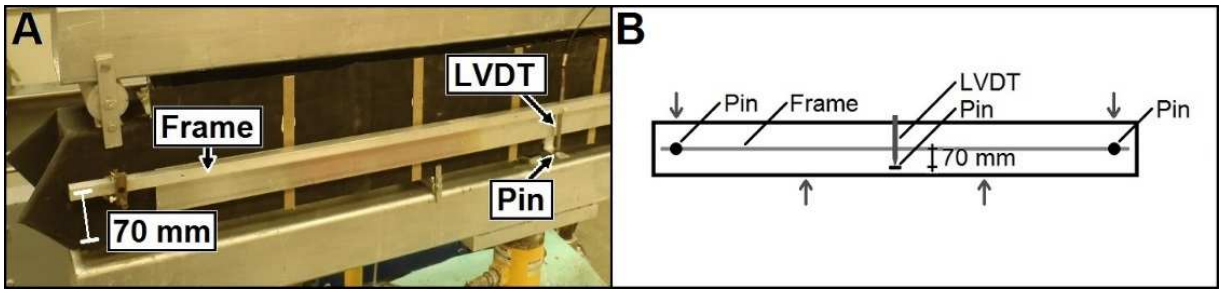

Figure 4-10: Method to monitor the vertical deflections. Figure 4-10-A shows a picture of a part of the beam. Figure 4-10-B shows an illustration of the situation.

4.2.2 Configuration of the beams

The dimensions of the beam, the support distances, and the mix design of the concrete were standardized within the IS2C program [122]. The RC beams were 1500 mm in length, 100 mm in width, and 150 mm in height [123]. The beams were reinforced with one single ribbed steel bar with a diameter of 12 mm. The quality of the reinforcing steel was the same as the quality of the plain steel bars in the Bar Test (FEB 500 HKL, Section 4.1.1). The concrete cover on this bar was 30 mm. The beams were loaded with two concentrated loads: one load at both ends of the beam. Two supports were positioned between the applied loads. Figure 4-11 shows an illustration of a RC beam and the distances between the loads and the supports.

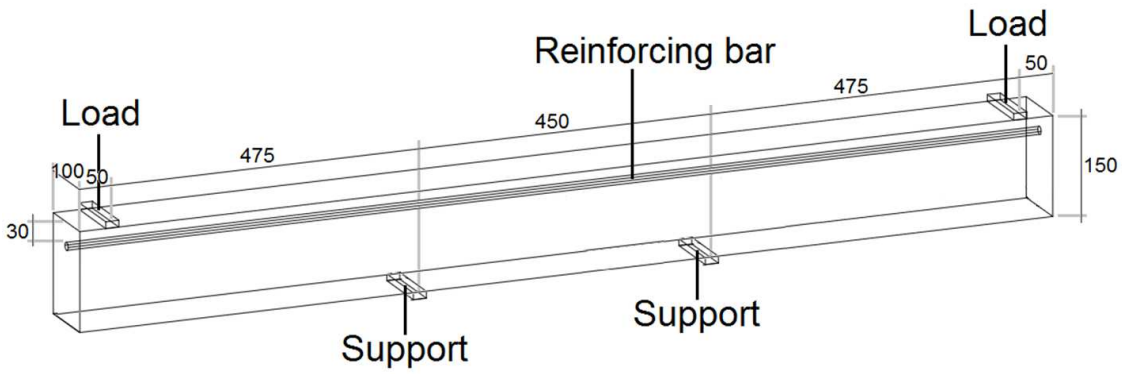

Figure 4-11: Illustration of a RC beam including the distance between the supports and the locations of the loads (dimensions in mm).

All tested beams were cast using the same mix (Table 4-5). Similar to the dimensions of the RC beam and the wetting/drying cycles, the mix design of the concrete was standardized within the IS2C program. After three days hardening in a room with a temperature of T=20 ±5°C and an ambient humidity of RH=70 ±25%, the formwork was removed and the beams were stored in a room with a temperature of T=20 ±2°C and an ambient humidity of RH=100%. One day before the RC beams were loaded, the RC beams were transferred to the test room (T=20 ±2°C and RH=50 ±10%). Table 4-6 shows the age of the beams at the first moment of loading.

Table 4-5: Mix design of concrete.

Type	Size	Mass
Aggregate	0.125 – 0.250 mm	78.3 kg/m^3
Aggregate	0.250 – 0.500 mm	256.2 kg/m^3
Aggregate	0.500 – 1.00 mm	256.2 kg/m^3
Aggregate	1.00 – 2.00 mm	157.7 kg/m^3
Aggregate	2.00 – 4.00 mm	98.5 kg/m^3
Aggregate	4.00 – 8.00 mm	394.2 kg/m^3
Aggregate	8.00 – 16.00 mm	729.2 kg/m^3
Cement	CEM I 42.5 N	260.0 kg/m^3
Water	Tap water	156.0 kg/m^3
Superplasticizer	Glenium 51, con.35% SPL	0.26 kg/m^3
		2387 kg/m^3 (in total)

Table 4-6: Age of beams at first moment of loading.

Test	1A	1B	2A	2B	2C	2D	2E	3A	3B	4A	4B	4C
Age (days)	29	92	28	49	51	50	126	31	28	45	41	51

Beside each set of beams, also thee cubes (150*150*150 mm^3) were cast. These cubes were used to determine the compressive strength of the concrete at the first day of loading. Parallel to casting the beams of Test 3A, fifteen cubes were cast. These cubes were cast to measure the evolution of the compressive strength with time. Fifteen cubes were also cast parallel to casting the beams of Test 4B. The measured compressive strengths are plotted in Figure 4-12. The average compressive strength was 35.5 N/mm^2. The standard deviation in the compressive strength was 3.0 N/mm^2 (8.5%).

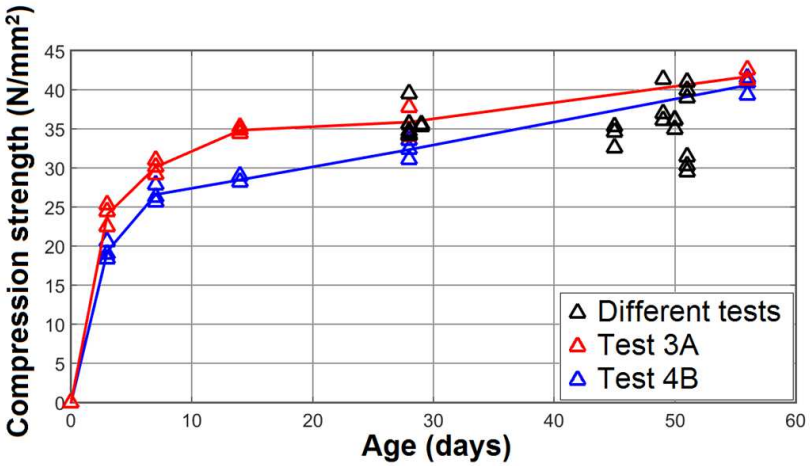

Figure 4-12: Measured concrete compressive strengths.

The main reinforcement of all RC beams was one ribbed steel bar with a diameter of 12 mm. Two static tests on a plain steel bar showed that the steel had a yield stress of 600 N/mm^2, an ultimate stress of 630 N/mm^2, and a Young's modulus of 191,000 N/mm^2. Figure 4-13 shows the stress-strain diagram of the steel in the static tensile tests. The measured properties were used in manual calculations (Section 4.3) and in Finite Element (FE) simulations (Chapter 5).

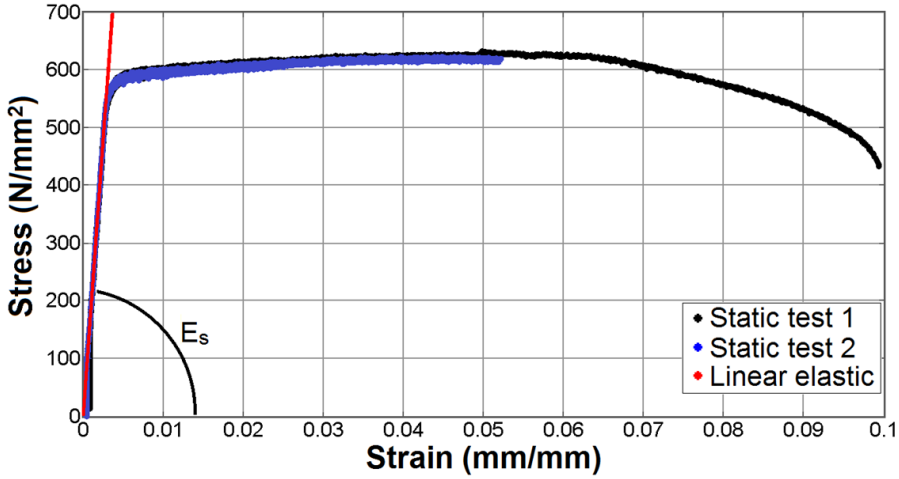

Figure 4-13: Stress-strain diagram of two static loaded plain steel bars, including the linear elastic part and the Young's modulus. The stresses were calculated using the initial cross-section of the bar.

Three different reinforcement configurations were investigated. In the first reinforcement configuration, the RC beam was only reinforced with one single steel bar (main reinforcement). In the second and in the third reinforcement configuration, the RC beams were strengthened with shear reinforcement as well. In the second reinforcement configuration, ribbed steel stirrups with a diameter of 6 mm and in the shape of a rectangle were applied. One ribbed steel bar with a diameter of 10 mm was installed in each of the corners of the stirrup (additional reinforcement). The steel quality of the stirrups and the additional reinforcement was the same as the steel quality of the main reinforcement. The stirrups were only applied at the locations where the shear stresses are highest. These locations are between the loads and the supports (Figure 4-14). The

additional reinforcement was applied only at these locations as well. Figure 4-15 shows a drawing of the RC beams with the second reinforcement configuration.

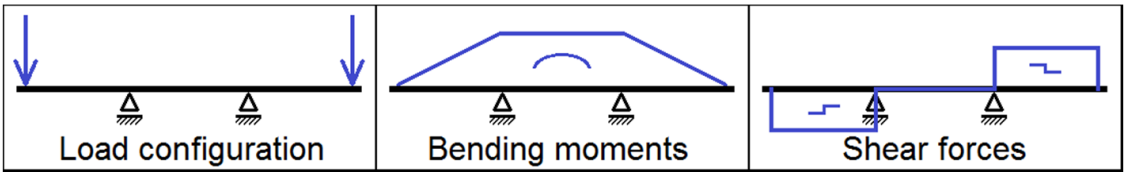

Figure 4-14: Schematic representation of the load configurations, the bending moments and the shear forces for the RC beams.

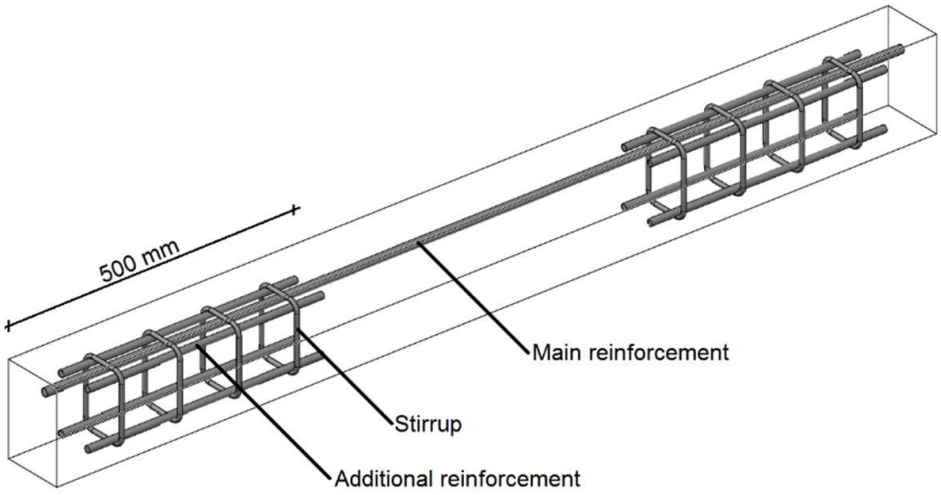

Figure 4-15: A drawing of the RC beam with the second reinforcement configuration.

Since the stirrups and the additional reinforcement were only positioned at the locations where the shear stresses are largest, the reinforcement configuration is discontinuous over the length of the beam. The total cross-sectional area of the additional reinforcement (2*79 mm^2) is larger than the cross-sectional area of the main reinforcement (1*113 mm^2). This configuration results in a significant increase (130%) of the stresses in the main reinforcement at the locations were the additional reinforcement ends. The discontinuity in the reinforcement was reduced in the third reinforcement configuration (Figure 4-16), whereby ribbed steel stirrups with a diameter of 6 mm and in a triangle shape were applied. Due to the triangular shape of these stirrups, additional reinforcement in the top of the RC beam was not required. To limit discontinuities of the configuration of the RC beam, the additional reinforcement at the bottom of the beam was continued over the total length of the RC beam.

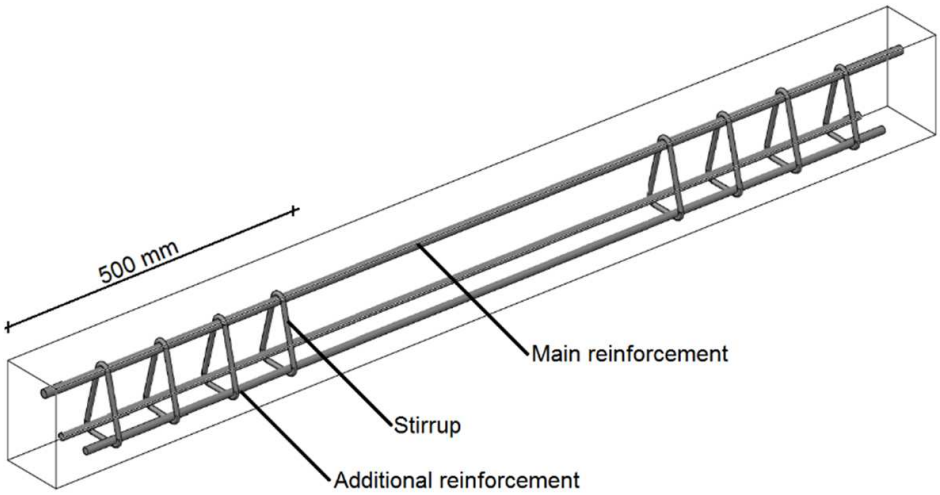

Figure 4-16: A drawing of the RC beam with the third reinforcement configuration.

4.2.3 Loading and exposure conditions

Twelve sets of two beams were tested with three different reinforcement configurations and two different loading conditions. The different reinforcement configurations were described in Section 4.2.2. The RC beams without shear reinforcement were loaded under two different loading conditions: from 1.7 kN to 17.0 kN and from 2.0 kN to 12.0 kN. The RC beams with stirrups were loaded with one load configuration (2.0 kN to 12.0 kN). An overview of the tested RC beams is given in Table 4-7.

Table 4-7: Overview of the tested RC beams.

Test number	Load	Calculated stresses *	Shear reinforcement
Test 1A, 1B	1.7 – 17.0 kN	30 – 340 N/mm^2	No stirrups
Test 2A, 2B, 2C, 2D, 2E	2.0 – 12.0 kN	40 – 240 N/mm^2	No stirrups
Test 3A, 3B	2.0 – 12.0 kN	40 – 240 N/mm^2	Rectangular stirrups
Test 4A, 4B, 4C	2.0 – 12.0 kN	40 – 240 N/mm^2	Triangular stirrups

* The steel stress was calculated using force equilibrium between compressive stresses in the concrete section and tensile stresses in the steel bar.

The RC beams were loaded with an alternating load as presented in Figure 4-17. The load frequency of all RC beams was 0.5 Hz. This frequency was the highest possible frequency for the available force actuator. The maximum load was 17.0 kN (70% of the measured static load bearing capacity of the RC beam, Table 4-9) or 12.0 kN (50% of the measured static load bearing capacity of the RC beam). The applied forces are presented in Table 4-8. The results of a static tests were presented in Section 4.3.

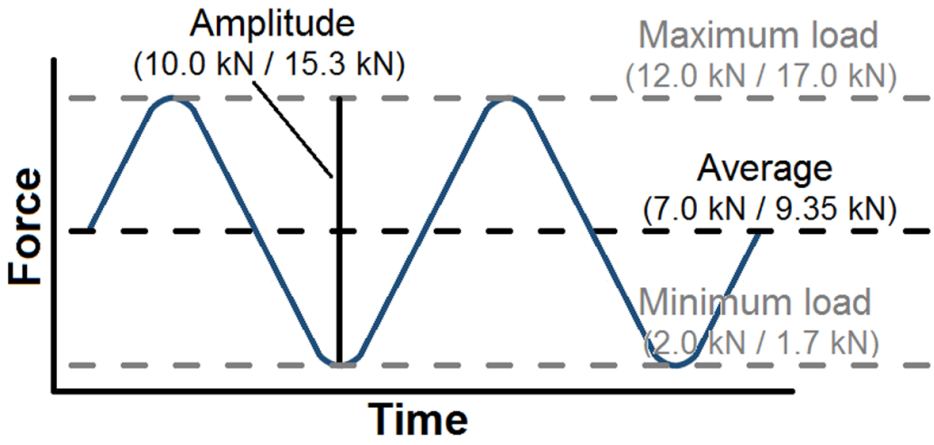

Figure 4-17: Illustration of the applied alternating loads on the RC beams.

Table 4-8: Overview of the loads on the RC beams.

Minimum load	Maximum load	Load average	Load amplitude
1.7 kN	17.0 kN *	9.35 kN	15.3 kN
2.0 kN	12.0 kN **	7.0 kN	10.0 kN

* 70% of measured static load bearing capacity

** 50% of measured static load bearing capacity

Large fluctuations in the deflections of the RC beams as result of fluctuations in the ambient condition were avoided by conducting the Beam Test under in a climate controlled room with an ambient temperature of T=20 ±2°C and an ambient humidity of RH=50 ±10%. Changes in the deflections of the RC beam as result of fluctuations in the ambient temperature are discussed in Section 4.5.1. The effect of changes of the humidity on the deflections of the RC beams is discussed in Section 4.5.2.

For each set of RC beams, one beam was exposed at the top side to water with a concentration of 10% Sodium Chloride (NaCl) (2.25 l water and 0.25 kg NaCl) and one beam was exposed at the top side to tap water (2.5 l). The chloride-solution was used to generate corrosion in the reinforcing bar. The RC beam exposed to tap water was used as reference beam. For exposing the RC beams to a chloride solution or to tap water, a bath was mounted on top of both beams. To avoid leakage via the cracks, the vertical and bottom sides of the RC beams were sealed. Wetting-drying cycles are identified as most unfavourable environmental condition for RC elements [82, 124]. In this study, a wetting/drying cycle of two days wet (filled bath), followed by five days dry (empty bath) was used.

4.3 Static defections and the static load bearing capacity of a Reinforced Concrete beam

One RC beam was loaded by a static load to determine the static load bearing capacity of the beams. The configuration of the RC beam was similar as those of Test 1A and 1B (without shear reinforcement). The static test was conducted before the first dynamic test. The static test was executed in a displacement-controlled mode. After 12 minutes of

increasing the deflection of the RC beam, shear failure of the beam occurred at a load of 24.9 kN (including a dead load of 0.6 kN).

Figure 4-18 shows the force-deflection diagram of the statically loaded RC beam. Three interesting details can be observed in this diagram. The first detail is the section of the curve between 5.0 kN and 6.5 kN. Between these loads, the cracks were developed and the stiffness of the RC beam decreased. The second detail concerns the top of the curve, whereby the curve shows an increase of the load while the deflections of the beam hardly change. This limited change of the deflection of the beam was caused by a limitation in the range of the LVDTs. Larger deflections could not be measured by these LVDTs. For the dynamically loaded RC beams, LVDTs with a larger range have been used. Therefore, this limitation had no influence on the measurements of the deflections of the dynamically loaded RC beams. The third interesting detail is the sudden decrease of the applied force at the end of the diagram. This decrease was caused by failure of the beam (shear failure).

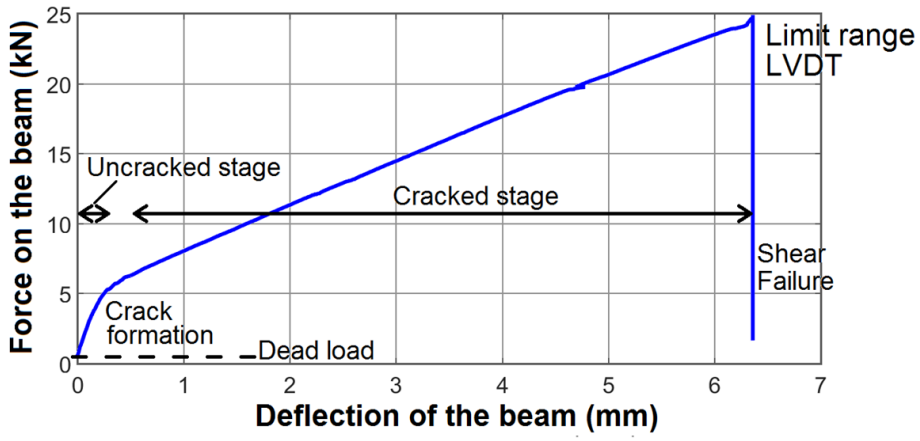

Figure 4-18: Force-deflection diagram of the statically loaded RC beam.

The static flexural load bearing capacity of the RC beam was calculated manually using force equilibrium between tensile forces in the reinforcing bar and compression forces in the cross-section of the beam. For the calculation of the compression force, a bi-linear stress-strain relation has been used. The flexural load bearing capacity of the RC beam was calculated using the compressive strength and the dimensions of the beam [101]. Table 4-9 shows the calculated flexural load bearing capacity, the calculated shear load bearing capacity, and the measured load bearing capacity.

Table 4-9: Load bearing capacity of a RC beam.

Calculated flexural load bearing capacity	Calculated shear load bearing capacity	Measured load bearing capacity (shear failure)
29.7 kN	26.8 kN	24.9 kN

4.4 Cyclic deflections of a Reinforced Concrete beam

Before the dynamic loads were applied, the RC beams were loaded statically until the maximum load (12.0 kN or 17.0 kN, Table 4-8). The number of cracks per RC beam was

between 6 and 9 cracks. The measured distance between two cracks varied between 70 and 140 mm. After unloading, LVDTs were placed across the cracks on the top surface of the RC beams to measure the width of three of the main cracks during the dynamic test. A second load cycle was performed to check whether the LVDTs were installed correctly. The second cycle was also used to check the stability of the RC beams in the test setup. Figure 4-19 the shows the deflections of one RC beam of Test 3A during the first two load cycles. The formation of the cracks can be observed at the loading part of the first cycle. Figure 4-19 also shows that the deflections of the beam during the unloading part of the first cycle, the loading part of the second cycle, and the unloading part of the second cycle are close to each other. This indicated a stable setup. The amplitude and the average of the deflections of the beams and the forces on the beams were stored every minute. Also the amplitude and the average of the width of three of the main cracks were stored every minute.

The deflections of the RC beam were used to discuss the development of the deflections of the beams. The crack widths were only used to explain a specific situation in detail (Section 4.6.2 and Section 4.6.4).

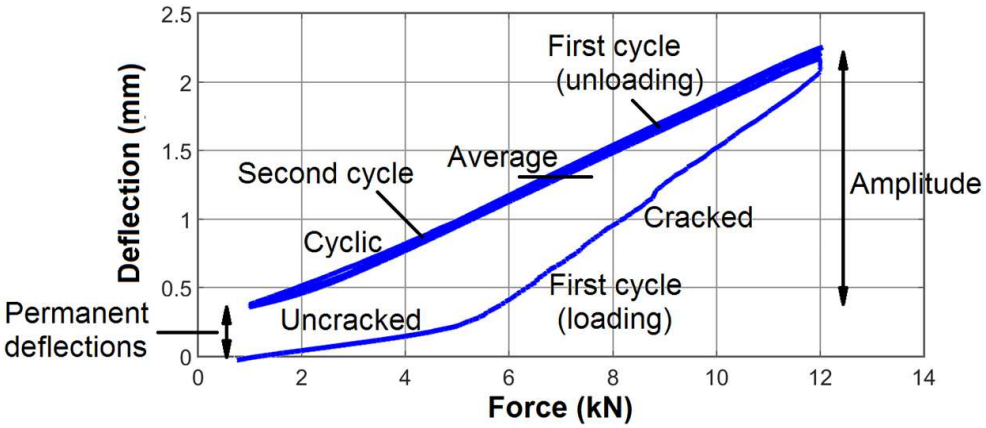

Figure 4-19: Cyclic deflection of a RC beam in Test 3A.

4.5 Effect of ambient conditions on the deflections of a Reinforced Concrete beam

Fluctuations in the ambient conditions result in changes in the deflections of the RC beams. In order to better understand the development of the deflections of the RC beam as result of damage in the reinforcing bar, changes in the deflections of the RC beams as result of fluctuations in the ambient conditions should be eliminated from the measured deflections.

Although changes in the deflections of the RC beams as result of fluctuations in the ambient conditions are relatively small, they can result in an incorrect interpretation of the deflections of the RC beams. In this section, the effect of fluctuations in the ambient

temperature on the deflections of the RC beams, and the effect of wetting/drying cycles on the deflections of a the RC beams are discussed.

4.5.1 Effect of temperature on the deflections of a beam

The ambient temperature in the room where the Beam Test was conducted fluctuated two degrees Celsius. Every 6-8 minutes, fresh air (with a certain temperature and humidity) was blown in the room to keep the temperature and humidity in the room rather constant. Figure 4-20 shows the deflections of one of the RC beams of Test 4B (beam exposed to tap water for two days per week) after 20 days of loading for a period of 0.05 days (72 minutes). These 72 minutes were within the drying period (exposed to air with an ambient temperature of T = 20 ±2°C and an ambient humidity of RH=50 ±10%). To compare the deflections of the RC beams with the ambient temperature, the ambient temperature around the RC beams is plotted on a second vertical axis of the same figure.

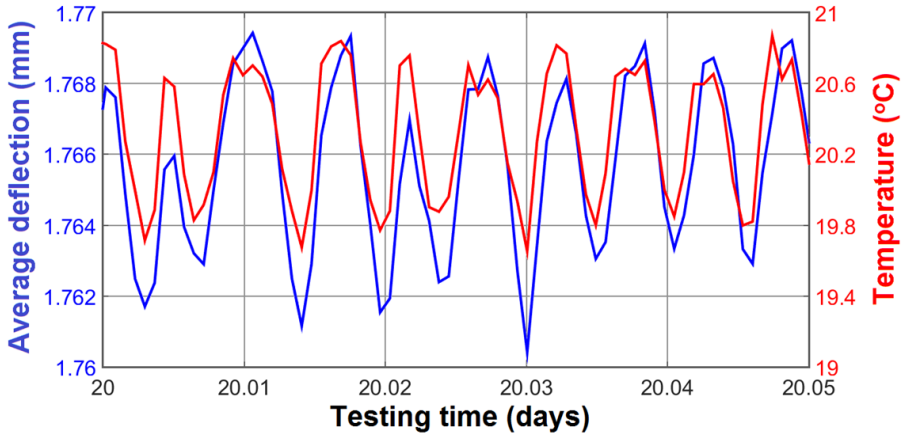

Figure 4-20: Deflection of the beam of Test 4B which was exposed to tap water at a load of 7.0 kN (blue curve), and the ambient temperatures around this beam (red curve). The presented curves concern the deflections and the temperatures after twenty days of loading over a period of 0.05 days (72 minutes).

Figure 4-20 shows that the curve of the deflections of the RC beam has similar fluctuations as the curve of the ambient temperature around the beam. This indicates a relation between changes in the ambient temperature around the beam and changes of the deflections of the beam. To obtain this relation, more than 100,000 data points from both beams of Test 4B were analysed. The results of this analysis is given in Figure 4-21.

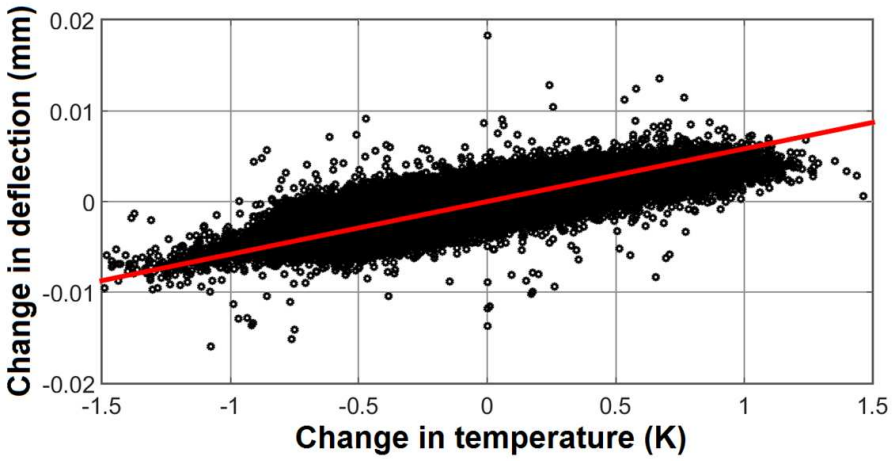

Figure 4-21: Relation between changes in the ambient temperature and de deflections of the RC beam. The back dots are the measurements. The red curve indicates a linear relation between changes in the ambient temperature and changes in the deflections of the RC beam.

Figure 4-21 shows that the deflections of the RC beam increase when the ambient temperature around the beam increases. A linear relation between changes in the ambient temperature and changes in the deflections of the RC beam was derived from the measurements. This relation is expressed in Equation (4-1) and presented as red curve in Figure 4-21. The variation coefficient in this equation is 0.25. Since this equation contains changes in the average temperature, changes in the temperature differential, and changes in the eigen temperature of the beam, this equation is only valid for the RC beams loaded with a load of 7.0 kN.

$$\Delta\delta = C_{\Delta,\text{def,measured}}\Delta T_a \qquad (4\text{-}1)$$

where:

$C_{\Delta,\text{def,measured}}$ = factor (0.0058 mm/K);
$\Delta\delta$ = change in deflection;
ΔT_a = change in ambient temperature.

As result of changes in the ambient temperature, the temperature in the RC beam changes. Changes in the temperature of the beam can be divided in three components: an average temperature in the beam, a temperature differential and the eigen temperature of the beam. Since changes in the eigen temperature of the beam do not result in changes in the deflections of the beam [41], changes in the eigen temperature of the beam are not further discussed.

A temperature differential in the RC beam results in a curvature in the beam. Changes in the curvature of the beam result in changes in the deflections of the beam. A part of the measured changes in the deflections of the RC beam were caused by a temperature differential in the RC beam. Another part of the measured changes in the deflections of the RC beam were caused by changes in the average temperature of the beam. Changes in the humidity of the beam (wetting/drying cycles) result in changes in the deflections of the RC beam as well (Section 4.5.2).

A change in the average temperature causes a change in the volume of the beam and a change in the Young's modulus of the beam. It was shown in Section 4.2.1 that the vertical distance between the measurement point at the ends of the beam and the measurement point at the middle of the beam was 70 mm. With a thermal expansion of $10*10^{-6}$/K [101, 125], the vertical thermal expansion of the RC beam is 0.0007 mm/K. Since the measurements include this vertical thermal expansion, the factor between difference in the ambient temperature and difference in the deflections of the RC beam ($C_{\Delta,def,measured}$) is 0.0058-0.0007= 0.0051 mm/K. This factor was used in a sensitivity analysis (Section 6.3).

An increase of the average temperature in the RC beam results in a reduction of the Young's modulus of concrete [42]. An indication of temperature-dependent Young's modulus of concrete was obtained from Modelcode 2010 [80]. Under applied loads, a reduction of the Young's modulus of concrete results in an increase of the deflections of the RC beam.

The deflections of the RC beam under the applied loads can be calculated using standard calculations for a single supported beam and a cantilever beam [44]. When the Young's modulus of concrete was considered as function of the temperature, the deflections of the RC beam can be calculated with Equation (4-2).

$$\delta_{tot} = \frac{F_{average} L_{end} (8L_{end}^{2} + 12 L_{end} L_{mid} + 3L_{mid}^{2})}{48(1.06 - 0.003T) E_{cm,cr} I} \quad (4\text{-}2)$$

where:

δ_{tot} = total deflection;
$F_{average}$ = average load (7.0 kN);
L_{end} = distance between load and support (475 mm);
L_{mid} = distance between the supports (450 mm);
T = temperature (^{o}C);
$E_{cm,cr}$ = Young's modulus of cracked concrete ($0.33*31{,}000$ N/mm^2);
I = moment of inertia ($28.1*10^6$ mm^4).

The first degree of the Tayler Series [126] was used to derive a linear relation between changes in the average temperature in the beam and changes in the deflections of the RC beam as result of temperature-induced changes in the Young's modulus of concrete. As result of temperature-induced changes in the Young's modulus of concrete, the deflections of the RC beam increases 0.0032 mm/K (at an applied load of 7.0 kN). It was assumed that changes in the average temperature of the RC beam are similar to changes in the ambient temperature around the beam. Therefore, the relation between changes in the average temperature of the RC beam and changes in the deflections of the beam was assumed to be the same as the relation between changes in the ambient temperature and changes in the deflections of the beam (Equation (4-3)).

The measured changes in the deflections of the RC beam as result of changes in the ambient temperature around the beam and the calculated changes in the deflections of the RC beam as result of temperature-induced changes in the Young's modulus of concrete are given in Figure 4-22.

$$\Delta\delta = C_{\Delta E \Delta \delta} C_{\Delta T \Delta E} \Delta T_a \qquad (4\text{-}3)$$

where:

$C_{\Delta T \Delta E}$ = factor, relation between difference in the average temperature and difference in the Young's modulus (0.0027 /K);

$C_{\Delta E \Delta \delta}$ = factor, relation between difference in the Young´s modulus and difference in the deflections of the RC beam (0.00017 mm/N);

$\Delta\delta$ = change in deflection;

ΔT_a = change in average temperature.

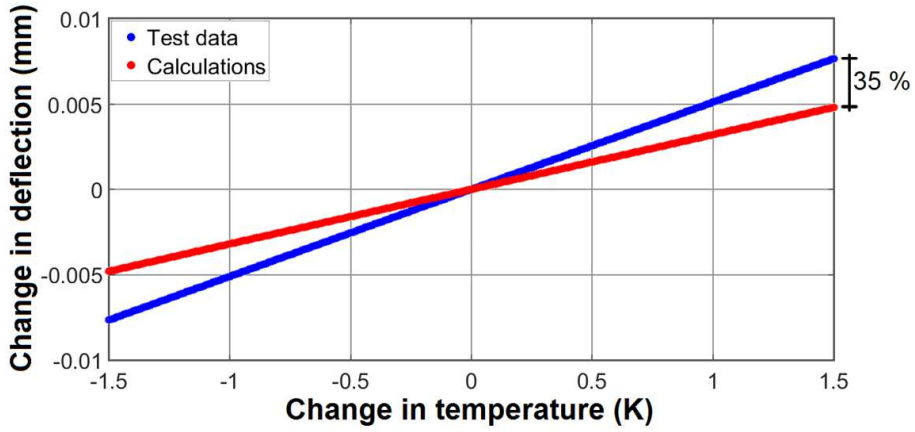

Figure 4-22: Effect of changes in the ambient temperature on the deflections of the RC beams.

Figure 4-22 shows that the difference between the measured changes in the deflections of the RC beam and the calculated changes in the deflections of the RC beam is approximately 35%. It was assumed that this 35% was caused by the temperature differential in the RC beam. The 65% of the deflections of the RC beam which was found by the calculations influence both the deflections and the natural frequencies of the RC beam. The difference in the deflections of the RC beam of 35% hardly results in changes in the natural frequencies of the beam.

4.5.2 Effect of wetting/drying cycles on the deflections of a beam

During curing, the RC beams were stored in a room with a ambient humidity of RH=100%. During the dynamic loads, the ambient humidity was RH=50 ±10%. A wetting/drying cycle of two days wet and five days dry was applied during loading. Due to the sealing on the bottom and both sides of the RC beam, leakage of water via the cracks was avoided. A side-effect of the sealing is that all sides of the RC beam were wet during the wetting period. Figure 4-23 shows an illustration of the humidity to which the top of the RC beams was exposed during a test.

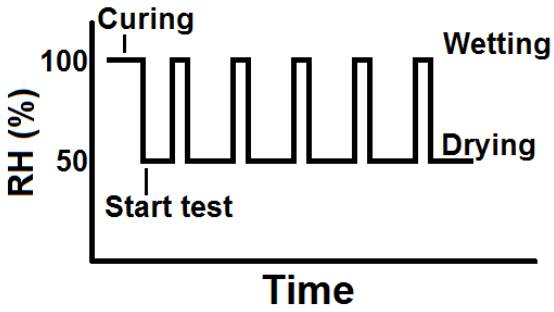

Figure 4-23: Illustration of the local humidity around the RC beams during a test.

For investigating the effect of wetting/drying cycles on the static deflections of the RC beams, the beams of Test 2D were used before these beams were loaded dynamically. The beams were loaded with a constant force of 6 kN for four weeks in the same four-point-bending configuration as presented in Section 4.2. In order to better understand the deflections of the RC beam by wetting and drying of the beam, the wetting/drying cycles as presented in Section 4.2.3 were changed. After five days of static load, the beams were wetted for two days, followed by twelve days of drying. A second wetting cycles started on the nineteenth day of static loading. The deflections of the RC beam exposed to tap water of Test 2D between day 14 and day 28 are presented in Figure 4-24. In this figure, the wetting period is presented as a grey area. Figure 4-24 shows that the measurements of the deflections of the RC beam during and after the wetting period are not significantly different from the measurements of the deflections of the RC beam before the wetting period. Obviously, the wetting/drying cycles hardly influence the deflections of the RC beam under a static load. In other words: changes in the temperature of the RC beam and changes in the humidity of the beam as result of the wetting/drying cycles are limited.

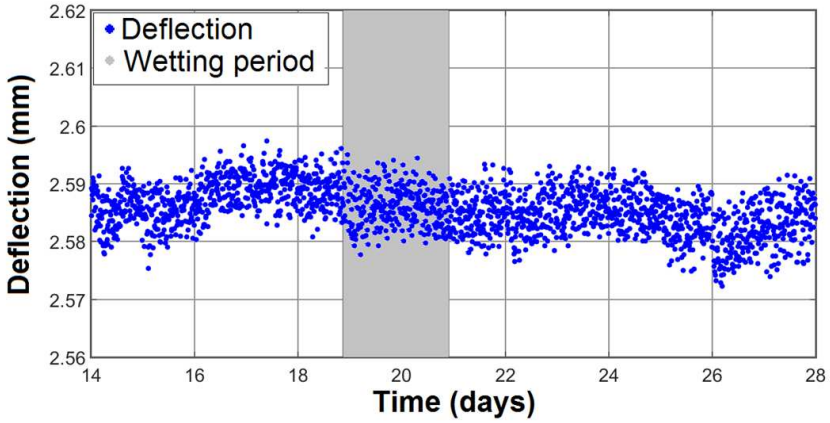

Figure 4-24: Deflections of the RC beam exposed to tap water of Test 2D during two weeks of loading. The RC beam was loaded with a static load of 6.0 kN. The wetting period is presented as grey area.

The effect of wetting/drying cycles can be different for a dynamically loaded RC beam than for a statically loaded beam. The deflections of the RC beam exposed to tap water of Test 4B is used to show the effect of wetting/drying cycles on the deflections of a dynamically loaded beam. The deflections of the beam loaded by 2.0 kN (minimum load) and the deflections of the beam loaded by 12.0 kN (maximum load) are presented in Figure 4-25. The wetting periods are presented as grey areas.

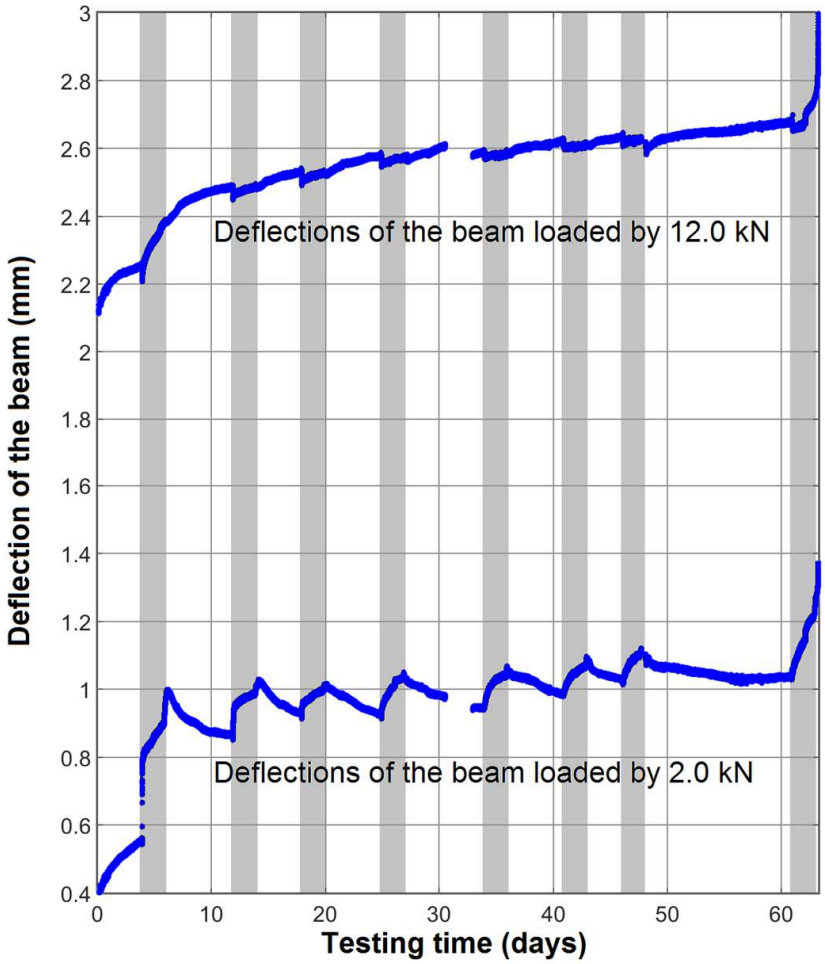

Figure 4-25: Deflections of the beam exposed to tap water of Test 4B. The deflection of the beam loaded by 2.0 kN and the deflections of the beam loaded by 12.0 kN are both presented in this figure. The wetting periods are presented as grey areas.

Figure 4-25 shows that the deflections of the beam at a lower load (2.0 kN) are strongly influenced by the wetting/drying cycles. At a load of 2.0 kN, the deflections of the beam increase in the wetting periods and decrease in the drying periods. Except for the changes in the first wetting/drying cycle, the changes in the deflections of the RC beam as result of the wetting/drying periods are reversible. At a load of 12.0 kN, the deflections of the beam as result of the wetting/drying cycles show much smaller fluctuations than the deflections of the beam at a load of 2.0 kN.

By applying water on top of the RC beams, the mass on top of the RC beams increases, the temperature of the beams changes, the degree of saturation in the RC beams increases, and the cracks are filled with water. The observed changes in the deflections can be explained by one or a combination of more of the effects given above.

When the mass of the water, the change of the temperature, or the change in the moisture content results in significant changes in the deflections of the RC beam, these changes should be visible in the deflections of a statically loaded RC beam and in the deflections of a dynamically loaded RC beam. Since the deflections of the statically loaded

RC are hardly influenced by the wetting/drying cycles, the measured changes in the deflections of the RC beam cannot be caused by changes in mass, temperature, or moisture content. It was concluded that the changes in the deflections of the RC beams as result of changes in the wetting/drying cycles were heavily influenced by the dynamic loading of the RC beam.

During the wetting period, water flows into the cracks when the cracks open and water is pushed up when the cracks close. It was assumed that the water in the cracks results in forces, which hamper closure of the cracks. Van Mier [127] suggested that water in a crack results in forces on the surfaces of the crack. When a crack close, the water in the cracks is pumped out and the volume of water in the cracks decreases. The resistance of the water against pumping out increases when the volume of the water in the cracks decreases [128]. The resistance of the water can be large enough to avoid closure of the crack.

The amount of water in the cracks decreases slowly during the drying period. Several days are required to lower the water level in the cracks. At the end on the drying period, the amount of water in the cracks is reduced and the deflections of the RC beam were nearly the same as the deflections of the RC beam before the wetting period. This mechanism explains why changes in the deflections of the RC beam as result of wetting/drying cycles are observed during dynamic loading of the beam and not during static loading of the beam. It also explains why the deflections of the RC beam change rapidly during the wetting period and change more slowly in the drying period.

4.5.3 Combined effect of temperature changes and a drying/wetting cycle

The climate controller failed during Test 4C. The consequence of this failure was that the ambient temperature in the test room raised up to 29 degrees Celsius between the 35th and the 38th day of loading. The period between the 35th and the 38th day of loading was part of a drying period. In this period, the beams were not wetted and exposed to the ambient condition in the room. Measurements of the deflections of the beams during this (unscheduled) period were used to investigate the effect of larger changes in the ambient temperature on the deflections of the RC beams. The blue curve in Figure 4-26 shows the average deflection of one of the beams of Test 4C (the beam which was exposed to tap water for two days per week) during the period that the climate controller failed. During this period, the beam was exposed to the air with high temperature. The ambient temperature around the RC beams was plotted as a red curve on a second vertical axis in the same figure.

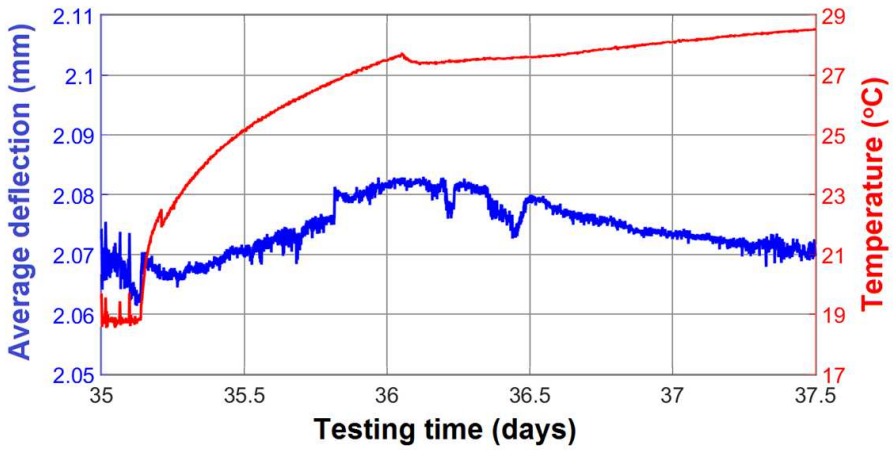

Figure 4-26: The deflection of the beam of Test 4C which was exposed to tap water at a load of 7.0 kN (blue curve), and the ambient temperatures around this beam (red curve). The presented curves concern the deflection after 35 days of loading over a period of 2.5 days.

The relation between changes in the ambient temperature and changes in the deflections of the RC beam on a small timescale (hours) was established in Section 4.5.1. When this relation can also be used for a larger timescale (days), the blue curve in Figure 4-26 should have the same development as the red curve in the same figure. This could, however, not be observed in Figure 4-26.

It was discussed in Section 4.5.2 that the deflections of the RC beam increase in the wetting period and decrease in the drying period. The period between the 35th day and the 38th day of loading was part of a drying period. During the drying periods, the average deflections of the RC beam decrease 0.01 mm per day compared to a situation with a constant moisture content in the RC beam. For the comparison between changes in the ambient temperature and changes in the deflections of the RC beam, the effect of drying of the concrete on the deflections of the RC beam should be eliminated.

To eliminate the effect of drying of the concrete on the deflections of the RC beam, the deflection curve in Figure 4-26 was increased 0.01 mm/day from the moment that the climate controller failed. The obtained deflection curve is plotted in Figure 4-27. This figure shows that the corrected curve of the deflections have distinct similarities with the curve of the ambient temperature. The scatter in the results between the relation between changes in the ambient temperature and changes in the deflections of the RC beam by larger changes in the ambient temperature is larger than the scatter in the results between the relation between changes in the ambient temperature and changes in the deflections of the RC beam by smaller changes in the ambient temperature. When the RC beam was exposed to the fluctuations in the ambient condition in the Dutch climate, the scatter in the relation between changes in the ambient temperature and changes in the deflections of the RC beam were probably far larger that found during the Beam Test.

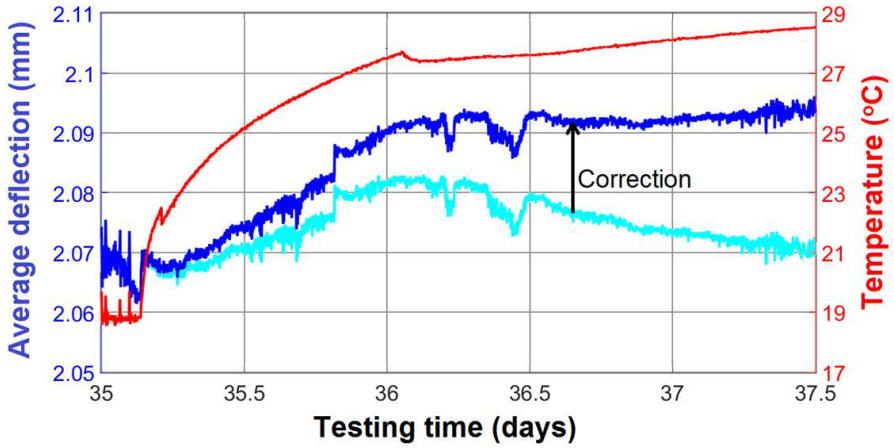

Figure 4-27: The effect of an increased temperature on the deflection of the RC beam (load on the beam was 7.0 kN). The correction is the effect of drying of the RC beam on the deflections of the RC beam (0.01 m per day).

4.6 Failure of dynamically loaded Reinforced Concrete beams

This section deals with the failure mechanisms of the RC beams and the maximum number of load cycles the beams can withstand until failure. Also the deflections of the RC beams and the width of different cracks are presented in this section.

4.6.1 Performance of the beams of Test 1A and 1B

Test 1A took 12 days. Within these 12 days, one wetting period was included. After 478,127 load cycles, flexural failure occurred in the RC beam which was exposed to a chloride solution. Both RC beams of Test 1A were broken deliberately to check whether corrosion of the steel bar had occurred. Although the exposure time was limited, corrosion of the steel bar in the chloride-exposed beam was clearly visible. At several locations the surface of the bar was corroded. At the failed section, corrosion was observed at approximately 30% of the cross-section of the bar. The thickness of the corrosion products was, however, limited to several tenths of millimetres. Little corrosion (small areas at the surface of the bar) was observed on the steel bar of the RC beam exposed to tap water. Figure 4-28 shows the reinforcing bars of both RC beams of Test 1A.

Figure 4-28: Reinforcing bars of the RC beams of Test 1A. Bar 1 was the reinforcing bar of the chloride-exposed beam. Bar 2 was the reinforcing bar of the beam exposed to tap water.

The RC beam of Test 1B, which was intended to be exposed to a chloride solution, failed before the first wetting period. After 6,309 load cycles, shear failure occurred. Test 1B was aborted and the second RC beam, which was intended to be exposed to tap water, was loaded statically until failure. This RC beam failed in shear at a load of 27.2 kN. The difference between this failure load and the measured load bearing capacity of a static test (Section 4.3) can be explained by the (large) scatter in the measured compressive strength (Section 4.2.2). The maximum number of load cycles and the failure mechanisms of the RC beams in Tests 1A and 1B are given in Table 4-10.

Table 4-10: Maximum number of load cycles and failure mechanisms in the beams of Test 1A and 1B.

Test	Exposure condition	Load cycles at failure	Failure mechanism	Comments
Test 1A	Chloride	478,127	Flexural failure	Beam was broken deliberately to observe corrosion
Test 1A	Tap water	478,127	Did not fail	Beam was broken deliberately to observe corrosion
Test 1B	Chloride	6,309	Shear failure	-
Test 1B	Tap water	6,309	Did not fail	Beam was statically loaded until failure (27.2 kN, shear)

As result of (local) damage in the reinforcing bar, the tensile strength of the reinforcing bar decreases. A reduction of the tensile strength of the reinforcing bar results in a reduction of the flexural capacity of the RC beam. The effect of a reduction of the tensile strength of the reinforcing bar on the shear capacity is, however, limited. To investigate the effect of localized corrosion on the maximum number of load cycles, flexural failure should be considered in the RC beams. A lower load on the RC beams results in a higher number of load cycles until failure. When the loads were applied with the same frequency (limitations of the force actuator), a larger number of load cycles results in a longer duration of the test, which can result in a larger amount of corrosion. This increases the probability of flexural failure instead of shear failure. In order to increase the duration of the test, the applied load was decreased from an alternating load between 1.7 and 17.0 kN to an alternating load between 2.0 and 12.0 kN.

4.6.2 Performance of the beams in Test 2A till 2E

Five sets of RC beams (Tests 2A, 2B, 2C, 2D, and 2E) without shear reinforcement were tested. In two of these sets (Tests 2A and 2C), flexural failure occurred in the chloride-exposed RC beam. Both RC beams failed at almost the same number of load cycles (1,920,030 and 1,942,000). Two other chloride-exposed RC beams (Tests 2B and 2E) failed in shear, whereby the beam of Test 2E failed at a far lower number of load cycles (27,734) than the beam of Test 2B (843,333). The bond between concrete and the reinforcing bar failed in the RC beam exposed to tap water in Test 2D. The maximum number of load cycles and the failure mechanisms of the beams in Test 2A till 2E are given in Table 4-11. None of the reference beams in Test 2A till 2E could be used to investigate the effect of

localized corrosion on the maximum number of load cycles the RC beam can accommodate until failure.

Table 4-11: Maximum number of load cycles and failure mechanisms of the beams of Test 2A till 2E (no shear reinforcement).

Test	Exposure condition	Load cycles at failure	Failure mechanism	Comments
Test 2A	Chloride	1,920,030	Flexural failure	-
Test 2A	Tap water	1,920,030	Did not fail	Beam was statically loaded until failure (24.0 kN, shear)
Test 2B	Chloride	654,969	Shear failure	-
Test 2B	Tap water	654,969	Did not fail	Test was stopped
Test 2C	Chloride	1,942,000	Flexural failure	-
Test 2C	Tap water	1,942,000	Did not fail	Continued with higher stress amplitude, immediately shear failure
Test 2D	Chloride	843,333	Did not fail	Beam was statically loaded until failure (23.1 kN, shear)
Test 2D	Tap water	843,333	Debonding	-
Test 2E	Chloride	17,734	Shear failure	-
Test 2E	Tap water	17,734	Did not fail	Beam was statically loaded until failure (26.0 kN, shear)

The deflections of both RC beams of Test 2A are given in Figure 4-29 (Loaded by 12.0 kN). The red curve starts at a deflection of 2.8 mm. The blue curve starts at a deflection of 2.5 mm. This starting difference in caused by a different number of cracks. The RC beam exposed to a chloride solution contained eight cracks. The RC beam exposed to tap water contained nine cracks. The curve of the deflections of the chloride-exposed beam shows an increase in the first few thousand load cycles, an increase during the last few thousand load cycles and some fluctuations in between. The increase of the deflections in the first thousand load cycles and the fluctuations in the deflections of the beam were also observed in the curve of the deflections of the RC beam exposed to tap water. Since the test of the RC beam exposed to tap water was aborted at the moment that the chloride-exposed beam failed, the increased deflections in the last few thousand were not measured in this beam. The development of the deflections of RC beams that failed in bending are further discussed in Section 4.6.4.

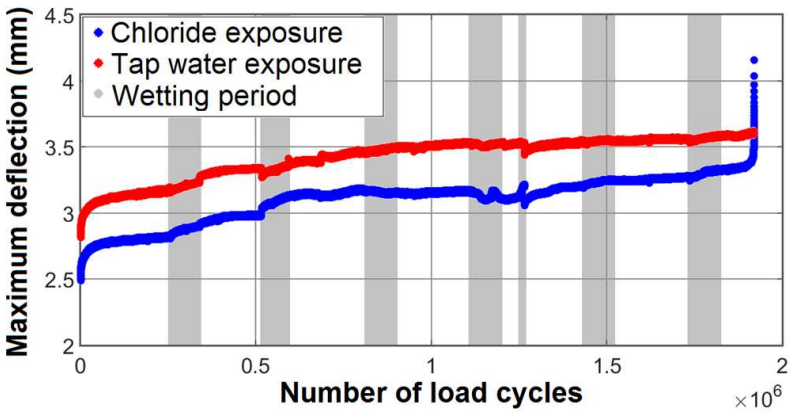

Figure 4-29: Deflections of the beams of Test 2A at a load of 12.0 kN (maximum deflection per load cycle). Flexural failure occurred at the chloride-exposed RC beam. The RC beam exposed to tap water did not fail under the dynamic load.

The maximum deflections of both RC beams of Test 2B are given in Figure 4-30 (Load = 12.0 kN). Since both RC beams had seven cracks, the deflections of the beams at the first loading cycle were similar. After approximately 260,000 cycles (start of the first wetting period), the deflections of the chloride-exposed RC beam increased more than the deflections of the beam exposed to tap water. During the last few thousand load cycles, the chloride-exposed beam showed a significant increase of the deflections of the beam.

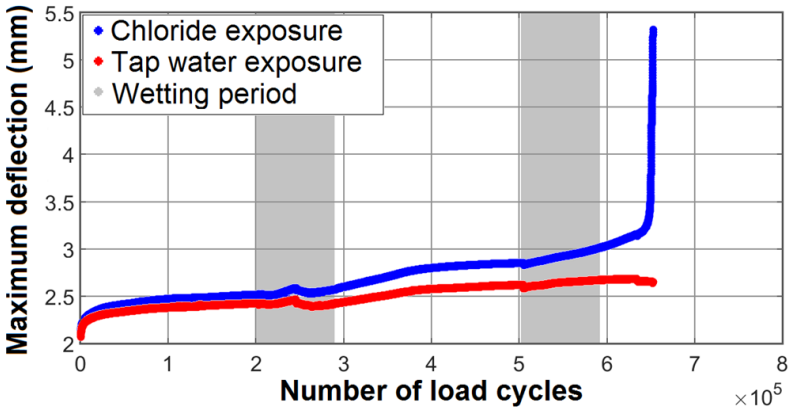

Figure 4-30: Deflections of the beams of Test 2B at a load of 12.0 kN (maximum deflection per load cycle). Shear failure occurred in the chloride-exposed beam. The beam exposed to tap water did not fail under the dynamic load.

The deflections of both RC beams of Test 2D (at a load of 12.0 kN) are given in Figure 4-31. This figure shows that in the first 500,000 load cycles, the deflections of the chloride-exposed RC beam were similar to the deflections of the RC beam exposed to tap water. During the second wetting period (second grey block), the curve of the deflections of the beam exposed to tap water shows a clear inclination. Such inclination was not visible in the curve of the deflections of the chloride-exposed RC beam. During the third wetting period, the deflections of the beam increased significantly (compared to the initial deflections of the beam). Although the RC beam could still resist the applied dynamic loads, it was assumed that the bond between the reinforcing bar and the concrete had failed.

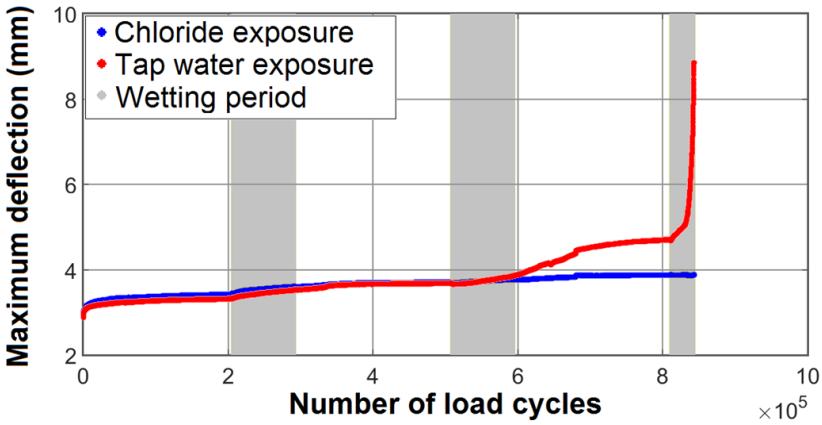

Figure 4-31: Deflections of the beams of Test 2D at a load of 12.0 kN (maximum deflection per load cycle). Bond failure occurred at the RC beam exposed to tap water.

Beside the deflections of the RC beam, the width of one of the cracks increased significantly due to bond failure. The width of this crack (crack 1) is plotted in Figure 4-33 as a blue curve. The widths of two other cracks are plotted in Figure 4-33 as well (red and green curve). The red curve corresponds to the width of crack 2, which was closest to the largest crack. The green curve corresponds to the width of crack 3, which was hardly influenced by bond failure. The positions of the cracks are indicated in Figure 4-32. After 650,000 load cycles, the width of crack 1 was larger than the range of the LVDT. Therefore, larger crack widths were not presented in Figure 4-33. A crack width of 2-3 mm was visually observed during the tests.

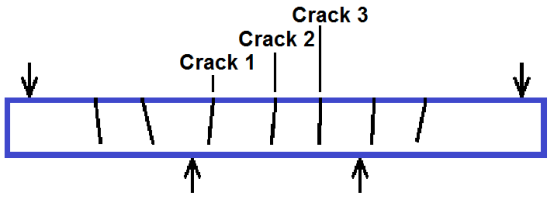

Figure 4-32: Indication of the position of the measured cracks in the beam exposed to tap water of Test 2D. The widths of these cracks are presented in Figure 4-33.

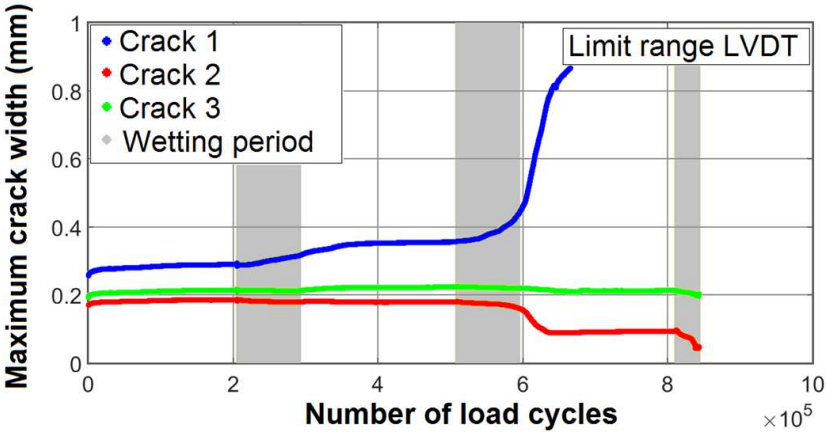

Figure 4-33: Crack width of three cracks of the RC beam of Test 2D exposed to tap water. The position of the cracks are given in Figure 4-32. The load on the beam was 12.0 kN. The presented crack widths were the maximum widths per load cycle.

The slope of the blue curve in Figure 4-33 increases slightly during the first wetting period and increases more significantly during the second wetting period. Changes in the slope of the curve indicates that force equilibrium in the RC beam was disturbed. A new equilibrium between the compression forces in the concrete and the tensile forces in the steel bar was found at larger strains. Disturbance of the force equilibrium could be caused by pumping of the water in the cracks [128]. When water was pressed into the concrete, non-hydrated cement around the reinforcing bar can be flushed away. Pumping of the water was also mentioned as explanation of the effect of wetting/drying cycles on the deflections of the RC beams (Section 4.5.2). Changes in the slope of the deflection-curve can be seen as indicators for bond failure. It is also noticeable from Figure 4-33 that the width of crack 3 (closest to the largest crack) decreases. This decrease of the crack width can be seen as indicator for bond failure as well.

4.6.3 Performance of the beams in Test 3A and 3B

The RC beams in Tests 3A and 3B contain steel stirrups with a rectangular shape (Figure 4-15, Section 4.2.2). These stirrups increase the shear capacity of the RC beams. Furthermore, stirrups can control the development of cracking and hence increase the confinement of the reinforcing bar, which reduces the probability of bond failure. It was mentioned in Section 4.2.2 that these stirrups were positioned only at the locations of the RC beam where the shear stresses are highest. The stirrups increase the bending stiffness of the RC beam locally, which results in stress concentrations in the main reinforcing bar at the locations where the stiffness of the beam changes. These stress concentrations can result in large cracks at the locations where the bending stiffness changes (Figure 4-34). At four other locations, a smaller crack was developed.

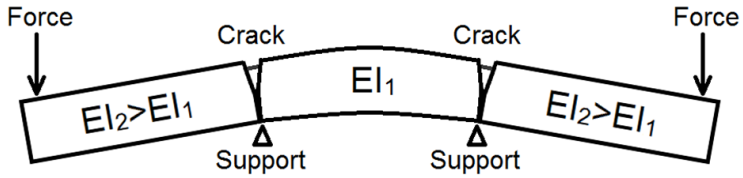

Figure 4-34: Illustration of the formation of two mail cracks due to difference in bending stiffness. The four smaller cracks are not presented in this illustration.

The additional reinforcing bars in the edges of the stirrups result in a reduction of the stresses in the main reinforcing bar by 58% (by comparing the cross-sectional areas of the reinforcing bars). When both of the additional reinforcing bars ends at the same position (Figure 4-15, Section 4.2.2), an abrupt change of the stress in the main reinforcing bar occurs. Flexural failure of the RC beams in Tests 3A and 3B occurred at a lower number (early failure) of load cycles compared to flexural failure of the beams in Tests 2A and 2C (compare values in Table 4-11 and in Table 4-12). Imperfection in the reinforcement configuration had a larger impact on the reduction of the maximum number of load cycles that corrosion of the reinforcing bar. Therefore, in this early failure, the difference between the number of load cycles until failure of the chloride-exposed RC beams and the RC beams exposed to tap water can be small. Table 4-12 shows the maximum number of load cycles and the failure mechanisms of the RC beams in Tests 3A and 3B.

Table 4-12: Maximum number of load cycles and failure mechanisms of the beams of Test 3A and 3B.

Test	Exposure condition	Load cycles at failure	Failure mechanism	Comments
Test 3A	Chloride	854,225	Flexural failure	Due to concentrated stresses, The maximum number of load cycles until failure of all RC beams of Test 3A and 3B is lower than the maximum number of load cycles of Test 2A and 2C (Table 4-11).
Test 3A	Tap water	1,001,781	Flexural failure	
Test 3B	Chloride	1,041,985	Flexural failure	
Test 3B	Tap water	965,814	Flexural failure	

4.6.4 Performance of the beams in Test 4A till 4C

Continuity of the reinforcement configuration was created by applying steel triangular stirrups as shear reinforcement in the RC beam (Figure 4-16). Since the additional reinforcement was applied over the total length of the beam, stress concentrations as mentioned in Section 4.6.3 did not occur. Since the triangular stirrups increase the shear capacity of the RC beam and stress concentrations were avoided, it was expected that flexural failure occurred at a similar number of load cycles as in Tests 2A and 2C.

Large vertical deflections and one large crack were measured in Test 4A (Figure 4-35). After observing lateral deformations of the RC beams, the test was stopped. After removing the sealing (Section 4.2.3), the concrete in the compression zone fell apart and it was shown that the RC beam had already failed.

Figure 4-35: Cracks on top of one of the beams (beam exposed to tap water) of Test 4A, during dynamic loading.

Early failure of the RC beams of Tests 4B and 4C was avoided by increasing the anchorage length of the stirrups. Both RC beams of Tests 4B and both RC beams of Test 4C were dynamically loaded until failure. The maximum number of load cycles of the chloride-exposed RC beams of these tests was similar to the maximum number of load cycles of the chloride-exposed beams of Tests 2A and 2C. The maximum number of load cycles of the beams exposed to tap water was 30-50% higher. Table 4-13 shows the maximum number of load cycles and the failure mechanisms of all RC beams in this reinforcement configuration.

Table 4-13: Maximum number of load cycles and failure mechanisms of beams of Test 4A till 4C.

Test	Exposure condition	Load cycles at failure	Failure mechanism	Comments
Test 4A	Chloride	256,686	Compression failure	Increased stresses in the concrete compression zone
Test 4A	Tap water	464,986	Compression failure	Increased stresses in the concrete compression zone
Test 4B	Chloride	1,957,494	Flexural failure	-
Test 4B	Tap water	2,608,396	Flexural failure	-
Test 4C	Chloride	1,410,206	Flexural failure	-
Test 4C	Tap water	3,100,347	Flexural failure	-

The curves of the maximum deflections of both RC beams of Test 4B are plotted in Figure 4-36. In this figure, the blue curve corresponds to the deflections of the chloride-exposed RC beam and the red curve to the deflections of the RC beam exposed to tap water. Both curves in Figure 4-36 show a similar behaviour, whereby the deflections slightly increase during the first 99% of the load cycles and increase more significantly during the last few thousand cycles. The main difference between the two curves in Figure 4-36 is the maximum number of load cycles at which failure occurred.

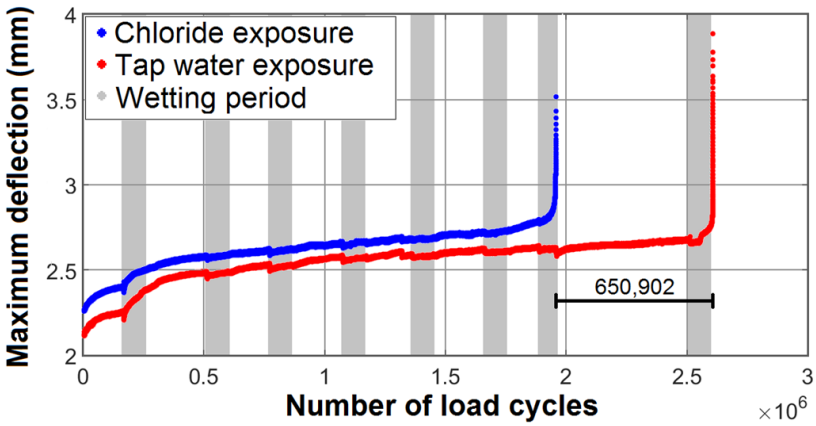

Figure 4-36: Deflections of the beams of Test 4B at a load of 12.0 kN (maximum deflection per load cycle). Flexural failure occurred at both RC beams.

The maximum deflections of both RC beams of Test 4B during the last 5,000 load cycles are plotted in Figure 4-37. In this figure, the blue curve corresponds to the deflections of the chloride-exposed beam and the red curve to the deflections of the beam exposed to tap water. Linear extrapolations of both curves are plotted in Figure 4-37 as well. These extrapolations show that the increase of the deflections starts approximately 2,000 cycles before failure. This behaviour is similar for both RC beams.

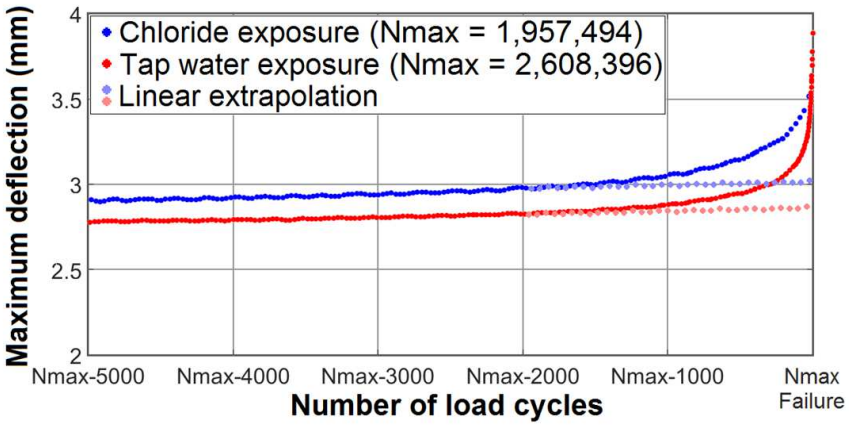

Figure 4-37: Deflections of the beams of Test 4B at a load of 12.0 kN (maximum deflection per load cycle) of the last 5,000 cycles until failure of both RC beams.

Besides the deflections of the RC beams, the width of three cracks of each RC beam were measured during the tests as well. Figure 4-38 shows the development of three of the nine cracks of the RC beam of Test 4B exposed to tap water. The width of these three cracks fluctuated. These fluctuations were caused by exposing the RC beams to water. This phenomenon was discussed in Section 4.5.2.

Fluctuations of the width of the cracks as result of fluctuations in the temperature and humidity of the RC beam can be observed at all of the three curves presented in Figure 4-38. The width of the cracks was not the same in the first load cycles (crack 1: 0.184 mm; crack 2: 0.160 mm; crack 3: 0.189 mm). Due to failure in the reinforcing bar at the location of crack 1, the width of crack 1 increased more than the width of the other cracks. This implies that RC beams do not automatically fail at the location where the largest crack is observed. In the conducted tests, the width of the cracks could not be used to predict at which of the cracks failure will occur.

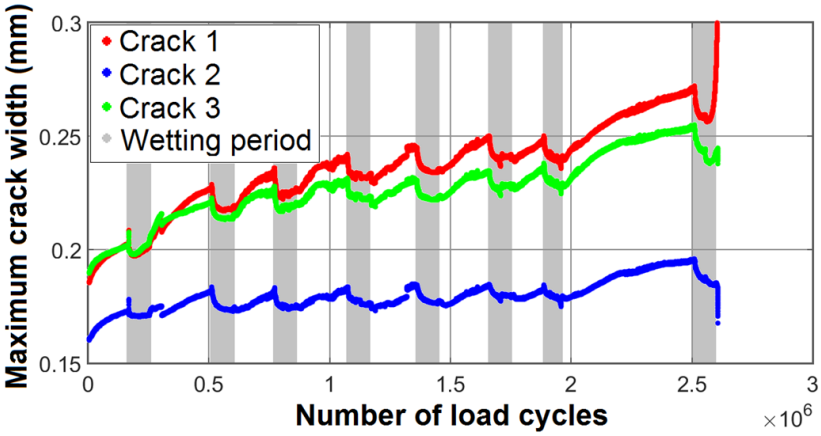

Figure 4-38: Crack width of three cracks of the RC beam of Test 4B exposed to tap water.

4.7 Corrosion monitoring

The corrosion activities were measured in four sets of RC beams (Tests 1A, 2A, 2B, and 2C). Corrosion measurements were performed to discover when the reinforcing bar starts

to corrode and how the corrosion rate changes with time and type of exposure. The methods which were used to measure the corrosion activity are Half-cell Potential (HCP) and Linear Polarisation Resistance (LPR) [123].

Three internal electrodes were installed to measure corrosion activity: a working electrode, a reference electrode, and a counter electrode. An electrical wire was connected to the reinforcing bar, which acts as a working electrode. An internal platinized titanium (Pt/Ti) reference electrode was positioned at 4-8 millimetre distance from the reinforcing bar. Both working electrode and reference electrode were installed in the formwork before casting. A titanium mesh, which acts as a counter electrode, was embedded in the concrete during casting. This titanium mesh was positioned approximately 20 mm from the concrete surface opposite to the surface of the reinforcing bar (100 mm from the reinforcing bar).

The electrodes were connected to an analog-to-digital converter (ADC). This ADC was connected to a computer and to a power supply. The power, which is needed for the LPR method (Section 4.7.2), is controlled by the computer. The ADC converted the measured potentials into digital signals, which were read by the computer. An illustration of the electrodes in the RC beam is presented in Figure 4-39.

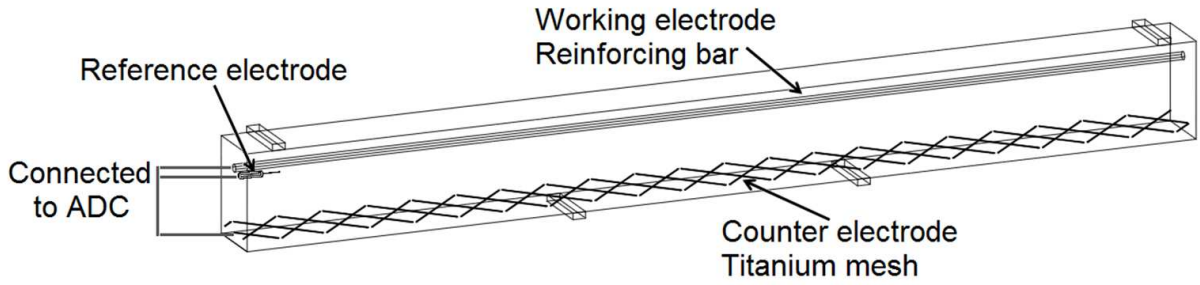

Figure 4-39: Illustration of the electrodes in the RC beam. The dimensions of the RC beam were presented in Figure 4-11. The connection to the ADC is presented in Figure 4-40.

The potentials between the working electrode (reinforcing bar) and the reference electrode (Pt/Ti electrode), called U1, as well as the potentials between the working electrode (reinforcing bar) and the counter electrode (titanium mesh), called U2, were measured automatically. The potentials were stored every minute [129]. This frequency was the same as the frequency of storing the deflections of the RC beams (Section 4.4).

The potential U1 was used for the HCP method (Section 4.7.1). The currency and the potential U2 were used for the LPR method (4.7.2). Figure 4-40 shows a schematic representation of the three electrode electrochemical cell in the RC beam and the measured potentials.

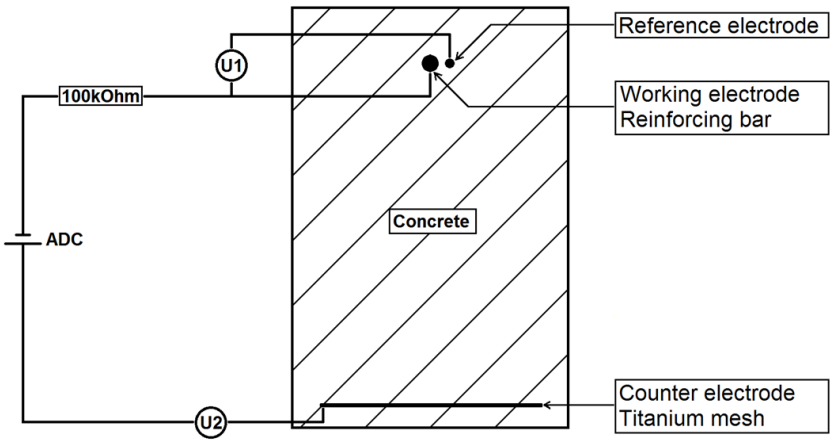

Figure 4-40: Schematic representation of the three electrode electrochemical cell in the RC beam and the measured potentials (U1 and U2). An illustration of the electrodes in the RC beam is given in Figure 4-39.

4.7.1 Half-Cell Potential

Measuring potentials U1 (HCP method) provide information about the average potential losses around the reinforcing bar. In the presented method, only a probability of corrosion of the reinforcing bar can be obtained. The actual amount of corrosion and the location of the corrosion along the length of the bar cannot be obtained with presented method.

The measured potentials U1 of Test 2A are given in Figure 4-41, whereby Figure 4-41-A corresponds to the potentials U1 of the chloride-exposed beam and Figure 4-41-B to the potentials U1 of the beam exposed to tap water. The wetting periods are presented as grey blocks. It can be observed that the potentials before the start of the first wetting period are not the same in both subfigures. This difference can be caused by a number of factors. The degree of saturation and the temperature of the concrete are important factors [28]. Also the differences in the position of the electrodes and the distance between the electrodes in the three electrode electrochemical cell in the RC beams are important factors. The differences between the potentials before the first wetting period do not automatically mean that one bar is more sensitive for corrosion than the other bar.

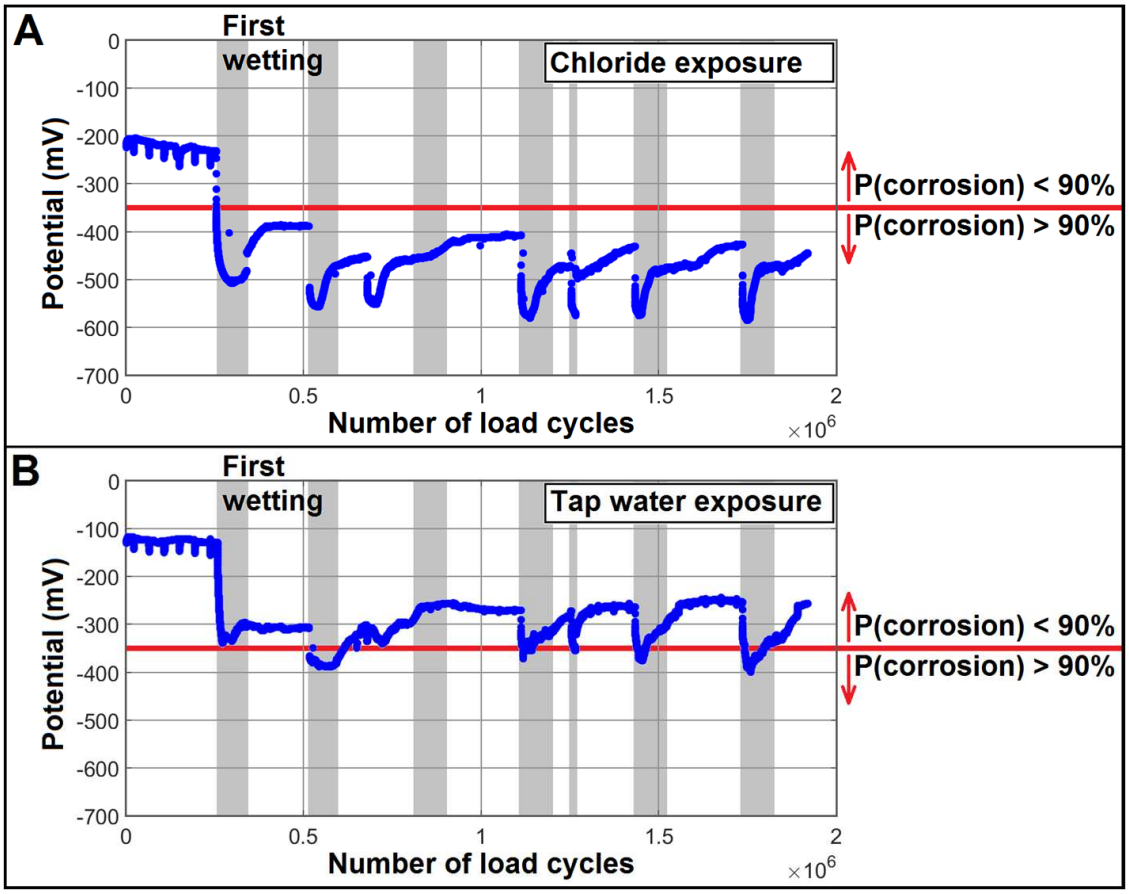

Figure 4-41: Potentials U1 of Test 2A. Figure 4-41-A shows the potentials of the chloride-exposed RC beam. Figure 4-41-B shows the potentials of the RC beam exposed to tap water. The wetting periods are presented as grey blocks.

Figure 4-41 shows a clear decline of the potentials directly after the start of the first wetting period. The decline of the curve in Figure 4-41-A is larger than the decline of the curve in Figure 4-41-B. The potentials presented in Figure 4-41-A re-stabilize at -400 mV (in dry condition) and is decreasing with the number of load cycles. The potentials in Figure 4-41-B re-stabilize at -260 mV (in dry condition) and remains constant. The probability of corrosion is, therefore, higher in the RC beam exposed to a chloride-solution that the RC beam exposed to tap water. Changes in the probability of corrosion in the bar over its service-life could not be obtained by HCP.

Both curves in Figure 4-41 show fluctuations. The small fluctuations before the first wetting period are initiated by applying a voltage which is required for the LPR measurements (Section 4.7.2). The larger fluctuations are initiated by the wetting/drying cycles. Except for these fluctuations, the potentials of the chloride-exposed beam slightly decreases. This indicates that the probability of corrosion slightly increases. Since the potential of the RC beam exposed to tap water hardly changes in dry condition, the probability of corrosion of the reinforcing bar in this beam hardly changed.

4.7.2 Linear Polarisation Resistance

The first measured polarization resistance of the Beam Test was in both RC beams of Test 1A. To measure the actual polarization resistance of the RC beams in this test (by LPR), the potential of U2 was lowered by 10 mV, followed by ten minutes of stabilization. After this stabilization, the potential was increased by small steps (0.15 mV per second) until a value of $U2_{original}$+5mV was reached. The scatter in measurements of the potentials and the currency of the RC beam where rather high. These measurements did not result in stable values of the polarization resistance. It was decided to increase the voltage and the time of stabilization in the next tests.

For the RC beams of Test 2A, 2B, and 2C, the potential of U2 was lowered by 20 mV. After twenty minutes of stabilization, the potential was increased by small steps (0.15 mV per second) until a value of $U2_{original}$+10mV was reached. The potential U2 and the electric current intensity were measured during this period of potential increase. The polarization resistance was calculated using the measured potentials and the measured electrical current intensity [129].

When the potentials U2 were changed, the potentials U1 changed as well. These changes are visible as small fluctuations in the curves of Figure 4-41, whereby the changes before the first wetting period are better visible than after the first wetting period. In the beginning of Test 2A, a LPR measurement was performed every hour. This frequency was applied to check whether the installation of the electrodes were correct and the to check the stability of the measurements. For a valid LPR measurement, re-stabilization of the potentials is required. The first measurements showed that re-stabilisation of the potentials took 4 till 6 hours. The frequency of a LPR measurement was reduced to one measurement per day.

The potential resistance of Test 2A is given in Figure 4-42, whereby the polarization resistance of the chloride-exposed RC beam and the polarization resistance of RC beam exposed to the tap water are given in Figure 4-42-A and Figure 4-42-B, respectively. The wetting periods are presented as grey blocks. The polarization resistance before the first wetting period was not the same in both RC beams. The differences in the polarization resistance can have various causes and do not automatically indicate corrosion activity in the reinforcing bar [31].

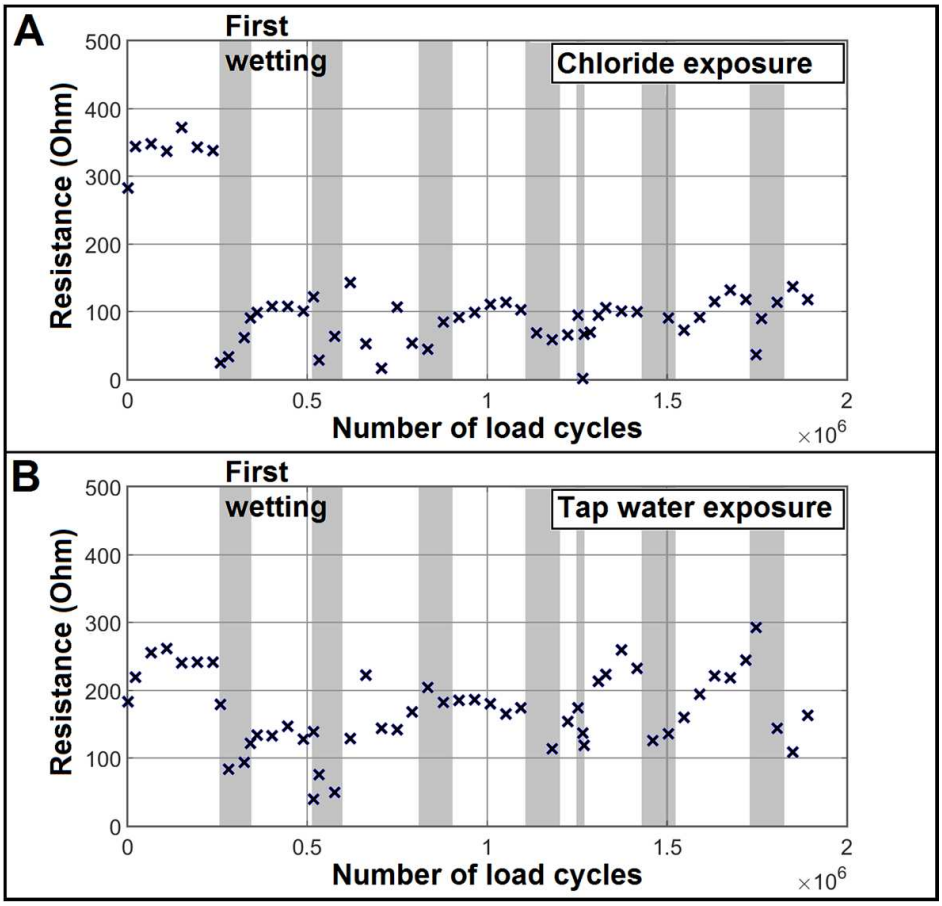

Figure 4-42: Polarization resistance of test 2A. Figure 4-42-A shows the polarization resistance of the chloride exposed RC beam. Figure 4-42-B shows the polarization resistance of the RC beam exposed to tap water. The wetting periods are presented as grey blocks.

Both figures in Figure 4-42 show a clear decrease of the polarization resistance after the start of the first wetting cycle. This decrease indicates a change in the polarization resistance (the lower the resistance, the higher the corrosion rate). After the first wetting period, the polarization resistance of the chloride-exposed RC beam (Figure 4-42-A) fluctuates around 100 Ohm. Therefore, it was suggested that the corrosion rate of the reinforcing bar in this beam hardly changed after the first wetting cycle. The polarization resistance of the RC beam exposed to tap water (Figure 4-42-B) fluctuates around 200 Ohm. Since also the scatter in the resistance is larger, it was suggested that the corrosion rate in the chloride-exposed RC beam was larger than the corrosion rate of the RC beam exposed to tap water. A change in the corrosion rate during the service-life of the RC beam could not be obtained by LPR.

4.7.3 Splitting Reinforced Concrete Beams

Both HCP and LPR indicated a larger corrosion activity in the reinforcing bar of the chloride-exposed RC beam of Test 2A than in the reinforcing bar of the beam exposed to tap water in the same test. To check whether the reinforcing bar of the chloride-exposed RC beam was corroded, two sections of approximately 200 mm of this RC beam were split, whereby the surface of the reinforcing bar became visible [130]. Figure 4-43 shows these sections. It was observed that the reinforcing bar was corroded at the failed section. At

the failed section, corrosion was observed over the total surface of the bar. The length of the corroded section was a few centimetres. Approximately 40% of the cross-section of the bar was corroded. The thickness of the corrosion products at the cross-section of the bar was limited to several tenths of millimetres. Since the height of the corroded section was limited, the exact cross-section loss was not defined.

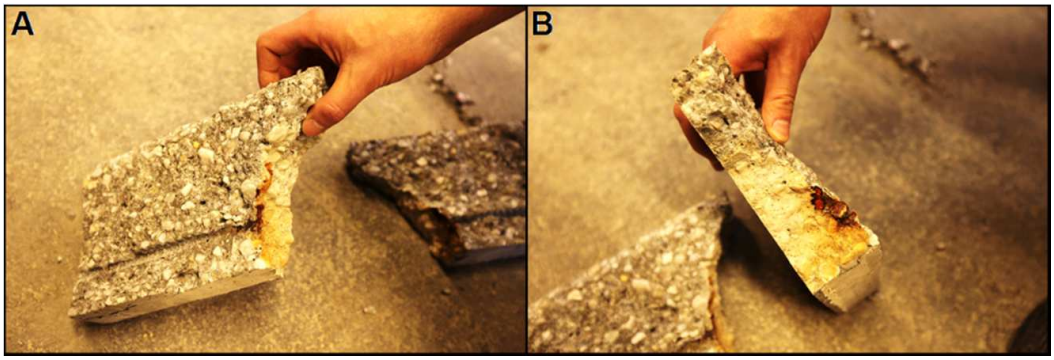

Figure 4-43: Corrosion activity after frexural failure of the chloride-exposed RC beam of Test 2A.

After failure of the chloride-exposed RC beam of Test 2C, this beam was cut in five sections of approximately 300 mm each. To observe corrosion activity over the total length of the reinforcing bar, all these sections were split (Figure 4-44). Corrosion of the reinforcing bar was observed at the section were the beam had failed. At this section, approximately 40% of the cross-section was corroded. The thickness of the corrosion products was approximately half a millimetre. At four other locations of the bar, corrosion at the surface of the bar was observed. These locations correspond to the locations of four larger cracks. At the locations where corrosion had developed, corrosion was spread over 1-2 centimetres along the length of the reinforcing bar. At the location of the smallest cracks (closure to the ends of the beam, crack width not measured), no corrosion products were observed.

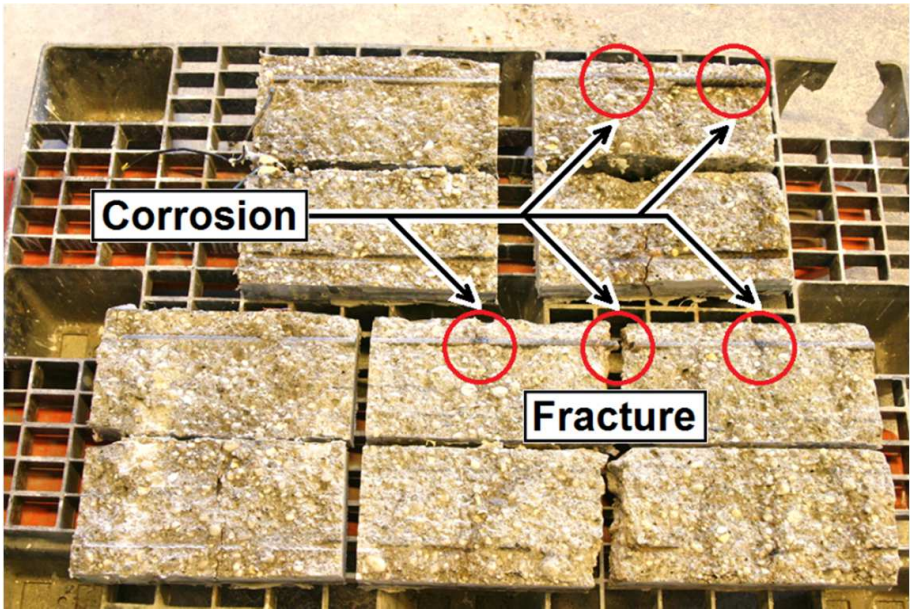

Figure 4-44: Corrosion activity of the total reinforcing bar of the chloride-exposed RC beam of Test 2C.

It was shown in Figure 4-44 that the reinforcing bar of the chloride-exposed RC beam of Test 2C was corroded at several locations. The second beam (exposed to tap water) of the same test was also cut in five sections of approximately 300 mm each. At the reinforcing bar of this RC beam, a small amount of corrosion at the surface of the bar was observed. From the HCP and the LPR measurements, a small amount of corrosion could be expected.

4.8 Bending stiffness of Reinforced Concrete beams

Structural Health Monitoring (SHM) systems often contain sensors to measure the vibrations of a structure. These vibrations can be used to calculate the natural frequency of the structure. Changes in the natural frequencies are considered as damage indicators of bridges (Section 2.5.1). The deflections of the RC beams were measured during the Beam Test. Since the deflections and the natural frequencies depend on the bending stiffness of the RC beams, changes in the natural frequencies can be calculated using changes in the deflections of the RC beam.

The bending stiffness of the RC beam was calculated with Equation (4-4), which was derived from Equation (4-2) (Section 4.5.1) for an ambient temperature of 20°C. Figure 4-45 shows the development of the bending stiffness with the number of load cycles as calculated with Equation (4-4).

$$EI_{beam} = \frac{F_{amplitude} L_{end} (8L_{end}^2 + 12 L_{end} L_{mid} + 3L_{mid}^2)}{48 \delta_{amplitude}} \qquad (4\text{-}4)$$

where:

EI_{beam} = bending stiffness of the RC beam;
$F_{amplitude}$ = load amplitude (10.0 kN);
L_{end} = distance between load and support (475 mm);
L_{mid} = distance between the supports (450 mm);
$\delta_{amplitude}$ = deflection amplitude (measured).

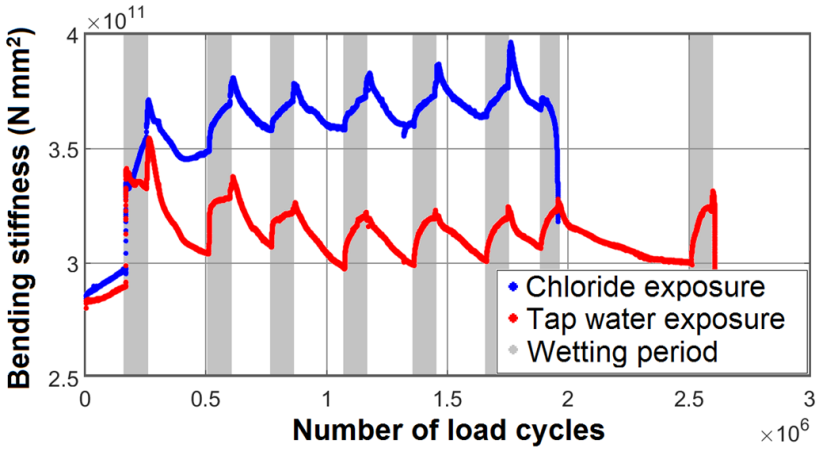

Figure 4-45: Bending stiffness of the beams derived from the deflection amplitudes of the beams of Test 4B.

The deflection amplitudes were used to calculate the bending stiffness (Equation (4-4)). It was discussed in Section 4.5.2 that the wetting/drying cycles have a large effect on the deflections of the RC beams. It was mentioned that the cracks do not completely close during the wetting period. As result of this, the measurements of the deflections could not be used to calculate the actual bending stiffness correctly.

Figure 4-46 shows an illustration of a force-deflection diagram of a RC beam with (wet) and without (dry) water in the cracks. Only the minimum and the maximum deflection (deflections at respectively 2.0 and 12.0 kN) of the beam were measured. The actual bending stiffness is indicated by angle α. When the measurements were used to calculate the bending stiffness, angle α* was obtained instead of angle α. Since α* is larger than α, the bending stiffness of the RC beam was overestimated. Therefore, the natural frequencies which are calculated by Equation (4-4) were overestimated as well. Since only the maximum and the minimum deflection were stored, the real bending stiffness of the RC beam could not be obtained from the measurements. Since the bending stiffness was used to calculate the natural frequencies of the RC beam, the natural frequencies could not be obtained from the measurements either.

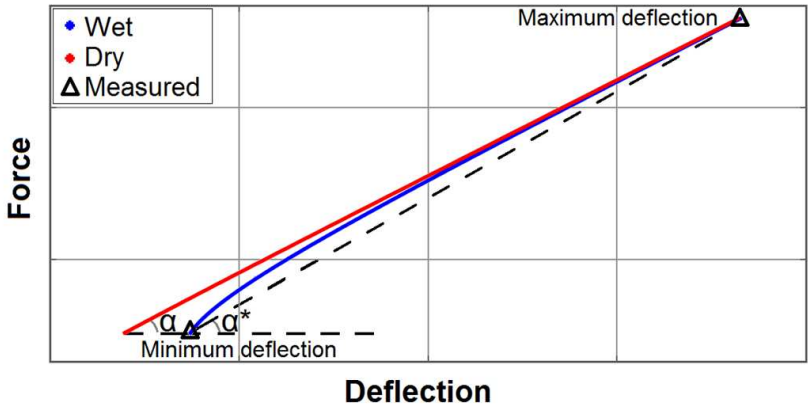

Figure 4-46: Illustration of a force-deflection diagram. The blue curve illustrates a RC beam with water in the cracks (wet). The red curve illustrates a RC beam without water in the cracks (dry). As results of the measurements, the angle α could not be obtained.

4.9 Discussion and summary

Tests on plain steel bars (Bar Test) and tests on RC beams (Beam Test) have been conducted in this research. These tests provided information concerning the research questions: How do deflections of a cyclic loaded RC structure under change over its service-life, and how does chloride-induced corrosion influence the deflections of a cyclic loaded RC structure?

The Bar Test provided information about failure of a plain steel bar under axial dynamic loads. The Bar Test contained 13 dynamically loaded plain steel bars. Within these 13 plain steel bars, two different load configurations and four different exposure conditions have been investigated. The Bar Test showed that the plain steel bars with localized corrosion failed at a lower number of load cycles than plain steel bars without corrosion. Within the conducted tests, localized corrosion reduced the maximum number of load cycles by 30%. The difference in chloride concentration (5%, 10%, or 20%) was of minor importance for the reduction of the number of load cycles until failure of the bar.

The elongations of the plain steel bar were measured in the Bar Test. In the first 99% of the load cycles, the elongations of the steel bar hardly changed. In the last few thousand load cycles until failure, the elongations of the bar increased. This increase was the result of a reduction of the axial stiffness of the steel bar and local yielding of the bar. The increase of the elongations of the bar at the last few thousand load cycles of a bar with localized corrosion was similar to the elongations of the bar at the last few thousand load cycles of an uncorded bar.

The Beam Test contains 12 sets of two RC beams. Each RC beam was loaded dynamically in a four-point-bending configuration. In four sets of two beams, the corrosion activity was monitored by Half-Cell Potential (HCP) and by Linear Polarization Resistance (LPR). The HCP method indicated that the probability of corrosion increases during the first wetting period and remained constant after the first witting period. The LPR method indicated that the corrosion rate was constant after the first wetting period. A change in the corrosion activity in the reinforcing bar after the first wetting period could not be obtained by HCP or by LPR.

Different failure mechanisms were observed during the tests. Since steel corrosion reduces the load bearing capacity of the reinforcing bars, flexural failure was intended to occur. For the beams with this failure mechanisms, the maximum number of load cycles until failure was 30-50% higher in RC beams with a sound reinforcing bar compared with the RC beams with a corroded reinforcing bar. In the first 99% of the load cycles, the deflections of the RC beam with a corroded reinforcing bar were similar to the deflections of the RC beam with an uncorroded reinforcing bar. Also the increase of the deflections during the last few thousand load cycles was not changed by the corrosion activity. The main difference between a corroded reinforcing bar and an uncorroded reinforcing bar is the moment at which damage-induced changes in the deflections started.

The variations in the reinforcement configuration and in the loading conditions were limited. No tests were conducted with different dimensions of the RC beam or with multiple reinforcing bars in the RC beams, different stress amplitudes, or different stress levels. For a more general conclusion about the reduction of the maximum number of load cycles for different structures and different loading conditions, more tests are required.

Wetting/drying cycles influence the deflections of the RC beam. It was observed that the minimum deflections increase in the wetting period and decrease in the drying period. This is probably caused by the presence of water in the cracks. Due to the presence of water, cracks do not completely close and initiate residual deflections. It was observed that fluctuations in the ambient temperature and fluctuations in the ambient humidity influence the deflections of the RC beam.

A slight increase of the deflections of the RC beam was measured in all RC beams during the first 99% of the load cycles. The deflections of the RC beams whereby the reinforcing bar failed increase more significantly during the last few thousand load cycles. Similar, during the Bar Test, an increase of the elongations of plain steel bars were observed during the last few thousand load cycles. From this observation, it was concluded that the reinforcing bars of the RC beams had a similar failure mechanism as the plain steel bars.

Since the deflections of the RC beam only increase more significantly during the last few thousand load cycles, the deflections of RC structures cannot be used as early warning system. As late warning system (warning just before failure), the deflections of the RC beam might an indicator. However, small fluctuations in the deflections of the RC beam could be caused by fluctuations in the ambient condition (Temperature and Relative Humidity). Since the fluctuations in the ambient condition in the Dutch climate are larger than those under ambient condition in the laboratory, the effect of fluctuations in the ambient condition on the deflections of RC beams in real structures will be larger. Therefore, it is conceivable that the increase of the deflections of a RC structure during the last few thousand load cycles cannot be observed. Finite Element calculations (Chapter 5) and a sensitivity analysis (Chapter 6) have been developed to investigate whether the deflections during the last few thousand load cycles can be obtained in structures under more realistic ambient conditions.

Chapter 5

Finite Element Analyses of a Reinforced Concrete Beam

Finite Element (FE) calculations can be used to analyse complex situations numerically. In this chapter, FE calculations are used to obtain the relation between damage in a reinforcing bar and changes in the deflections of a Reinforced Concrete (RC) beam. This relation can be used to predict the development of the deflections of a RC beam as function of damage in reinforcing bars. When this development is validated with the results of the laboratory tests of Chapter 4, the development of the deflections of the RC beam can be used as a predictive model to estimate the end of the fatigue life of a RC beam with and without corrosion in the reinforcing bar.

5.1 General introduction of Finite Element models

Deformations of a structure and stresses in a structure can be simulated numerically using a FE program. Such a numerical simulation is called a FE model. Two FE models have been developed in this study. The first FE model concerns the simulation of a plain steel bar. Different levels of damage in the plain steel bar were simulated in this FE model. The FE model calculates stresses in the bar and elongations of the bar at different damage levels. The second FE model concerns the simulation of a RC beam. In this FE model, different levels of damage in the reinforcing bar were simulated at different locations on the beam. The stresses in the steel bar and in the concrete beam, the width of different cracks, and the deflections of the RC beam were calculated. The results of these calculations provide information about the relation between damage in a reinforcing bar, the increase of stresses in the reinforcing bar, the increase of the cracks in the RC beam, and the increase of deflections of the RC beam.

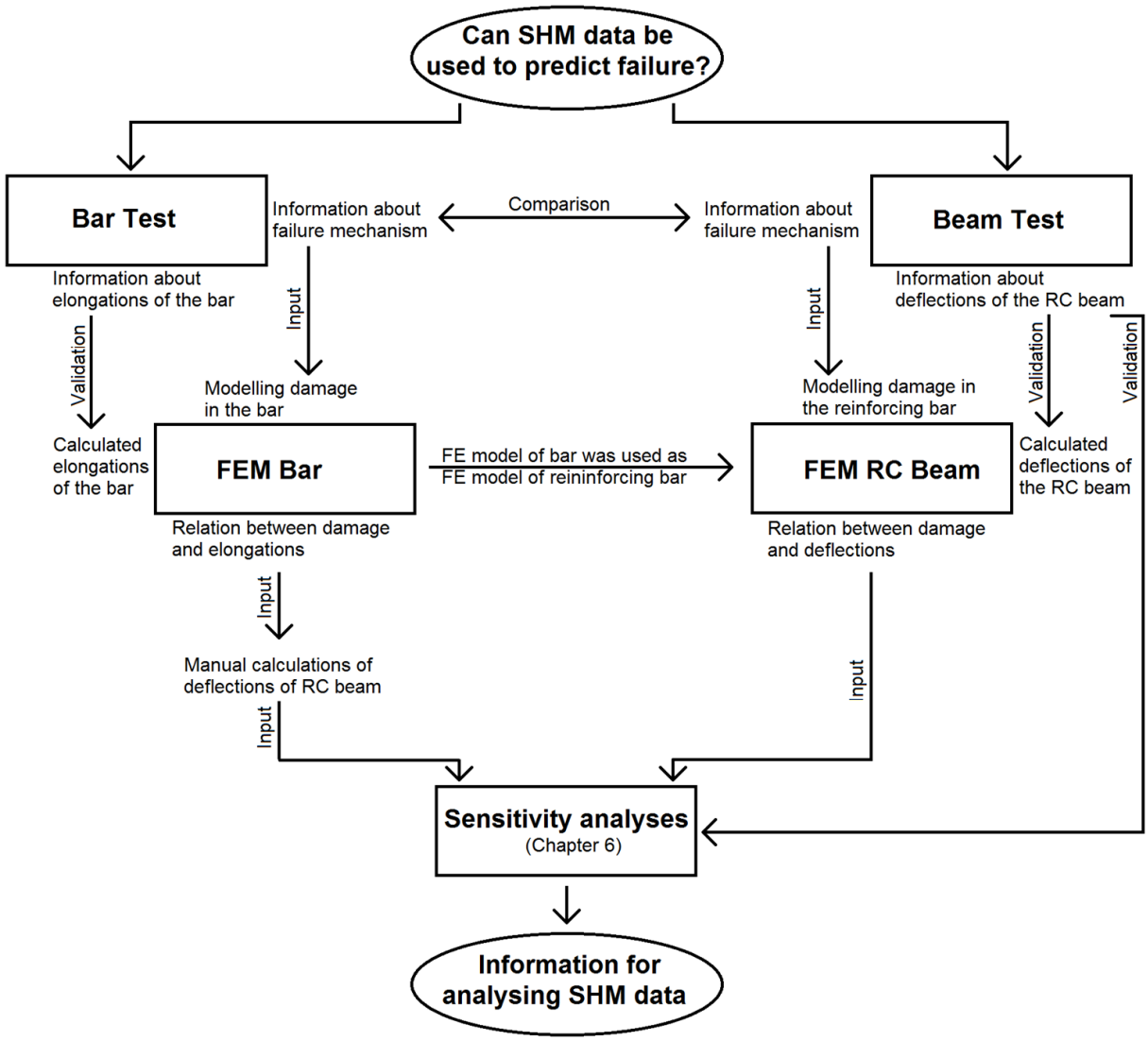

Figure 5-1: Relations between test results, FE models, Sensitivity analyses, and a SHM system. (FEM = Finite Element Method, SHM = Structural Health Monitoring).

Figure 5-1 shows the relations between test results (Chapter 4), and FE models (this chapter), sensitivity analyses (Chapter 6). This figure shows that the information about the failure mechanisms of the plain steel bars and the RC beams, obtained during the tests, were used as input for the FE models. Figure 5-1 also shows that the relation between damage in reinforcing bars and the deflections of the RC beam, obtained by the FE calculations, was used as input for sensitivity analyses (Chapter 6).

5.2 Finite Element calculations of a plain steel bar

A 3D FE model of a plain steel bar was developed (using the DIANA FEA [96]) to calculate the stresses in the bar and the elongations of a bar at different damage levels. The FE model was validated by comparing the calculated elongations of the bar with the measured elongations of the bar during the Bar Test (Section 4.1).

5.2.1 Configuration of the model

A plain steel bar with a diameter of 12 mm and a length of 105 mm was simulated in a FE model. The steel bar was modelled with volume elements with a shape of a tetrahedron and sizes of approximately 2.0*2.0*2.0 mm^3. At the damaged cross-section, a finer mesh (0.4*0.4*0.4 mm^3) was used. The computation time was reduced by simulating only half of the cross-section of the bar. Figure 5-2 shows a cross-section of the bar as simulated in the FE model. A part of the FE model is presented in Figure 5-3. Note that in this figure, the length of the bar is not plotted in the same scale as the width of the bar. In this figure, the location of the simulated damage is presented as well. The cross-sections of the bar at different damage levels is given in Figure 5-5.

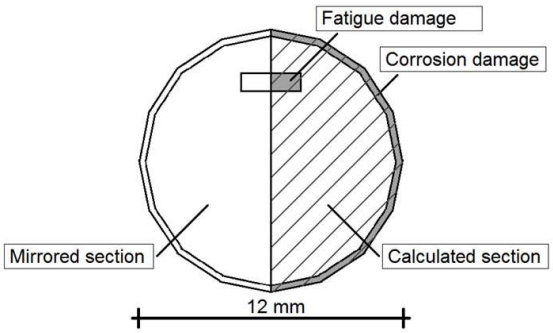

Figure 5-2: Cross-section of the plain steel bar with the representatives of fatigue damage and corrosion damage.

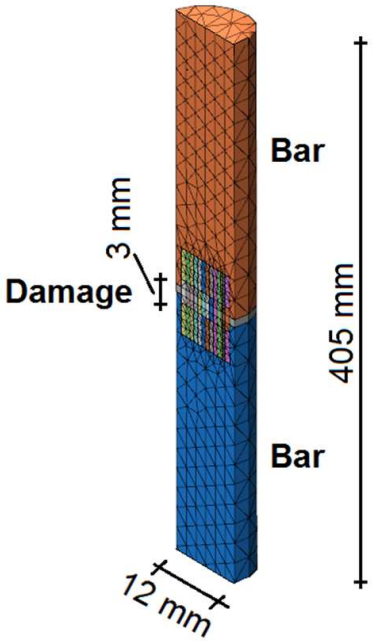

Figure 5-3: Part of the FE model. The damaged cross-section is presented in Figure 5-5.

Material properties

The mechanical properties used in the FE model of the plain steel bar have been determined in a static test (Section 4.2.2). The Young's modulus, the yield stress, and the Poisson ratio are given in Table 5-1. Beyond the yield strain of the steel the stresses hardly changed. For a more stable FE calculation algorithm, strength hardening and strength softening of the steel were not taken into account. The stress-strain diagram used in the FE model is given in Figure 5-4.

Table 5-1: Mechanical properties of steel bar.

Young's modulus (E_s) **	Yield stress (f_y) *	Poisson ratio (v) **
191,000 N/mm^2	600 N/mm^2	0.2

* In the FE model, no strength hardening was considered.

** The Young's modulus and the yield stress were determined by a static test. The Poisson ratio was not.

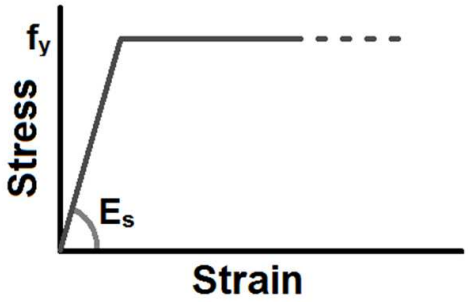

Figure 5-4: Stress-strain relation which was used in the FE model.

Fatigue damage and corrosion damage

The plain steel bars were damaged by the combined action of fatigue and corrosion (Section 4.1). Fatigue damage was initiated by cyclic loading. The amount of fatigue damage depended on the stress amplitudes and on the number of load cycles. With a constant load frequency, fatigue damage can be expressed as a function of time. Corrosion damage was initiated by chloride exposure. The amount of corrosion damage depended on the exposure time.

Generally, corrosion starts at the surface of a steel bar and proceeds towards the core of the bar. Fatigue damage (fatigue cracks) can theoretically start at every location of the cross-section of the bar. Normally, multiple fatigue cracks are developed before fatigue failure occurs. Since it is unknown which of the fatigue cracks will initiate failure, the decisive fatigue crack can start at any location of the cross-section of the steel bar [131].

Changes in the stresses in the bar are easier to analyse when damage was simulated with a rectangular defect than when damage was simulated with a circular defect. In the FE model, a rectangular defect was schematized by simulating the starting position of damage in the core of the cross-section of the bar. Damage in the steel bar was simulated by removing elements from the cross-section of the steel bar. Eleven FE calculations were performed. The first FE calculation concerned the bar in an undamaged situation. In the remaining calculations, ten damage levels were simulated, whereby the amount of damage was limited in damage level 1 and relatively high in damage level 10.

The length of the damaged section (3.0 mm, Figure 5-3) was constant for all damage levels. The length and the width of the simulated damage were related to the damage level. The different simulated damage levels are given in Table 5-2. Figure 5-5 shows an illustration of the cross-sections of the different simulated damage levels. The position of the damaged section was shown in Figure 5-3.

Table 5-2: Dimensions of the damaged sections per damage level.

Damage level	Width damage*	Height damage	Relative damage
Damage level 0	No damage		0
Damage level 1	0.4 mm	0.8 mm	0.6 %
Damage level 2	0.8 mm	1.6 mm	2.3 %
Damage level 3	1.2 mm	2.4 mm	5.1 %
Damage level 4	1.6 mm	3.2 mm	9.1 %
Damage level 5	2.0 mm	4.0 mm	14.2 %
Damage level 6	2.4 mm	4.8 mm	20.4 %
Damage level 7	2.8 mm	5.6 mm	27.8 %
Damage level 8	3.2 mm	6.4 mm	36.2 %
Damage level 9	3.6 mm	7.2 mm	45.6 %
Damage level 10	4.0 mm	8.0 mm	56.6 %

* The width of the damaged section is mirrored. Related to the total cross-section of the bar, the total damage section is two times this value.

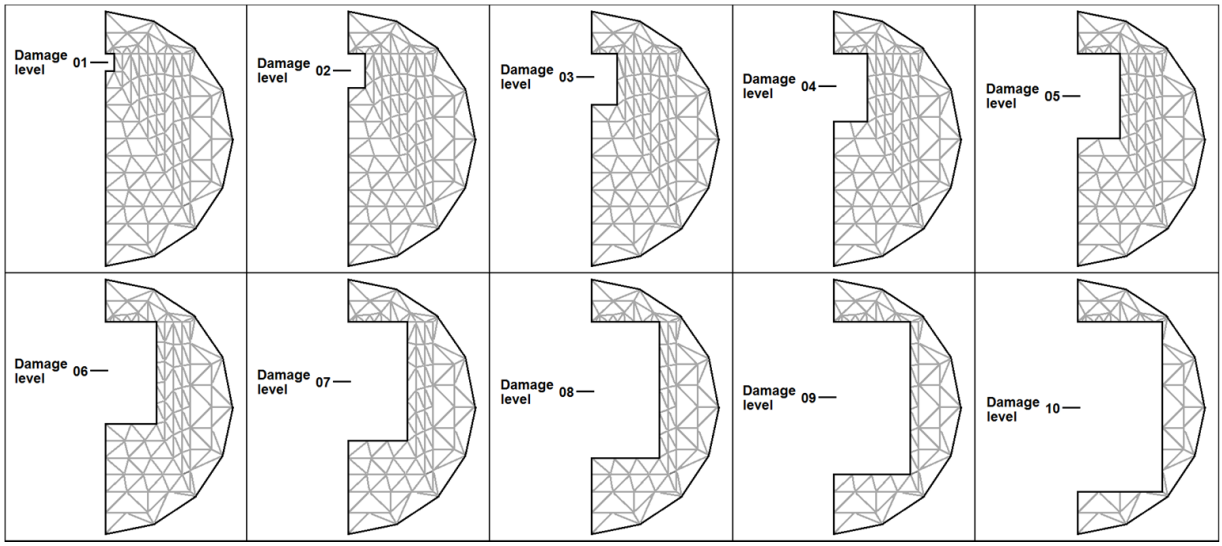

Figure 5-5: Illustration of the different cross-sections corresponding to the different simulated damage levels. The position of the cross-sections along the length of the bar was given in Figure 5-3. The dimensions of the damaged sections are presented in Table 5-2.

FE calculations with non-linear parameters in the material properties are more stable in a deformation-controlled mode than in a load-controlled mode. To simulate the post-yielding behaviour of the steel better, the loads on the bar were simulated as imposed elongations. The elongations were increased with 150 steps of 0.01 mm each. In each step, the stresses in the bar and the loads on the bar were calculated.

The plain steel bars were loaded by a dynamic load (load controlled) with a constant average load and a constant load amplitude (Section 4.1). The maximum load on the bar was 36.7 kN, which corresponds to 325 N/mm^2 related to the initial cross-section of the bar. Due to the shape of the tetrahedron elements, the cross-section of the bar in the FE model is slightly different from the cross-section of the tested bars. Since the schematized cross-section is approximately 97.5% of the real cross-section, an load of 35.8 kN was required to simulate an average stress of 325 N/mm^2 in the initial cross-section. The results of the calculation which resulted in a force on the bar of 35.8 kN were used in the analyses.

5.2.2 Calculation results

Stresses in different elements

When failure was reached in one of the elements, this element could not contribute further to the load bearing capacity of the bar. After failure of an element, the stresses in the adjacent elements increased.

In the fatigue analysis (Section 6.2), the average stresses over a certain area are used. Ten different areas are considered in the calculation. These areas are presented in Figure 5-6 as ‘stress areas’. The stresses in the other elements were taken into account in the FE calculation and used for the equilibrium of the system. These stresses were not

considered in the fatigue analysis. The stresses which were used in the fatigue analysis are presented in Table 5-3.

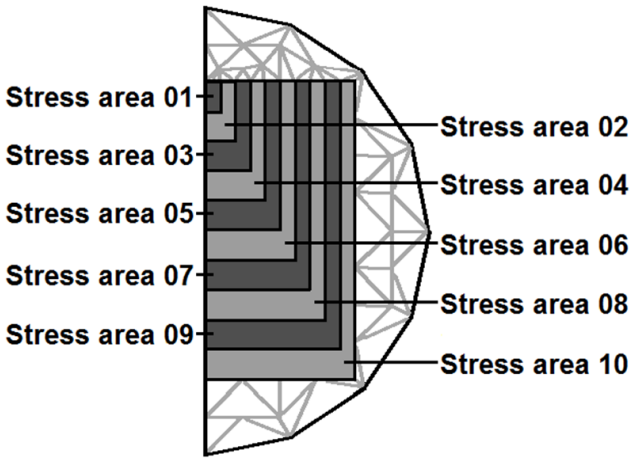

Figure 5-6: Areas is the cross-section of the bar in which the average stresses are used for a fatigue analysis (Section 6.2). Table 5-3 shows the stresses for the corresponding areas.

Table 5-3: Average stresses per area of the cross-section of the bar for different areas. The load on the bar was 35.8 kN. The units in this table are N/mm^2. The position of the areas are given in Figure 5-6. The damage levels are given in Figure 5-5.

	Area									
	1	2	3	4	5	6	7	8	9	10
Damage level 0	325	326	326	326	326	326	326	325	325	325
1	-	352	338	332	329	328	327	326	325	325
2	-	-	395	359	344	336	332	330	328	326
3	-	-	-	432	385	360	347	339	334	330
4	-	-	-	-	473	412	379	360	347	339
5	-	-	-	-	-	516	441	400	373	357
6	-	-	-	-	-	-	556	474	421	390
7	-	-	-	-	-	-	-	588	512	455
8	-	-	-	-	-	-	-	-	600	565
9	-	-	-	-	-	-	-	-	-	600

Relation between damage in the cross-section of the bar and the increase of the elongations of the bar

The relation between the elongations of the bar and the amount of damage in the bar is given in Figure 5-7. To compare the calculated elongations of the bar with the measured elongations of the bar, the relation between the number of load cycles and the amount of damage must be obtained. This relation is presented in Section 6.2.

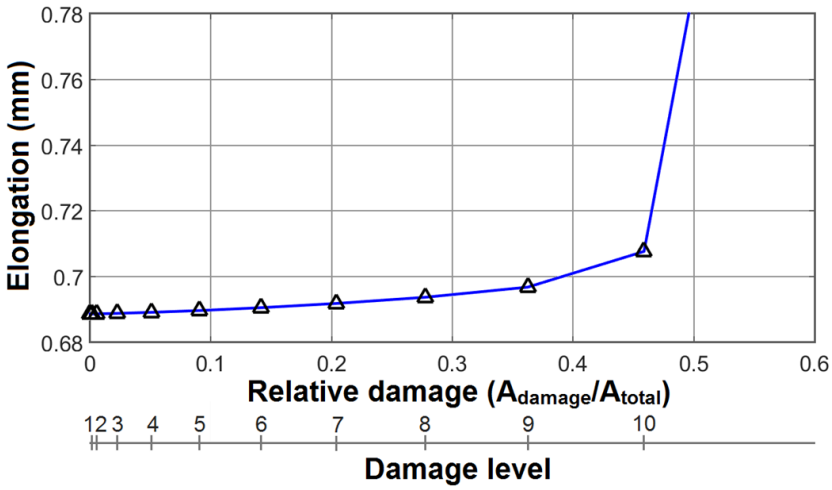

Figure 5-7: Calculated elongations of the bar as function of the relative damage. The load on the bar is 35.8 kN, the total length of the bar is 405 mm, and the length of the damage sections is 3 mm. The different damage levels (Figure 5-3) are presented in a second X-axis.

Fatigue damage and corrosion damage

It was shown above that a small amount of damage hardly changed the stresses in the bar and the elongations of the bar. More significant changes in the stresses and changes in the elongations can only be observed at a larger amount of damage. For larger amounts of damage, it hardly matters whether damage started in the core or at the surface of the bar. It was assumed that the situation whereby damage started in the core of the bar and proceeded to the surface of the bar resulted in a similar damage-stress diagram and a similar damage-elongation diagram as in the situation whereby damage started at the surface of the bar and proceeded to the core. Therefore, the effect of fatigue damage on the stresses in the bar and on the elongations of the bar, and the effect of corrosion damage on the stresses in the bar and on the elongations of the bar can be both described with the simulation of damage in the bar as presented above.

5.3 Finite Element calculation of a Reinforced Concrete beam

A FE model of a RC beam was developed to investigate the effect of damage in a reinforcing bar on the deflections of the RC beam. Different damage levels were considered in this FE model. For each damage level, the deflections of the RC beam were calculated. In order to investigate whether the damage-induced changes in the deflections of the RC beam can be obtained by a SHM system, a sensitivity analysis concerning damage-induced deflections and the effect of changes in the ambient temperature on the deflections of the RC beam is performed (Chapter 6). The deflections of the RC beam, presented in this section, are used as input in the sensitivity analysis.

5.3.1 Configuration of the model

A 3D FE model of the RC beam was developed to calculate the effect of damage in the reinforcing steel on the behaviour of the RC beam. For simulating the reinforcing bar in the RC beam, the FE model of the plain steel bar was used.

Damage of the reinforcing bar can initiate at different locations along the length of the bar. Since at each crack in the concrete beam the stresses in the reinforcing bar were concentrated, it was assumed that damage in the bar can initiate in each crack. To simulate cracks at the different locations, the total length of the RC beam had to be simulated. It was assumed that the RC beam has a symmetrical behaviour in the width of the beam. Therefore, half of the width of the RC beam, half of the reinforcing bar, and half of the amount of damage could be schematized to simulate the behaviour of the total RC beam. The FE model of the RC beam is given in Figure 5-8.

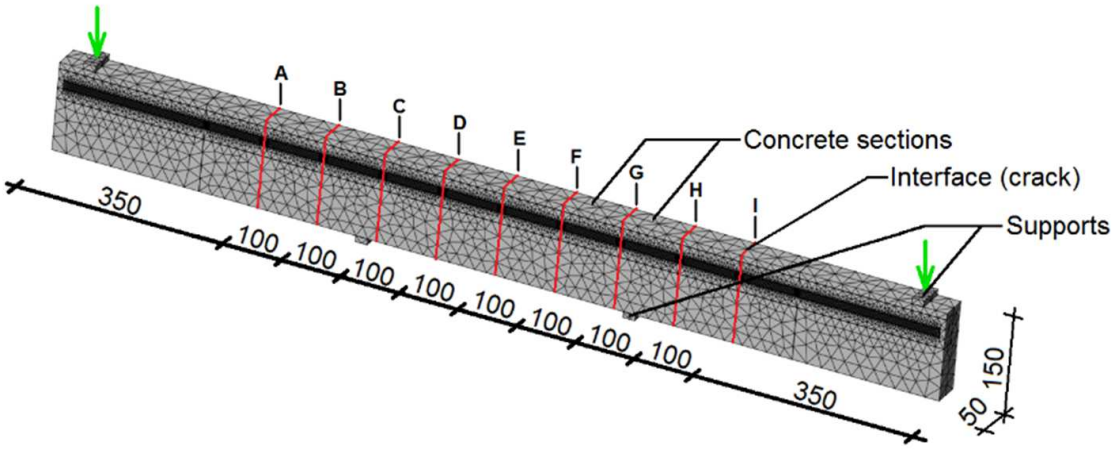

Figure 5-8: FE model of the RC beam. The dimensions are in mm.

Simulating cracks in the RC beam

The RC beams tested in this study were cracked at different locations. Although the number of cracks (between 6 and 9 cracks) and the distance between the cracks (varied between 70 and 140 mm) were different for the different RC beams, all RC beams whereby the reinforcing bar failed showed similar damage-induced changes in the deflections of the RC beam. Therefore, it was assumed that the development of the deflections of the RC beam mainly depends on changes in the properties of the RC beam and hardly on the number of cracks and their positions in the RC beam.

Interface elements were used to simulate the cracking behaviour of concrete. The nine locations with interface elements correspond to nine cracks in the RC beam. The cracks were numbered from 'A' till 'I' (Figure 5-8). The length of each interface element was 1.0 mm. The nine simulated cracks divide the beam in 8 (middle) sections of 100 mm and 2 (end) sections of 350 mm (first and last section). All concrete sections were simulated with volume elements with a shape of a tetrahedron and sizes between 10*10*10 mm^3 and 25*25*25 mm^3. The reinforcing steel bar was modelled with volume elements with a shape of a tetrahedron and sizes of approximately 2.0*2.0*2.0 mm^3. The steel supports of the beam (10*20*100 mm^3) were modelled with tetrahedron elements of approximately 10*10*10 mm^3. The elements of the supports were rigidly connected to the elements of the concrete sections.

Material properties

Since the cracks are explicitly simulated in the FE model, it was assumed that cracks do not develop in the simulated concrete sections. Therefore, the concrete sections were schematized with linear mechanical properties (Figure 5-9-A). The Young's modulus of concrete was estimated at 31,000 N/mm^2, which corresponds to the Young's modulus of concrete strength class C20/25 [101]. For the interface elements which simulated the cracks in the RC beam, the 5% lower limit of the of the concrete tensile strength was used (1.8 N/mm^2 [101]). A linear energy-based softening model was used for the stress-strain relation of the interface elements. For this energy-based softening model, a value of the fracture energy G_f=0.15 N/mm [132] was used (Figure 5-9-B). For the steel reinforcing bar, the same properties were used as in the FE model of the plain steel bar (E_s = 191,000 N/mm^2; f_y= 600 N/mm^2; Figure 5-4) (Figure 5-9-C). Since the supports were only applied to spread the load on the RC beam, the supports were simulated with linear mechanical properties. For the Young's modulus of the supports, the Young's modulus of the reinforcing steel was used (E_s= 191,000 N/mm^2) (Figure 5-9-D). The mechanical properties of the different materials are given in Table 5-4.

Table 5-4: Mechanical properties of the different materials.

Material	Young's modulus	Poisson ratio	Comments
Concrete	31,000 N/mm^2	0.2	Linear behaviour
Crack interface	31,000 N/mm^2	0.2	f_{ct}=1.8 N/mm^2 (tensile strength) G_f=0.15 N/mm (fracture energy)
Reinforcing steel	191,000 N/mm^2	0.2	f_y=600 N/mm^2 (yield stress) No strength hardening
Support steel	191,000 N/mm^2	0.2	Linear behaviour
Reinforcement interface	31,000 N/mm^2	0.2	See Figure 5-10 for bond-slip

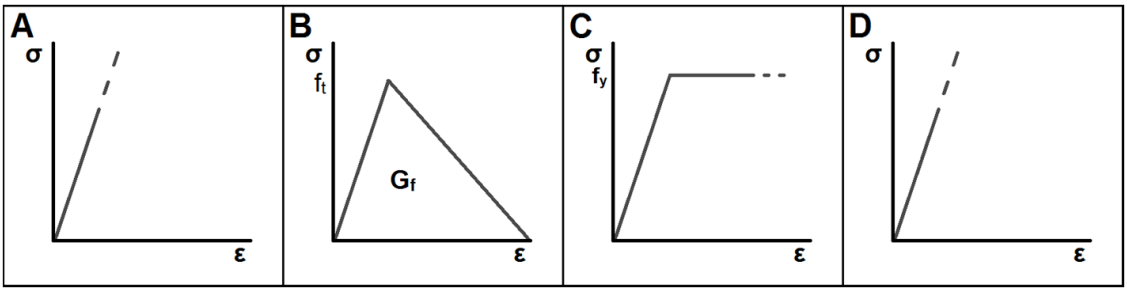

Figure 5-9: Stress-strain relations of the used material properties in FE model of the RC beam. Figure 5-9-A shows the stress-strain relation of the concrete. Figure 5-9-B shows the stress-strain relation of the crack interfaces. Figure 5-9-C shows the stress-strain relation of the reinforcing steel. This figure is similar as the stress-strain relation in Figure 5-4. Figure 5-9-D shows the stress-strain relation of the steel supports.

The stress distribution in the concrete beam and in the steel bar depends on the interaction between both materials. This interaction was simulated by interface elements with a bond-slip relation. Due to this bond-slip relation, a small movement of the

reinforcing bar in relation to the concrete could be simulated. This is a more realistic simulation of the stress transfer between steel and concrete than a fixed connection. The bond-slip relation is presented in the DIANA FEA documentation [132] and plotted in Figure 5-10. Different values for the maximum bond strength can be found in the literature [101, 132, 133]. Based on the recommendations in Eurocode 2 [101], a value of 5.85 N/mm^2 was chosen for the maximum bond strength between the concrete beam and the steel reinforcing bar.

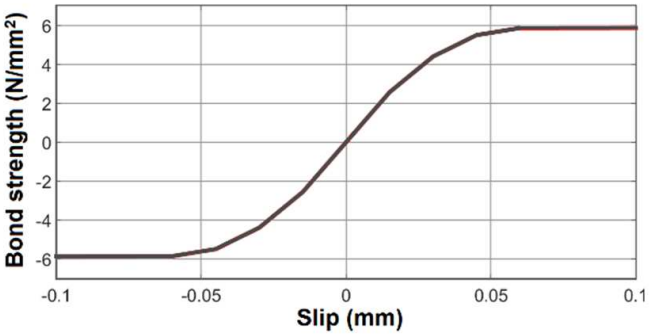

Figure 5-10: Bond strength-slip diagram.

Similar to the calculations with the FE model of the plain steel bar (Section 5.2), the calculations with the FE model of the RC beam were more stable in a deformation-controlled mode than in a load-controlled mode. The deflections were simulated with 150 steps of 0.02 mm each. In each step, the loads on the beam were calculated. The calculations which resulted in a load on the RC beam of 2.0 kN or 12.0 kN (the minimum load and maximum load on the RC beams during the Beam Test, Table 4-7, Section 4.2.3) were selected. The stresses in the reinforcing bar and the deflections of the RC beam, obtained from these calculations, were used as input in a fatigue analysis (Section 6.2).

Damage in the reinforcing bar

Damage in the reinforcing bar was simulated in ten damage levels (similar to the FE model of the plain steel bar, Section 5.2.1). Damage in the reinforcing bar was simulated at the locations where the stresses are highest (Table 5-5). These locations are at cracks B, C, D, and E.

Is was observed that corrosion was spread over a few centimetres along the length of the reinforcing bar (Beam Test, Section 4.7). The simulated amount of damage could be used to simulate the effect of both fatigue and corrosion on the stresses in the bar and the elongations of the bar (Section 5.2.2).

In the FE model of the RC beam, damage in the reinforcing bar was simulated over a length of 11 mm instead of the 3 mm in the plain steel bar (Figure 5-3). This increased length simulated the effect of a reduced bond strength. This reduced bond strength could be caused by corrosion or by fatigue.

5.3.2 Tensile stresses in the concrete beam and in the steel bar

Due to the four-point-bending load configuration, loads on the RC beam result in bending moments in the RC beam. As result of these bending moments, the bottom section of the RC beam was loaded in compression and the top section was loaded in tension. When the RC beam is cracked, the tensile stresses in the concrete reduce. At the cracked sections of the RC beam, the largest part of the tensile forces is carried by the reinforcing steel. Figure 5-11 shows the tensile stresses in the concrete sections of the RC beam. This figure shows that at the locations of the cracks, the tensile stresses in the concrete are approximately 1.0 N/mm^2. Due to the remaining tensile stresses in the concrete, the tensile stresses in the reinforcing bar are lower than the calculated steel stresses (Table 4-7, Section 4.2.3). Figure 5-11 shows that the maximum tensile stresses in the concrete around the reinforcing bar were approximately 2.6 N/mm^2, which is the average tensile strength of concrete class C20/25. The area in the RC beam with compressive stresses has a grey colour.

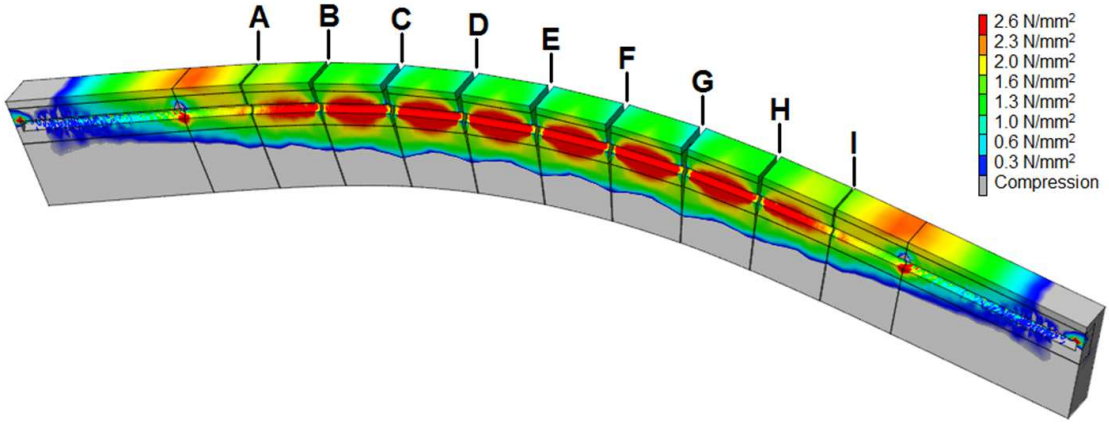

Figure 5-11: Concrete tensile stresses in the RC beam without damage in the reinforcing bar. The load on the beam was 6 kN (for half of the beam, so 12 kN in total).

The stresses shown in Figure 5-11 are the result of loading the RC beam with 12.0 kN. In the fatigue analysis (Section 6.2), the stresses in the bar calculated by the minimum load of 2.0 kN and the maximum load of 12.0 kN are required. The stresses in the bar as result of both loading conditions are given in Table 5-5.

Table 5-5: Tensile stresses in the sound steel reinforcing bar. The stresses are expressed in N/mm^2.

Load	Crack number								
	A	B	C	D	E	F	G	H	I
2.0 kN	9	18	26	26	26	26	26	18	9
12.0 kN	52	107	153	154	155	154	153	105	51

The stresses in Table 5-5 are the stresses in the sound bar. The increase of the stresses in the reinforcing bar as result of damage in the bar were not obtained from the FE calculation of the RC beam. It was assumed that the increase of the stresses in the reinforcing bar in the RC beam were similar to the increase of the stresses in the plain steel bar. These stresses were presented in Section 5.2.2 (Table 5-3).

5.3.3 Deflections of the Reinforced Concrete beam

Validation of the FE model

The formation of the cracks and the force-deflection diagram were used to validate the FE model of the RC beam. Figure 5-12 shows a deformed shape of the RC beam including the simulated cracks. The load on top of the RC beam was 12 kN. Damage in the reinforcing bar was not considered.

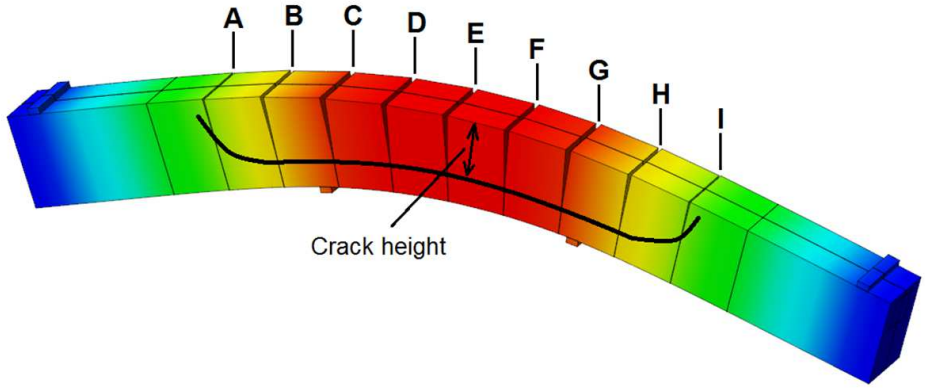

Figure 5-12: Deformed shape of the FE model of the RC beam, including the crack openings. The load on the RC beam was 6 kN (for half of the beam).

The static load bearing capacity was calculated by increasing the imposed deformations of the RC beam until failure was simulated. The results of these calculations are presented with a red curve in Figure 5-13. The blue curve in the same figure corresponds to the measured deflections during a static test (Section 4.3). Both curves show a similar behaviour in the uncracked stage. The development of the cracks (between 5.0 kN and 6.5 kN) are similar as well. In the cracked stage, the calculated forces on the RC beam were higher than those measured during the static test.

The maximum load of the tested RC beams was 12.0 kN. Within the range between 0 and 12.0 kN, the difference between the results of the FE calculations and the test results are limited. The difference between the calculated and the measured load bearing capacity does not influence the fatigue analysis.

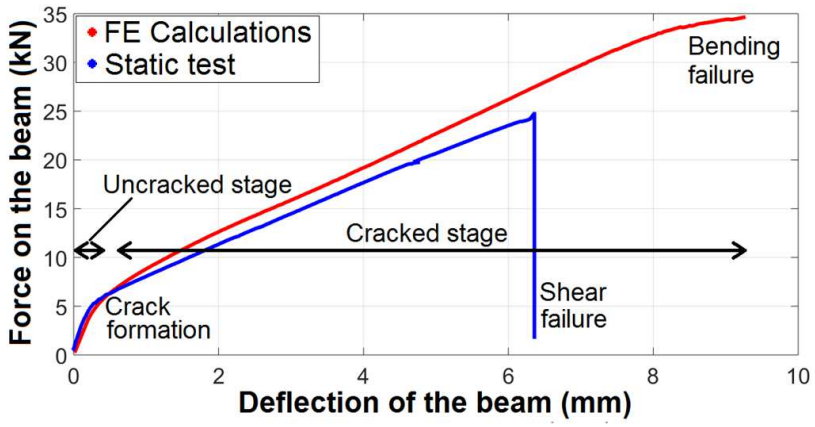

Figure 5-13: Load-displacement diagram. The red curve corresponds to the results of the FE calculations. The blue curve corresponds to the monitored deflections (Section 4.3).

Deflections of the Reinforced Concrete beam as result of damage in the reinforcing bar

Damage in the reinforcing bar was simulated at four different locations (at crack B, C, D, and E). The deflections of the RC beam were calculated for ten damage levels (Section 5.2.1) at each of these locations. The results of these calculations indicate the development of the deflections of the RC beam as result of damage in the reinforcing bar at different locations. Since the cracks are schematized symmetrically, damage in the reinforcing bar at crack F, G, or H results in a similar development of the deflections as damage in cracks D, C, or B respectively. The development of the deflections of the RC beam as function of the amount of damage is given in Figure 5-14. In this figure, the blue curve corresponds to damage in crack E, the red curve to damage in cracks D or F, the green curve to damage in cracks C or G, and the cyan curve to damage in cracks B or H. All curves in Figure 5-14 show a nonlinear relation between the deflections of the RC beam and the amount of damage in the reinforcing bar. This behaviour was also observed in the elongations of the plain steel bar (Figure 5-7) and was caused by (partially) yielding of the steel bar.

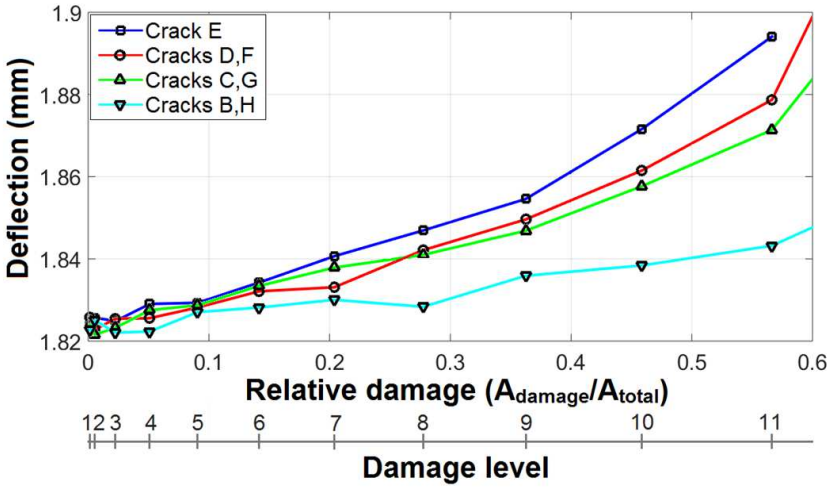

Figure 5-14: Deflections of the calculated RC beam as function of the relative damage in the reinforcing bar. The different curves represent damage of the reinforcing bar at different crack locations. The different damage levels (Section 5.2.1; Figure 5-3) are presented in a second x-axis. The load on the beam was 6 kN (for half of the beam, so 12 kN in total).

5.4 Effect of multiple reinforcing bars on the development of the deflections of a Reinforced Concrete structure

In Section 5.3, the deflections of a RC beam with a single reinforcing bar were calculated for different damage levels in the reinforcing bar. RC bridges contain a large number of reinforcing bars. Due to the large number of the reinforcing bars, failure of a single reinforcing bar does not automatically result in failure of the RC bridge. Due to redistribution of forces, the development of the deflections of a RC bridge can be different from the development of the deflections of a RC beam with a single reinforcing bar. Potential changes in the deflections of a RC beam with multiple reinforcing bars and potential changes in the deflections of a RC bridge are discussed in this section.

5.4.1 Deflections of a Reinforced Concrete girder

Most of the girders of RC bridges are larger and contain more reinforcing bars than the RC beam which was calculated in Section 5.3. Normally, the reinforcing bars in the tensile zone of these girders are equally distributed over the width of the girder. When the loads on these girders are equally distributed over the width of the girder as well, the tensile stresses are about the same in the different reinforcing bars. Considering the same material properties for all reinforcing bars, all remaining reinforcing bars are probably heavily damaged after one of the reinforcing bars had failed on fatigue and corrosion. When the RC beam is loaded with a constant load frequency, the remaining reinforcing bars will probably fail within a limited number of load cycles after failure of the first reinforcing bar. When the RC beam is loaded with cyclic loads with variable stress amplitudes, failure of the remaining reinforcing bars depends on how damage accumulates [59].

5.4.2 Deflections of a Reinforced Concrete bridge

Since the loads on the deck of a RC bridge are not equally distributed over the width of the bridge, the load distributions over the deck of the RC bridge can be different from the load distribution over a RC beam. In contrast to a RC beam with multiple reinforcing bars, not all reinforcing bars in a RC deck of a bridge are loaded similarly. When a reinforcing bar in a RC deck of a bridge failed, it is possible that the forces from the broken reinforcing bar are redistributed over the remaining reinforcing bars. Redistribution of the forces in the reinforcing bars in the deck of a RC bridge are not further investigated in this research.

5.5 Discussion and summary

When the development of the deflections of a RC structure are used as indicator for damage in the structure, it is important to understand how the deflections of the structure change as result of damage. To obtain the relation between damage in the reinforcing bar (as results of fatigue and corrosion) and the deflections of a RC beam, two FE models have been developed. The first FE model considered a plain steel bar. A RC beam was simulated in the second FE model.

The effects of local damage of a plain steel bar on the stresses in the remaining cross-section of the bar and on the elongations of the bar were calculated. In the FE model, it was assumed that damage started in the core of the bar and proceeded towards the surface of the bar. Calculation results showed that significant changes in the stresses and in the elongations of the bar only occur at a large amount of damage.

At a large amount of damage it becomes less important where damage has started. Therefore, it was assumed that the effect of damage in the bar on the stresses in the bar and on the elongations of the bar was similar in the situation whereby damage started in the core of the bar to the situation whereby damage started at the surface of the bar. With this assumption, the simulated amount of damage can be used for fatigue damage as well as for corrosion damage in the bar.

In the FE model of the plain steel bar, damage was simulated over a length of 3.0 mm. In the FE model of the RC beam, damage in the reinforcing bar was simulated over a length of 11 mm. This increased length of the damaged section simulated a reduction of the bond strength between steel and concrete. The bond strength could be reduced by repeating load cycles or by corrosion of the reinforcing bar.

A numerical relation between the amount of damage in a reinforcing bar and changes in the deflections of the RC beam was derived from the results of the FE calculations. This relation is used in a sensitivity analysis. In this sensitivity analysis (Chapter 6), the probability that damage-induced changes in the deflections of a RC beam can be obtained from measurements of the deflections or the natural frequencies of a RC beam is determined.

Chapter 6

Sensitivity of Deflections and Natural Frequencies to Local Damage

Damage in a Reinforced Concrete (RC) bridge can result in changes in the deflections and in the natural frequencies of the bridge. Dynamic tests on RC beams showed that local damage in the reinforcing bar of the beam increases the deflections and decreases the natural frequencies of the beam in the last few thousand load cycles before fatigue failure occurred. These tests also showed that fluctuations in the ambient temperature and in the ambient humidity influence the deflections and the natural frequencies of the RC beam during the total service-life of the beam. As result of the effect of fluctuations in the ambient temperature on the deflections and on the natural frequencies of the RC beam, damage-induced changes in the deflections and in the natural frequencies of the beam are difficult to obtain. In Monte Carlo simulations, damage-induced changes in the deflections of the RC beam were compared with the effect of changes in the ambient temperature on the deflections of the beam. The probability that a measured change in the deflections of the RC beam was initiated by local damage in a reinforcing bar of the RC beam was calculated with Monte Carlo simulations. Similar Monte Carlo simulations were performed to calculate the probability that a measured change in the first natural frequency of the RC beam was initiated by local damage in the reinforcing bar of the RC beam.

6.1 General introduction sensitivity analysis

The deflections and the natural frequencies of concrete structures are not constant in time. Tests (Chapter 4) showed that fatigue damage in a reinforcing bar of a RC beam increases the deflections of the RC beam during the last few thousand load cycles before failure. Since the deflections and the natural frequencies of the RC beam depend on the bending stiffness of the beam, is was assumed that fatigue damage in a reinforcing bar of a RC beam also changes the natural frequencies of the beam during the last few thousand load cycles (Section 4.6).

Tests showed changes in the deflections of the RC beam in the first 99% of the load cycles (Section 4.5). These changes can have different causes like fluctuations in the ambient temperature, fluctuations in the ambient humidity, changes in the loading conditions, creep, and shrinkage.

The tests were conducted under climate controlled conditions. Therefore, changes in the ambient temperature were limited (T = 20 ±2°C) during the tests. In the Dutch climate, changes in the ambient temperature are much larger. When the tests were not conducted under climate controlled conditions but in the Dutch climate (exposed to larger fluctuations in temperature and humidity, but also to wind, snow, and sunlight radiation), the effect of changes in the ambient temperature on the deflections is far larger. It is possible that, under these climate conditions, the effect of changes in the ambient temperature on the deflections of the RC beam is in the same order of magnitude as damage-induced changes in the deflections of the RC beam. In this chapter, the effect of damage in the reinforcing bar on the deflections of the beam is compared with the effect of changes in the ambient temperature on the deflections of the RC beam. This comparison shows whether damage-induced changes in the deflections of the RC beam can be obtained from measurements of the deflections.

Monitoring data of a real bridge showed that fluctuations in the ambient temperature also change the natural frequencies of a Prestressed Concrete (PC) bridge. It was assumed that the natural frequencies of the RC beam change in the same manner under fluctuations in the ambient conditions. The effect of damage in the reinforcing bar on the first natural frequency of the beam is compared with the effect of changes in the ambient temperature on the first natural frequency of the RC beam as well.

The RC beam which was presented in Section 4.2 has been considered in the comparison between damage-induced changes in the deflections / natural frequencies and the effect of changes in the ambient temperature on the deflections / natural frequencies (sensitivity analysis). This beam had a length of 1500 mm, a width of 100 mm, and a height of 150 mm. The beam was reinforced with a single steel reinforcing bar with a diameter of 12 mm. The dynamic load on the RC beam was 2.0-12.0 kN. This load was the same as the load on most of the RC beams in the Beam Test.

The sensitivity analysis was performed by three Monte Carlo simulations using a calculation script in the Matlab software [134]. The first Monte Carlo simulation considered damage-induced changes in the deflections and in the first natural frequency of the RC beam (Section 6.2). In the second Monte Carlo simulation, the effect of changes in the ambient temperature on the deflections and on the first natural frequency of the RC beam was simulated (Section 6.3). The third Monte Carlo simulation considered the comparison between the results of the first and the second Monte Carlo simulation.

In the first Monte Carlo simulation, damage in the cross-section of the reinforcing bar was simulated as function of the number of load cycles, the stress amplitudes, and the presence/absence of corrosion damage. The increase of the deflections of the RC beam was calculated as function of the simulated damage. The relation between the amount of damage and the increase of the stress amplitude, and the relation between the amount of damage and the increase of the deflections of the RC beam were obtained by Finite Element (FE) calculations (Chapter 5). The maximum number of load cycles at which failure of the reinforcing bar was simulated was verified by the results of the Beam Test (Chapter 4).

In the second Monte Carlo simulation, the effect of fluctuations in the ambient temperature on the deflections and on the first natural frequency of the RC beam was simulated. For the relation between changes in the ambient temperature and changes in the deflections of the RC beam, measurements of the Beam Test were used (Chapter 4). For the relation between changes in the ambient temperature and changes in the natural frequencies, Structural Health Monitoring (SHM) data of the Hollandse Brug were used (Chapter 3). Figure 6-1 shows the relations between the tests, the FE models, and the probabilistic models for deflections of a RC beam. A similar figure can be drawn for the relations between SHM data, the FE models, and the probabilistic models for the natural frequencies of a RC beam.

In the third Monte Carlo simulation, the probability that a measured change in the deflections or in the natural frequencies of the RC beam was caused by local damage in the reinforcing bar of the beam was calculated.

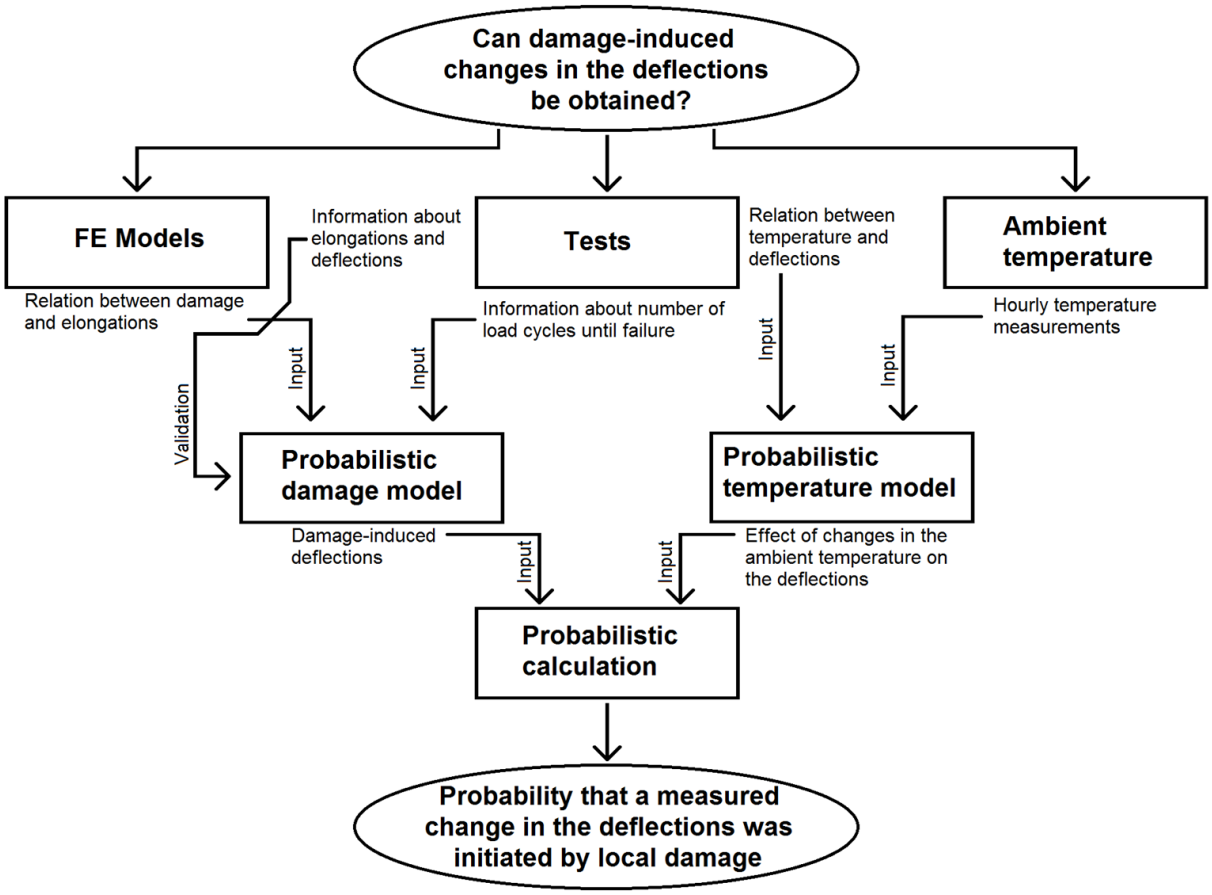

Figure 6-1: Relation between tests, FE models, and Probabilistic models for the deflections of the RC beam.

6.2 Mont Carlo simulation for fatigue damage in a Reinforcing bar in a Reinforced Concrete beam.

In the first Monte Carlo simulation, fatigue damage and corrosion damage in the reinforcing bar of the RC beam were simulated. Since FE calculations (Section 5.2.2) showed that it hardly matters whether damage started in the core or at the surface of the bar, fatigue damage and corrosion damage were simulated in a similar way in the Monte Carlo simulation.

The cross-section of the reinforcing bar was divided in a large number of elements (Section 6.2.1). Variations in the steel tensile strength were simulated by assigning different (strength) properties to individual elements in the cross-section. The strength varied in such a way that the cross-section of the reinforcing bar was divided in strong sections and in weak sections (Section 6.2.1). Corrosion damage was simulated by reducing the steel tensile strength of the elements which are suffering from corrosion (Section 6.2.3).

An alternating load with a constant load amplitude was simulated in the Monte Carlo simulation. In a sound reinforcing bar the stress amplitude and the amount of damage per

load cycle was the same in each element. When the element with the lowest tensile strength failed ($N > N_{max}$), this element could not contribute to the load bearing capacity of the bar anymore. When this occurred, the stress amplitude and the amount of damage per load cycle in the remaining elements increased (Section 6.2.2). Fatigue failure of the total reinforcing bar was reached when failure had occurred in each element. Figure 6-2 shows a flowchart for the Monte Carlo simulation.

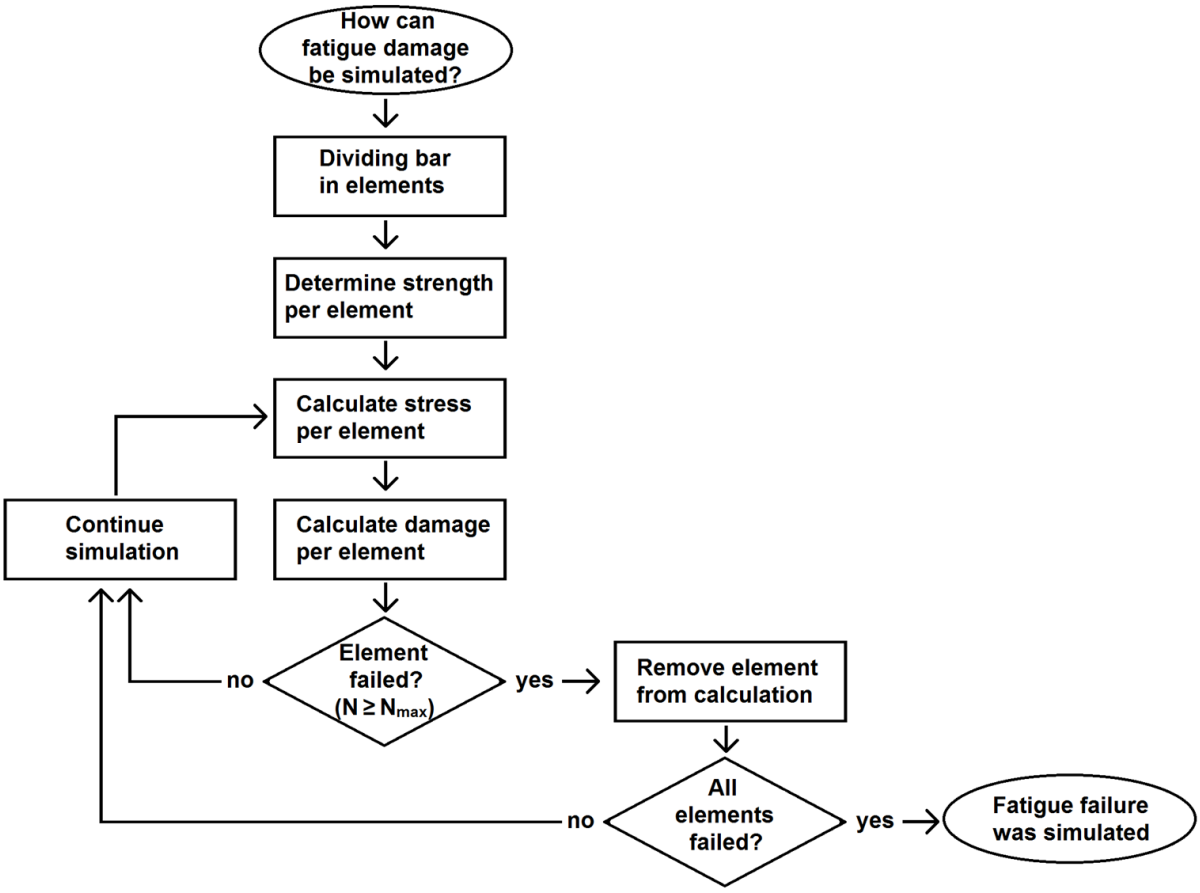

Figure 6-2: Flowchart for the Monte Carlo simulation.

6.2.1 Strength of the elements in the cross-section of the bar

In the Monte Carlo simulation the reinforcing bar was divided in 34*34 (=1156) elements. These elements were considered as sections of a circle (Figure 6-4-B). The dimensions of the elements were chosen in such a way that each element had the same surface area of approximately 0.098 mm^2 and all elements together simulated the total cross-section of the bar (113 mm^2). By assigning different tensile strengths to the different elements (presented below), progressive failure of different elements can be simulated at different numbers of load cycles.

A static tensile tests (Section 4.2.2) showed that the average yield stress in the steel bar was approximately 600 N/mm^2. To determine the steel tensile strength of the different elements in the Monte Carlo simulation, the cumulative density function of a normal

distribution (Equation (6-1)) [135] with a mean value of μ=600 N/mm^2 was used. The standard deviation in this cumulative density function was estimated to 30 N/mm^2.

$$f(x,\mu,\sigma)=\frac{1}{2}\left(1+erf\left(\frac{x-\mu}{\sigma\sqrt{2\pi}}\right)\right) \qquad (6\text{-}1)$$

where:

x = random value;

μ = mean value (μ=600 N/mm^2);

σ = standard deviation (σ=30 N/mm^2).

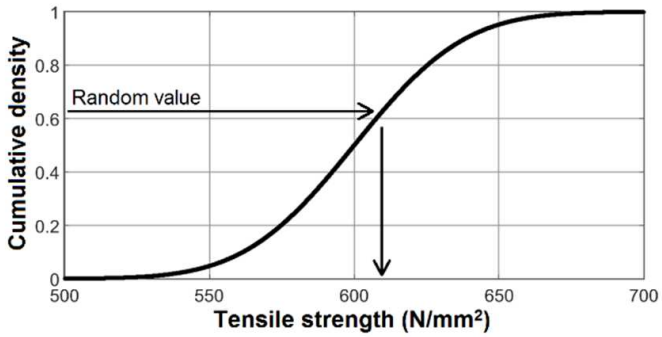

Figure 6-3: Cumulative density function of the tensile strength of steel and determination of the tensile strength per element (normal distribution with μ=600 N/mm^2, σ=30 N/mm^2).

A random value on the vertical axis of the cumulative density curve (Figure 6-3) was taken to determine the tensile strength of each of the elements separately. To avoid large differences in the tensile strength between two adjacent elements, the maximum difference between the chosen values of two adjacent elements was 0.1. This was realized by taking another random value on the vertical axis of the cumulative density function when the taken value of an element differs more than 0.1 with the taken value(s) of the adjacent element(s). An example of the variation in the tensile strength over the cross-section of the steel bar is given in Figure 6-4. Figure 6-4-A shows the strength over the cross-section of the bar in a 3D view. Figure 6-4-B shows a top view of the cross-section. In this figure, the values of the strength are presented at the coordinates of the elements.

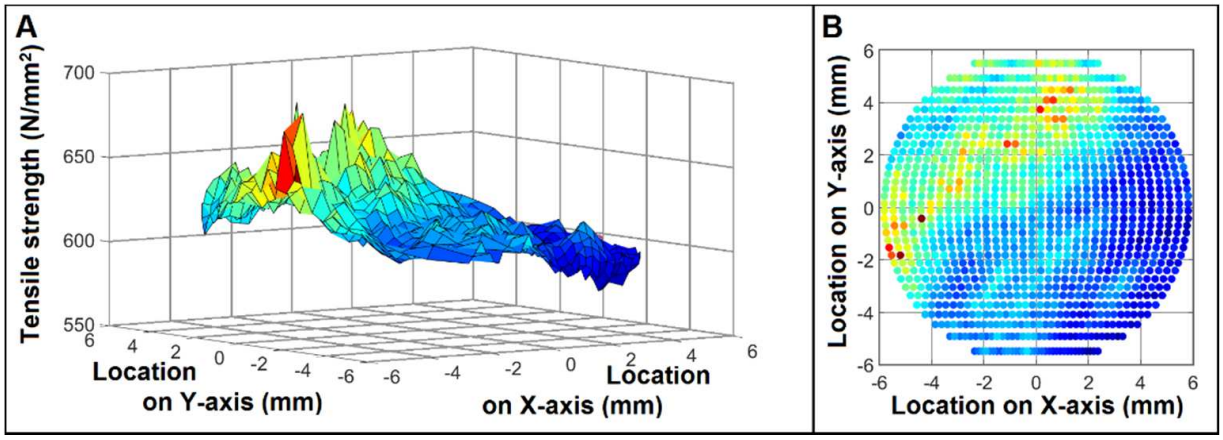

Figure 6-4: Example of the tensile strength of the cross-section of the plain steel bar. Figure 6-4-A shows the strength in a 3D view. Figure 6-4-B shows a top view of the cross-section. In this top view, the values of the strength are presented at the coordinates of the elements.

6.2.2 Fatigue damage

The maximum number of load cycles a structure can accommodate until failure depends on the strength of the structure and on the stress amplitude. Since the strength of the different elements in the Monte Carlo simulation was taken randomly, the maximum number of load cycles until failure differs from element to element. The relation between a constant stress amplitude and the maximum number of load cycles, used in this simulation, is presented in Figure 6-5 (Wöhler curve) and in Equation (6-2).

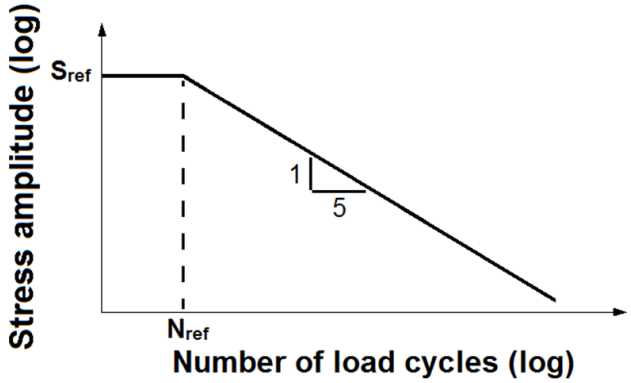

Figure 6-5: The Wöhler curve which was used to simulate fatigue damage in the different elements.

$$N_{max,i,j} = N_{ref}\left(\frac{S_{ref}}{S_{i,j}}\right)^5 \qquad (6\text{-}2)$$

where:

$N_{max,i,j}$ = maximum number of load cycles for element i,j;

N_{ref} = reference number of load cycles (1800);

$S_{i,j}$ = stress amplitude for element i,j (in N/mm^2, value depends on damage);

S_{ref} = reference stress amplitude (in N/mm^2, value depends on material properties).

Simulating damage in the reinforcing bar of the RC beam

Two different load amplitudes were used in the Beam Test: two sets of beam were loaded between 1.7 and 17.0 kN, and ten sets of beams were loaded between 2.0 and 12.0 kN. Only one of the RC beams loaded between 1.7 and 17.0 kN were dynamically loaded until fatigue failure whereby the reinforcing bar failed. In this beam, the reinforcing bar was partially corroded (Section 4.6.1), which reduced the maximum number of load cycles until failure of the RC beam (Section 4.6.4). Therefore, the test results of the RC beams could not be used to obtain the relation between the stress amplitude and the maximum number of load cycles.

For the exponent of the term in brackets in Equation (6-2) the value 5 is often used in the literature [80]. Since the value of the exponent could not be derived from the test results, this value was used in the Monte Carlo simulations.

The steel tensile strength (Section 6.2.1) was used for the value of the reference stress (S_{ref}) in Equation (6-2). By using the tensile strength as reference stress, the amount of damage per load cycle is different from element to element. The element with the lowest tensile strength had the highest amount of damage per load cycle. This element fails at the lowest number of load cycles.

The value of the reference number of load cycles (N_{ref}) was validated with the results of the Beam Test (Section 4.6.4). The results of preliminary Monte Carlo simulations with different values of N_{ref} showed that the predicted number of load cycles until failure of the reinforcing bar corresponds best with the maximum number of load cycles until flexural failure of the RC beams in the Beam Test by a reference number of load cycles of N_{ref} = 1800. This value was used for all Monte Carlo simulations whereby damage in the reinforcing bar was simulated.

It was assumed that the amount of damage is linear related to the number of load cycles. With this assumption, Equation (6-3) was used in the Monte Carlo simulation to simulate the amount of damage in the bar as function of the number of load cycles.

$$Dam_{N,i,j} = \frac{N_{applied}}{N_{max,i,j}} \qquad (6\text{-}3)$$

where:

$Dam_{N,i,j}$ = damage per N-cycles in element i,j;

$N_{applied}$ = applied number of load cycles;

$N_{max,i,j}$ = maximum number of load cycles for element i,j (Equation (6-2)).

Fatigue damage was simulated in the Monte Carlo simulation every 1000 load cycles. When the amount of damage in the element with the lowest tensile strength is equal to 1 ($Dam_{N,i,j}$ = 1), this element failed. After failure of an element, the element could not withstand the applied stresses anymore and the element was removed from the simulation. As result of removing an element from the simulation, the stresses in the

adjacent elements increased. Since the maximum number of load cycles is lower at a higher stress amplitude, the amount of damage per load cycle increased in the adjacent elements. The total amount of damage in an element loaded with different stress amplitudes was calculated with Equation (6-4). For this equation, it was assumed that damage accumulates in a linear manner (the Palmgren-Miner damage model). Failure of an element loaded with different stress amplitudes was simulated when the total amount of damage of an element is equal to 1 ($Dam_{N,i,j,tot} = 1$).

$$Dam_{N,i,j,tot} = \sum_{p=1}^{q} \frac{N_{applied,p}}{N_{max,i,j,p}} \qquad (6\text{-}4)$$

where:

$Dam_{N,i,j,tot}$ = total damage per N-cycles in element i,j;

p = number of different stress amplitudes;

$N_{applied,p}$ = applied number of load cycles per stress amplitude;

$N_{max,i,j,p}$ = maximum number of load cycles for element i,j per stress amplitude.

Relation between the amount of damage and the increase of the stresses in the reinforcing bar of the RC beam

Changes in the stresses in a plain steel bar were calculated in Section 5.2.2. Changes in the stresses in the reinforcing bar were not obtained from the FE calculation of the RC beam (Section 5.3). It was assumed that changes in the stresses in the reinforcing bar of the RC beam were similar to changes in the stresses in the plain steel bar. The effect of damage in the plain steel bar on the stresses in the plain steel bar was used to indicate the effect of damage in the reinforcing of a RC beam bar on the stresses in this bar. Table 5-3 showed the average stresses per area of the cross-section of the bar for different areas. The stresses as presented in that table divided by initial stress were used in the Monte Carlo simulation. The stress ratio as function to the initial stress is given in Table 6-1.

Table 6-1: Stress ratio as function of the amount of damage. The ratios in this table are the stresses in Table 5-3 divided by the initial stress (325 N/mm²). The position of the areas were given in Figure 5-6. The damage levels were given in Figure 5-5.

	Area									
Damage level	1	2	3	4	5	6	7	8	9	10
0	1.00	1.00	1.00	1.00	1.00	1.00	1.00	1.00	1.00	1.00
1	-	1.08	1.04	1.02	1.01	1.01	1.01	1.00	1.00	1.00
2	-	-	1.22	1.10	1.06	1.03	1.02	1.02	1.01	1.00
3	-	-	-	1.33	1.18	1.11	1.07	1.04	1.03	1.02
4	-	-	-	-	1.46	1.27	1.17	1.11	1.07	1.04
5	-	-	-	-	-	1.59	1.36	1.23	1.15	1.10
6	-	-	-	-	-	-	1.71	1.46	1.30	1.20
7	-	-	-	-	-	-	-	1.81	1.58	1.40
8	-	-	-	-	-	-	-	-	1.85	1.74
9	-	-	-	-	-	-	-	-	-	1.85

The sizes and the number of elements in the FE calculations (Section 5.2) were not the same as those used in the Monte Carlo simulation. A transition of the results of the FE calculations was required to use the numerical relation between the amount of damage and the stresses in the bar in the Monte Carlo simulation. An equation (Equation (6-5)) was derived (below) to establish an analytical relation between the amount of damage and the stresses in the remaining part of the cross-section of the bar. The only purpose of this equation is to be able to use the results of the FE calculations (Table 6-1) in the Monte Carlo simulations. Since the new stresses are a function of the initial stresses, Equation (6-5) could be used for different initial stresses.

$$\sigma_N = \sigma_0 \left(\frac{A_0}{A_0 - \Delta A} + \sqrt{\frac{\Delta A}{A_0}} \right) \qquad (6\text{-}5)$$

where:

σ_N = new stress (limited to the yield stress per element);
σ_o = initial stress (depends on location, Section 6.2.4);
A_o = undamaged area (113 mm^2, 1156 elements);
ΔA = damaged area.

Equation (6-5) was divided in two terms. The first term concerns the increase of the average stresses in the elements as result of a reduction of the cross-section of the bar. Since it was assumed that only the stresses in the adjacent elements increase, the stresses in these elements increase more than the average value. The second term in Equation (6-5) covers this effect. The summation of both terms was considered as total stress ratio around a failed section of the bar. The stresses in the elements cannot exceed the steel tensile strength of the elements. Therefore, the stresses were limited to the strength of the element (Section 6.2.1). The results of Equation (6-5) with σ_o = 325 N/mm^2 and a yield stress of 600 N/mm^2. were verified with the results of the FE calculations (Table 5-3). The coefficient of determination between the results of the FE model and the results of Equation (6-5) is R^2=0.99. Figure 6-6 shows the steel stresses as function of the relative damage for both methods.

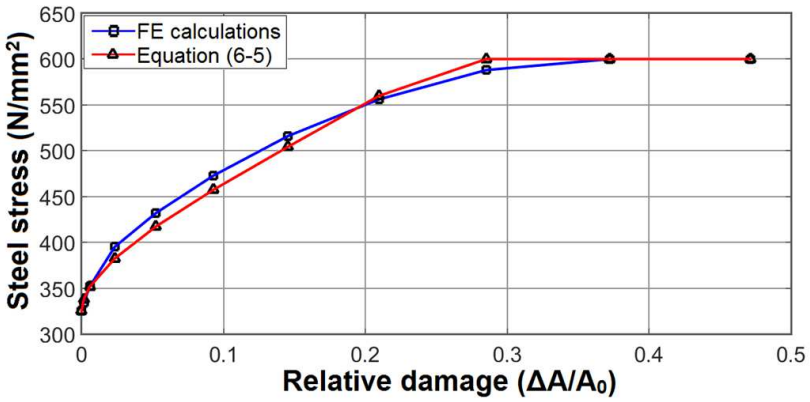

Figure 6-6: Steel stresses as function of the relative damage. The blue curve corresponds to results of the FE calculation. The red curve corresponds to the results of Equation (6-5). A strength of 600 N/mm^2 was used for the curves in this figure.

6.2.3 Corrosion damage

In 12 of the 24 RC beams which were tested in the Beam Test (Section 4.2.3), corrosion in the reinforcing bar was generated by exposing the RC beam to a chloride solution. This corrosion started at the surface of the reinforcing bar and extended to the core of the bar. In the Monte Carlo simulations, corrosion in the reinforcing bar was simulated by reducing the strength of the outer elements. To determine the steel tensile strength of the outer elements under corroded conditions, the mean value of the steel stresses calculated with Equation (6-1) was reduced from μ=600 N/mm^2 to 530 N/mm^2. The standard deviation of the steel stresses this equation was unchanged (σ=30 N/mm^2). The results of preliminary Monte Carlo simulations showed that this reduction of the average steel stresses corresponds best with the maximum number of load cycles until flexural failure of the RC beams with a corroded reinforcing bar in the Beam Test.

6.2.4 Maximum number of load cycles until failure

The stress amplitude is an important parameter to calculate the maximum number of load cycles until failure in an element. Table 5-5 (Section 5.3.2) showed that the stresses in the reinforcing bar at the locations of cracks C, D, E, F, and G in the RC beam were larger than the stresses in the reinforcing bar at the locations of cracks A, B, H, and I. Therefore, for the Monte Carlo simulation it was assumed that failure only occurs at the locations of crack C, D, E, F, and G. The stresses in the reinforcing bar at these locations for a load of 2.0 kN and a load of 12.0 kN are given in in Table 6-2. The stresses in the reinforcing bar as result of a load with an amplitude between 2.0 and 12.0 kN are given in Table 6-2 as well.

Table 6-2: Stresses in different cracks and the stress amplitudes at these cracks. These stresses are derived from FE calculations (5.3.2). The stresses are expressed in N/mm^2.

	Crack C	Crack D	Crack E	Crack F	Crack G
Load = 2.0 kN	26	26	26	26	26
Load = 12.0 kN	153	154	155	154	153
Amplitude (between 2.0 and 12.0 kN)	127	128	129	128	127

Two versions of a Monte Carlo simulation were developed in which damage in the reinforcing bar was simulated. In the first version of the Monte Carlo simulation, only fatigue damage in the reinforcing bar was simulated. In the second version of the Monte Carlo simulation, corrosion damage in the reinforcing bar was simulated as well.

In both versions of the Monte Carlo simulation, 1000 damage situations were simulated. In each damage situation, stresses in the reinforcing bar, damage in the reinforcing bar, and the deflections of the RC beam were calculated. The mean values and the standard deviations of the maximum number of load cycles were calculated using Equation (6-6) and (6-7).

$$\mu = \frac{1}{w}\sum_{v=1}^{w} N_{max,v} \qquad (6\text{-}6)$$

$$\sigma = \sqrt{\frac{1}{w-1}\sum_{v=1}^{w}\left(N_{max,v} - \mu\right)^2} \qquad (6\text{-}7)$$

where:

μ = mean value;

σ = standard deviation;

w = number of values;

$N_{max,v}$ = maximum number of load cycles in a simulation.

The results of both versions of the Monte Carlo simulation are presented in Table 6-3, expressed in average values and standard deviations. The results of the Beam Test (Test 4B and Test 4C, Section 4.6.4) are presented in Table 6-3 as well. The average values of the maximum number of load cycles of the Monte Carlo simulations match well with the average values of the maximum number of load cycles of the Beam Test. In the Monte Carlo simulations, the standard deviation of the maximum number of load cycles is lower than the standard deviation of the maximum number of load cycles obtained in the Beam Test. This difference can have different causes. Two possible causes for this difference are: 1, the number of simulations in the Monte Carlo simulation is far larger than the number of conducted tests, and 2, variations in the concrete quality, fluctuations in the loading condition and fluctuations in the ambient humidity were not considered in the Monte Carlo simulations.

Table 6-3: Maximum number of load cycles until failure of the RC beam obtained from the Beam Test and calculated with the Monte Carlo simulations.

	Average (μ)		Standard deviation(σ)	
Condition	**Monte Carlo**	**Tests**	**Monte Carlo**	**Tests**
Corroded	1,713,840	1,683,850	145,394	386,991
Uncorroded	2,867,275	2,854,372	230,913	347,862

6.2.5 Damage-induced changes in the deflections of a Reinforced Concrete beam

In the Monte Carlo simulation, fatigue damage and corrosion damage were simulated in the reinforcing bar of the RC beam. It was assumed that damage in the reinforcing bar increased the stresses in the bar and the elongations of the bar. Changes in the stresses in the bar were discussed in Section 6.2.2. Changes in the elongations of the bar are presented below. It was assumed that changes in the deflections of the RC beam were the result of changes in the elongations of the bar.

Elongation of a plain steel bar

Since the sizes and the number of elements in the FE calculations were not the same as those used in the Monte Carlo simulation (Section 6.2.2), a transition of the results of the

FE calculations (Section 5.2.2) was required to use the results of the FE calculation in the Monte Carlo simulation. This transition was done using Equation (6-8).

$$\delta_{el} = \left(\sigma_0 C_{el,1} \frac{\Delta A}{A_0} \right)^1 + \left(\sigma_0 C_{el,2} \frac{\Delta A}{A_0} \right)^8 \quad (6\text{-}8)$$

where:

δ_{el} = increase of the elongation (in mm);
σ_o = initial stress (N/mm^2);
$C_{el,1}$ = elongation factor (6.4*10^{-5} mm^3/N);
$C_{el,2}$ = elongation factor (4.8*10^{-3} $\sqrt[8]{mm^3/N}$);
A_o = initial area; $\sqrt[8]{(mm^3/N)}$
ΔA = damaged area.

Equation (6-8) is divided in two terms. The first term concerns a linear relation between the amount of damage in the bar, the stresses in the bar, and the increase of the elongations of the bar. When the stresses in the bar (locally) exceed the yield stress (600 N/mm^2 in the FE calculations, Section 5.2.1), the elongations of the bar can be far larger than in a linear situation. The second term in Equation (6-8) simulates (partial) yielding of the bar. The elongation factor of both terms were such chosen that the results of Equation (6-8) matched well with the calculated elongations of the plain steel bar (Section 5.2.2). The coefficient of determination between the results of the FE model and the results of Equation (6-8) is R^2=0.97. Since it was assumed that the effect of damage in the plain steel bar on the elongations of the bar was similar to the effect of damage in the reinforcing bar on the elongations of the bar, Equation (6-8) was also be used to calculate the elongations of the reinforcing bar in the RC beam as function of the amount of damage in this bar.

<u>Relation between the deflection of a Reinforced Concrete beam and the elongations of the reinforcing bar</u>

The theory of plasticity [136] was used to schematize plastic hinges in the RC beam at the locations of the cracks (damaged sections). These hinges were used to simulate the relation between changes in the elongations of the reinforcing bar and changes in the deflections of the RC beam.

Figure 6-7 shows an illustration of a hinge. In this illustration, the relation between changes in the elongations of the bar and changes in the rotation of the hinge was presented. The effect of changes in the elongations of the reinforcing bar on the rotation of the hinge depends on the location of the bar in the RC beam and the depth of the crack. The concrete cover on the reinforcing bar was 30 mm (constant in all tested bars). The depth of the crack was estimated at 75 mm (half of the height of the RC beam). The factor between the increase of the elongations of the bar and the rotation of the hinge was calculated using Equation (6-9). This factor was constant in all simulations.

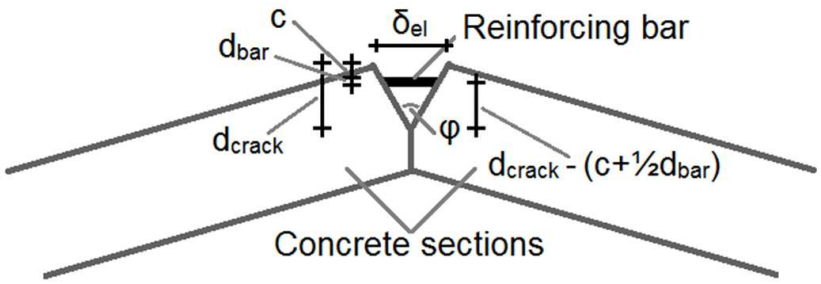

Figure 6-7: Illustration of a hinge in the RC beam. This illustration shows the relation between the elongation of the bar and the rotation of the hinge. This relation is expressed in Equation (6-9)

$$C_{def,1} = \frac{\varphi}{\delta_{el}} = \frac{1}{d_{crack} - (c + \frac{1}{2} d_{bar})} \quad (6\text{-}9)$$

where:

$C_{def,1}$ = factor between the increase of the elongations of the bar and the rotation of the hinge (1/mm);

φ = rotation of the hinge (rad);

δ_{el} = increase of the elongation of the bar (mm);

d_{crack} = depth of the crack (mm);

c = concrete cover (30 mm)

d_{bar} = diameter of the bar (12 mm).

The effect of the rotation of the hinge on the deflection of the RC beam depends on the location of the hinge in the length of the beam (location of the cracks C, D, E, F, and G). The relation between the rotation of the hinge and the deflection of the beam is illustrated in Figure 6-8. In this figure, the value L_{end} depends on the setup of the test and was constant for all beams (475 mm, Section 4.2.1). The values a and b depend on the location of the hinges (locations of the cracks). These values are given in Table 6-4. The factor between the rotation of the hinge and the location of the hinge was calculated using Equation (6-10). Since the locations of the cracks did not change, the values of factor $C_{def,2,r}$ were constant in all simulations.

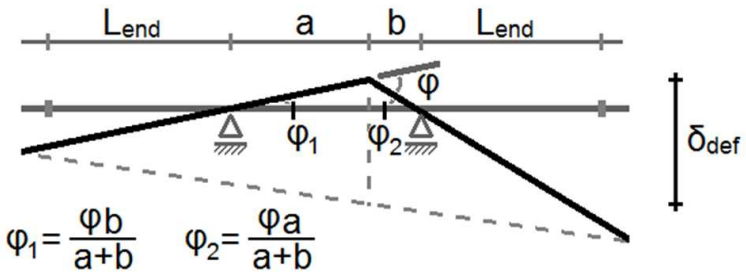

Figure 6-8: Relation between φ (rotation of the hinge) and δ_{def} (deflection of the RC beam).

$$C_{def,2,r} = \frac{\delta_{def}}{\varphi} = \frac{\frac{1}{2}(\varphi_1 L_{end} + \varphi_2 L_{end}) + \varphi_1 a_r}{\varphi} = \frac{1}{2} L_{end} + \frac{a_r b_r}{a_r + b_r} \quad (6\text{-}10)$$

where:

$C_{def,2,r}$ = factor between the rotation of the hinge at location 'r' and the increase of the deflection of the RC beam (mm);

δ_{def} = increase of the deflections of the RC beam (mm);

φ = rotation of the hinge (rad);

L_{end} = distance between the load and the support (475 mm);

a_r = distance between location of hinge at location 'r' and the support (mm);

b_r = distance between location of hinge at location 'r' and the support (mm).

Table 6-4: Vales 'a_r', 'b_r', and '$C_{def,2,r}$' for different positions along the length of the RC beam. The values are expressed in mm.

	Crack C	Crack D	Crack E	Crack F	Crack G
Value a_r	25	125	225	325	425
Value b_r	425	325	225	125	25
Value $C_{def,2,r}$	261	328	350	328	261

The effect of the damage in the reinforcing bar on the deflections of the RC beam is a combination of the effect of changes in the elongations of the reinforcing bar on the rotation of the hinge, and the effect of the rotation of the hinge on the deflection of the RC beam. The relation between the elongations of the reinforcing bar and the deflections of the RC beam is expressed in Equation (6-11). The coefficient of determination between the results of the FE calculations (Section 5.3.3) and the results of Equation (6-11) is R^2=0.99.

$$\delta_{def} = \sum_{r=1}^{5} C_{def,1} C_{def,2,r} \delta_{el,r} \qquad (6\text{-}11)$$

where:

δ_{def} = increase of the deflection of the RC beam;

$C_{def,1}$ = factor between the increase of the elongations of the bar and the rotation of the hinge (Equation (6-9));

$C_{def,2,r}$ = factor between the rotation of the hinge at location 'r' and the increase of the deflection of the RC beam (Equation (6-10));

$\Delta_{el,r}$ = increase of the elongation of the bar per section (Equation (6-8)).

Results of the Monte Carlo simulations

In the Monte Carlo simulation, the effect of damage in the reinforcing bar on the deflections of the RC beam was calculated every 1000 load cycles (damage-induced changes in the deflections of the beam). Figure 6-9 shows the damage-induced changes in the deflections of the RC beam during the last 50,000 load cycles. Three curves are given in this figure: the 5% lower limit (green), the average values (blue curve), and the 95% upper limit (red curve). For all simulations, it was obtained that the damage-induced changes in the deflections of the RC beam before the last 50,000 load cycles were limited (<0.02 mm).

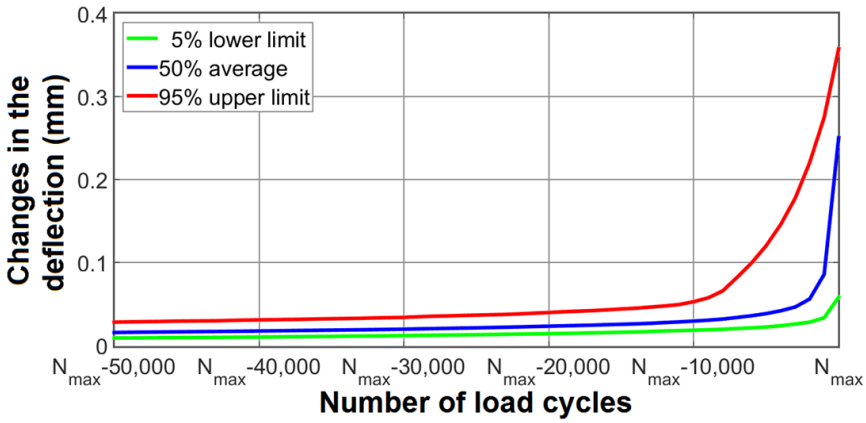

Figure 6-9: Damage-induced deflections of the RC beam during the last 50,000 load cycles. The green curve represents the 5% lower limit. The blue curve represents the average values. The red curve represents the 95% upper limit of the deflections.

Figure 6-9 shows that damage in the reinforcing bar of the RC beam resulted in an increase of the deflection of the RC beam during the last few thousand load cycles. The values of the 5% lower limit (green curve) and the average values (blue curve) show that the deflections increase rapidly during the last 2000 load cycles. This was also observed at the Beam Test (Section 4.6.4). The 95% upper limit (red curve) shows an increase of the deflections over a larger number of load cycles.

The last simulation (N_{max}) indicates that the RC beam fails within a limited number of load cycles (1-1000). The second last simulation (N_{max}-1000) indicates that the RC beam can resist 1000-2000 load cycles. When this simulations could be used to predict failure, there is still a little time to stop the simulation before the RC beam fails. Therefore, changes in the deflections of the RC beam at N_{max}-1000 were used in the comparison between damage-induced changes in the delectations of the RC beam and the effect of changes in the ambient temperature on the deflections of the beam (Section 6.4.1). The probability that a certain damaged-induced change in the deflection can occur at N_{max}-1000 is given in Figure 6-10. In this figure, changes in the deflections are plotted on the horizontal axis. The vertical axis shows the probability of the number of simulations in which the given damage-induced changes in the deflections was calculated. This figure shows that a change in the deflections of the RC beam smaller than 0.02 mm occurred in all simulations and a change in the deflections of the RC beam larger than 0.3 mm hardly occurred in the simulations.

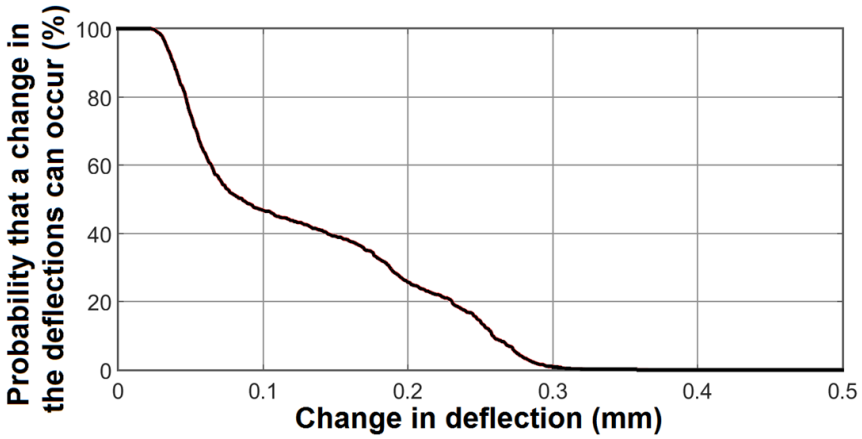

Figure 6-10: The probability that a certain damaged-induced change in the deflections of the RC beam can occur at N_{max}-1000.

6.2.6 Damage-induced changes in the first natural frequency

Damage-induced changes in the deflections of the RC beam were probably the effect of a reduction of the bending stiffness. A reduction of the bending stiffness results in an increase of the deflections, but also in a reduction of the natural frequencies of the beam. SHM systems installed on a concrete bridge often contain sensors to measure the vibrations of the bridge. Since the natural frequencies of a bridge can be calculated from vibration measurements, damage-induced changes in the natural frequencies of the RC beam are investigated as well.

In the Monte Carlo simulation, damage-induced changes in the bending stiffness of the RC beam were calculated by dividing the deflections of the RC beam with a damaged reinforcing bar by the deflections of the RC beam with an undamaged reinforcing bar. Since changes in the deflections of the RC beam are linearly related to changes in its bending stiffness and changes in bending stiffness are quadratic related to changes in the first natural frequency, the square root of the reduction of the bending stiffness was used to calculate damage-induced changes in the first natural frequency of the RC beam. The deflections and the first natural frequency of the beam with an undamaged reinforcing bar were calculated in the FE calculation (δ_o = 1.52 mm and $f_{1,o}$ = 87.1 Hz). Equation (6-12) was used to calculate damage-induced changes in the first natural frequency of the RC beam as function of damage-induced changes of the deflection of the beam.

$$f_1 = \sqrt{\frac{\delta_{def}}{\delta_o}} f_{1,o} \qquad (6\text{-}12)$$

where:

f_1 = first natural frequency (Hz);
δ_{def} = increase of the deflection of the RC beam (in mm);
δ_o = deflection of the undamaged RC beam (1.52 mm);
$f_{1,o}$ = first natural frequency of the undamaged RC beam (87.1 Hz).

Figure 6-11 shows damage-induced changes in the first natural frequency of the RC beam. In this figure, three curves are presented: a curve with the 5% lower limit (green), a curve with the average values (blue), and a curve with the 95% upper limit (red). The curves in Figure 6-11 show a similar behaviour to the curves in Figure 6-9. Similar to damage-induced changes in the deflections of the RC beam, damage-induced changes in the first natural frequency of the beam at N_{max}-1000 were used in the comparison between damage-induced changes in the first natural frequency of the RC beam and the effect of changes in the ambient temperature on the first natural frequency of the beam (Section 6.4.2).

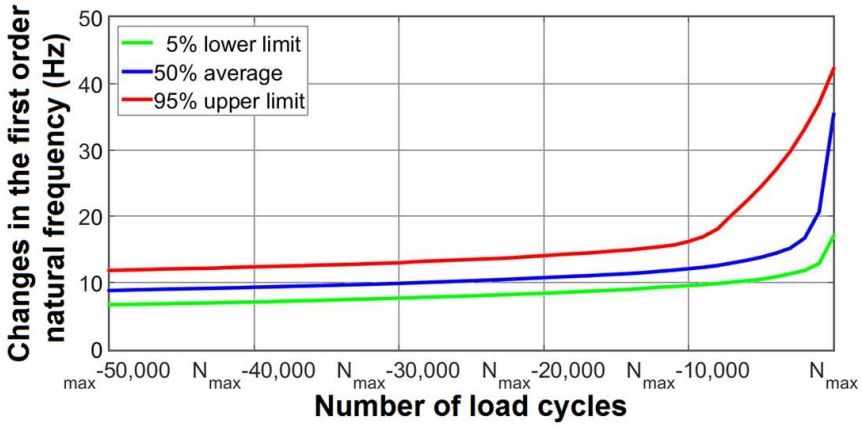

Figure 6-11: Damage-induced change of the first natural frequency. The green curve represents the 5% lower limit. The blue curve represents the average values. The red curve represents the 95% upper limit of the deflections.

The probability that a certain damaged-induced change in the first natural frequency of the RC beam can occur at N_{max}-1000 is given in Figure 6-12. In this figure, changes in the first natural frequency are plotted on the horizontal axis. The vertical axis shows the probability of the number of simulations in which the given damage-induced change in the first natural frequency was calculated. This figure shows that a change in the first natural frequency of the RC beam smaller than 10 Hz occurred in all simulations and a change in the first natural frequency of the RC beam larger than 40 Hz hardly occurred in the simulations.

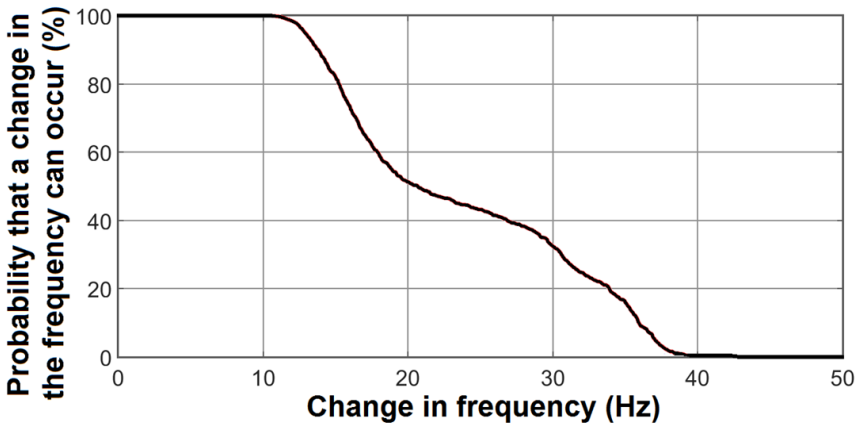

Figure 6-12: The probability that a certain damaged-induced change in the first natural frequency of the RC beam can occur at N_{max}-1000.

6.3 Monte Carlo simulation for fluctuations in the ambient temperature.

The deflections and the natural frequencies of the RC beam depend on the temperature of the beam. The temperature in the beam depends on the ambient temperature around the beam. Since the ambient temperature is more easy to measure than the temperature in a beam, the ambient temperature were used to calculate the effect of changes in the temperature on the deflections and on the natural frequencies of the RC beam.

The second Monte Carlo simulation simulated the effect of changes in the ambient temperature on the deflections and on the first natural frequency of a RC beam. For this simulation, changes in the ambient temperature in the Netherlands were used. This second Monte Carlo simulation is presented in this section.

6.3.1 Ambient temperatures

The second Monte Carlo simulate was used to simulate the effect of changes in the ambient temperature on the deflections and on the first natural frequency of the RC beam.

The KNMI (Royal Netherlands Meteorological Institute) [137] measures the ambient temperature in the Netherlands at several locations. The temperature measurements (per hour) in De Bilt between January 2011 and December 2015 were used in the Monte Carlo simulation. These measurements are given in Figure 6-13. In this figure, the seasons are clearly visible (lower temperatures in winter times and higher temperatures in summer times). As example of the temperature changes per day, the hourly temperatures on October 1st and October 2nd 2015 are presented in Figure 6-14. In this figure, day and night are clearly visible (lower temperatures at night-time and higher temperatures at day-time).

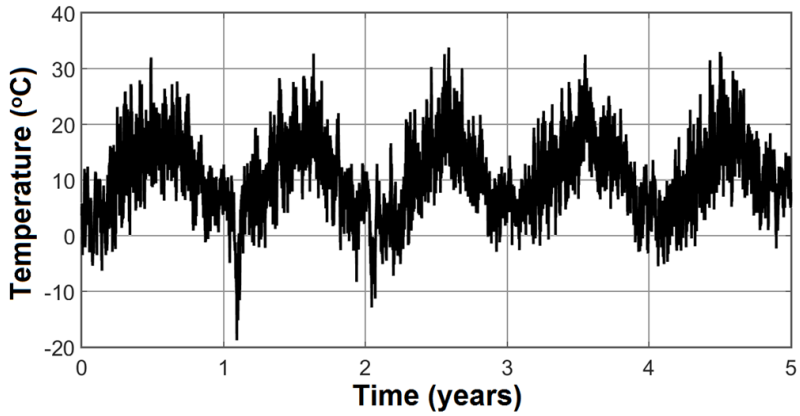

Figure 6-13: Ambient temperature in De Bilt (the Netherlands) between January 2011 (time = 0 year) and December 2015 (time = 5 years).

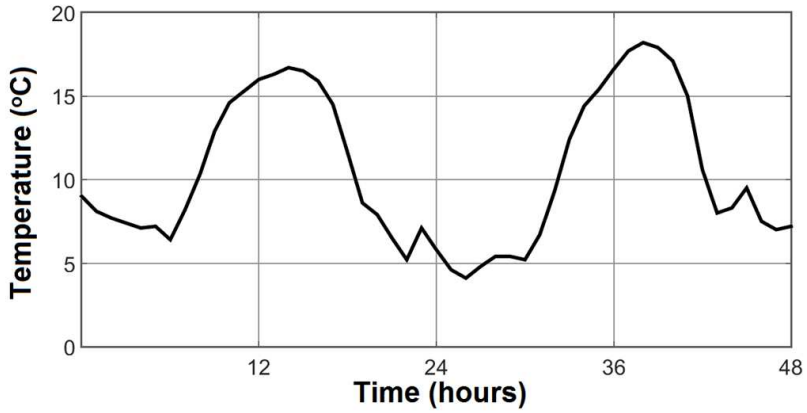

Figure 6-14: Ambient temperature in De Bilt (the Netherlands) per hour on October 1st and October 2nd 2015 (time 0 hour = midnight October 1st, time 48 hour = midnight October 3rd).

Period of time

Damage-induced changes in the deflections and in the natural frequencies of the RC beam, and the effect of changes in the ambient temperature on the deflection and on the first natural frequency of the RC beam are compared in a third Monte Carlo simulation (Section 6.4). For a good comparison, the period of time should be the same in both simulations.

In the first Monte Carlo simulation, damage was calculated every 1000 load cycles. According to Eurocode 1 [121], a bridge in a highway should be strong enough to resist 2 million heavy vehicles per year, which means that 1000 load cycles will probably occur in less than 24 hours. Since the number of heavy vehicles is larger at rush hour than during the night, the period of time per 1000 load cycles is not constant. Fluctuations in the period of time (between 1 and 24 hours) were taken into account in the Monte Carlo simulation.

Changes in ambient temperature

A moment on the timeline of Figure 6-13 was chosen randomly. A second moment was randomly chosen within the first 24 hours after this first moment. The difference in the

ambient temperature between both moments indicates a change in the ambient temperature in a time period between 1 and 24 hours. This difference was used to calculate the effect of changes in the ambient temperature on the deflections and on the first natural frequency of the RC beam (Section 6.3.2 and Section 6.3.3). A probability density histogram of changes in the ambient temperature is given in Figure 6-15.

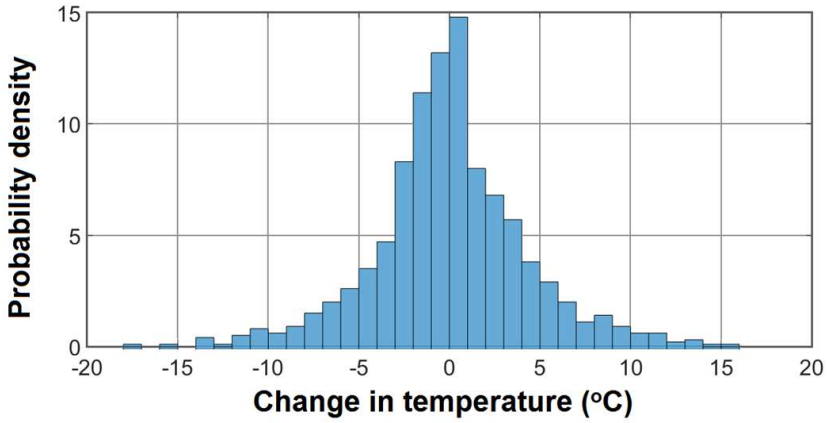

Figure 6-15: Probability density histogram of the changes in the ambient temperature.

6.3.2 Effect of changes in the ambient temperature on the deflections of the RC beam

A relation was found between the measurements of the ambient temperature and the measurements of the deflections of the RC beam (Section 4.5.1). The measured changes in the deflections of the beam is the combined effect of changes in the mean temperature and changes in the temperature differential. This relation was used in the Monte Carlo simulation.

Since the loading conditions of the Beam Test (2.0 – 12.0 kN) were also used in the Monte Carlo simulations, the effect of temperature-induced changes in the Young's modulus of concrete on changes in the deflections of the RC beam (loaded by a load of 7.0 kN) can be used in the Monte Carlo simulations as well.

When the RC beams were exposed to the Dutch climate, the fluctuations in the ambient temperature around the beams were higher and less predictable than the fluctuations in the ambient temperature of the room where the tests were conducted. The variation coefficient (which was 0.25 during the Beam Test) will increase as well. Therefore, a relation between changes in the ambient temperature and changes in the deflections of the RC beam could probably not be found when the RC beam were exposed to the Dutch climate. A comparison between damage-induced changes in the deflections of the RC beam and the effect of changes in the ambient temperature on the deflections of the beam should be made.

Equation (6-13) was used to calculate the effect of changes in the ambient temperature on the deflections of the RC beam. The value of factor $C_{\Delta T,def}$ (0.0051 mm/K) is equal to the

value of factor $C_{\Delta T,def,measured}$ (0.0058 mm/K, Equation (4-1)) minus the vertical expansion of the RC beam (0.0017 mm/K, Section 4.5.1). This value includes changes in the mean temperature and changes in the temperature differential.

$$\Delta\delta = C_{\Delta t,def}\,\Delta T_a \qquad (6\text{-}13)$$

where:

$C_{\Delta t,def}$ = factor (0.0051 mm/K);
$\Delta\delta$ = change in deflection;
ΔT_a = change in ambient temperature.

Figure 6-16 shows a probability density histogram of changes in the deflections of the RC beam as result of changes in the ambient temperature. The probability that a certain effect of changes in the ambient temperature on the deflections of the RC beam (loaded by a load of 7.0 kN) can occur is given in Figure 6-17. According to this figure, a change in the deflections of the RC beam larger than 0.09 mm as result of changes in the ambient temperature around the RC beam hardly occurs.

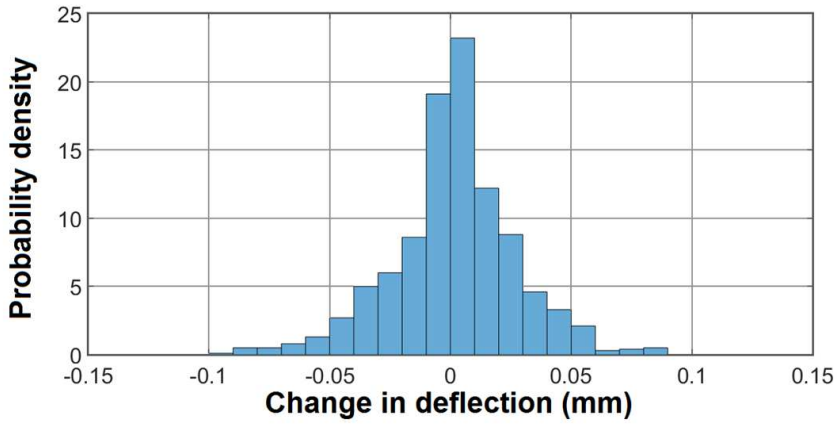

Figure 6-16: Probability density histogram of the effect of changes in the ambient temperature (shown in Figure 6-15) on the deflections of the RC beam (loaded with a load of 7.0 kN).

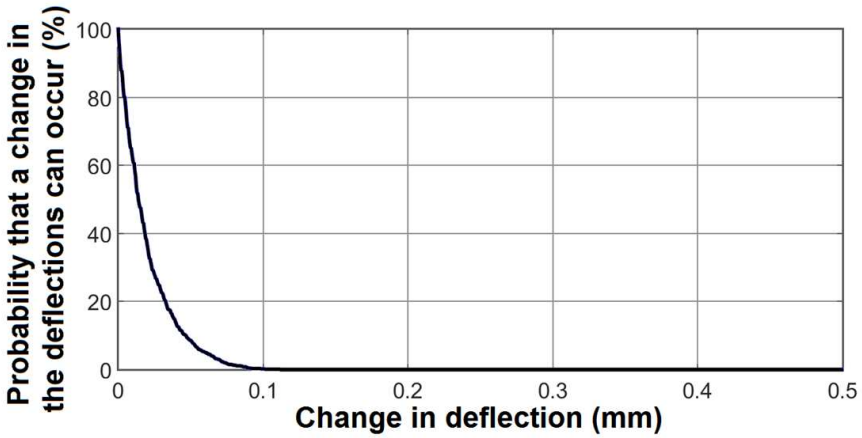

Figure 6-17: The probability that a certain effect of changes in the ambient temperature on the deflections of the RC beam (loaded by a load of 7.0 kN) can occur.

6.3.3 Effect of changes in the ambient temperature on the first natural frequency of the RC beam.

The natural frequencies of a structure can be obtained (direct method) using measurements of the vibrations of the structure (Section 3.3). The natural frequencies can also be derived (indirect) from the bending stiffness of the structure, which could be obtained from the deflections of the structure. Changes in the deflections of the RC beam were presented in Section 6.3.2. This section only contains information about the effect of changes in the ambient temperature on the natural frequencies of the RC beam using the direct method.

The vibrations of the RC beam were not measured during the Beam Test. Since the real bending stiffness of the beam could not be obtained from the measurements (Section 4.8), other sources for obtaining the effect of changes in the ambient temperature on the natural frequencies of the beam had to be found. SHM (vibration) data of a real concrete bridge were used to obtain the natural frequencies of a concrete bridge (Section 3.3). Information of these data were used in the Monte Carlo simulation to obtain the effect of changes in the ambient temperature on the first natural frequency of the RC beam.

It was discussed in Section 3.3 that the scatter (0.27 Hz/K) in the second order natural frequency (9.0 – 13 Hz) was larger than the scatter (0.12 Hz/K) in the first order natural frequency (2.1 – 6.2 Hz). The first natural frequency of the RC beam (87 Hz) is far larger than the obtained natural frequencies of the RC beam. Therefore, the scatter in the first natural frequency of probably larger as well. In the Monte Carlo simulation, it was assumed that the scatter in the first natural frequency of the RC beam was 1.8 Hz/K due to changes in the ambient temperature (Equation (6-14)).

$$\Delta_{nf} = C_{\Delta t,nf} \Delta T_a \qquad (6\text{-}14)$$

where:

$C_{\Delta t,nf}$ = factor (1.8 Hz/K);

Δ_{nf} = change in natural frequency;

ΔT_a = change in ambient temperature.

Figure 6-18 shows a probability density histogram of changes in the first natural frequency of the RC beam as result of changes in the ambient temperature. The probability that a certain effect of changes in the ambient temperature on the first natural frequency of the RC beam can occur is given in Figure 6-19. This figure shows that changes in the ambient temperature can result in changes in the first frequency of the RC beam up to 20 Hz (23% of the obtained frequency).

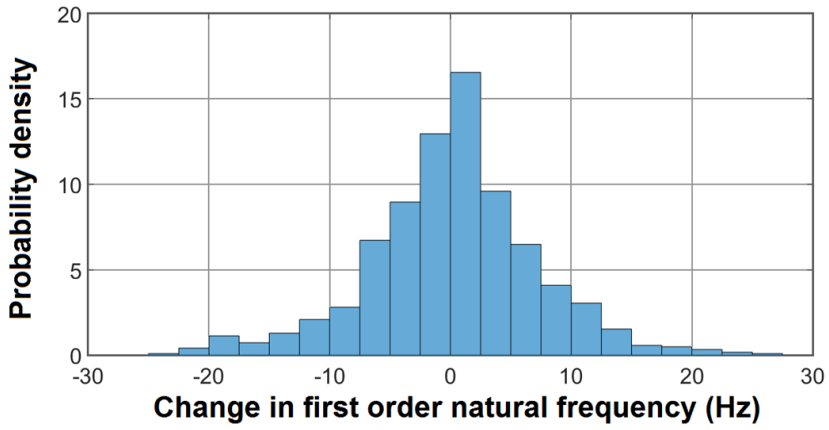

Figure 6-18: Probabilistic density histogram of the effect of changes in the ambient temperature (shown in Figure 6-15) on the first natural frequency of the RC beam.

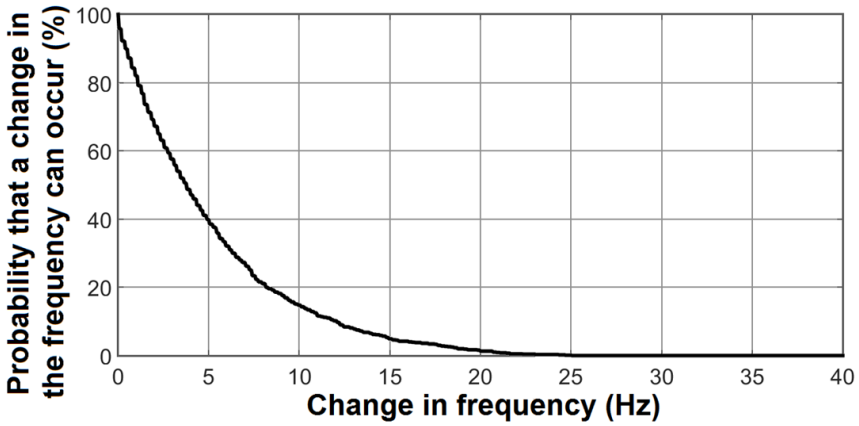

Figure 6-19: The probability that a certain effect of changes in the ambient temperature on the first natural frequency of the RC beam can occur.

6.4 Comparison between the probabilistic damage model and the probabilistic temperature model.

In the first Monte Carlo simulation, damage-induced changes in the deflections and in the first natural frequency of a RC beam were calculated. In the second Monte Carlo simulation the effect of changes in the ambient temperature on the deflections and on the first natural frequency of the RC beam was calculated. In the third Monte Carlo simulation (this section), the results of the first and the second Monte Carlo simulations are combined.

6.4.1 Changes in the deflections

Local damage in the reinforcing bar of the RC beam changes the deflections and the natural frequencies of the beam. Local damage could be initiated by fatigue and by corrosion. It was shown (Section 4.6) that localized corrosion reduced the number of load cycles until failure, but hardly influenced the damage-induced changes in the deflections of the RC beam. For the comparison between damage-induced changes in the deflections

of the RC beam and the effect of changes in the ambient temperature on the deflections of the beam, only fatigue damage was taken into account.

Damage-induced changes in the deflections of the RC beam were calculated in a Monte Carlo simulation (Section 6.2) per 1000 load cycles. The deflections of the RC beam at N_{max}-1000 were used in the comparison between damage-induced changes in the delectations of the RC beam and the effect of changes in the ambient temperature on the deflections of the beam. The probability that a certain damaged-induced change in the deflection of the RC beam can occur at N_{max}-1000 was given in Figure 6-10. The probability that a certain effect of changes in the ambient temperature on the deflections of the RC beam can occur was given in Figure 6-17. The probability that a certain change in the deflections of the RC beam as result of changes in the ambient temperature occurs is the same in each simulation.

In each simulation between N=1000 till N=N_{max}-2000, fluctuations in the ambient temperature can change the deflections of the RC beam, while the amount of damage-induced changes in the deflections of the beam is limited. Local damage in the reinforcing bar only results in damage-induced changes in the deflections of the RC beam during the last few thousand load cycles. When a RC beam fails at 2.8 million load cycles (average values of the RC beam with an uncorroded reinforcing bar, Table 6-3) and the deflections were measured every 1000 load cycles (as considered in the Monte Carlo simulations), 2800 simulations have taken place before damage-induced changes in the deflections of the RC beam could be obtained.

Within the first 2800 simulations, a large scatter in the effect of changes in the ambient temperature on the deflections of the RC beam can be observed. Due to this large scatter, small damage-induced changes in the deflections of the RC beam will probably not be recognized as the effect of damage but as the effect of changes in the ambient temperature. Only larger changes in the deflections of the RC beam will be recognized as damage-induced changes in the deflections of the RC beam.

When damage-induced changes in the deflection of the RC beam and the effect of changes in the ambient temperature on the deflections of the beam are compared, the probability that a certain change in the deflections of the RC beam was caused by damage in the reinforcing bar (Equation (6-15)) is far smaller than the probability that the same change in the deflections of the beam was caused by changes in the ambient temperature (Equation (6-16)). The sum of the values obtained with Equation (6-15) and Equation (6-16) is 1 (Probability =1).

$$P_{\Delta\delta\_\mathrm{ind}\_dam} = \frac{P_{\Delta\delta\_dam}}{P_{\Delta\delta\_dam} + C_{MC} P_{\Delta\delta\_temp}} \tag{6-15}$$

$$P_{def\_ind\_temp} = \frac{C_{MC} P_{def\_temp}}{P_{def\_dam} + C_{MC} P_{def\_temp}} \tag{6-16}$$

where:

$P_{\Delta\delta\_caused\_dam}$ = probability that a change in the deflection was caused by damage;

$P_{\Delta\delta\_caused\_temp}$ = probability that a change in the deflection was caused by changes in the ambient temperature;

$P_{\Delta\delta\_dam}$ = probability that a change in the deflection caused by damage in the reinforcing bar can occur;

$P_{\Delta\delta\_temp}$ = probability that a change in the deflections caused by changes in the ambient temperature can occur;

C_{MC} = number of simulations in the Monte Carlo simulation (2800).

The results of the Monte Carlo simulation are plotted in Figure 6-20. This figure shows the probability that a measured change in the deflection was initiated by damage (red curve) or by changes in the ambient temperature (blue curve). It can be observed from this figure that small changes in the deflections of the RC beam ($\Delta\delta < 0.09$ mm) are probably initiated by fluctuations in the ambient temperature. Larger changes in the deflections of the RC beam ($\Delta\delta \geq 0.09$ mm) are probably initiated by damage in the reinforcing bar.

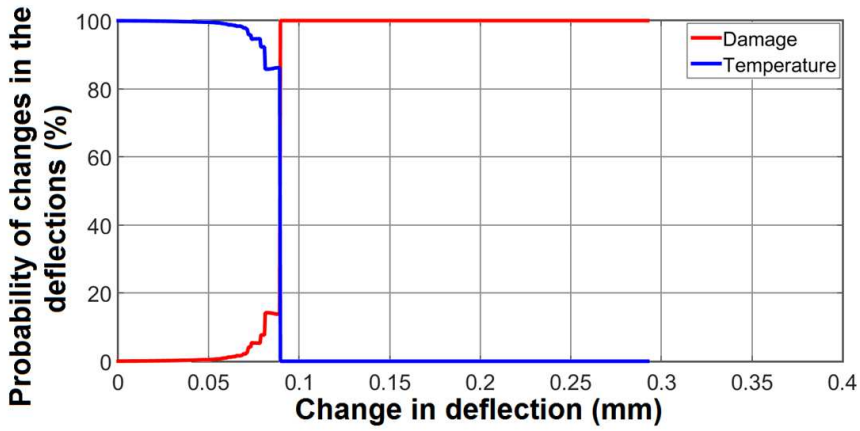

Figure 6-20: Probability that a simulated change in the deflections of the RC beam was caused by damage in the reinforcing bar (red curve) or by fluctuations in the ambient temperature (blue curve).

Damage-induced changes of the deflections of the RC beam larger than 0.09 mm/1000 load cycles occur only in 50% of the simulations (Figure 6-10). In the remaining 50% of the simulations, damage-induced changes in the deflections of the RC beam (at N_{max}-1000) were less than 0.09 mm/1000 load cycles. In these simulations, the RC beam has probably failed before such damage-induced change in the deflections of the RC beam could be obtained.

6.4.2 Changes in the first natural frequency

The probability that a certain change in the first natural frequency of the RC beam was caused by damage in the reinforcing bar was calculated in a similar way as the probability that a certain change in the deflections of the RC beam was caused by damage in the reinforcing bar. Equation (6-17) was used to calculate the probability that a certain change in the first natural frequency of the RC beam was caused by damage in the reinforcing bar

of the RC beam. The probability that a certain change in the first natural frequency of the RC beam was caused by changes in the ambient temperature was calculated with Equation (6-18).

$$P_{\Delta nf\_ind\_dam} = \frac{P_{\Delta nf\_dam}}{P_{\Delta nf\_dam} + C_{MC} P_{\Delta nf\_temp}} \quad (6\text{-}17)$$

$$P_{\Delta nf\_ind\_dam} = \frac{C_{MC} P_{\Delta nf\_temp}}{P_{\Delta nf\_dam} + C_{MC} P_{\Delta nf\_temp}} \quad (6\text{-}18)$$

where:

$P_{\Delta nf\_caused\_dam}$ = probability that a change in the first natural frequency was caused by damage;

$P_{\Delta nf\_caused\_temp}$ = probability that a change in the first natural frequency was caused by changes in the ambient temperature;

$P_{\Delta nf\_dam}$ = probability that a change in the first natural frequency caused by damage in the reinforcing bar can occur;

$P_{\Delta nf\_temp}$ = probability that a change in the first natural frequency caused by changes in the ambient temperature can occur;

C_{MC} = number of simulations in the Monte Carlo simulation (2800).

The results of Monte Carlo simulation are presented in Figure 6-21. Similar to changes in the deflections of the RC beam, small changes in the first natural frequency (Δ_{nf} < 25 Hz) were probably the effect of changes in the ambient temperature and larger changes in the first natural frequency (Δ_{nf} ≥ 25 Hz) were probably caused by damage in the reinforcing bar.

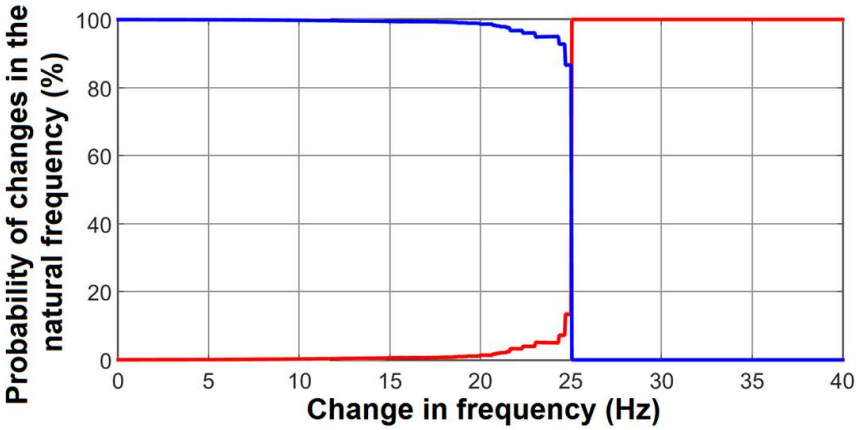

Figure 6-21: Probability that a simulated change in the first natural frequency of the RC beam was caused by damage in the reinforcing bar (red curve) or by fluctuations in the ambient temperature (blue curve).

Damage-induced changes of the first natural frequency of the RC beam larger than 25 Hz/1000 load cycles occur only in 45% of the simulations (Figure 6-10). In the remaining 55% of the simulations, damage-induced changes in the first natural frequency of the RC beam (at N_{max}-1000) was less than 25 Hz/1000 load cycles. In these simulations, the RC

beam has probably failed before such damage-induced change in the first natural frequency of the RC beam could be obtained.

6.5 Discussion and summary

The Monte Carlo simulations simulated a situation whereby the deflections and the first natural frequency of the RC beam were measured. Changes in the deflections and in the first natural frequency of the RC beam could be caused by damage in the reinforcing bar. Changes in the deflections and in the natural frequencies could also be the effect of changes in the ambient temperature. The Monte Carlo simulations presented in this chapter resulted in a probability that a certain change in the deflections or in the first natural frequency of the RC beam was caused by damage in the reinforcing bar. This probability indicates whether a potential change in the deflections or in the first natural frequency, obtained by a SHM system, was caused by local damage in the reinforcing bar of the beam.

The results of FE calculations (Chapter 5) were used as input for the Monte Carlo simulation whereby damage-induced changes in the deflections and in the first natural frequency of the RC beam were simulated. Since the sizes and the number of elements in the FE calculations were not the same as those used in the Monte Carlo simulations, a transition of the results FE calculations was required to use the results of the FE calculation in the Monte Carlo simulation. Equations were derived to establish an analytical relation between damage in the reinforcing bar and the stresses in the bar, and an analytical relation between damage in the bar and the deflections of the RC beam. The results of the FE calculations were used to validate the values of the factors in the equations. These values were constant in all simulations.

The results of the Monte Carlo simulations could be more accurate when a transition of the results of the FE calculation was not required. Such a transition could only be avoided when the elements of the FE calculation had the same size as the elements used in the Monte Carlo simulation and the development of the damage was the same as well. This implies that for each Monte Carlo simulation, new FE calculations are required. Due to time limitations, this situation was not further elaborated.

Damage in the reinforcing bar of the RC beam was calculated every 1000 load cycles. With the available hardware, the computational time per Monte Carlo simulation was more than 48 hours. Due to limitation in time, damage was not calculated every 100 load cycles. When this was done, damage in the reinforcing bar was simulated between N_{max}-1000 and N_{max}-100. At N_{max}-100, damage-induced changes in the deflections and in the first natural frequency of the RC beam were probably larger than those at N_{max}-1000. Furthermore, the time in which 100 load cycles occurs is lower than the time required for 1000 load cycles. Therefore, changes in the ambient temperature and the effect of these changes on the deflections and on the first natural frequency are probably smaller. Since larger damage-induced changes in the deflection of the RC can be obtained and the effect of changes in

the ambient temperature on the deflections of the RC beam are smaller, the probability that a certain change in the deflections or in the first natural frequency was caused by damage in the reinforcing bar increased.

The relation between changes in the ambient temperature and changes in the deflections of the RC beam as obtained from measurements of the Beam Test (Chapter 4) was used in the Monte Carlo simulation. It was assumed that the relation between changes in the ambient temperature and changes in the deflections of the RC beam could not be obtained when the beams were exposed to the Dutch climate. Therefore, the total effect of changes in the ambient temperature on the deflections of the RC beam were compared with damage-induced changes in the deflections of the RC beam. When the relations between changes in the ambient temperature and the deflections of the RC beam was obtained, only the uncertainty in these relations had to be compared with damage-induced changes in the deflections of the RC beam.

SHM data of a real concrete bridge (Chapter 3) were used to obtain a scatter in the natural frequencies of the bridge as result of changes in the ambient temperature. Since the first natural frequency of the RC beam was far larger than the first order natural frequencies and the second order natural frequencies of the RC bridge, the scatter in the relation between changes in the ambient temperature and changes in the first natural frequency of the RC beam had to be estimated. A more accurate approach to simulate the effect of changes in the ambient temperature on the deflections and on the natural frequencies of the RC beam could not be made with the available information.

Only the effect of changes in the ambient temperature on the deflections and on the first natural frequency of the RC beam were compared with damage-induced changes in the deflections and with damage-induced changes in the first natural frequency of the RC beam. When other effects, like changes in the ambient temperature or sunlight radiation, were taken into account, the probability that a simulated change in the deflections or in the first natural frequency of the RC beam was caused by damage in the reinforcing bar decreases.

This chapter provided information about whether damage-induced changes in the deflections and/or in the first natural frequency could be obtained from monitoring data. From the Monte Carlo simulations presented in this chapter it was concluded that changes in the deflections or in the natural frequencies of a RC beam could not be used to obtain fatigue damage in the reinforcing bar of the RC beam. Since concrete bridges are more complex than the RC beam, changes in the deflections and changes in the natural frequencies of concrete bridges could not be used to obtain fatigue damage in concrete bridges either.

Chapter 7

Conclusions

Information from inspections and investigations of bridges can be used to ensure the safety of the concrete bridges in the Dutch road infrastructural network. To avoid human errors, visual inspections are often replaced by Structural Health Monitoring (SHM) systems. Sensors in a SHM system can monitor the deflections and the vibrations of a bridge. This research obtained information concerning changes in the deflections and/or in the natural frequencies of the structure and the service-life of concrete structures. This chapter presents the answers of the following research questions:

- How can the comparison between the results of data-driven modal calculations and the results of Finite Element (FE) modal calculations be used to identify structural damage and to predict the remaining service-life of a RC structure?
- How do deflections of a cyclic loaded RC structure change over its service-life?
- How does chloride-induced corrosion influence the deflections of a cyclic loaded RC structure?
- How can damage-induced changes in the deflections and/or in the natural frequencies of Reinforced Concrete (RC) bridges be obtained from monitoring data?

7.1 Identification of structural damage and prediction of the service-life of a concrete bridge

SHM systems are installed on concrete bridges to obtain information about the health of the bridge. In this research, it was investigated how SHM data can be used to investigate damage in a concrete bridge and to predict the remaining service-life of the bridge. This investigation was performed by comparing the results of data-driven modal calculations with the results of FE modal calculations.

Natural frequencies of a prestressed concrete bridge (The Hollandse Brug in the Netherlands) were calculated using SHM data and predicted by FE calculations. The difference between the results of data-driven modal calculations and the results of FE modal calculation was 5-10% in the first order natural frequencies and 10-20% in the second order natural frequencies. Due to this difference, small damage-induced changes in the natural frequencies of the bridge could probably not be obtained by comparing the actual natural frequencies (obtained from monitoring data) with the predicted natural frequencies (using FE calculations). Therefore, it was concluded that the comparison between the actual natural frequencies and the predicted natural frequencies could not be used for the identification of structural health and could not be used for the prediction of the service-life of concrete bridges.

7.2 Changes in the deflections of a Reinforced Concrete structure during its total service-live

It was assumed that the deflections and the natural frequencies of a concrete bridge can be used as damage indicators for the bridge. Changes in the deflections of a RC structure as result of damage in the reinforcement of this structure can probably be earlier detected than changes in the deflections of a prestressed concrete structure as result of damage in the reinforcement in that structure. Therefore, the deflections of a RC beam during the service-life of the beam were analysed in this research to investigate the degree to which the deflections of a concrete bridge could change during its service-life.

Dynamic tensile tests on plain steel bars showed that the elongations of the bar hardly changed during the first 99% of the load cycles. Only during the last few thousand load cycles before failure, the elongations of the bar increased more significantly. Dynamic bending tests on RC beams whereby the reinforcing bar failed (flexural failure) showed that the deflections of the beam increased during the last few thousand load cycles. This suggested that the flexural failure mechanism of the RC beams was similar to tensile fatigue failure of the plain steel bars. The deflections of the RC beams also changed during the first 99% of the load cycles. Fluctuations in the deflections of the RC beam were mainly the effect of the wetting/drying cycles and the effect of changes in the ambient temperature around the RC beams.

7.3 Influence of chloride-induced corrosion on the deflections of a Reinforced Concrete structure

Corrosion in a reinforcing bar can change the behaviour of a RC structure. To which extent the deflections of a RC beam are influenced by corrosion of a reinforcing bar was investigated by dynamic tests RC beams with a corroded reinforcing bar and RC beams with an uncorroded reinforcing bar.

Tests showed that the maximum number of load cycles until flexural failure of the RC beam was 30-50% higher in the RC beams with a sound reinforcing bar compared to the RC beams with a corroded reinforcing bar. For the RC beams with a corroded reinforcing bar as well as for the RC beams with an uncorroded reinforcing bar, fluctuations were observed in the deflections of the RC beams in the first 99% of the number of load cycles. At all beams which failed on fracture of the reinforcing bar, a more significant change of the deflections was observed during the last few thousand load cycles. It could not be concluded from the deflections of a RC beam whether the beam failed in fatigue or as a combination of fatigue and localized corrosion.

The tested RC beams were loaded for 2-10 weeks (depended on the number of load cycles). To generate corrosion, the RC beams were exposed to a chloride solution for two days per week. The exposure conditions of real bridges are different, i.e. real bridges can be exposed to chlorides during several winters (de-icing salts) or for several years (marine environment). The relation between the applied exposure condition on the RC beam and ambient exposure conditions on concrete bridges in the Netherlands was not investigated. To understand the effect of corrosion in the reinforcing bars of existing concrete bridges over longer time periods, it is recommended to investigate this relation in a future research.

A small amount of damage increases the stresses of a tensile loaded bar locally. Under static loading, a local increase of the stresses in the bar can be redistributed over the total cross-section of the bar. Under dynamic loading, a local increase of the stresses in the bar can result in fatigue cracks and local failure at a lower number of load cycles. A larger number of fatigue cracks and larger fatigue cracks can result in earlier fatigue failure. Therefore, a small amount of local damage can accelerate relatively fast under cyclic loading. The effect of chloride-induced corrosion on the deflections of a Reinforced Concrete structure is far larger under cyclic loading than under static loading.

7.4 Changes in the deflections and/or natural frequencies obtained from monitoring data

Dynamic bending tests on RC beams showed that fatigue damage increases the deflections of a RC beam only during the last few thousand load cycles before failure. It was also observed that changes in the ambient condition (temperature and humidity) influence the deflections and the natural frequencies of the RC beam. In a sensitivity

analyses, damage-induced changes in the deflections and in the first natural frequency of a RC beam were compared with the effect of changes in the ambient temperature on the deflections and on the first natural frequency of the RC beam. The sensitivity analysis was done by Monte Carlo simulations.

Monte Carlo simulations showed that in 50% of the simulations damage-induced changes in the deflections of the RC beam could not be obtained from the simulated changes in the deflections of the RC beam. In the other 50% of the simulations, damage-induced changes in the deflections of the RC beam was obtained between 1000 and 2000 load cycles until failure. Monte Carlo simulations also showed that in only 45% of the simulations, damage-induced changes in the first natural frequency could be obtained between 1000 and 2000 load cycles until failure. It was concluded that changes in the deflections of the RC beam as well as changes in the natural frequencies of the beam cannot be used to detect damage in the reinforcing bar with a sufficient degree of reliability.

A RC bridge is a more complex structure than the RC beams investigated in this research. Therefore, damage-induced changes in the deflections of a RC bridge are more difficult to observe than damage-induced changes in the deflections of the RC beam. Since a sensitivity study showed that only in 50% of the simulations damage-induced changes in the deflections of the RC beam in the second last 1000 load cycles could be observed, the probability that these changes can be obtained from measured changes in the deflections of a concrete bridge and these changes can be used as warning system is limited. A similar conclusion was drawn for changes in the first natural frequency of a concrete bridge. It is unlikely that changes in the deflections or changes in the natural frequencies of a concrete bridge can be used to obtain information about fatigue damage in a concrete bridge.

Bibliography

[1] Rijkswaterstaat (2007) Inventarisatie Kunstwerken (Survey Infrastructural Objects), Dutch Ministry of Infrastructure and Environment

[2] J. Visscher (2016) Hoofdbrekens over Bruggen in Nederland (Worries about Bridges in the Netherlands), reformatorisch dagblad

[3] C. B. M. Blom, et al. (2014) Restlevensduur van bestaande constructies (Remaining service-life of existing structures), SBRCUR Committee 1958

[4] Koninklijk_Instituut_van_Ingenieurs (1962) GBV 1962 - Gewapend-Betonvoorschriften, Koninklijk Instituut van Ingenieurs

[5] C. M. P. S. Eurlings (2007) Inventarisatie Kunstwerken (Inventarisation Objects), Ministery of Infrastructure and Environment

[6] FHWA (2001) Reliability of Visual Inspection for Highway Bridges, Federal Highway Administration

[7] J. M. Ndambi, J. Vantomme and K. Harri (2002) Damage assessment in reinforced concrete beams using eigenfrequencies and mode shape derivatives, Engineering Structures 501-515

[8] STW (2009) STW Perspective Program - Integral Solutions for Sustainable Construction, STW

[9] E. A. B. Koenders (2011) Integral Solutions for Sustainable Construction (IS2C) - A Structural Health Monitoring Program in The Netherlands, SMAR - First Middle East Conference on Smart Monitoring, Dubai, UAE 8-10 Februari 2011

[10] T. Xiang and R. Zhao (2007) Reliability evaluation of chloride diffusion in fatigue damaged concrete, Engineering Structures 1539-1547

[11] O. S. Salawu (1997) Detection of Structural Damage Through Changes in Frequency: a Review, Engineering Structures 718-723

[12] D. Inaudi (2009) Overview of 40 Bridge Structural Health Monitoring Projects, International Bridge Conference, Pittsburgh, USA June 15–17, 2009

[13] T. M. Ahlborn, et al. (2010) The State-of-the-Practice of Modern Structural Health Monitoring for Bridges: A Comprehensive Review, Michigan Tech Research Institute

[14] J. Maeck, B. Peeters and G. d. Roeck (2001) Damage Identification on the Z24 Bridge Using Vibration Monitoring, Smart Materials and Structures 512

[15] Medical_Dictionary (2016) Health, http://medical-dictionary.thefreedictionary.com/health

[16] European_Committee_for_Standardization (2002) Eurocode: Basic of Structural Design NEN-EN 1990, The Netherlands Standardization Institute

[17] E. Bastidas-Arteaga, P. Bressolette, A. Chateauneuf and M. Sánchez-Silva (2009) Probabilistic lifetime assessment of RC structures under coupled corrosion–fatigue deterioration processes, Structural Safety 84-96

[18] G. C.Lee and E. Sternberg (2015) Bridges - Their engineering and planning, State University of New York Press ISBN 978-1-4384-5525-9

[19] C. R. Farrar and K. Worden (2012) Structural Health Monitoring - A Machine Learning Perspective, Wiley ISBN 978-1-119-99433-6

[20] H. Sohn, C. R. Farrar, F. M. Hemez and J. J. Czarnecki (2002) A Review of Structural Health Monitoring Literature 1996-2001, Third World Conference on Structural Control, Como Italy April 7-12 2002

[21] E. Reynders (2012) System Identification Methods for (Operational) Modal Analysis: Review and Comparison, Archives of Computational Methods in Engineering 51-124

[22] S. Priya and D. J. Inman (2009) Energy Harvesting Technologies, Springer New York, ISBN 978-0-387-76463-4

[23] B. Glisic (2013) An Overview on Distributed Fiber Optic Strain Sensort, The 6th International Conference on Structural Health Monitoring of Intelligent Infrastructure, Hongkong China 9-11 December 2013

[24] A. L. Window and G. S. Holister (1982) Strain Gauge Technology, Elsevier Applied Science ISBN 0-85334-118-4

[25] Y. Xia, et al. (2012) Temperature Effect on Vibration Properties of Civil Structures: a Literature Review and Case Studies, Journal of Civil Structural Health Monitoring 29-46

[26] S. K. Verma, S. S. Bhadauria and S. Akhtar (2013) Review of Nondestructive Testing Methods for Condition Monitoring of Concrete Structures, Journal of Construction Engineering 11

[27] V. Leelalerkiet, J.-W. Kyung, M. Ohtsu and M. Yokota (2004) Analysis of half-cell potential measurement for corrosion of reinforced concrete, Construction and Building Materials 155-162

[28] A. Poursaee and C. M. Hansson (2009) Potential Pitfalls in Assessing Chloride-induced Corrosion of Steel in Concrete, Cement and Concrete Research 391-400

[29] J. Farias (2015) Corrosion of Steel in Cracked Concrete, Delft University of Technology, The Netherlands

[30] Y. Schiegg (2005) Monitoring of Corrosion in Reinforced Concrete Structures, Corrosion in reinforced concrete structures (ISBN 0-8493-2583-8),

[31] M. Stern and A.L.Geary (1957) Electrochemical Polarization, Journal of the electrochemical society 56-63

[32] B. H. Kim, J. Lee and D. H. Lee (2010) Extracting Modal Parameters of High-speed Railway Bridge using the TDD Technique, Mechanical Systems and Signal Processing 707-720

[33] B. Peeters, et al. (1998) Comparision of System Identification Methods using Operational Data of a Bridge Test, International Conference on Noise and Vibration Engineering, Leuven Belgium

[34] W.-X. Ren and Z.-H. Zong (2004) Output-only Modal Parameter Identification of Civil Engineering Structure, Structural Engineering and Mechanics

[35] G. Zhang, B. Tang and G. Tang (2012) An Improved Stochastic Subspace Identification for Operational Modal Analysis, Measurement 1246-1256

[36] B. Peeters and G. d. Roeck (1999) Reference-based stochastic subspace identification for output-only modal analysis, Mechanical Systems and Signal Processing 855-878

[37] Z. P. Bažant (2002) Concrete fracture models: testing and practice, Engineering Fracture Mechanics 165-205

[38] P. Augustin and T. Onet (2012) Elastic Deformation of Concrete - Determination of Secant Modulus of Elasticity in Compression., Acta Technica Napocensis: Civil Engineering & Architecture

[39] A. Ghali, R. Favre and M. Elbadry (2012) Concrete Structures, Spon Press ISBN 978-0-415-58561-3

[40] J. J. Brooks (2014) Concrete and Masonary Movements Chapter 13 Thermal Movement, Elsevier Oxford, ISBN 978-0-12-801525-4

[41] K. v. Breugel, C. R. Braam and E. A. B. Koenders (2013) Concrete Structures under Imposed Thermal and Shrinkage Deformations, Delft University of Technology

[42] S. N. Shoukry, G. W. William, B. Downie and M. Y. Riad (2011) Effect of moisture and temperature on the mechanical properties of concrete, Construction and Building Materials 688-696

[43] P. Sandberg (1996) Durability of Concrete in Saline Environment The Complete Solution of Fick's Second Law of Diffusion with Time-dependent Diffusion Coefficient and Surface Concentration, Cementa Danderyd Sweden,

[44] C. Hartsuijker and H. Welleman Toegepaste Mechanica, deel 3 Statisch Onbepaalde Constructies en Bezwijkanalyse (Applied Mechanics, part 3 Statically Undeterminded Structures and Failure Analyses), ISBN 9-789039-505953

[45] Z. P. Bažant and L. J. Najjar (1972) Nonlinear Water Diffusion in Nonsaturated Concrete, Matériaux et Construction 3-20

[46] Z. Bofang (2014) Thermal Stresses and Temperature Control of Mass Concrete Chapter 2 - Conduction of Heat in Mass Concrete, Boundary Conditions, and Methods of Solution, Butterworth-Heinemann Oxford, 978-0-12-407723-2

[47] D. Vandepitte (1979) Berekening van constructies; bouwkunde en civiele techniek, Boekdl. 1, Story-Scientia Gent, ISBN 90-6439-154-8

[48] J. M. J. Spijkers, A. W. C. M. Vrouwenvelder and E. C. Klaver (2005) Lecture notes CT 4140 - Structural Dynamics - part 1 - Structural Vibrations, Delft University of Technology

[49] A. Kareem and K. Gurley (1996) Damping in Structures: its Evaluation and Treatment of Uncertainty, Journal of Wind Engineering and Industrial Aerodynamics 131-157

[50] C. R. Farrar and K. M. Cone (1995) Vibration Testing of the I-40 Bridge Before and after the Introduction of Damage, International Modal Analysis Conference, Nashville TU United States Feb 13-16 1995

[51] C. Liu and J. T. DeWolf (2007) Effect of Temperature on Modal Variability of a Curved Concrete Bridge under Ambient Loads, Journal of Structural Engineering 1742-1751

[52] H. Sohn, et al. (1999) An Experimental Study of Temperature Effect on Modal Parameters of the Alamosa Canyon Bridge, Earthquake Engineering & Structural Dynamics 879-897

[53] S. L. Desjardins, N. A. Londoño, D. T. Lau and H. Khoo (2006) Real-Time Data Processing, Analysis and Visualization for Structural Monitoring of the Confederation Bridge, Advances in Structural Engineering 141-157

[54] C. Modena, D. Sonda and D. Zonta (1999) Damage Localization in Reinforced Concrete Structures by using Damping Measurements, Key Engineering Materials 132-141

[55] F. Stüssi and A. Wöhler (1955) Die Theorie der Dauerfestigkeit und die Versuche von August Wöhler (The Theory of Fatigue Strength and the Attempts of August Wöhler), Mitteilungen der T.K.V.S.B. 13

[56] R. A. Smith and S. Hillmansen (2004) A brief historical overview of the fatigue of railway axles, Proceedings of the Institution of Mechanical Engineers, Part F: Journal of Rail and Rapid Transit 267-277

[57] H. Mughrabi (2001) Encyclopedia of Materials: Science and Technology (Second Edition) Fatigue Life and Cyclic Stress–Strain Behavior, Elsevier Oxford, 978-0-08-043152-9

[58] K. J. Miller and M. F. E. Ibrahim (1981) Damage Accumulation During Initiating and Short Crack Growth Regimes, Fatigue & Fracture of Engineering Materials & Structures 263-277

[59] A. Fatemi and L. Yang (1998) Cumulative Fatigue Damage and Life Prediction Theories: a Survey of the State of the Art for Homogeneous Materials, International Journal of Fatigue 9-34

[60] J. O. Holmen (1979) Fatigue of Concrete by Constant and Variable Amplitude Loading, Norwegian Institute of Technology, University of Trondheim

[61] G. Mallett (1991) Fatigue of Reinforcement Concrete, HMSO ISBN 0-11-550979-8

[62] ACI (1992) Considerations for Design of Concrete Structures Subjected to Fatigue loading, ACI 215R-7

[63] M. F. E. Ibrahim and K. J. Miller (1979) Determination of Fatigue Crack Initiation Life, Fatigue & Fracture of Engineering Materials & Structures 351-360

[64] J. W. Murdock (1965) A Critical Review of Research on Fatigue of Plain Concrete, University of Illinois, Office of Publications Urbana,

[65] T. T. C. Hsu (1981) Fatigue of Plain Concrete, ACI Journal

[66] A. Lindorf and M. Curbach (2010) S–N Curves for Fatigue of Bond in Reinforced Concrete Structures under Transverse Tension, Engineering Structures 3068-3074

[67] Rijkswaterstaat (2014) Strooien en zout (using de-icing salts), http://rws.nl/actueel/winter_op_weg_en_water/strooien/index.aspx

[68] Cement.org (2013) Corrosion of Embedded Metals, URL http://www.cement.org/tech/cct_dur_corrosion.asp

[69] A. A. Almusallam (2001) Effect of Degree of Corrosion on the Properties of Reinforcing Steel Bars, Construction and Building Materials 361-368

[70] R. Capozucca (1995) Damage to Reinforced Concrete due to Reinforcement Corrosion, Construction and Building Materials 295-303

[71] L. Abosrra, A. F. Ashour and M. Youseffi (2011) Corrosion of Steel Reinforcement in Concrete of Different Compressive Strengths, Construction and Building Materials 3915-3925

[72] F. Li and Y. Yuan (2013) Effects of Corrosion on Bond Behavior between Steel Strand and Concrete, Construction and Building Materials 413-422

[73] Y. Zhao, J. Yu and W. Jin (2011) Damage Analysis and Cracking Model of Reinforced Concrete Structures with Rebar Corrosion, Corrosion Science 3388-3397

[74] V. H. Dang and R. François (2013) Influence of Long-term Corrosion in Chloride Environment on Mechanical Behaviour of RC Beam, Engineering Structures 558-568

[75] A. Castel, R. Francois and G. Arliguie (2000) Mechanical Behaviour of Corroded Reinforced Concrete Beams - Part 2: Bond and Notch Effects, Materials and Structures 545-551

[76] A. Castel, D. Coronelli, R. Francois and D. Cleland (2010) Modelling the Stiffness Reduction of Corroded Reinforced Concrete Beams after Cracking, Modelling of corroding concrete structures (ISBN 978-94-007-0676-7), Madrid, Spain

[77] C. Fang, K. Gylltoft, K. Lundgren and M. Plos (2006) Effect of Corrosion on Bond in Reinforced Concrete under Cyclic Loading, Cement and Concrete Research 548-555

[78] K. Lundgren and M. Plos (2006) The Effect of Corrosion on Bond in Reinforced Concrete, Proceedings European Symposium on Service Life ans Serviceability of Concrete Structures, Espoo, Finland June 2006

[79] X. Zhiqiang, S. Yujiu and T. Mingjing (1991) Crack Closure Induced by Corrosion Products and its Effect in Corrision Fatigue, International Journal of Fatigue 69-72

[80] Federation_Internationale_du_Beton (2013) FIB Model Code for Concrete Structures 2010, Wiley Hoboken, ISBN: 9783433604083

[81] S. Ahmad (2003) Reinforcement corrosion in concrete structures, its monitoring and service life prediction—a review, Cement and Concrete Composites 459-471

[82] H. Ye, et al. (2013) Influence of cracking on chloride diffusivity and moisture influential depth in concrete subjected to simulated environmental conditions, Construction and Building Materials 66-79

[83] C. A. Apostolopoulos, S. Demis and V. G. Papadakis (2013) Chloride-induced corrosion of steel reinforcement – Mechanical performance and pit depth analysis, Construction and Building Materials 139-146

[84] Federation_Internationale_du_Beton (2006) Model Code for Service Life Design, ISBN 2-88394-074-6

[85] S. Guzmán, J. C. Gálvez and J. M. Sancho (2011) Cover Cracking of Reinforced Concrete due to Rebar Corrosion Induced by Chloride Penetration, Cement and Concrete Research 893-902

[86] G. Markeset and R. Myrdal (2009) Modelling of Reinforced Corrosion in Concrete - State of the Art, SINTEF Building and Infrastructure ISBN 978-82-536-1073-3

[87] Wegenwiki (2016) A6 The Netherlands, https://www.wegenwiki.nl/A6_(Nederland)

[88] Cobouw (2007) Mediator moet conflict Hollandse Brug slechten (Mediator must solve conflict Hollandse Brug), Cobouw

[89] E. v. d. Wal (2013) Raad van State: Toch Schadevergoeding voor Transportbedrijven na Sluiting Hollandse Brug (Compensation for Transport Companies after Closing Dutch Bridge), transport-online.nl

[90] C. Bosma, et al. (2011) Verkeers Trillingen Hollandse Brug (Traffic Vibratuib Dutch Bridge), Cement 03-2011

[91] C. Bosma, et al. (2011) Meetsysteem Hollandse Brug (Monitoring System Dutch Bridge), Cement 04-2011

[92] S. Miao (2014) Structural Health Monitoring Meets Data Mining, Leiden University, The Netherlands

[93] S. Miao, R. Veerman, E. Koenders and A. Knobbe (2013) Modal Analysis of a Concrete Highway Bridge - Structural Calculations and Vibration-based Results, The 6th International Conference on Structural Health Monitoring of Intelligent Infrastructure, Hongkong China 9-11 December 2013

[94] R. Veerman, S. Miao, E. Koenders and A. Knobbe (2013) Data-intensive Structural Health Monitoring in the Infrawatch Project, The 6th International Conference on Structural Health Monitoring of Intelligent Infrastructure, Hongkong, China 9-11 December 2013

[95] Nemetschek_Scia (2011) Scia Engineer, http://nemetschek-scia.com

[96] tnodiana (2014) TNO DIANA - A TNO Company, http://tnodiana.com/

[97] Rijkswaterstaat - Directie Bruggen (1967) Brug bij Muiderberg - Maten en Kabelverloop van de Liggers (Bridge near Muiderberg - Dimensions and Reinforcing Cables of the Girders), C12275

[98] Rijkswaterstaat - Directie Bruggen (1967) Brug bij Muiderberg - Maten van Rijvloer (Bridge near Muiderberg - Dimensions of Deck), C12257

[99] Rijkswaterstaat - Directie Bruggen (1992) Rekonstruktie Hollandse Brug - Capaciteitsvergroting - Rijksweg 6 - Overzicht (Reconstruction Hollandse Brug - Increase Capacity - Highway 6 - Overview), 19920034

[100] Rijkswaterstaat (2013) Richtlijnen Beoordeling Kunstwerken (Guideline Assessment Structures), Ministry of Infrastructure and Environment

[101] European_Committee_for_Standardization (2005) Eurocode 2: Design of concrete structures - Part 1-1: General rules and rules for buildings NEN-EN 1992-1-1, The Netherlands Standardization Institute Delft,

[102] Spanbeton (2015) Een Oplossing voor Elk Prefab Vraagstuk (a Solution for All Prefab Problems), http://www.spanbeton.nl/nl/

[103] European_Committee_for_Standardization (2011) Eurocode 1: Actions on Structures - Part 1-1: General actions - Densities, self-weight, imposed loads for buildings NEN-EN 1991-1-1, The Netherlands Standardization Institute

[104] M. F. Ashby and D. R. H. Jones (2012) An Introduction to Properties Applications, and Design Engineering Materials 1, Elsevier ISBN 978-0-08-096665-6

[105] European_Committee_for_Standardization (2005) Structural Bearings - Part 3: Elastomeric Bearings NEN-EN 1337-3, The Netherlands Standardization Institute

[106] Nemetschek_Scia (2011) Scia Engineer - Advanced Professional Training Dynamics,

[107] tnodiana (2014) DIANA - Training Course Manual & Tutorials, TNO DIANA

[108] J. Forshaw and G. Smith (2009) Dynamics and Relativity Section 4.3.1 - The Parallel-axis Theorem, Wiley ISBN 9780470014592

[109] D. Durban, D. Givoli and J. Simmonds (2002) Advances in the mechanics of plates and shells, Kluwer Academic ISBN 0306469545

[110] C. R. Steele and C. D. Balch (2009) Introduction to the Theory of Plates, Division of Mechanics and Computation - Department of Mecanical Engineering

[111] tnodiana (2014) DIANA - User's Manual: Element Library,

[112] J. C. Walraven and C. R. Braam (2011) Lecture notes Prestressed Concrete, Delft University of Technology

[113] Rijkswaterstaat (2016) N311: Aanpak Nijkerkerbrug (Renovation Nijkerkerbrug), http://www.rijkswaterstaat.nl/wegen/projectenoverzicht/n301-aanpak-nijkerkerbrug/index.aspx

[114] Rijkswaterstaat (2016) Start Aanbesteding Nijkerkerbrug (Start Tender Nijkerkerbrug), https://www.rijkswaterstaat.nl/over-ons/nieuws/nieuwsarchief/p2016/04/start-aanbesteding-nijkerkerbrug-met-project-doen.aspx

[115] L. Yin and Z. Wang (2012) Review of studying on Fatigue Damage of Concrete Bridge, Advanced Engineering Forum (Volume 5) 207-210

[116] K. Wang, D. E. Nelsen and W. A. Nixon (2006) Damaging effects of deicing chemicals on concrete materials, Cement and Concrete Composites 173-188

[117] International_Standard_Organisation (2009) ISO 6892-1 Metallic Materials - Tensile Testing ISO

[118] Kiwa (2010) Nationale Beoordeling NBL 0501 voor Betonstaal (National Review BRL 0501 of Reinforcement Steel), KIWA Nerderland BV

[119] G. P. Tilly (1979) Fatigue of Steel Reinforcement Bars in Concrete: a Review, Fatigue & Fracture of Engineering Materials & Structures 251-268

[120] R. Veerman, K. v. Breugel and E. Koenders (2015) Effect of Corrosion on the Fatigue Service-life on Steel and Reinforced Concrete Beams, FIB Symposium 2015, Copenhagen Danmark 18-20 May 2015

[121] European_Committee_for_Standardization (2003) Eurocode 1: Actions on structures - Part 2: Traffic loads on bridges NEN-EN 1991-2, The Netherlands Standardization Institute

[122] A. Blagojevic (2016) The Influence of Cracks on the Durability and Service Life of Reinforced Concrete Structures in relation to Chloride-Induced Corrosion, TU Delft

[123] A. Blagojević, D. Koleva and J. C. Walraven (2013) Corrosion resistance of reinforced concrete beams under the synergetic action of chloride ingress, loading and varying crack width: preliminary studies on the methods suitability and derived parameters reliability through the application of electrochemical techniques (LPR, PDP and EIS), Submitted to Materials & Corrosion

[124] A. Taheri (1998) Durability of Reinforced Concrete Structures in Aggresive Marine Environment, TU Delft Delft, ISBN 9040716773

[125] The_Netherlands_Standardization_Institute (1995) TGB 1990 - Voorschriften Beton NEN 6720, The Netherlands Standardization Institute

[126] J. Stewart (2003) Calculus, McMaster University ISBN 0-534-27409-9

[127] J. G. M. v. Mier (1997) Fracture Processes of Concrete - Assessment of Material Parameters for Fracture Models, CRC ISBN 0-8493-9123-7

[128] W. H. Wisman (1990) Inleiding Thermodynamica (Introduction Thermodynamics, Delftse Uitgevers Maatschappij Delft, ISBN: 90-6562-116-4

[129] R. P. Veerman and E. A. B. Koenders (2014) Automatic Degradation Detection During a Dynamic Loaded Beam Test, CIC - Concrete Innovation Conference, Oslo, Norway 11-13 June 2014

[130] R. P. Veerman and E. A. B. Koenders (2014) Dynamic Loaded Beam Failure Under Corroded Conditions, 3rd International Conference on Service Life Design for Infrastructures, Zhuhai, China 15-17 oct 2014

[131] L. Giordano and F. Tondolo (2011) Crack width evolution of RC structures subjected to corrosion and fatigue, Key Engineering Materials 417-420

[132] tnodiana (2014) DIANA - User's Manual: Material Library,

[133] Federation_Internationale_du_Beton (1999) FIB Bulletin 1 - Structural Concrete, fib ISBN 2-88394-041-X

[134] Mathworks (2015) Matlab, http://nl.mathworks.com/

[135] European_Union_Brite_Euram_3 (1999) DuraCrete - Probabilistic Methods for Durability Design,

[136] J. M. J. Spijkers, A. W. C. M. Vrouwenvelder and E. C. Klaver (2005) Lecture notes CT 4150 - Plasticity, Delft University of Technology

[137] Royal_Netherlands_Meteorological_Institute (2016) Uurgegevens van het weer in Nederlands (hourly data of the wheather in the Netherlands), http://projects.knmi.nl/klimatologie/uurgegevens

List of Abbreviations

ADC	Analog-to-Digital Converter
EMA	Experimental Modal Analyses
FE	Finite Element
FEA	Finite Element Analyser
FEM	Finite Element Method
HCP	Half-Cell Potential
IS2C	Integral Solution for Sustainable Construction
KNMI	Royal Netherlands Meteorological Institute
LPR	Linear Polarization Resistance
LVDT	Linear Variable Differential Transformers
NWO	Netherlands Organization for Scientific Research
OMA	Operational Modal Analyses
PC	Prestressed Concrete
PP	Peak-Picking
R	Resistance
RC	Reinforced Concrete
RH	Relative Humidity
S	Stresses
SHM	Structural Health Monitoring
SSI	Stochastic Subspace Identification
STW	Stichting Technische Wetenschappen
T	Temperature

List of Symbols

Latin upper case letters

A_o = undamaged area

$C_{def,1}$ = factor between the increase of the elongations of the bar and the rotation of the hinge (1/mm)

$C_{def,2,r}$ = factor between the rotation of the hinge at location 'r' and the increase of the deflection of the RC beam (mm)

$C_{el,1}$ = elongation factor (mm^3/N)

$C_{el,2}$ = elongation factor ($\sqrt[8]{mm^3/N}$

C_{MC} = number of simulations in the Monte Carlo simulation

$C_{\Delta,def,calculated}$ = factor (mm/K)

$C_{\Delta,def,measured}$ = factor (mm/K)

$C_{\Delta t,def}$ = factor (mm/K)

$C_{\Delta t,nf}$ = factor (Hz/K)

$D_{amN,i,j}$ = damage per N-cycles in element i,j

$D_{amN,i,j,tot}$ = total damage per N-cycles in element i,j

EI_{beam} = bending stiffness of the RC beam

$E_{cm,cr}$ = Young's modulus of cracked concrete

$F_{amplitude}$ = load amplitude

$F_{average}$ = average load

I = moment of inertia

K = spring stiffness

L_{end} = distance between load and support

L_{mid} = distance between the supports

N = number of cycles

$N_{applied}$ = applied number of load cycles

$N_{applied,p}$ = applied number of load cycles per stress amplitude

N_p = number of cycles per amplitude

N_{max} = maximum number of load cycles

$N_{max,i,j}$ = maximum number of load cycles for element i,j

$N_{max,i,j,p}$ = maximum number of load cycles for element i,j per stress amplitude

$N_{max,p}$ = maximum number of cycles until failure for amplitude 'p'

$N_{max,v}$ = maximum number of load cycles in a simulation

N_{ref} = reference number of load cycles

$P_{\Delta nf\_caused\_dam}$ = probability that a change in the first natural frequency was caused by damage

$P_{\Delta nf\_caused\_temp}$ = probability that a change in the first natural frequency was caused by changes in the ambient temperature

$P_{\Delta nf\_dam}$ = probability that a change in the first natural frequency caused by damage in the reinforcing bar can occur

$P_{\Delta nf\_temp}$ = probability that a change in the first natural frequency caused by changes in the ambient temperature can occur

$P_{\Delta\delta\_caused\_dam}$ = probability that a change in the deflection was caused by damage

$P_{\Delta\delta\_caused\_temp}$ = probability that a change in the deflection was caused by changes in the ambient temperature

$P_{\Delta\delta\_dam}$ = probability that a change in the deflection caused by damage in the reinforcing bar can occur

$P_{\Delta\delta\_temp}$ = probability that a change in the deflections caused by changes in the ambient temperature can occur

S = stress amplitude

$S_{i,j}$ = stress amplitude for element i,j (in N/mm^2, value depends on damage)

S_{ref} = reference stress amplitude (in N/mm^2, value depends on material properties)

T = temperature (^oC)

Latin lower case letters

a_r = distance between location of hinge at location 'r' and the support

b_r = distance between location of hinge at location 'r' and the support

c = concrete cover

d_{bar} = diameter of the bar

d_{crack} = depth of the crack

f_1 = first natural frequency

$f_{1,o}$ = first natural frequency of the undamaged RC beam

f_n = n^{th} order natural frequency

g = gravitation acceleration (9.81 m/s^2)

i = element

m = mass

m_i = mass per element

n = order natural frequency

p = number of different stress amplitudes

t = time

u = displacement

u_o = initial displacement

w = number of values

x = random value

Greek upper case letters

ΔA = damaged area

$\Delta\delta$ = change in deflection

ΔT_a = change in ambient temperature

Δ_{nf} = change in natural frequency

Greek lower case letters

$\delta_{amplitude}$ = deflection amplitude

δ_{def} = increase of the deflection of the RC beam

δ_{el} = increase of the elongation of the bar (mm)

$\delta_{el,r}$ = increase of the elongation of the bar per section

δ_o = deflection of the undamaged RC beam

δ_{tot} = total deflection

ζ = damping ratio

μ = mean value

σ = standard deviation

σ_N = new stress

σ_o = initial stress

$\upsilon_{s,m}$ = stationary displacement of the mass

$\upsilon_{i,n}$ = displacement of the mass per element and per natural frequency

φ = rotation of the hinge

ψ = phase

ω_o = angular frequency

English summary

The Dutch road infrastructure contains a large number of concrete bridges and viaducts. Malfunctioning of these bridges and viaducts has large financial consequences. Also the social impact of malfunctioning of these bridges and viaducts can be enormously. Asset owners make plans for maintenance and replacement to avoid malfunctioning of their assets. As result of increased traffic loads and potential degradation of bridges, the maintenance and replacements plans need to be checked and updated frequently. The input for these updates can be obtained from visual inspections. Visual inspections are, however, time consuming and are not always reliable. The reliability of the investigations of the health of a bridge could be increased by monitoring the deflections and/or the vibrations of the bridge. The main idea of a Structural Health Monitoring system is that degradation of a bridge results in detectable changes in the deflections and in the modal properties of the bridge. The relation between damage in a concrete bridge and changes in the deflections and natural frequencies of the bridge has been investigated in this research.

The first and second order natural frequencies of an existing concrete bridge (the Hollandse Brug in the Netherlands) were calculated using monitoring data of the bridge and predicted using Finite Element (FE) calculations. The mode shapes of the bridge were used to compare the natural frequencies obtained from data-driven calculations with the corresponding natural frequencies obtained from FE calculations. It was shown that the difference between the results of the data-driven modal calculations and the results of the FE modal calculations of the Hollandse Brug was 5-10% in the first order natural frequencies and 10-20% in the second order natural frequencies. Due to the scatter in the calculation results, small damage-induced changes in the natural frequencies cannot be inferred from a comparison between the results of data-driven modal calculations and the results of FE modal calculations.

Changes in the deflections of Reinforced Concrete (RC) beams during the duration of the their total service-life were investigated by laboratory tests. In these tests, 24 RC beams were dynamically loaded in a four-point-bending configuration. Each beam was reinforced with one single steel reinforcing bar. In 12 of the beams, corrosion in the reinforcing bar was generated by one-sided exposure of the beams to chloride ingress. The other 12 RC beams were one-sided exposed to tap water and were used as reference beams. The deflections of the tested beams were measured from the first cycle until failure of the beam. Changes in the deflections of the beams as result of fluctuations in the ambient condition were measured during the total service-life of the beams. Changes in the deflections of the beams as result of fatigue damage were only measured during the last few thousand load cycles (less than 0.1% of the total number of load cycles). The maximum number of load cycles until failure of the RC beam was reduced by generating corrosion in the reinforcing bar of the beam. In the conducted tests, the maximum number of load cycles for the RC beam with a sound reinforcing bar was 30-50% higher than the maximum number of load cycles for RC beams with a corroded reinforcing bar.

Except for this reduction in the number of load cycles, corrosion hardly changed the deflections of the RC beam.

In FE calculations, the effect of different damage levels in the reinforcing bar of the RC beam were simulated. With these simulations, the stresses in the reinforcing bar, the stresses in the beam, and the deflections of the beam were calculated as function of the amount of damage in the reinforcing bar. The results of the FE calculations were used in a sensitivity analysis of deflections and natural frequencies of beams with damage in the reinforcing bar.

As result of fluctuations in the exposure conditions, the deflections and the natural frequencies of a concrete bridge change. In a sensitivity analysis the effect of changes in the ambient temperature on the deflections and on natural frequencies of the RC beam were compared with damage-induced changes in the deflections and in the natural frequencies of the RC beam. The sensitivity analysis was done by Monte Carlo simulations. The results of the FE calculations and measurements of the ambient temperature were used as input for the Monte Carlo simulations. Intermediate results of the Monte Carlo simulations were validated with the results of the laboratory tests.

The comparison between damage-induced changes in the deflections of the RC beam and the effect of changes in the ambient temperature on the deflections of the RC beam showed that it is unlikely that damage-induced changes in the deflections of the beam can be inferred from measurements of the beam. A similar conclusion was drawn for the comparison between damage-induced changes in the first natural frequency of the RC beam and the effect of changes in the ambient temperature on the first natural frequency of the RC beam.

Damage-induced changes in the deflections or in the natural frequencies of concrete bridges depend on the location of the damaged section. Damage in one of the reinforcing bars in a concrete bridge can be initiated at multiple locations. Therefore, a large number of potential changes in de deflections and in the natural frequencies of the bridge can be simulated. Due to this large number, it is very unlikely that damage-induced changes in the deflections or in the natural frequencies of concrete bridges can be inferred from measurements of the bridge. Therefore, deflections and natural frequencies cannot be used as indicator for fatigue damage in concrete bridges.

Nederlandse samenvatting

Het Nederlandse wegennetwerk bevat een groot aantal bruggen en viaducten. Wanneer deze bruggen en viaducten disfunctioneren, heeft dit grote financiële gevolgen. Ook kan het disfunctioneren van bruggen en viaducten voor grote sociale problemen zorgen. Brugeigenaren maken onderhouds- en vervangingsplannen voor de bruggen die ze in eigendom hebben om disfunctioneren van deze bruggen te voorkomen. Als gevolg van een groeiende hoeveelheid verkeer en mogelijke degradatie van bruggen is het nodig om deze plannen regelmatig te controleren en te updaten. Informatie voor deze updates kan worden gehaald uit visuele inspecties. Visuele inspecties zijn echter tijdrovend en zijn niet altijd betrouwbaar. De betrouwbaarheid van onderzoeken naar de conditie van een brug zou kunnen worden vergroot door de doorbuigingen en/of de trillingen van de brug te meten. Het idee van 'Structural Health Monitoring' is dat degradatie van een brug resulteert in meetbare veranderingen in de doorbuigingen en in de modale eigenschappen van de brug. De relatie tussen schade in een betonnen brug en veranderingen in de doorbuigingen en in de eigenfrequenties van de brug is onderzocht in dit onderzoek.

Meetdata van een bestaande brug (de Hollandse Brug in Nederland) zijn gebruikt om de eerste en tweede orde eigenfrequenties van de brug te bepalen. Deze eigenfrequenties zijn eveneens voorspeld aan de hand van Eindige Elementen (EE) berekeningen. De trillingsvormen van de brug zijn gebruikt om de eigenfrequenties van op data gebaseerde modale berekeningen te vergelijken met de corresponderende eigenfrequenties gebaseerd op EE modale berekeningen. Het verschil tussen de resultaten van de op data gebaseerde modale berekeningen en de resultaten van de EE berekeningen was 5-10% voor de eerste orde eigenfrequenties en 10-20% voor de tweede orde eigenfrequenties. Door de verschillen in de berekeningsresultaten kunnen kleine door schade geïnduceerde verschillen in de eigenfrequenties niet worden waargenomen door de resultaten van op data gebaseerde berekeningen te vergelijken met de resultaten van EE berekeningen.

Veranderingen in de doorbuigingen van gewapend betonnen balken gedurende de totale levensduur van de balken zijn experimenteel onderzocht met laboratorium proeven. In deze proeven zijn 24 balken dynamisch belast in een vier-punts-buig opstelling. Elke balk was gewapend met één stalen wapeningsstaaf. In 12 van de balken was corrosie in de wapeningsstaaf gegenereerd door de balk eenzijdig bloot te stellen aan een chlorideconcentratie. De andere 12 balken werden eenzijdig blootgesteld aan kraanwater en zijn gebruikt als referentie balken. De doorbuigingen van de balken zijn gemeten vanaf de eerste lastwissel tot het bezwijken van de balk. Veranderingen in de doorbuigingen van de balk als gevolg van fluctuaties in de omgevingsomstandigheden zijn gedurende de hele levensduur van de balken waargenomen. Veranderingen in de doorbuigingen van de balk als gevolg van vermoeiingsschade zijn alleen waargenomen gedurende de laatste paar duizend lastwisselingen (minder dan 0.1% van het totaal aantal lastwisselingen). Het maximaal aantal lastwisselingen tot bezwijken neemt af als gevolg van corrosie van de wapeningsstaaf in de balk. In de uitgevoerde proeven was het maximale aantal lastwisselingen in een gewapend betonnen balk met een onbeschadigde (niet

corroderende) wapeningsstaaf 30-50% hoger dan het aantal lastwisselingen tot bezwijken van een balk met een corroderende wapeningsstaaf. Naast deze reductie van het aantal lastwisselingen, verandert corrosie de doorbuigingen van de balk nauwelijks.

In EE berekeningen zijn de effecten van verschillende schadeniveaus in de wapeningsstaaf op het gedrag van de balk gesimuleerd. Met deze simulaties zijn de spanningen in de wapeningsstaaf, de spanningen in de balk en de doorbuigingen van de balk berekend als functie van de hoeveelheid schade in de wapeningsstaaf. De resultaten van de EE berekeningen zijn gebruikt in een gevoeligheidsanalyse van de doorbuigingen en eigenfrequenties op schade in de wapeningsstaaf.

Als gevolg van fluctuaties in de omgevingscondities veranderen de doorbuigingen en de eigenfrequenties van een betonnen brug. In een gevoeligheidsanalyse is het effect van veranderingen in de omgevingstemperatuur op de doorbuigingen en op de eigenfrequenties van een gewapende betonnen balk vergeleken met de door schade geïnduceerde veranderingen in de doorbuigingen en in de eigenfrequenties van een gewapend betonnen balk. Deze gevoeligheidsanalyse is uitgevoerd met Monte Carlo simulaties. De resultaten van de EE berekeningen en metingen van de buitentemperatuur zijn gebruikt als input voor Monte Carlo simulaties. Tussen resultaten van de Monte Carlo simulaties zijn gevalideerd met de resultaten van de laboratorium proeven.

De vergelijking tussen de door schade geïnduceerde veranderingen of in de doorbuiging van de gewapende betonnen balk en het effect van veranderingen in de omgevingstemperatuur op de vervormingen van de balk geeft aan dat het onwaarschijnlijk is dat de door schade geïnduceerde veranderingen in de doorbuigingen van de balk kunnen worden gehaald uit potentiële metingen van de balk. Een gelijke conclusie is getrokken bij de vergelijking tussen schade-geïnduceerde veranderingen in de eerste eigenfrequentie van de balk en het effect van veranderingen in de omgevingstemperatuur op de eerste eigenfrequentie van de balk.

De door schade geïnduceerde veranderingen in de doorbuigingen en in de eigenfrequenties van betonnen bruggen hangen af van de locatie van de beschadigde sectie. Schade in één van de wapeningsstaven in een betonnen brug kan op vele locaties beginnen. Daardoor kan er een groot aantal mogelijke veranderingen in de doorbuigingen en in de eigenfrequenties van de brug worden gesimuleerd. Door dit grote aantal is het zeer onwaarschijnlijk dat de door schade veroorzaakte veranderingen van de doorbuigingen of de eigenfrequenties van betonnen bruggen kunnen worden afgeleid uit vervormingsmetingen aan de brug. Om deze reden kunnen de doorbuigingen en de eigenfrequenties niet worden gebruikt als indicator voor vermoeiingsschade in betonnen bruggen.

Acknowledgements

Many people supported me during my PhD journey. Especially, I want to thank the following people:

First, I like to thank STW (Dutch Technology Foundation) and their partners (Rijkswaterstaat, ProRail, Strukton, BiG Grid) for the finance of this project. I like to thank Harrie Kuijper and Marco Ossendrijver (both ARCADIS) for their trust in me and for the financial support during my PhD period. Also thanks to the members of the IS2C committee.

Many thanks to my promotor Klaas van Breugel (TU Delft) for his shared knowledge, for his patience, and for his help during my research. Also many thanks to Eddy Koenders (TU Darmstadt) and Ton van Beek (TU Delft, SKG-IKOB) for their supervising. Furthermore, I like to thank the members of the scientific committee (Klaas van Breugel, Eddy Koenders, Ton van Beek, Rolf Breitenbücher, Joost Kok, Dick Hordijk, and Rob Polder) for their contributions.

Thanks to Gerd-Jan Schreppers and Jantine van Steenbergen (both DIANA FEA) for providing me their software. Many thanks to Coen van der Vliet (ARCADIS) for his support and expertise in 3D modelling. Thanks to the technicians of the microlab: John van den Berg, Maiko van Leeuwen, Gerrit Nagtegaal, and Arjan Thijsen. Thanks to the technicians of the macrolab: Kees van Beek, Ton Blom, and Fred Schilperoort. Thanks to the secretaries of the section Materials and Environment: Claudia Baltussen, Melanie Holzapffel, Nynke Verhulst, and Claire de Bruin.

I like to thank my roommates: Haoliang Huang in the first two years and Damien Palin in the second two years for the great time. I like to thank my colleagues from TU Delft and ARCADIS. I also like to thank my partners at Leiden University: Joost Kok, Arno Knobbe, Shengfa Miao, Ugo Vespier, and Ricardo Cachucho.

Last, but not least, I want to say thanks to my parents, brother, sisters, parents in law, brothers in law, sisters in law, and of course my lovely wife Margriet. I am very grateful for their mental support, their patience, their time, the possibilities they gave me, and their enthusiasm although they hardly understand the scope of my research. It helped me a lot to complete my PhD story. Many thanks.

Curriculum Vitae

René Paul Veerman

I was born in Naarden, The Netherlands on January 21, 1985.

In 2003, I started my education in Civil Engineering at the University of Applied Science of Amsterdam. In 2006, I received a degree of Bachelor in Build Environment (BBE). I conditioned my education at Delft University of Technology. I received a degree of Master of Science (MSc) in 2009.

Since 2009, I work at ARCADIS as structural engineer of concrete structures. I have a broad experience in the design of bridges, tunnels, and railway structures. The second Countunnel in Amsterdam, the railway station of Eindhoven, and the A2 tunnel in Maastricht are examples of the projects where I was involved in the engineering.

In November 2011, I obtained a PhD position at Delft University of Technology, under supervising of prof.dr.ir. K. van Breugel and prof.dr.ir E.A.B Koenders. My PhD research was part of the InfraWatch Project. Together with two PhD candidates of Leiden University, I worked in order to find the opportunities for using Structural Health Monitoring data in predicting the health and the remaining service-life of a monitored concrete bridge. My part of this research was to investigate how deflections and natural frequencies of concrete bridges change during their service-life, and how the deflections and natural frequencies are influenced by damage in the bridge.

In January 2016, I continued my work as structural engineer at ARCADIS. I was involved in re-calculations of existing bridges and houses. Most of my work exists in complex seismic calculations to upgrade the seismic strength of houses in the Groningen Earthquake area in the Netherlands. Beside my engineering work, I continued writing my dissertation and finishing my PhD research.

List of publications

Impact of Cyclic Loading and Corrosion on the Deflections of Reinforced Concrete Beams

R.P. Veerman
FIB Symposium 2017, Maastricht The Netherlands 12-14 June 2017.

Dynamic Deformations of Reinforced Concrete Beams During Their Total Service-Life

R.P. Veerman and A. v Beek
Fifth International Symposium on Life-Cycle Civil Engineering 2016, Delft The Netherlands 16-19 October 2016.

Effect of Corrosion on the Fatigue Service-life on Steel and Reinforced Concrete Beams

R. Veerman, K. v Breugel, and E. Koenders
FIB Symposium 2015, Copenhagen Denmark 18-20 May 2015.

Dynamic Loaded Beam Failure Under Corroded Conditions

R.P. Veerman and E.A.B. Koenders
3rd International Conference on Service Life Design for Infrastructures, Zhuhai China, 15-17 October 2014.

Measuring Deflections of a Corroded Beam Loaded Dynamically by a Four-point-bending Test

R.P. Veerman
The 10th FIB International PhD Symposium in Civil Engineering, Québec Canada, 21-23 July 2014.

Automatic Degradation Detection During a Dynamic Loaded Beam Test

R.P. Veerman and E.A.B. Koenders
CIC – Concrete Innovation Conference, Oslo Norway, 11-13 June 2014.

Changing Model Properties with Time due to Corrosion of a Dynamically Loaded Reinforced Concrete Beam

R.P. Veerman and E.A.B. Koenders
The 1st International Conference on Ageing of Materials & Structures, Delft The Netherlands, 26-28 May 2014.

Structural Monitoring Modal Properties of a Real Time Bridge and Lab Tests

R.P. Veerman and E.A.B. Koenders
The 4th International FIB congress, Mumbai India, 10-14 February 2014.

Data-intensive Structural Health Monitoring in the Infrawatch Project

R. Veerman, S Miao, E. Koenders, and A Knobbe
The 6th International Conference on Structural Health Monitoring of Intelligent Infrastructure, Hongkong China, 9-11 December 2013.

Modal Analysis of a Concrete Highway Bridge – Structural Calculations and Vibration-based Results

S Miao, R. Veerman, E. Koenders, and A Knobbe
The 6th International Conference on Structural Health Monitoring of Intelligent Infrastructure, Hongkong China, 9-11 December 2013.

Understanding the impact of Degradation of Concrete Structures

R.P. Veerman and E.A.B. Koenders
International IABSE Conference, Rotterdam The Netherlands, 6-8 May 2013.

The Dutch road infrastructural network contains a large number of concrete bridges. 60% of these concrete bridges are built before 1975. In the last fifty years, road traffic has increased significantly. As result of the increased traffic loads, the probability of fatigue damage increased. Also the use of de-icing salts has increased significantly in the last fifty years. De-icing salts can penetrate into concrete structures and potentially generate corrosion of the steel reinforcement. The combined effect of fatigue and corrosion can reduce the service-life of concrete bridges.

Deflections and natural frequencies of a damaged concrete bridge are different from deflections and natural frequencies of the same bridge under undamaged conditions. The deflections and the natural frequencies of a concrete bridge could be used as indicators for damage in a bridge. Therefore, Structural Health Monitoring systems on bridges often contain sensors to obtain the deflections or the vibrations of the bridge. In this dissertation, the effect of fatigue and corrosion on the deflections and the natural frequencies of Reinforced Concrete beams was investigated to obtain information on these potentially parameters for Structural Health Monitoring.